



HAL
open science

Large Eddy Simulation of the steam cracking process in refinery furnaces

Sreejith Nadakkal Appukuttan

► **To cite this version:**

Sreejith Nadakkal Appukuttan. Large Eddy Simulation of the steam cracking process in refinery furnaces. Physics [physics]. Institut National Polytechnique de Toulouse - INPT, 2022. English. NNT : 2022INPT0024 . tel-04192227

HAL Id: tel-04192227

<https://theses.hal.science/tel-04192227v1>

Submitted on 31 Aug 2023

HAL is a multi-disciplinary open access archive for the deposit and dissemination of scientific research documents, whether they are published or not. The documents may come from teaching and research institutions in France or abroad, or from public or private research centers.

L'archive ouverte pluridisciplinaire **HAL**, est destinée au dépôt et à la diffusion de documents scientifiques de niveau recherche, publiés ou non, émanant des établissements d'enseignement et de recherche français ou étrangers, des laboratoires publics ou privés.



Université
de Toulouse

THÈSE

En vue de l'obtention du

DOCTORAT DE L'UNIVERSITÉ DE TOULOUSE

Délivré par :

Institut National Polytechnique de Toulouse (Toulouse INP)

Discipline ou spécialité :

Energétique et Transferts

Présentée et soutenue par :

M. SREEJITH NADAKKAL APPUKUTTAN

le mercredi 12 janvier 2022

Titre :

Large Eddy Simulation of the steam cracking process in refinery furnaces

Ecole doctorale :

Mécanique, Energétique, Génie civil, Procédés (MEGeP)

Unité de recherche :

Centre Européen de Recherche et Formation Avancées en Calcul Scientifique (CERFACS)

Directeur(s) de Thèse :

MME BÉNÉDICTE CUENOT

MME ELEONORE RIBER

Rapporteurs :

M. RONAN VICQUELIN, CENTRALESUPELEC GIF SUR YVETTE

M. TAPAN SENGUPTA, INDIAN INSTITUTE OF TECHNOLOGY

Membre(s) du jury :

MME FRÉDÉRIQUE BATTIN-LECLERC, UNIVERSITÉ LORRAINE, Président

M. GILLES THEIS, John Zink International Luxembourg, Membre

MME BÉNÉDICTE CUENOT, CERFACS, Membre

MME ELEONORE RIBER, CERFACS, Invité(e)

सुखार्थिनः कुतो विद्या नास्ति विद्यार्थिनः सुखम् ।
सुखार्थी वा त्यजेद्विद्यां विद्यार्थी वा त्यजेत्सुखम् ॥

-महाभारथा, उद्योगपर्वन, 40.6

There is no knowledge for the seekers of comfort, and no comfort for the seekers of knowledge. A seeker of comfort should give up knowledge, and a seeker of knowledge should give up comfort.

-Mahabharatha, Udyogaparvan 40.6

Abstract

There has been a tremendous increase in the production of ethylene over the last few decades and this trend is expected to be so in the future as well. Steam cracking being the principal process used for producing ethylenes has been the subject of various experimental and numerical studies in the past. With depleting sources of non-renewable energy, increasing cost of fuel and stringent norms on emissions from steam cracking plants there has been considerable focus on making the combustion process inside the furnace more energy efficient and lesser polluting. This study, performed as a part of IMPROOF (**I**ntegrated guided **M**odel **P**ROcess **O**ptimization of steam cracking **F**urnaces) project, is intended towards attaining that goal.

Large Eddy Simulation (LES)- a promising tool towards gaining in-depth understanding of the flow and combustion processes is at a stage of being mature enough to be used in design and optimization of processes in industrial equipments. However, the application of LES to study large flow equipments is still a technical challenge due to the high computational cost arising from numerical stiffness. In this study, a novel, chimera-based, local time stepping scheme is developed to speed up explicit time integration based LES solvers and applied (for the first time) to study the reactive flow inside a steam cracking furnace. This new numerical technique is studied for its numerical properties using Global Spectral Analysis (GSA) and the impact of local time stepping on the accuracy and resolution of the baseline numerical scheme is analysed. The method is found to incur minimal changes in the numerical properties of the baseline numerical scheme. The speed up obtained using this method is also ascertained with the help of canonical 2D and 3D non-reactive as well as reactive flow simulations.

Numerical predicting of combustion inside a steam cracker comes with its own challenges. While detailed chemical mechanisms are ruled out from being used in simulations with a transported species framework due to its high cost, simple global chemical mechanisms are not accurate enough to predict the flame structure and flame properties accurately. Flamelet models provide computationally feasible solutions although the assumption of equilibrium chemistry or the use of probability density functions can be far-fetched. In this study, species transport equations are used with an analytically reduced chemical (ARC) mechanism. These chemical mechanisms are reduced from an up-to-date detailed mechanism using Directed Relational Graph with Error Propagation (DRGEP) technique and quasi-steady state (QSS) assumptions. The reduced mechanism is validated with respect to the detailed mechanism and is found to be in excellent agreement with it for all the flame properties of interest in this study. Furthermore, the reduced mechanism is also validated with experimental data on a real laminar diffusion flame and is found to have good match with experimental measurements underlining its superior accuracy to be used in the LES of the steam cracking furnace.

Radiative heat transfer is the predominant mode of heat transfer in steam cracking furnaces and hence cannot be avoided in realistic furnace simulations. In

this study, the LES solver (along with the newly developed acceleration technique) is coupled with a radiative transfer equation (RTE) solver to carry out a coupled LES-RTE simulation. The approach is validated with experimental data from an axisymmetric jet diffusion flame and the experimental and numerical data is observed to be in good agreement with each other.

Finally, all these methodologies are simultaneously applied to study the reactive flow occurring in the fire side of a steam cracking furnace. The LES acceleration technique speeds up the computations while ARC mechanism assists in predicting combustion reactions in an accurate manner. The radiative heat transfer effects are included by coupling the LES solver with the RTE solver as mentioned previously. Unsteady LES simulations of the combustion occurring inside the firebox is carried out. The computed and measured data for temperature and heat flux is found to be in close agreement with each other. LES of such a furnace demonstrates revealing information on the flame stabilization mechanism and the mean flame properties such as its shape and length. As expected, two combustion zones are found to be present in the firebox- the primary zone located inside the burner and confined by the burner tiles while the secondary zone which is attached to the burner tile. Flame inside the furnace is observed to be stabilized by the recirculation of flue gases aided by heat loss to the process gas. Most of the heat of reaction was found to occur in the first 2 m from the furnace floor while the remaining volume of the firebox is predominantly filled with exhaust gases. The flow field and turbulence in the furnace is also studied and reported.

This study is intended to be a technology demonstrator by addressing three of the core challenges in the numerical modeling of steam cracking furnaces. While most of the industrial sectors such as aviation and transportation have adopted LES as a design tool today, the petrochemical industry is still relying on RANS as its workhorse CFD tool. By addressing three of the current day challenges in performing LES of steam cracking furnaces through this thesis, it is hoped that the petrochemical community is taking one step closer to using LES for their design and analysis processes in the near future.

Acknowledgments

I would like to render my sincere gratitude to Prof. Vicquelin and Prof. Sengupta for carefully reviewing this thesis report and providing valuable feedback on its technical content. I would like also like to thank the other members of the thesis jury, namely, Prof. Leclerc and Mr. Gilles for accepting my invitation and attending my thesis defense.

I would like to thank Prof. Thierry Poinot for introducing me to CERFACS. My experience at CERFACS was enlightening in every sense of the word. Fluid dynamics and its core subject of turbulence is in itself a very challenging subject. The addition of combustion chemistry and the changes brought about by the presence of multiple species, their transport and thermal properties makes the subject even more challenging and captivating at the same time. In spite of my past work experience in the gas turbine industry, there was something new for me to learn everyday at CERFACS.

Words alone cannot express my gratitude towards both of my advisors- Dr. Eleonore Riber and Dr. Benedicte Cuenot for providing me technical guidance and support for my thesis related work. I should be very honest in admitting that they were extremely patient and helpful in answering some of my really weird and at times silly technical doubts. Working with them was also an enriching experience even beyond the technical realm- I was reintroduced into the world of research and academia after a considerable gap of six years of industrial job, interactions with them helped me to look at real world technical challenges in a critical and analytical manner and improved my technical narration and documentation skills.

My gratitude also extends to Prof. Tapan k. Sengupta (High Performance Computing Lab, IIT Dhanbad, India) for introducing me to the world of high performance computing. I consider the time I spent at HPCL as a turning point in my career. He has been more than a Masters' thesis advisor to me, guiding me through tough times in my life. I would also like to thank the senior staff at CERFACS- Dr. Laurent Gicquel, Dr. Gabriel Stafflebach and Dr. Florant Duchaine for their technical guidance related to HPC and solvers. Dr. Jerome Dombard, was always welcoming my questions and queries and used to enthusiastically provide me with suggestions/answers. Dr. Olivier Vermorel was also someone whom I could walk upto and enquire about AVBP and get my queries clarified.

I would also like to thank my ex-colleagues from CERFACS- Lucas Escaplez, Dario Maestro, Robin Campet, Aravind Balan and Christoff Corexias for their support in getting accustomed to a new phase of my life at CERFACS.

My gratitude also goes to my current colleagues- Dr. David Laera who has been really helpful in guiding and helping me with general research related activities. My coffee sessions and hilarious conversations that I had with Varun, Abhijeet, Soumyo, Shubham and Pavan are moments I am going to cherish for the rest of my life. My stay at CERFACS wouldn't have been enjoyable without the assistance of the non-technical staff- Marie Labadens, Michelle Campassens and

Nicole Boutet. They have helped me in all administrative processes especially the ones involving French. The CSG team (Dr. Dast, Fabrice and Gerard) and the librarian- Severine Toulouse were also immensely helpful, helping me solve issues almost instantly.

Last but not the least, I would like to thank my Mother and (late) Father for having me provided such wonderful things in life and helping me reach my career goal. I would also like to thank my sister and my brother-in-law for their support. Suman Moparthy, my friend has always been a motivation for me. The discussions we had over science and anything under the sun has helped me look at the way I should organise my thesis. Finally, I would love to thank my partner-to-be, Krishna Gopinath for words of love, affection and respect which kept me going through tough times.

Dedication

To Achan, Amma, my Gurus and the Almighty
Not to forget the three sweet ladies in my life- Sudha, Aparna and Krishna
for their unconditional love and support

Contents

List of Figures	viii
List of Tables	xv
1 Introduction	1
1.1 Relevance of combustion today	1
1.2 Olefins production and market	4
1.2.1 Methanol to Olefins (MTO) process	5
1.2.2 Fischer-Tropsch Synthesis (FTS)	6
1.2.3 Oxidative Coupling of Methane (OCM)	6
1.2.4 Steam Cracking	6
1.3 Details of the steam cracking process	7
1.3.1 <i>Cold section</i>	8
1.3.2 <i>Hot section</i>	8
1.3.3 Refractory	11
1.3.4 Radiant tubes	11
1.3.5 Burners	12
1.3.6 Latest improvements	14
1.4 Current challenges faced in steam cracking	16
1.5 Role of numerical modeling	19
1.6 Objectives and organization of the thesis	24
1.7 Acknowledgment	27
I Governing Equations and Numerical Methods	28
2 Governing equations	31
2.1 Objectives	31
2.2 Fluid flow equations, assumptions and boundary conditions	31
2.2.1 Governing Equations	32
2.2.2 Physical Assumptions	33
2.2.3 LES Governing Equations	36

2.2.4	Numerical Assumptions	36
2.2.5	Turbulent source terms	39
2.2.6	Boundary conditions	39
2.3	Radiative heat transfer	41
2.3.1	Governing equations	41
2.3.2	Physical assumptions	43
2.3.3	Boundary conditions	44
2.4	Conclusions	44
3	Numerical methods and their analysis	46
3.1	Literature survey	47
3.2	Objectives of this chapter	51
3.3	Numerical methods in AVBP	51
3.4	Analysis of numerical schemes in AVBP	54
3.4.1	1D Linear Convection Equation (LCE)	54
3.4.2	1D Linear Convection-Diffusion Equation (LCDE)	62
3.4.3	1D Linear Convection-Diffusion-Reaction Equation (LCDRE)	75
3.5	Conclusions	81
4	Development and analysis of LESAULTS method	84
4.1	Introduction	84
4.2	Literature Survey	85
4.3	Objectives of this chapter	89
4.4	LESAULTS Method	89
4.5	Theoretical Computational Speedup	94
4.6	Design of LESAULTS method	97
4.7	Error Analysis	106
4.7.1	GSA of LESAULTS method	106
4.7.2	Application to LCDE	110
4.7.3	Validation of LESAULTS method	114
4.7.4	Order of accuracy	123
4.7.5	Conservation property of LESAULTS	124
4.8	Numerical Validation	126
4.8.1	2-Dimensional isentropic vortex convection	126
4.8.2	Flow past 3D circular cylinder	130
4.8.3	Sandia-D	133
4.9	Conclusions and Perspectives	142

II	Application to Furnace Simulation	146
5	Analytical chemical mechanism reduction	148
5.1	Introduction	148
5.2	Literature survey	149
5.3	Objectives of this chapter	156
5.4	A comparison of methane-air combustion mechanisms	157
5.5	Chemical mechanism reduction using ARCANE	162
5.5.1	DRG with error propagation (DRGEP)	162
5.5.2	Chemical lumping	163
5.5.3	QSS Assumption	163
5.5.4	Thermal and Transport properties	164
5.6	Validation of reduced mechanism	165
5.6.1	Validation using 1DUP flames	165
5.6.2	Validation using IDT	167
5.6.3	Validation using 1DCD flames	168
5.6.4	Application to a 3-dimensional laminar flame	170
5.7	Conclusions	176
6	Modeling radiative heat transfer effects	178
6.1	Introduction	178
6.2	Literature Survey	179
6.3	PRISSMA RTE Solver	181
6.3.1	Angular discretisation	182
6.3.2	Spatial discretisation	183
6.3.3	Spectral discretisation	184
6.4	LESAULTS-PRISSMA Coupling Strategy	185
6.5	Validation of LESAULTS-PRISSMA Coupled solver	189
6.6	Conclusions	194
7	Application to LES of steam cracking furnace	197
7.1	Test Furnace Configurations	197
7.2	Geometric modeling	199
7.2.1	Computational Domain	199
7.2.2	Boundary conditions	200
7.3	Grid generation	201
7.4	Computational settings	203
7.5	Results	204
7.6	Conclusions	212

8	Conclusions and Perspectives	214
A	Analytically reduced mechanism	217
	Bibliography	219

List of Figures

1.1	EIA 2020 Report [1] (a) Historical and projected energy production in the United States by fuel in Quadrillion BTUs (b) Historical and projected energy consumption in the United States by sector in Quadrillion BTUs	2
1.2	EIA 2020 Report [1] (a) Historical and projected industrial energy consumption by source in the United States (Quadrillion BTUs) (b) Historical and projected energy consumption in the United States by industrial sector (Quadrillion BTUs)	3
1.3	EIA 2020 Report [1] (a) Historical and projected CO ₂ emissions (in MT) in the United States by fuel (b) Historical and projected CO ₂ emissions (in MT) in the United States by sector	3
1.4	Goods produced from olefin derivatives used in our day-to-day life	5
1.5	Schematic of a typical steam cracking plant. The boxes colored in green indicate the hot section while the one colored in blue refers to the cold section. Figure courtesy: [23]	7
1.6	Schematic of a typical hot section in SC plant.	8
1.7	Classification of furnace fireboxes based on shapes	10
1.8	Classification of furnace fireboxes based on burner arrangement	11
1.9	A typical steam cracking burner schematic	12
1.10	Different types of steam cracking burners ((a) PVYD burner (b) HAWAStar burner (c) PSFFG burner (d) PSMR burner)	14
1.11	(a) Cutaway of CoolSTAR burner (b) Flame generated from CoolSTAR burner [27]	16
1.12	Total, resolved, and modeled scales in RANS (a) and LES (b)	21
1.13	The organization of this thesis	26
3.1	Scatter and gather operation in AVBP	52
3.2	Stencil used in viscous flux calculation in AVBP	54

3.3	Dispersion relation properties for LW and TTGC scheme when applied to the 1D linear convection equation.	60
3.4	q-Waves observed in the solution of LCE using LW and TTGC schemes. $kh = 1.8$ and $N_c = 0.01$ values are used. The LW solution is can be observed to propagate upstream while TTGC scheme propagates at half the right speed.	61
3.5	Contours of G_{rel} for LW scheme at various values of Pe	67
3.6	Contours of G_{rel} for TTGC scheme at various values of Pe	68
3.7	Numerical solution of LCDE with initial wavepacket solution. LW-CD ₂ is used with $k_0h = 1.8$, $N_c = 0.01$, $Pe = 0.5$	69
3.8	Contours of non-dimensionalised numerical group velocity $V_{g,n}/C$ for LW scheme at various values of Pe	70
3.9	Contours of non-dimensionalised numerical group velocity $V_{g,n}/C$ for TTGC scheme at various values of Pe	71
3.10	Contours of non-dimensionalised numerical diffusion coefficient α_{num}/α for LW-CD ₂ scheme at various values of Pe	72
3.11	Contours of non-dimensionalised numerical diffusion coefficient α_{num}/α for TTGC-CD ₂ scheme at various values of Pe	73
3.12	Numerical solution of 1D LCDE calculated using LW-CD ₂ for a wavepacket with $kh = 1.0$ at time $t=0.315$. $Pe = 0.0001$ and $N_c = 0.35$	74
3.13	Contours of G_{rel} for various values of Da and Pe computed for the LW scheme	78
3.14	Contours of G_{rel} for various values of Da calculated for LW (left column) and TTGC (right column) schemes. The Pe value used is 10^{-5}	79
3.15	Iso-surface of $ G_{num} = 1$ in the $Da - N_c - Pe$ space for the LCDRE equation for (a) LW (b) TTGC	80
3.16	Contours of $V_{g,num}/c$ for various values of Da calculated for LW (left column) and TTGC (right column) schemes. The Pe value used is 10^{-5}	81
3.17	Contours of α_{num}/α for various values of Da calculated for LW (left column) and TTGC (right column) schemes. The Pe value used is 10^{-5}	82
4.1	Schematic showing time step in LES using (a) Conventional LES solver (b) LESAULTS method based LES solver	90
4.2	Schematic of conventional and LESAULTS method applied to a 1D domain. (a) single domain used in conventional solver and sub-domains used in LESAULTS method. (b) An exaggerated view of overlapped zones	91
4.3	Various stages in the LESAULTS method (a) Intermediate time	

LIST OF FIGURES

4.5	Solution in the two sub-domains and in the overlapped zone after the intermediate time integration stage	97
4.6	Variation of the weighing function α_c along the overlapped zone .	99
4.7	Schematic of error at boundary nodes after intermediate time integrations	99
4.8	Variation of $\epsilon_{bnd,i}$ as a function of kh at $N_c = 0.1$ for various nodes near the boundary.	104
4.9	Node number at which the maximum error is less than or equal to cutoff error plotted for various $R_{\delta t}$ values	105
4.10	1D domains used to solver 1D LCE	107
4.11	Weighing function α_c and the error ϵ in the sub-domains while using LESAULTS method	109
4.12	Contours of ϵ_G for LW and TTGC schemes at various values of $R_{\delta t}$	111
4.13	Contours of ϵ_{CN} for LW and TTGC schemes at various values of $R_{\delta t}$	112
4.14	Contours of ϵ_{Vgn} for LW and TTGC schemes at various values of $R_{\delta t}$	113
4.15	Contours of ϵ_G for LW and TTGC schemes at various values of Pe and $R_{\delta t} = 2$	115
4.16	Contours of ϵ_G for LW and TTGC schemes at various values of Pe and $R_{\delta t} = 5$	116
4.17	Contours of ϵ_G for LW and TTGC schemes at various values of Pe and $R_{\delta t} = 10$	117
4.18	Contours of ϵ_{Vgn} for LW and TTGC schemes at various values of Pe and $R_{\delta t} = 2$	118
4.19	Contours of ϵ_{Vgn} for LW and TTGC schemes at various values of Pe and $R_{\delta t} = 5$	119
4.20	Contours of ϵ_{Vgn} for LW and TTGC schemes at various values of Pe and $R_{\delta t} = 10$	120
4.21	LESAULTS method applied to the solution of LCE. The initial solution is provided as a wavepacket centered at $x = 0.5$ and $kh = 0.5$	122
4.22	LESAULTS approach used to solve the test case with initial solution of Gaussian curve using TTGC scheme.	123
4.23	Error calculated for various mesh size h using LW and TTGC schemes for $R_{\delta t} = 10$	124
4.24	Conventional and a two-domain LESAULTS decomposition on a 1-D domain. ω_C and ω_L denote overlapped zones.	125

4.25	(a) Computational domain used in 2d COVO test case, (b,c,d) Non-dimensional pressure along the centerline at various time instants. Solution shown is that of Case 8	127
4.26	Error ϵ_{cov0} calculated for (a) Uniform mesh spacing (b) Variable mesh spacing	130
4.27	(a) Computational domain and boundary conditions used to solve the 3D flow past a circular cylinder. (b) Zoomed view on the LESAULTS partitioning	131
4.28	Variation of non-dimensional mean longitudinal velocity along non-dimensional y-coordinate at longitudinal planes calculated using conventional and LESAULTS method	134
4.29	Variation of non-dimensional mean lateral velocity along non-dimensional y-coordinate at longitudinal planes calculated using conventional and LESAULTS method	135
4.30	Variation of non-dimensional U_{rms} along non-dimensional y-coordinate at longitudinal planes calculated using conventional and LESAULTS method	136
4.31	Variation of non-dimensional V_{rms} along non-dimensional y-coordinate at longitudinal planes calculated using conventional and LESAULTS method	137
4.32	Variation of non-dimensional UV_{rms} along non-dimensional y-coordinate at longitudinal planes calculated using conventional and LESAULTS method	138
4.33	Computational domain and mesh generated for the Sandia-D flame using LESAULTS method	139
4.34	Radial profiles of mean and rms temperatures plotted at axial downstream planes	143
4.35	Radial profiles of mean mixture fraction and CH4 mass fraction plotted at axial downstream planes	144
4.36	Radial profiles of CO and CO2 mass fraction plotted at axial downstream planes	145
5.1	Increase in computing power (a) and chemical mechanism size (b) in the past decades	152
5.2	Schematic of DRG applied to species in a chemical mechanism	155

LIST OF FIGURES

5.3	Computed and measured values of (a) laminar flame speed (S_L) at various equivalence ratios (ϕ) (b,c,d) Ignition delay time for three different equivalence ratios	159
5.4	Computed and measured (a,b) temperature profiles for strain rates of 20,35 respectively (c,d) NO profiles for strain rates of 20,35 respectively	160
5.5	A schematic of the chemical mechanism reduction process applied to POLIMI mechanism used in this study	164
5.6	Global properties of 1D laminar unstretched premixed flame computed using detailed and reduced mechanism for various values of ϕ . Error bars are plotted with respect to detailed mechanism . . .	166
5.7	Spatial profiles of species and temperature in an 1D, unstretched laminar premixed flame computed using detailed and reduced POLIMI mechanism	167
5.8	Spatial profiles of species and temperature in an 1D, unstretched laminar premixed flame computed using detailed and reduced POLIMI mechanism	168
5.9	Comparison of detailed and reduced mechanism for ignition delay time computations	169
5.10	Global diffusion flame properties computed using detailed and reduced mechanisms. Error bars are plotted with respect to the detailed mechanism	171
5.11	Spatial profiles of major species mass fractions at two different strain rates	172
5.12	Schematic of the (a) experimental flame configuration (b) computational domain used in this study	173
5.13	Radial profiles of CH_4 , O_2 and CO mole fractions plotted at axial downstream planes	174
5.14	Radial profiles of CO_2 , H_2O and H_2 mole fractions plotted at axial downstream planes	175
5.15	Radial profiles of temperature plotted at axial downstream planes	176
6.1	Coupling approaches used for the AVBP-PRISSMA configuration. (a) Synchronous coupling (b) Asynchronous coupling	186
6.2	Coupling approach used for the LESAULTS-PRISSMA configuration. LESAULTS configuration comprises of three sub-domains ($N_{sub} = 3$).	188

6.3	Computational domain used for simulating the diffusion flame. (a) The geometrical dimensions (b) Boundary conditions used in the analysis	191
6.4	Domain decomposition employed for LESAULTS method along with a view of the mesh at the mid-plane.	193
6.5	Computational domain used for simulating the diffusion flame. (a) The geometrical dimensions (b) Boundary conditions used in the analysis	194
6.6	Computed solution at the midplane	195
6.7	The computed radiative source term and heat flux at the midplane	195
6.8	A comparison of the measured and computed radiative heat flux .	196

LIST OF FIGURES

7.1	Schematic of the test furnace and the burner used in this study	199
7.2	(a) The computational domain and boundary conditions used for LES of furnace. (b) Nomenclature of staged and primary fuel pipes	202
7.3	(a) The domain decomposition strategy used in LES. Furnace divided into 3 overlapping sub-domains with different time steps (b)OH mass fraction contours on a vertical plane passing through the center of the burner	202
7.4	(a) The mean vertical velocity contours on the furnace mid-plane. (b) Streamlines from the mean velocity field inside the furnace	205
7.5	(a)Mean streamlines emanating from the staged and primary fuel ports outside the burner (b) Mean streamlines entering radially into the burner	205
7.6	Non-dimensional TKE (a) profiles at various heights along the furnace mid-plane (b) contours at the horizontal plane passing through fuel orifice.	206
7.7	(a) Mean mixture fraction field at a horizontal plane passing through the fuel injection holes. (b) Mean mixture fraction field inside the burner tile	208
7.8	(a) Mean temperature contours on a horizontal plane passing through the radial fuel injection holes. (b) The mean temperature contour at a horizontal plane immediately downstream of the burner tile	209
7.9	(a) Mean flame temperature observed at a plane in the vicinity of burner tile (b) Mean temperature field on the vertical plane passing through burner center	209
7.10	(a) Integrated heat release rate as a function of furnace height. (b) Scatter plot of instantaneous temperature in the mixture fraction space	210
7.11	(a) Measured and calculated temperature values at three vertical locations inside the furnace. (b) Measured and computed heat flux profiles	211
7.12	Mean species mass fraction profiles at various horizontal planes downstream of the burner	212

List of Tables

1.1	Some of the articles on the numerical simulation of furnaces performed in the past	23
4.1	Table showing the sub-domains, time steps and the number of intermediate time integration steps for the LESAULTS configuration shown in Figure 4.2	92
4.2	Numerical tests performed using LESAULTS method for the LCE. ϵ_G and ϵ_{Vgn} values provided are from GSA analysis	121
4.3	Numerical experiments performed using 2-D isentropic vortex convection test case	128
4.4	Numerical experiments performed using isentropic vortex convection test case	129
4.5	Theoretical and actual speed up obtained for the LES of 3D flow past a cylinder	132
4.6	Theoretical and actual speed up obtained for the LES of 3D flow past a cylinder	141
5.1	The detailed mechanisms used in this comparative study and the number of species and reactions in them	157
6.1	Details of the mesh and time step size used in the LESAULTS approach, along with the speed up obtained	192
7.1	Air and fuel flow rate and temperature measured in the test . . .	199
7.2	Fuel flow rates and temperature through various fuel circuits modeled as boundary conditions	200
7.3	Inlet and outlet water temperature and flow rate of water flowing through the reactor coils. The reactor coil T4 is the closest to the symmetry plane and T1 is the farthest	201
A.1	Transported species and their transport properties in the reduced mechanism	217

LIST OF TABLES

Chapter 1

Introduction

Contents

1.1	Relevance of combustion today	1
1.2	Olefins production and market	4
1.2.1	Methanol to Olefins (MTO) process	5
1.2.2	Fischer-Tropsch Synthesis (FTS)	6
1.2.3	Oxidative Coupling of Methane (OCM)	6
1.2.4	Steam Cracking	6
1.3	Details of the steam cracking process	7
1.3.1	<i>Cold section</i>	8
1.3.2	<i>Hot section</i>	8
1.3.3	Refractory	11
1.3.4	Radiant tubes	11
1.3.5	Burners	12
1.3.6	Latest improvements	14
1.4	Current challenges faced in steam cracking	16
1.5	Role of numerical modeling	19
1.6	Objectives and organization of the thesis	24
1.7	Acknowledgment	27

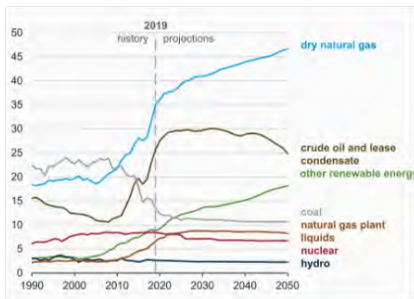
1.1 Relevance of combustion today

Combustion is the process involving chemical reactions between two or more species accompanied by the emission of energy mostly in the form of heat. It has been the primary source of energy for mankind since time immemorial and the basic use of combustion in olden days namely, lighting and heating, were superseded by its use in harnessing mechanical power after the industrial revolution in the 18th century. One of the first prime movers- steam engine, used coal as

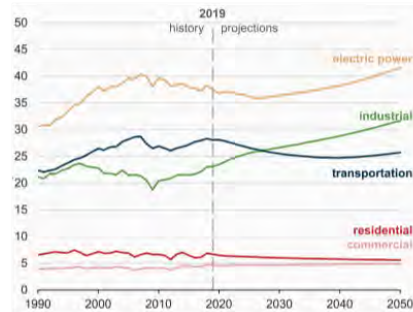
1. INTRODUCTION

fuel to burn and produced energy which was used to vaporize water to steam and produce power.

Even after two and a half centuries since the beginning of industrial revolution, our dependence on combustion as the main source of energy has seldom changed. Figure 1.1(a) shows the historical and forecasted energy production (in Quadrillion BTUs) by various fuel sources in the United States as documented by Energy Information Administration in its 2020 report [1]. Even though energy production from renewable sources is gaining momentum, the technology has not still evolved to meet the large global energy demand. While energy production from crude oil, nuclear and hydropower plants is expected to stabilize in the future, natural gas is expected to continue to be the prime source of energy owing to its low cost and wide availability. Figure 1.1(b) shows similar trends for energy consumption in various sectors in the United States. The demand for electric and industrial power is forecasted to increase monotonically at least till the middle of this century while transportation, commercial and residential energy requirements are expected to stay steady.



(a)



(b)

Figure 1.1: EIA 2020 Report [1] (a) Historical and projected energy production in the United States by fuel in Quadrillion BTUs (b) Historical and projected energy consumption in the United States by sector in Quadrillion BTUs

Figure 1.2(a) shows the energy consumed in the industrial sector based on the fuel sources used. Energy from coal is expected to be nearly constant in the coming years. Petroleum and other liquid fuels will see a gradual increase in their usage.

However, there is expected to be a strong increase in natural gas consumption in the future. Figure 1.2(b) shows the trends of energy consumption among various industry sectors. While manufacturing and non-manufacturing sector

1.1 Relevance of combustion today

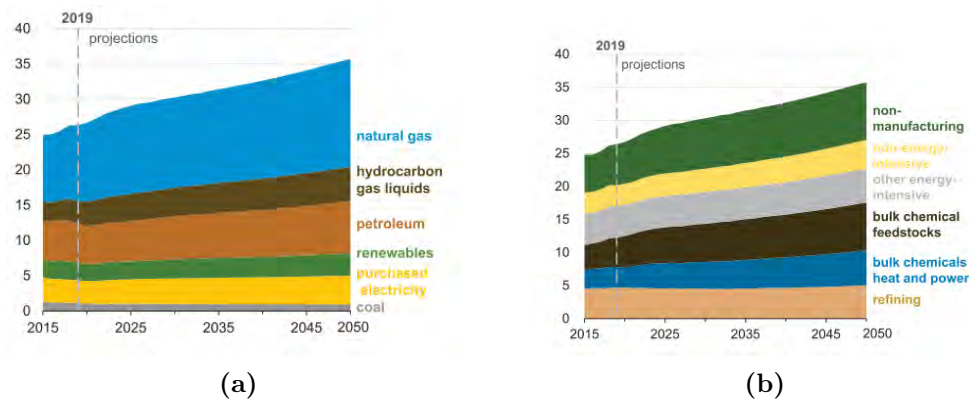


Figure 1.2: EIA 2020 Report [1] (a) Historical and projected industrial energy consumption by source in the United States (Quadrillion BTUs) (b) Historical and projected energy consumption in the United States by industrial sector (Quadrillion BTUs)

consumption is foreseen not to change appreciably, the bulk chemical, feedstock, and refining industry consumption is expected to increase in the coming decades. Combustion also brings with it challenges related to emissions of greenhouse gases and its concomitant effect on global warming. Figure 1.3(a) shows the past and projected CO_2 annual emissions (in Metric Tonnes) from various fuels in the United States. While CO_2 emissions from coal and petroleum is expected to reach a plateau by the middle of this century, contributions from natural gas is expected to increase due to its increased consumption as mentioned previously. In analogy to the energy consumption trends, the industrial sector is expected to contribute more CO_2 emissions in the coming years as can be observed in Figure 1.3 (b).

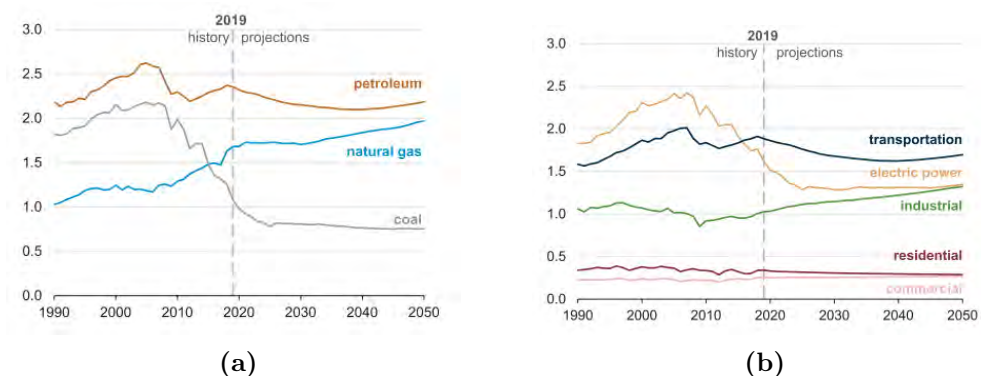


Figure 1.3: EIA 2020 Report [1] (a) Historical and projected CO_2 emissions (in MT) in the United States by fuel (b) Historical and projected CO_2 emissions (in MT) in the United States by sector

These forecasts are based on the views of current leading forecasters and

1. INTRODUCTION

demographers and the impact of unexpected global events such as Covid-19 on energy production and demand is not taken into account. The International Energy Agency in its report (Global Energy Review 2020 [2]) has studied the effect of Covid-19 on the global energy demand and consumption in 2020. It is observed that the global energy demand was reduced by a factor of 3.8% in the first quarter of 2020, due to the governmental restrictions imposed on people's movement and work. The severely hit fuel industries were that of coal (8% reduction in consumption) and crude oil (5% reduction in consumption). Natural gas was only moderately affected (2%) while renewable energy sources registered a positive growth due to its low operational cost. Even though the long-term impact of Covid-19 on global energy demands is beyond comprehension at this point in time, the trends indicate that the non-renewable sources of energy shall still continue to dominate the global energy market at the least till the middle of this century.

From the previously mentioned statistics, one could summarize the following. Firstly, even though renewable sources of energy are increasingly gaining popularity, the ubiquitous dependence of the energy sector on combustion is expected to continue at least till the middle of this century. Secondly, natural gas is predicted to be the major provider of global energy owing to its abundance and low processing cost. Finally, even in the industrial sector, energy needs will be addressed by natural gas in the immediate future and strict environmental laws and restrictions should drive innovations aimed at developing technologies that cause lesser pollution.

Among the various industry sectors, the olefin production industry and its market is one which has seen tremendous growth [3] in the last couple of decades. Also being a sector that is highly energy-intensive and contributing to emissions, salient aspects of olefin production is detailed in the next section.

1.2 Olefins production and market

Olefins are the basic building blocks of the chemical industry and their derivatives are used as raw materials in manufacturing products used in our day-to-day life (Figure 1.4).

Ethylene and propylene are the most commonly used olefins with their annual global production rates touching 150 and 80 MT [4] respectively. These production rates are expected to increase further as the standard of living of people improves. Ethylene is mainly used to produce derivatives such as polyethylene (packaging, cable insulation), ethylene oxide (fumigant, production of ethylene



Figure 1.4: Goods produced from olefin derivatives used in our day-to-day life

glycol), ethylene dichloride (PVC production) and ethyl benzene (plastics) while derivatives of propylene include polypropylene (plastic, packaging), propylene oxide (paints, cosmetics), acrylonitrile (fibers, plastics), acrylic acid (adhesives) and cumene (manufacture of rubber). Currently, many techniques are used for producing olefins and are briefly described below.

1.2.1 Methanol to Olefins (MTO) process

This method was first developed by Mobil corporation in 1977 [5] and since then significant progress has been made in gaining fundamental understanding ([6],[7],[8],[9]) on the chemical reactions involved in the process and in improving the technology ([10],[11]). MTO technique relies on catalytic conversion of methanol to lighter olefins such as ethylene and propylene. Methanol is already used in the production of a wide variety of chemicals [12] and is obtained from syngas- a mixture of CO and H₂. In the MTO process, methanol is converted to olefins in the presence of catalysts. Zeolyte catalyst (ZSM-5) and Silico-Aluminium Phosphate (SAPO)-34 are the common catalysts used in this process. MTO technology is well developed since the installation of the first plant in New Zealand in 1986 [11]. Today it is a popular technology and is used in China [13] where coal reserves are in plenty. The technique enjoys the advantage of liberty in varying ethylene to propylene ratio based on the operating conditions chosen.

1. INTRODUCTION

On the other hand, MTO requires high capital investment and produces much higher CO₂ emissions than any other olefin producing technology. The low H₂ content in syngas also demands high water consumption for H₂ enrichment which makes the process less energy efficient.

1.2.2 Fischer-Tropsch Synthesis (FTS)

This method was developed by Franz Fischer and Hans Tropsch in 1925 and is a topic of wide research ([14],[15],[16],[17],[18],[19]). Like MTO process, FTS also works on heterogeneous catalytic conversion of syngas to olefins and is the only olefin production technology that directly converts syngas to light olefins. Metals such as iron, cobalt, ruthenium and nickel are used as catalysts. The method is typically operated in two modes-low temperature and high-temperature modes, which determine the product selectivity. High-temperature mode leads to faster reactions but also favors methane production. The pressure is maintained between one to tens of Atmosphere. Some of the FTS plants operating today are in Ras Laffan, Qatar (operated by Oryx GTL), South Africa (operated by Sasol) and Malaysia (Shell). Although this process has been in existence for a long time, it is not widely popular due to its low product selectivity.

1.2.3 Oxidative Coupling of Methane (OCM)

While the previously mentioned methods involve the conversion of feedstock to syngas and then to olefins, OCM directly converts methane to ethylene and higher olefins using catalysts. The technique consists of a reactor supplied with methane and oxygen in 2:1 ratio [20]. The feedstock is provided at a temperature of 800°C and at a pressure of 250 kPa. The catalytic oxidation ensues in an exothermic manner [21] which requires cooling systems to maintain the reactor at the desired temperature. Although the direct conversion improves process efficiency, selecting suitable catalysts and the proper design of reactors to ensure safe operation has made this method nonviable for extensive commercialization.

1.2.4 Steam Cracking

Steam cracking is the principal process of producing light olefins today. In the United States, 70% of ethylene is produced by steam cracking naphtha and the remaining 30% is produced by cracking ethane [22]. In this method, lighter hydrocarbon feedstocks such as ethane, propane, and even higher hydrocarbons such as naphtha and gas oil are heated at high temperature and at specified pressure for a stipulated amount of time to produce light olefins such as ethylene and propylene.

1.3 Details of the steam cracking process

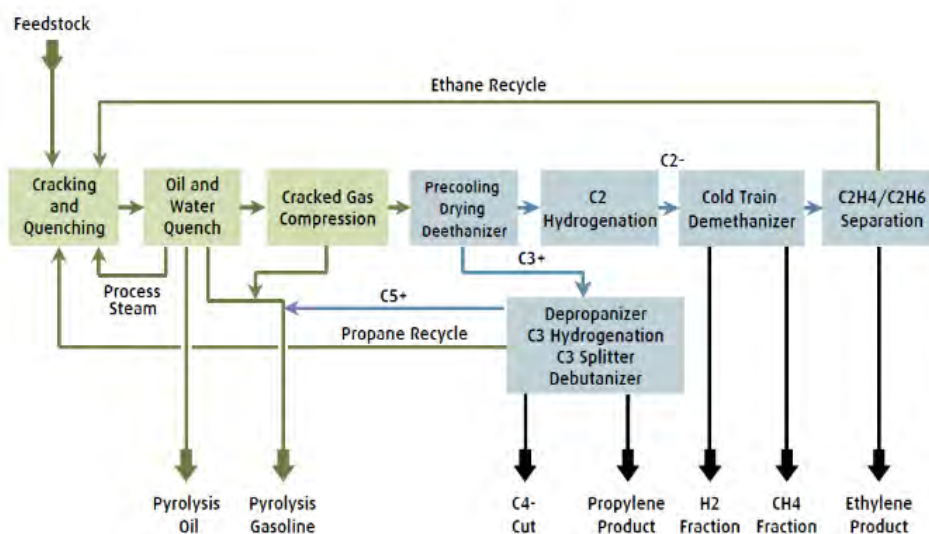


Figure 1.5: Schematic of a typical steam cracking plant. The boxes colored in green indicate the hot section while the one colored in blue refers to the cold section. Figure courtesy: [23]

Since its inception more than a century ago, the technology has matured to such an extent that an annual production of 1.5 MT [3] is feasible currently. Steam cracking also produces the least amount of CO_2 per ton of ethylene produced [3]. Due to these reasons, steam cracking is expected to continue to be the primary technology for olefin production at least for a coming couple of decades.

Since steam cracking is the subject of this thesis, the steam cracking process and the reactor configurations are detailed in the following section.

1.3 Details of the steam cracking process

As mentioned in the previous section, steam cracking is the principle and the most widely used process for the large-scale production of lighter olefins such as ethylene and propylene. In the steam cracking process, the hydrocarbon feedstock is heated to a temperature as high as 1050-1100 K at specific pressure and for a specific duration (typically 0.1-0.5 s). The hydrocarbon feedstock undergoes cracking reactions and are broken down into olefins. The product composition strictly depends on the feedstock composition and operating conditions of the reactor. In general, lighter feedstocks produce lighter olefins and higher feedstocks produce higher olefins. A schematic of a typical steam cracking plant is shown in Figure 1.5. It comprises of a cold section and a hot section.

1. INTRODUCTION

1.3.1 Cold section

The cold section consists mainly of distillation units. The compressed cracked gas coming from the hot section is sent successively through a series of complex distillation units. Firstly, it is sent through a demethanizer where methane and hydrogen are condensed and separated. This is followed by the deethanizer where ethane and ethylene are separated from the mixture, which is in turn followed by further units such as depropanizer and debutanizer based on the hydrocarbon feedstock used.

1.3.2 Hot section

The hot section consists of a furnace, a quenching system, and a cracked gas compressor as shown in Figure 1.6.

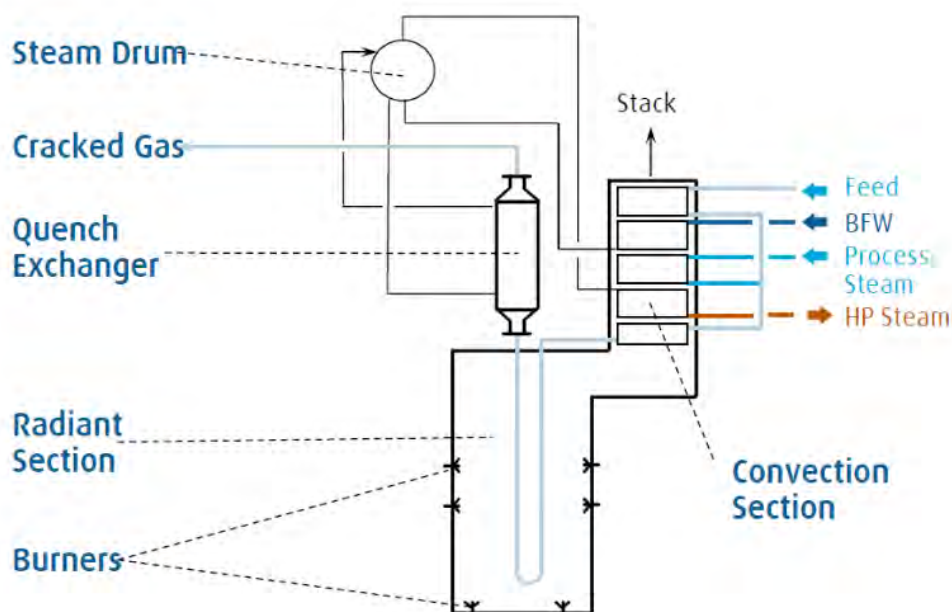


Figure 1.6: Schematic of a typical hot section in SC plant.

The furnace in the hot section consists of a convection section and a radiant section. The radiant section houses one or more burners which are used to provide heat to the process gas by burning gaseous or liquid fuels. The process gas flows through the reactor tubes hanging inside the radiant section. The convection section essentially consists of heat exchangers which are used to preheat the feedstocks before they enter the radiant section. The heated feedstock is then mixed with steam to reduce its partial pressure in order to disfavor the secondary

1.3 Details of the steam cracking process

reactions which hamper the selectivity of olefins. The mixture of feedstock and steam is then heated to a temperature of 770-950 K. They then traverse through the reactor tubes in the firebox where they are heated to a temperature of 1050-1100 K by the combustion occurring in the firebox. The residence time of the process gas inside the reactor tubes is typically 0.1-0.5 sec. Cracking reactions take place inside the reactor tubes within this time and the hydrocarbon feedstock molecules are broken down into smaller olefin molecules. The cracking reactions are endothermic in nature and the process gas picks up temperature by the time it exits the radiant section. The cracked gas mixture is at a high temperature and needs to be cooled (to approximately 870 K) to reduce the chances of any unwanted side reactions. This is achieved by using the heat from the cracked gas to boil water to form steam. This step is performed using the transfer line exchanger which carries the mixture to the quench boiler. The transfer line exchange is kept as short as possible in order to avoid any unfavorable secondary reactions. From the boiler, the cracked gas is then sent to a primary fractionation column where heavy residues are sent back to fractionation and the gasoline produced as a byproduct is separated. The dilution steam is then condensed at multiple levels and sent to the compression section. The gases are desulfurised by caustic scrubbing to remove sulphur content in the form of H_2S , COS as well as CO_2 . The remaining cracked gas is compressed, cooled and sent to the cold section.

Since this study focuses on the radiant portion of the hot section, its various components are elucidated in the following subsections.

Firebox

The firebox is a refractory-lined chamber where the process heat is provided to the feedstock. They are typically steel enclosures lined with refractory material. The burner(s) and reactor coils are located inside the firebox. Fireboxes can be either of a natural draft type where the air for combustion is induced into the firebox or a forced draft type where fans are provided upstream of the burners to force air into the firebox.

Fireboxes used in steam cracking furnaces can be classified based on their shape, layout of the reactor coils, or a combination of both [24].

Cylindrical fireboxes are easy to manufacture and take less floor space while rectangular fireboxes are used for large duties. Some of the different types of furnaces based on their shapes are shown in Figure 1.7.

Fireboxes can also be classified based on the burner arrangement as single cell, twin cell and twin cell without inner walls as shown in Figure 1.8.

1. INTRODUCTION

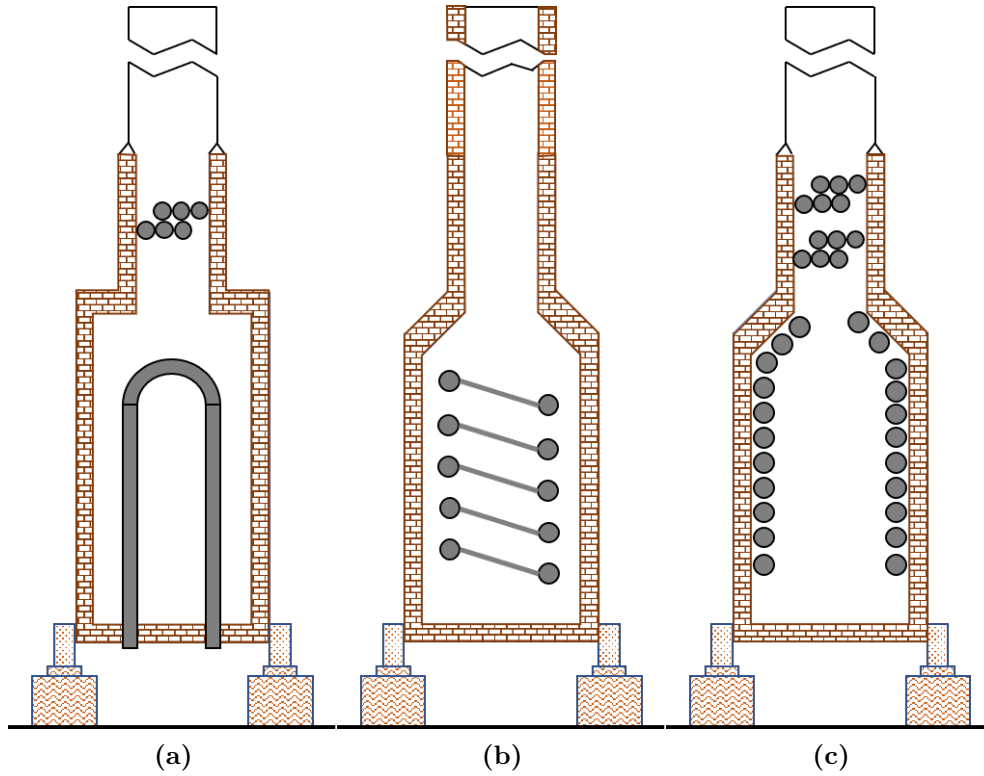


Figure 1.7: Classification of furnace fireboxes based on shapes

Steam cracker fireboxes typically come in four different burner layout configurations depending upon the furnace manufacturer, reactor coil configuration and size of the firebox:

- All wall-mounted burners
- All floor-mounted burners
- Wall and floor mounted burners
- Floor and terrace fired burners

In the early 1970s and 1980s the firing duty of a single burner was very low (typically 0.3 MW). An array of burners were then used in fireboxes in order to generate a uniformly heated firebox walls. This would in turn reradiate back to the reactor coils thereby avoiding hotspots and shadow effects. The number of burners used inside ranged from 160-170 in the 1970s to 240-300 by the late 1980s. The heat distribution to the radiant coils was varied by varying the air flow rates to these burners considering them as discrete sources of heat addition. Recently, the firing capacity of burners have drastically increased and considering the investment cost and ease of maintenance, furnace licensees have moved to

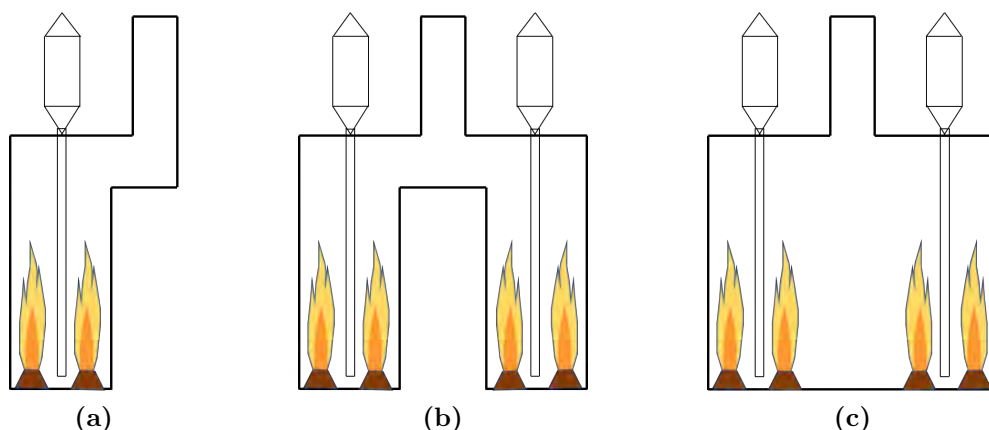


Figure 1.8: Classification of furnace fireboxes based on burner arrangement

using only a few, large-duty floor burners (typically 1.5-4 MW) in their latest designs.

1.3.3 Refractory

Refractory refers to the lining provided inside the firebox and is used to prevent heat losses from the firebox. They also aid in reflecting radiation from the flame to all sides of the reactor coils. They are made of materials like firebrick, cast refractory or ceramic blankets and are typically 10-30 cms in thickness.

1.3.4 Radiant tubes

Radiant tubes refer to the reactor coils present inside the radiant section of the firebox. They are either located close to the firebox walls or at the roof of the furnace. They can also be assembled based on the shape of the firebox. Rectangular fireboxes can accommodate both vertical and horizontal coils while only vertical coils are used in cylindrical fireboxes. Each coil is kept at a distance from each other and the firebox walls to enhance heat distribution from reradiation. Considerable attention is given to the shape and internal structure of the radiation tubes. Internally helically ribbed tubes such as Mixed Element Radiant Tubes (MERT) [25] have been shown to improve heat transfer. Slit-MERT and X-MERT tubes are improvements to MERT with 3D roughnesses and demonstrate even further improvements to heat transfer [26].

1. INTRODUCTION

1.3.5 Burners

Burners in the firebox provide the heat required to crack the feedstock by burning fuel with air. Burners used in steam cracking have a power rating ranging from (0.3 MW-4 MW) and excess air ratio ranging from 10-25%. The gauge pressure at which burner operates is typically -0.6-1.9 mBar and the pressure loss across the burner is typically 0.6-20 mBar. A typical steam cracking burner is shown in Figure 1.9. The air for combustion initially enters the burner through a noise suppression unit. The muffler is connected to an air control section which consists of blades or louvers which can be adjusted to partially open and close the inlet to let air in. The air enters the plenum (wind box) which is the section immediately before the burner tile. The purpose of the plenum is to serve air uniformly to the throat of the burner and to dampen the acoustic noise inside the burner. The burner tile is a refractory piece used to guide fuel and air flow for combustion. Fuel is injected through one or more injection ports either located inside the burner or located around the burner tile. A small pilot burner is also provided to act as an ignition source.

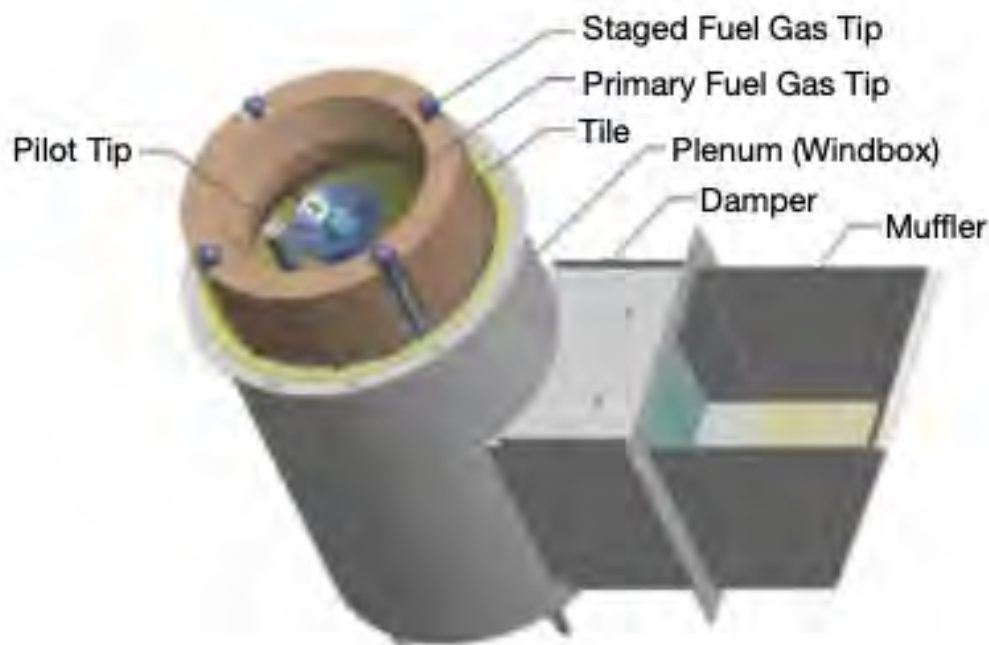


Figure 1.9: A typical steam cracking burner schematic

Burners can be classified broadly based on their NO_x emissions in the following manner [24].

- Conventional burners

- Low NO_x burners
- Ultra-low NO_x burners
- Lean premix burners

Conventional burners

Before 1980s, burner designs were aimed at creating quick mixing of fuel and air and thereby creating a short and compact flame. NO_x, CO and Unburnt Hydrocarbons (UHC) emissions and their control did not play any role in the design process. Hence, these burners were simplistic in their design and led to compact fireboxes. These burners were either premixed or partially-premixed with gas/oil as fuels. An example of such a conventional burner is the John Zink PVYD burner and is shown in Figure 1.10a.

LOW NO_x burners

As NO_x emission regulations became stringent, burner designs were aimed at producing lesser NO_x emissions. As one of the means towards achieving this objective, combustion is made to occur either under lean or rich conditions so that the flame temperature and hence thermal NO_x production is low. However, operating under such conditions also leads to high CO and UHC emissions. In order to circumvent this problem, combustion is made to occur in two zones- one rich and the other lean so that the temperature is kept low and thermal NO_x production is reduced. This is practically implemented by staging the fuel or air supply. In staged-air burners, the primary air (40% of total air) is made to burn with the complete fuel under rich conditions so that the thermal NO_x is low. Combustion is completed later by supplying the remaining secondary air at cooler conditions so that CO and UHC emissions are kept under check. An example of a staged-air Low NO_x burner is John Zink HAWAstar burner and is shown in Figure 1.10b. Staged fuel burners also work on a similar principle. Here the fuel is split into primary and staged circuits, and the combustion is forced to occur in a lean zone followed a rich zone. An example of a staged fuel burner is John Zink PSFFG burner and is shown in Figure 1.10c.

Ultra low-NO_x burners

In addition to fuel/air staging, NO_x can be further reduced by mixing the air used for combustion with flue gas from the burner. Flue gases reduce NO_x emissions in two ways. Firstly, mixing with flue gas reduces the O₂ concentration in the air

1. INTRODUCTION

available for combustion thereby reducing NO_x production. Secondly, after losing heat to the process gas, flue gas temperature is lower than the flame temperature. The dilution by flue gas hence reduces the flame temperature thereby reducing thermal NO_x. Both these factors aid in NO_x reduction. An example of Ultra low-NO_x burner is the PSMR burner shown in Figure 1.10d

Lean premix burner

Under rich conditions, lower NO_x is produced in both premix and non-premixed flames. However, under lean conditions, non-premixed flames produce much higher NO_x when compared to premixed flames. Hence, if fuel staging is implemented with a primary, lean premix flame followed later by a rich staged combustion zone, then the NO_x produced is even lower than Ultra-low NO_x burners. This is the principle of operation of a lean premix burner. An example of lean premix burner is the John Zink LPMF burner.

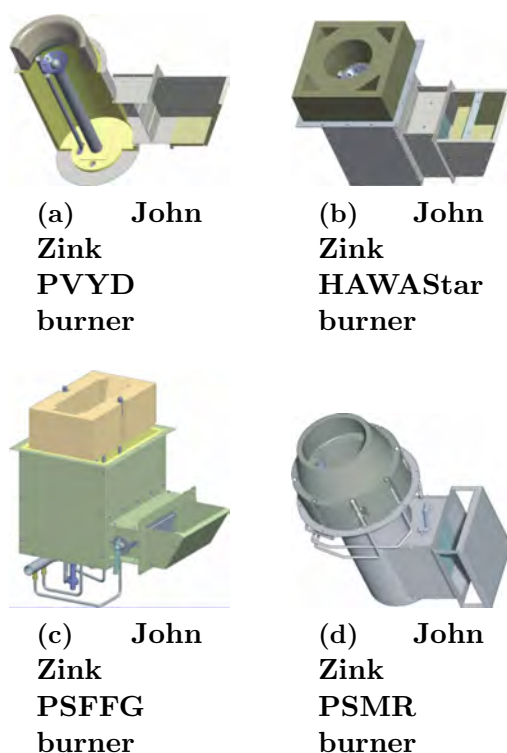


Figure 1.10: Different types of steam cracking burners ((a) PVYD burner (b) HAWAStar burner (c) PSFFG burner (d) PSMR burner)

1.3.6 Latest improvements

Further design improvements are made in the Ultra low NO_x burners to reduce the amount of NO_x produced. The first method is to improve the mixing of flue

1.3 Details of the steam cracking process

gas with fuel and air. This is implemented by incorporating a Coanda surface on the burner tiles close to the fuel injection ports. Coanda surface is able to entrain the fuel, air and flue gas efficiently thereby enhancing mixing and burning at low temperature producing lower NO_x. The second method to reduce NO_x is to increase the flame surface area in order to enhance fuel-air mixing. This is incorporated by modifying the burner tile geometry to alter the flame shape and increase the flame surface area. The third and final method is to use high pressure fuel jets located circumferentially around the burner to induce the flue gas inside the firebox and to enhance flue gas recirculation and thereby reduce NO_x as explained previously. An example of such a burner is the John Zink CoolStar burner shown in Figure 1.11 (a). Here the burner tile is divided circumferentially into multiple segments over which the secondary fuel injection occurs. This creates a folded, flower-like shaped flame as shown in Figure 1.11 (b). The increase in flame surface area, even while keeping the flame compact, aids in enhancing fuel-flue gas mixing and reducing NO_x.

1. INTRODUCTION

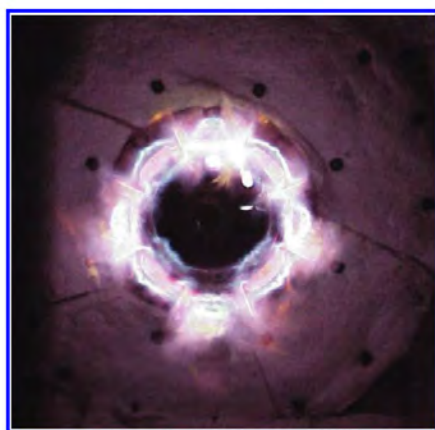
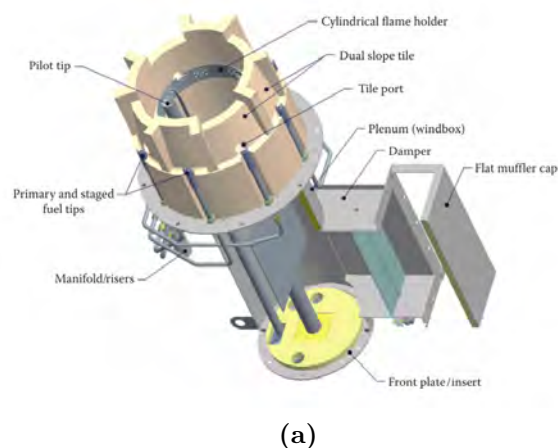


Figure 1.11: (a) Cutaway of CoolSTAR burner (b) Flame generated from CoolSTAR burner [27]

1.4 Current challenges faced in steam cracking

The first challenge faced in steam cracking furnaces is associated with coking. Coking is the undesired deposition of carbonaceous compounds on the inner walls of reactor coils. These are formed through three principle chemical pathways: (a) heterogeneous catalytic reactions (b) heterogeneous free radical mechanism and (c) homogeneous droplet condensation mechanisms. Coking adversely affects the cracking process in many ways. The carbon deposits reduce the heat transfer to the process tubes. This would demand the firebox to be run at a higher firing duty which in turn increases the radiant tube metal temperature hence weakening the tube metal. Coke deposits decrease the inner tube area and hence increase the pressure drop across the reactor coils. This in turn requires higher pressure to be applied at the coil inlet by the cracked gas compressor demanding a compressor with higher rating. The higher pressure at the coil inlet favors

1.4 Current challenges faced in steam cracking

undesirable reactions in the process gas and hence selectivity is adversely affected. Due to all these problems, the furnace might need to be periodically shut down to be decoked. This reduces the overall productivity of the steam cracker plant.

The second challenge is regarding emissions from steam crackers. It is estimated that approximately 300 MT of CO₂ [28] is being emitted annually from steam crackers all around the world. In Europe, steam crackers alone contribute to 18% of the greenhouse gas emissions from the chemical industry. 90% of CO₂ emissions from the steam cracker is associated to the high heat consumption of the endothermic cracking reactions. As mentioned previously, coking reduces the heat transfer to the process gases and hence the burner has to operate at a higher firing rate. This increases CO₂ emissions as more fuel is burnt to produce the same amount of olefins.

Regulating NO_x (NO and NO₂) emissions from burners also pose challenges to the steam cracking community. NO_x is produced as a result of oxidation of nitrogen present in air and fuel at high temperature in the flame and can cause damage to human and animal respiratory tract and lead to serious lung disorders. Presence of NO_x also leads to acid rains which can be harmful to animal life and vegetation. Currently, the best steam cracking burners use the ultra low NO_x technology emitting 35-50 ppmvd (at 3% O₂) using natural gas as fuel.

Thus any attempt to reduce the specific fuel consumption of cracking reactions will result in lower fuel being burnt and hence lower emissions. Such measures can be broadly classified as reactor side improvements and fire side improvements. Some of these measures are briefly mentioned as follows:

Reactor side innovations

One of the recent trends to improve cracking process efficiency is to use 3D reactor technology. 3D reactors rely on altering the inner surface of the reactor coils to increase the flow surface area. A higher surface area would enhance heat transfer thereby reducing the inner tube metal temperature and the propensity to cause coking. Several types of 3D reactors are available today. Longitudinal and helical finned tubes improve the heat transfer by 20-30% [28] and improve run lengths. However higher pressure drops and hence lower selectivity are some of its drawbacks. Swirl flow tubes (SFT) [29] involve straight tubes that are bent in such a manner that the tube's centerline follows a helical path. SFT enhances heat transfer rate by making the flow 3D instead of 2D. SFT does not create any obstruction to the flow and simulations indicate heat transfer improvement by a factor of 1.2-1.5 and improved run lengths. Intensified heat transfer technology (IHT) involves design modifications which enhance heat recovery such as helical

1. INTRODUCTION

baffles and coil inserts and is a proven technology which has increased the run length by 1.2-2 times. In addition, the pressure drop using this technology is least among all the 3D reactor technologies. However, several operational issues have been reported from the industry. MERT[®], SCOPE[®] and dimpled tubes also enhance heat transfer but at the cost of increased pressure drop.

Another approach to reducing coking on the reactor coils is to alter the coil material to improve its cracking/corrosion resistance. In the early days, plain carbon steel was used for this purpose. It loses strength and is susceptible to oxidation at 316-343°C. This material was replaced by alloys containing chromium (Cr) and molybdenum (Mo) through which the working temperature could be raised to 650°C. However, the corrosion resistance was still found to be poor. This paved the way for using high Cr and Nickel (Ni) alloys (25Cr-35Ni) in the 1960s and 70s. As carburization resistance improved with using 35Cr-45Ni alloys, it was employed later. Today, aluminum is added to the coil material matrix to reduce carburization and prevent coking. Tantalum is also added in small amounts to restore the deterioration of creep resistance due to the addition of Aluminium.

The final approach to mitigate coking is to use additives in the feedstock that prevent its oxidation to form coke. Dimethyl DiSulfide (DMDS), Dimethyl Sulfide (DMS) and CS₂ are used as coke production inhibitors. However, these additives have low flashing points and need special care in handling and often storage under nitrogen is required to prevent fire hazards.

Fire side innovations

Efficiency of steam crackers can also be improved by making modifications on the fire side as follows.

High emissivity coatings on the refractory linings and reactor coils can improve the energy efficiency of the furnace through three ways. Firstly, these coatings redirect the radiation to the firebox working units and reactor coils thereby making more energy available for the process gas. They also prevent heat losses to the outside of the furnace thereby improving the overall process efficiency. Finally, they also maintain uniform emissivity over a wide range of temperature thereby making the refractory more efficient. All these factors can result in considerable fuel savings. Typically these coatings consist of a refractory pigment, a high emissivity additive and a binder agent. The common refractory pigments used are Zirconia, Zirconia Silicate, Aluminum Oxide, Aluminium Silicate and Silicon Oxide. Some of the studies performed in the past demonstrate that the effect of high emissivity coatings in increasing the thermal efficiency of furnaces by 1%

([28]), lead to 5% increase in furnace performance and in reducing the furnace firing rate by 1.7%.

Another technology to improve firebox efficiency is to integrate the furnace with a gas turbine. The hot gas turbine exhaust can be used as combustion air to the furnace. This can reduce the specific fuel consumption by 19%, NO_x emission by 22%, and CO₂ emission by 5-10%. [30]. This technology has been implemented in Osaka Petrochemical's (OPC) plant in Japan and others.

A third approach is to use oxy-fuel combustion. In this method, pure oxygen is mixed with recycled flue gas. There are two benefits of using this technique. Firstly, NO_x emissions are reduced drastically due to the absence of atmospheric air for combustion. Secondly, using this technique a highly concentrated stream of CO₂ is produced as flue gas which can be processed through carbon capture and storage. However, this technique also demands the availability of pure O₂ and a firebox that recirculates flue gases. Flame stability can also be a challenge due to the low O₂ content.

The above discussion reemphasizes the relevance of steam cracking process in the industry and the present-day challenges associated with it. There is still scope for process improvements and even minor improvements can translate to indomitable benefits in terms of revenue and the impact on the environment. Experimental testing of these process improvement techniques can be one option to study the fundamental aspects to drive innovations. However, considering the size of the cracker facility and the hostile conditions of its operation, access to the detailed thermal and fluid phenomena is often impossible. An alternative which has gained considerable significance over the last couple of decades is numerical modeling which is detailed in the following section.

1.5 Role of numerical modeling

Numerical modeling involves calculating the numerical solution of governing equations describing relevant physical phenomena, subject to appropriate boundary and initial conditions. While earlier, numerical modeling of external aerodynamic flow configurations focused on solving the linear and later the full potential flow equations, today the CFD community depends on mainly three broad classes of numerical approximations namely, the Reynold's Averaged Navier-Stokes Equations (RANS), Large Eddy Simulation (LES) and Direct Numerical Simulation (DNS).

RANS governing equations are obtained by taking the time average of the full Navier-Stokes Equations. One then arrives at steady non-linear equations with

1. INTRODUCTION

mean flow properties as the dependent variables. The averaging procedure also gives rise to the well-known closure problem in turbulence modeling due to the mathematical inability to derive closure relations for the higher moments of the non-linear terms arising from averaging. These terms are often modeled using the Boussinesq approximation, or by solving transport equations for the unclosed terms (which in turn have even higher-order moments). RANS provides time-averaged results of the flow field since only a “statistically steady” solution is sought by solving the governing equations. As one is aware, turbulent flows possess spatial and temporal scales of a wide spectrum depending on the Reynold’s number of the flow (for incompressible, non-reacting flows). RANS does not resolve any of these scales; all the flow scales are modeled instead. This is an inherent drawback of RANS methods which limit its applicability to a narrow class of flow situations for which the turbulence model constants are designed for.

DNS relies on solving the full Navier-Stokes equations without relying on any sort of averaging or filtering. Hence, contrary to RANS methods, DNS resolves all spatial and temporal scales of the flow. However, in order to resolve all the spatial scales of the flow, one would need to spatially discretize the domain to scales close to the Kolmogorov scale. As the ratio of the Kolmogorov to that of the integral length scale of flow is proportional to $Re^{9/4}$ where Re denotes the Reynold’s number, very fine grid resolution is imperative at higher values of Re . This is aggravated by the requirement to have computationally costly, higher-order numerical methods to reduce discretization, dispersion and aliasing errors. While DNS of low Reynolds number flows have been performed in the past, the current computational abilities do not permit DNS of any practical turbulent flows of interest.

The third approach is that of LES. LES solves the Navier-Stokes equations after a spatial filtering operation is performed on the governing equations. This filtering operation also induces additional unclosed terms (sub-grid scale stresses) in the governing equations like in RANS. However, these terms only represent the effect of flow features which are not resolved by the grid due to the lack of grid resolution. At high Re , these small scales are found to be universal in their statistical nature and hence are modeled using sub-grid scale models, while the larger flow scales are resolved by the numerical method.

A comparison of RANS and LES modeling approaches is shown in Figure 1.12 where the extent of modeling and resolution are illustrated.

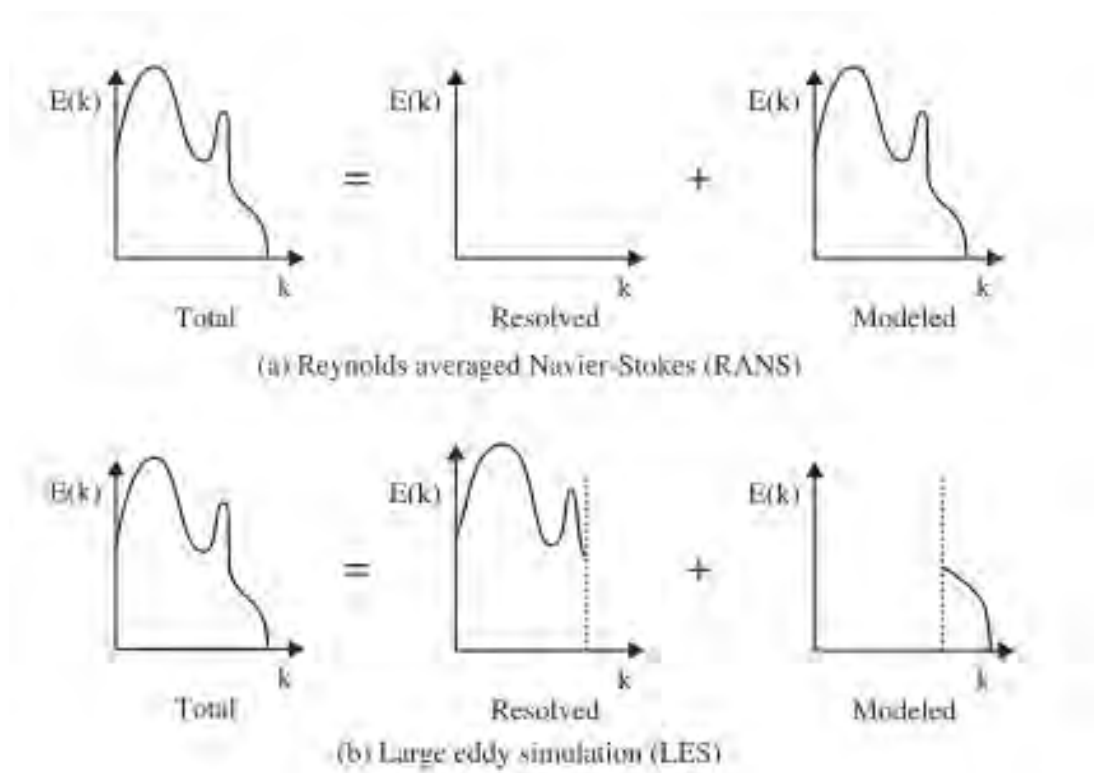


Figure 1.12: Total, resolved, and modeled scales in RANS (a) and LES (b)

While RANS computations are comparatively cheaper today (component level simulations taking less than a day with high-performance machines) they suffer from their inherent inability to predict the physics of the flow beyond a region of operating space for which the model is designed. DNS, on the other hand, is capable of providing finer details of information about the flow but is exorbitantly costly. A compromise between these two approaches is LES where accurate flow information can be obtained while resolving the large flow structures and modeling only the smaller ones which anyway exhibit universal behavior in their statistics. LES has hence been increasingly used in the design and analysis of practical flow configurations today.

Numerical simulations of cracking furnaces have been carried out in the past by researchers in the petro-chemical industries. Lobo and Evans [31] were the first to study the heat transfer occurring inside furnaces using empirical models for different gaseous and liquid fuels. Rigorous numerical studies began since the 1970s with more focus on the reactor side. Robertson and Hanesian [32] modeled the reactors inside the furnace as ideal plug flow reactors (PFR) using a global chemical mechanism. Similar studies were performed by other researchers [33, 34] with emphasis on the reactor side and only the radiative heat transfer modeled inside the furnace using zonal methods. Detemmerman and Froment [35] carried

1. INTRODUCTION

out one of the first coupled simulations of the furnace and reactor coils using a RANS solver and a global methane-hydrogen chemical mechanism. This was followed by other researchers [36, 37] who used k- ϵ RANS solvers along with the EBU combustion model to analyze methane-hydrogen combustion. Tang et al. [38] used a transported probability density function (PDF) model with in-situ adaptive tabulation for studying lean premixed combustion in low NO_x burners while Han [39] and Lan [40] studied a coupled furnace reactor system using the presumed PDF combustion model. In recent years, researchers [41, 42] have used k- ϵ RANS model with simple eddy dissipation combustion models coupled with the discrete ordinate method (DOM) for simulating radiative heat transfer. Table 1.1 summarises some of the past empirical, theoretical, and numerical research studies carried out on the fire side of steam cracking furnaces.

Two observations are quite evident from the above Table 1.1.

First is the unceasing dependence on RANS in steam cracking furnace simulations. Even though LES has started replacing RANS in design processes in other fields of engineering such as aerospace and transportation, the steam cracking community has kept LES at an arm's length. This is due to the challenge posed by numerics in carrying out LES for huge systems such as cracking furnaces. Flow in steam crackers pose a wide spectrum of spatial and temporal scales. The largest length scale in the furnace (the height of the furnace) is close to 10m while the smallest length scale (close to the fuel injectors) is less than a millimeter. This wide separation in spatial scales also results in a huge disparity in temporal scales. For example, while the residence time for the flue gas inside the furnace is of the order of 3-5 sec, the smallest time scale (due to near sonic flow at the choked primary fuel injection) is of the order of 10^{-8} seconds. For conventional LES solvers which are based on explicit time integration schemes, this would mean a small time step and a large residence time making computations exorbitantly costly to be carried out.

The second striking observation is regarding the modeling of fire side chemistry involving the combustion of fuel used. Most of the previous studies either used global chemical mechanisms using 6 species and a couple of reactions or detailed mechanisms in conjunction with flamelet models. While global mechanisms make computations amenable, they lack in accurately predicting the critical flame properties such as heat release rate, flame temperature, and the production of emissions. Flamelet models on the other hand, use detailed chemical mechanisms and make the computational cost amenable by reducing the dimension of the chemical system to one or two parameters. Often equilibrium chemistry is as-

Previous research carried out on steam cracking furnace							
Sl. No.	Reference	Year of publication	Fuel&Oxidizer	Turbulence Model	Chemical Mechanism	Combustion Model	Radiation Model
1	[31]	1939	Liquid fuels, air	None	None	None	None
2	[32]	1975	Ethane, air	None	None	None	None
3	[43]	1978	Ethane, air	None	Skeletal-9S, 8R	None	Zone method
4	[33]	1988	Ethane, air	None	Skeletal-9S, 8R	None	Zone method
5	[35], [36], [37], [44]	1998-2004	CH ₄ +H ₂ , air	RANS k- ϵ	Skeletal	EBU	Zone method
6	[38]	2004	CH ₄ +H ₂ , air	RANS k- ϵ	Detailed	Transported pdf	Zone method
7	[39]	2006	CH ₄ +H ₂ , air	RANS k- ϵ	Detailed	Presumed pdf	DO method
8	[40]	2007	Ethane+Propane, air	RANS k- ϵ	Detailed	Presumed pdf	DO method
9	[45], [46], [41],[42]	2011-2016	CH ₄ +H ₂ , air	RANS k- ϵ	Skeletal	EDM/EDC	DO method

Table 1.1: Some of the articles on the numerical simulation of furnaces performed in the past

sumed or presumed PDFs are used which predict finite rate chemical phenomena poorly.

1.6 Objectives and organization of the thesis

Having presented the current state of the art in the field of steam cracking furnace simulations in the previous section and having identified the gaps in the current CFD technologies in use today in the steam cracking community, the author of this thesis likes to address the following challenges associated in bridging these gaps. The organization of this thesis is also briefly described.

- **Address the challenge of numerical stiffness:** The objective here is to develop a numerical method to accelerate LES calculations within the framework of the available LES solver. The method is desired to provide considerable speed up in LES calculations while incurring minimal numerical error. This challenge is presented in this thesis in the following manner. Firstly, the governing fluid and radiative transport equations are described, along with the physical assumptions invoked and the justifications for making such assumptions. This is described in Chapter 2. A brief discussion on the boundary conditions used is also provided in this chapter. Before describing the LES acceleration method in detail, the numerical methods used in the LES solver-AVBP is discussed. Global spectral analysis is performed to study the dispersion relation preservation properties of two of the most popular numerical schemes in AVBP. These are described in Chapter 3. This chapter serves as a precursor to Chapter 4 where the details of the development of the LES acceleration method are elaborated. Chapter 4 discusses the development of the novel LES acceleration method, the theoretical speed up obtained, error analysis using global spectral analysis and finally its numerical validation using simulations.
- **Incorporate detailed chemistry effects:** The objective here is to incorporate sufficiently detailed and finite rate chemistry effects in simulating the combustion occurring inside the firebox. Contrary to the approaches used by previous researchers in the steam cracking community, an analytically reduced chemical mechanism is used in conjunction with the species transport model used in the LES solver. These details are provided in Chapter 5. The Chapter begins with a comparative study of the various detailed mechanisms used to describe methane combustion. The analytical reduction process is then detailed followed by the validation of the reduced

mechanism with the detailed mechanism using 1D and 3D flame configurations.

- **Incorporate radiation effects:** The details on how radiative heat transfer effect is incorporated in the LES solver is elucidated in Chapter 6. The approach taken in this thesis is to couple an available radiative transfer equation (RTE) solver with the accelerated LES solver to obtain a faster LES-RTE coupled solution. Discrete Ordinate Method (DOM) based RTE solver is used here in conjunction with the LES solver with the novel acceleration method. The details of the numerical method used in the RTE solver and the validation of the solver is explained in this chapter.
- **Application to furnace simulation** Finally, all the above-mentioned developments are implemented and the reactive flow inside a steam cracker is studied. The details of the simulation and the results are presented in chapter 7.

1. INTRODUCTION

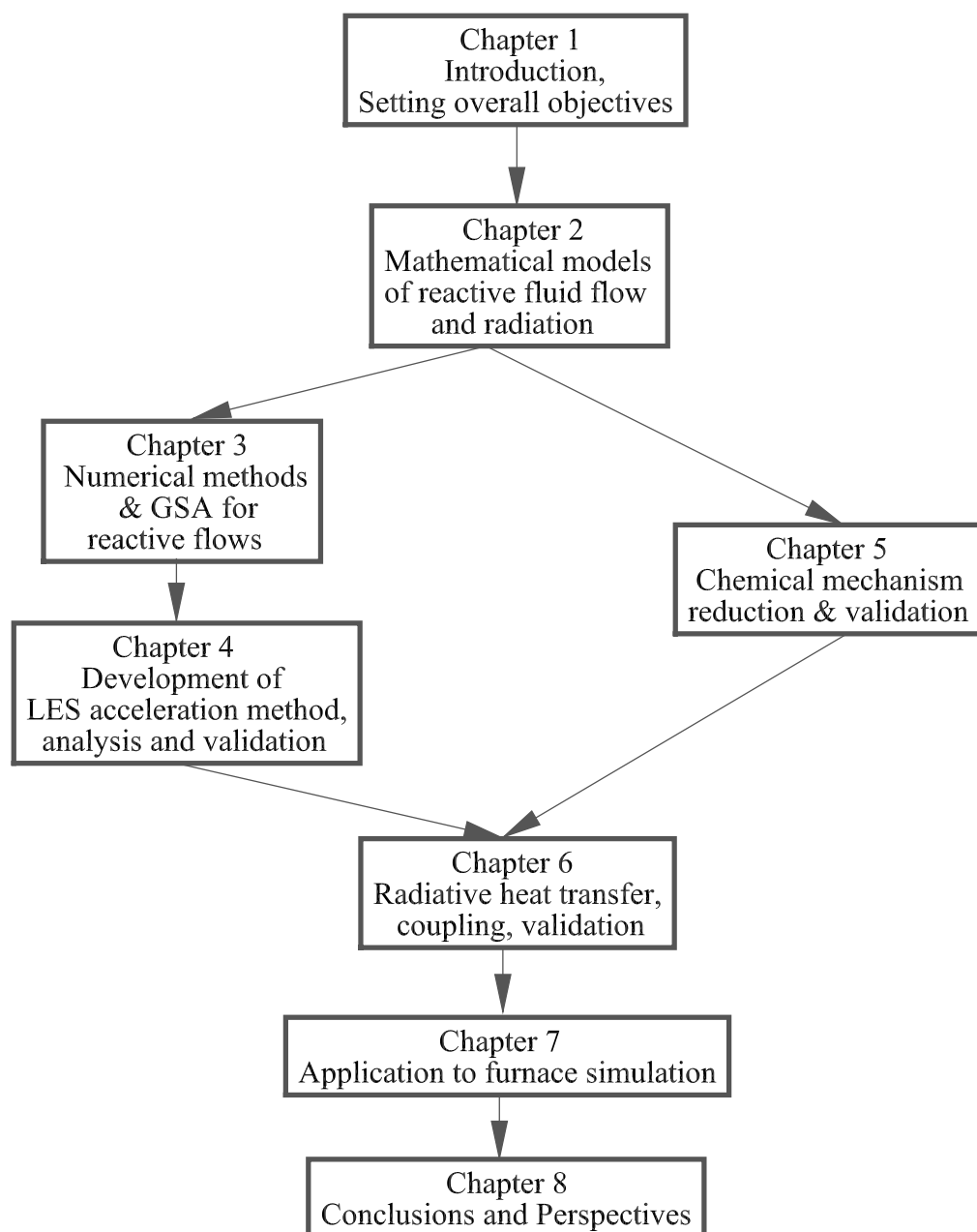


Figure 1.13: The organization of this thesis

By addressing the above-mentioned challenges, the author demonstrates the applicability of LES for steam cracking furnace simulations and believes in opening a new avenue to carry out accurate design and analysis of steam cracking furnaces and their components.

1.7 Acknowledgment

The author likes to acknowledge European Commission for funding this thesis through the IMPROOF project as a part of the Horizon 2020 Framework. The project consisted of 7 industry partners and 4 academic institutes including CERFACS. The technical discussions and feedback through the project partners have greatly enhanced the quality and accuracy of the work involved in this thesis. Specifically, the author likes to recognize John Zink Hamworthy Company, Luxembourg for providing geometrical and test data to carry out LES simulations. The author is also indebted to GENCI for providing access to perform LES calculations detailed in this thesis.

Part I

Governing Equations and Numerical Methods

Numerical simulation of any real, physical phenomenon involves the solution of one or a set of coupled governing equations either in differential or integral form. They are subjected to a set of constitutive equations that define material and transport properties and boundary conditions relevant to the case under study. Often the specific physics and operating conditions allow one to make reasonable physical assumptions. These assumptions can simplify the solution procedure drastically while having no appreciable difference to the solution of the original governing equations. Once these physical assumptions are invoked, the numerical solution to these governing equations can be obtained at various levels of resolution as mentioned in the previous chapter. The first chapter of this part of the thesis describes this particular aspect. The equations governing fluid flow and radiative heat transfer are explained under separate sections. The physical assumptions that are pertinent to this study are described and the rationale behind the validity of these assumptions are listed. In the section dealing with fluid flows, this is followed by a description of the LES governing equations and the SGS closure models used in the study. The numerical boundary conditions of fluid flow that are used in this study are also explained. In the section that follows, the governing equations of radiative heat transfer, used in this study are also detailed.

The role of numerical methods on the accuracy of the numerical solution cannot be understated. Every discrete computing method brings with it, associated numerical properties in terms of numerical dissipation, dispersion and diffusion which determine how accurately the method is able to resolve the exact solution. In Chapter 3, the numerical methods used in the LES solver (AVBP) used in this study, are discussed. This is followed by a discussion on the numerical properties of two of the most popular numerical schemes (Lax-Wendroff and TTGC) used in AVBP. Global Spectral Analysis (GSA) is employed in studying the spectral properties of these schemes. The implications of the results of this analysis are demonstrated through appropriate numerical tests. This study also serves as a precursor to the following chapter which discusses the LES acceleration method and its effect on the numerical accuracy of these schemes used in AVBP.

One of the central topics of this thesis is the development of a novel LES acceleration method to speed up computations in an explicit time-integration based LES solver. A domain decomposition based, local time-stepping method is designed that can be used to speed up LES computations when used in an overset grid framework. The details of the working of this method is explained in Chapter 4. The maximum theoretical speed up that this method can achieve is derived analytically. This is followed by a description of the method and how

the solution in the overlapped regions is treated. The GSA of the error incurred due to local time stepping is discussed next. Numerical tests are performed on 1D, linear governing equations and the results obtained are compared with that of the conventional (without the LES acceleration technique) methods derived in Chapter 3. Further, the effect of the grid element type, time step ratio (to be defined in chapter 4), and the numerical scheme are also studied through numerical tests involving Euler and Navier-Stokes solvers. All these topics are explained in Chapter 4.

Chapter 2

Governing equations

Contents

3.1	Literature survey	47
3.2	Objectives of this chapter	51
3.3	Numerical methods in AVBP	51
3.4	Analysis of numerical schemes in AVBP	54
3.4.1	1D Linear Convection Equation (LCE)	54
3.4.2	1D Linear Convection-Diffusion Equation (LCDE)	62
3.4.3	1D Linear Convection-Diffusion-Reaction Equation (LCDRE)	75
3.5	Conclusions	81

2.1 Objectives

The objectives addressed in this chapter are listed below.

- (O.1) To list the governing equations of fluid flow and radiative heat transfer
- (O.2) To list the physical assumptions invoked to simplify these governing equations
- (O.3) To discuss the numerical assumptions and turbulence closure models
- (O.4) To list and briefly describe the boundary conditions used in the present study

2.2 Fluid flow equations, assumptions and boundary conditions

The governing equations of fluid flow, appropriate physical and numerical assumptions and boundary conditions are elucidated in this section.

2. GOVERNING EQUATIONS

2.2.1 Governing Equations

The governing equations used in this study are the full set of compressible, NS equations [47] given by,

$$\frac{\partial \rho}{\partial t} + \frac{\partial(\rho v_j)}{\partial x_j} = 0 \quad (2.1)$$

$$\frac{\partial(\rho v_i)}{\partial t} + \frac{\partial(\rho v_i v_j)}{\partial x_j} = -\frac{\partial p}{\partial x_i} + \frac{\partial \tau_{ji}}{\partial x_j} + \rho \sum_{k=1}^{N_s} Y_k f_{k,i} \quad i, j = 1..N_{dim} \quad (2.2)$$

$$\begin{aligned} \frac{\partial(\rho E)}{\partial t} + \frac{\partial(\rho E v_j)}{\partial x_j} = & -\frac{\partial q_i}{\partial x_i} + \frac{\partial(\sigma_{ji} v_i)}{\partial x_j} + \rho \sum_{k=1}^{N_s} Y_k f_{k,i} (v_i + V_{k,i}) \\ & + \dot{\omega}_T + \dot{Q}_R + \dot{Q}_{ext} \end{aligned} \quad (2.3)$$

supplemented with the set of transport equations governing the evolution of species mass fractions Y_k given by,

$$\frac{\partial(\rho Y_k)}{\partial t} + \frac{\partial(\rho Y_k v_j)}{\partial x_j} = -\frac{\partial(\rho Y_k V_{k,j})}{\partial x_j} + \dot{\omega}_k \quad k = 1..N_s \quad (2.4)$$

Here, x_j and t refer to the j^{th} spatial coordinate and time respectively and follow Einstein's summation convention. N_{dim} is the physical dimension of the problem and is equal to three in the present study. N_s is the total number of species involved. ρ , p and E are the density, pressure and total sensible energy respectively. v_i and $V_{k,i}$ denote the instantaneous fluid velocity and diffusion velocities of species k in the i^{th} direction respectively. τ_{ji} is the second-order, symmetric viscous stress tensor and $f_{k,i}$ is the body force exerted by species k in the i^{th} direction. \dot{Q}_R and \dot{Q}_{ext} indicate the heat addition/loss due to radiation and external sources respectively. $\dot{\omega}_T$ and $\dot{\omega}_k$ are the heat release due to combustion and the species production rates.

The diffusion velocities \mathbf{V} , (bold symbols indicate vectors) are obtained [48] by the solution of the following system of equations,

$$X_k \mathbf{V}_k = -\sum_{j=1}^N D_{kj} \mathbf{d}_j - D_k^T (\nabla T / T) \quad (2.5)$$

where,

$$\mathbf{d}_j = \nabla X_j + (X_j - Y_j) \frac{\nabla p}{p} + \frac{\rho}{p} \sum_{k=1}^{N_s} Y_j Y_k (\mathbf{f}_k - \mathbf{f}_j) \quad (2.6)$$

Here, X_k is the mole fraction of species k and D_{kj} is the multicomponent diffusion coefficient of species k with species j which is ideally calculated by

2.2 Fluid flow equations, assumptions and boundary conditions

solving the Stefan-Maxwell-Boltzmann equation. The three terms on the right-hand side of Eq. 2.6 signifies the effect of species composition gradients, pressure differential and body force terms respectively on the diffusion velocities. The last term in Eq. 2.5 refer to species diffusion due to thermal gradients (Soret effect) where D_k^T is the thermal diffusion coefficient.

2.2.2 Physical Assumptions

The following physical assumptions pertinent to the present study, are enforced on the above-mentioned set of general governing equations in order to simplify them.

- (A.1) *The species involved and the mixture are perfect gases:* This study involves the combustion of natural gas (predominantly methane)-air mixture occurring at atmospheric pressure and temperature. The peak temperature in the mixture is estimated to be less than 2200 K (adiabatic flame temperature). Since these $p - T$ conditions are far away from the critical pressures and temperatures of every species involved, this is indeed a valid assumption [49]. Hence, the perfect gas equation,

$$p = \rho RT \quad (2.7)$$

serves as the equation of state, where R is the gas constant of the mixture. The calorific equations of state relating the sensible part of internal energy (E_s) and enthalpy (H_s) to temperature are then given by,

$$E_s = \int_{T_0}^{T_f} C_v(T) dT - RT_0 \quad (2.8)$$

$$H_s = \int_{T_0}^{T_f} C_p(T) dT \quad (2.9)$$

where C_v and C_p are the specific heats at constant volume and constant pressure respectively and are functions of temperature only. T_0 is a reference temperature and T_f is the temperature at which the above quantities are to be evaluated.

- (A.2) *The reactive and non-reactive mixture of gases are Newtonian in nature.* It is common to assume natural gas-air mixture to be Newtonian in nature. Hence the viscous stress tensor is related to velocity gradient by

$$\tau_{ij} = \left[\left(\mu' - \frac{2}{3}\mu \right) \frac{\partial u_k}{\partial x_k} \delta_{ij} + \mu \left(\frac{\partial u_i}{\partial x_j} + \frac{\partial u_j}{\partial x_i} \right) \right] \quad (2.10)$$

2. GOVERNING EQUATIONS

The bulk viscosity μ' is often neglected and set to zero [48]. Hence,

$$\tau_{ij} = \left[\left(-\frac{2}{3}\mu \right) \frac{\partial u_k}{\partial x_k} \delta_{ij} + \mu \left(\frac{\partial u_i}{\partial x_j} + \frac{\partial u_j}{\partial x_i} \right) \right] \quad (2.11)$$

where μ is the dynamic viscosity of the mixture of gases. The total stress tensor σ_{ji} used in Eq. 2.1 includes the isotropic pressure and hence is given by $\sigma_{ji} = -p \delta_{ji} + \tau_{ji}$.

(A.3) *Arrhenius chemical reaction model*: The chemical time scales in this study are large when compared to the mean free times of reacting molecules. Hence Maxwellian production rates from the Kinetic theory of gases are used. This results in the production/destruction rates of species $\dot{\omega}_k$ given by the equation,

$$\dot{\omega}_k = \sum_{j=1}^{N_r} \dot{\omega}_{kj} = W_k \sum_{j=1}^{N_r} \nu_{kj} Q_j \quad (2.12)$$

where $\dot{\omega}_{kj}$ is the rate of production/destruction of species k in reaction j . The total number of reactions is denoted by N_r . The molecular weight of species k is given by W_k and the rate of j^{th} reaction is denoted by Q_j . ν_{kj} is the stoichiometric coefficient of species k in the j^{th} reaction. The rate of reaction is in turn provided by the relation,

$$Q_j = K_{fj} \prod_{k=1}^{N_s} [X_k]^{\nu'_{kj}} - K_{rj} \prod_{k=1}^{N_s} [X_k]^{\nu''_{kj}} \quad (2.13)$$

where K_{fj} and K_{rj} are the forward and reverse reaction rate coefficients defined by,

$$K_{fj} = A_{fj} T^{\beta_j} \exp\left(-\frac{E_j}{RT}\right) = A_{fj} T^{\beta_j} \exp\left(-\frac{T_{aj}}{T}\right) \quad (2.14)$$

and $[X_k]$ is the molar concentration of species k .

(A.4) *Soret effect and Dufour effects are neglected*: The heat transfer term q_i in Eq. 2.1 is given by,

$$q = -\lambda \nabla T + \rho \sum_{k=1}^N h_k Y_k \mathbf{V}_k + R_u T \sum_{k=1}^N \sum_{j=1}^N \left(\frac{X_j D_{T_k}}{W_k D_{kj}} \right) (\mathbf{V}_k - \mathbf{V}_j) \quad (2.15)$$

In the above equation, T is the temperature, h_k the enthalpy of species k and R_u the universal gas constant. The first term on the RHS of the above equation is the heat transfer due to conduction where the thermal conductivity is denoted as λ . The second term is the heat transfer due

2.2 Fluid flow equations, assumptions and boundary conditions

to inter-species diffusion while the last term is the contribution due to the Dufour effect. It is studied that the effect of Soret and Dufour effects are negligible on the flame speed and structure of laminar methane-air flames [50]. For counter-flow diffusion flames, the effects of these phenomena are present although not critical in determining the extinction limits of the flame.

- (A.5) *Constant Lewis and Schmidt number for species and power-law of viscosity for the gas mixture:* The Lewis number (Le) and Schmidt number (Sc) are assumed constant for each species throughout the domain. These non-dimensional numbers are related to the transport coefficients as follows:

$$Le_k = \frac{\lambda}{\rho C_p D_k} = \frac{D_{th}}{D_{km}} \quad (2.16)$$

$$Sc_k = \frac{\nu}{D_{km}} = Pr Le_k \quad (2.17)$$

Pr refers to the Prandtl number of the gaseous mixture. The viscosity of the gas mixture is calculated using the power law and in this particular study is assumed the same as that of air. The species diffusion coefficient and the heat conductivity coefficient of the mixture are then calculated from the Sc_k and Pr relations provided above.

- (A.6) *Body forces comprise of only gravity force:* No other body forces are present in the domain other than the gravitational force ρg where g is the acceleration due to gravity.
- (A.7) *Reactive flow occurs at nearly constant pressure and body force is the same for all species:* Applying the constant pressure and zero body force assumptions in Equations 2.6 and 2.5, one obtains the simplified relation for \mathbf{V}_k ,

$$X_k \mathbf{V}_k = -D_{km} \nabla X_k \quad (2.18)$$

The above approximation does not ensure mass conservation. Hence, a correction velocity \mathbf{V}^c is included. The species transport equation is then modified as,

$$\frac{\partial(\rho Y_k)}{\partial t} + \frac{\partial(\rho Y_k (v_j + V_j^c))}{\partial x_j} = \frac{\partial}{\partial x_j} \left(\rho D_{km} \frac{W_k}{W} \frac{\partial X_j}{\partial x_j} \right) + \omega_k \quad (2.19)$$

The correction velocity is an artifact defined by the following equation and ensures that the mass conservation equation is satisfied.

$$V_j^c = \sum_{k=1}^N D_k \frac{W_k}{W} \frac{\partial X_k}{\partial x_j} \quad (2.20)$$

2. GOVERNING EQUATIONS

(A.8) *No external heat sources*: Since there are no additional heat sources such as plasma or laser actuation, \dot{Q}_{ext} is set to zero.

2.2.3 LES Governing Equations

The governing equations of LES are obtained by spatial filtering of the full NS equations described in Section 2.2.1. The filtering operations result in both filtered flow variables (which are resolved by the grid) as well as unresolved quantities which need to be modeled appropriately. Since, the governing equations are the compressible, NS equations, a favre filtering procedure is preferred for most of the terms. The filtered NS equations after invoking the assumptions mentioned in the previous section are given by,

$$\frac{\partial \bar{\rho}}{\partial t} + \frac{\partial (\bar{\rho} \tilde{v}_j)}{\partial x_j} = 0 \quad (2.21)$$

$$\frac{\partial (\bar{\rho} \tilde{v}_i)}{\partial t} + \frac{\partial}{\partial x_j} (\bar{\rho} \tilde{v}_i \tilde{u}_j) = -\frac{\partial \bar{p}}{\partial x_i} + \frac{\partial \bar{\tau}_{ji}}{\partial x_j} + \frac{\partial \bar{\tau}_{ji}^t}{\partial x_j} + \bar{\rho} g_i \quad (2.22)$$

$$\frac{\partial (\bar{\rho} \tilde{E})}{\partial t} + \frac{\partial}{\partial x_j} (\bar{\rho} \tilde{E} \tilde{v}_j) = -\frac{\partial \bar{q}_j}{\partial x_j} - \frac{\partial \bar{q}_j^t}{\partial x_j} + \frac{\partial (\bar{\sigma}_{ji} v_i)}{\partial x_j} + \bar{\rho} \sum_{d=1}^{N_{dim}} (g_d \tilde{v}_d) + \bar{\omega}_T + \bar{Q}_r \quad (2.23)$$

$$\frac{\partial (\bar{\rho} \tilde{Y}_k)}{\partial t} + \frac{\partial}{\partial x_j} (\bar{\rho} \tilde{Y}_k \tilde{u}_j) = -\frac{\partial \bar{J}_{j,k}}{\partial x_j} - \frac{\partial \bar{J}_{j,k}^t}{\partial x_j} + \bar{\omega}_k \quad (2.24)$$

where $\bar{(\cdot)}$ and $\widetilde{(\cdot)}$ refer to the non-favre and favre filtered quantities respectively and $\bar{(\cdot)}^t$ indicate the sub-grid scale (SGS) stresses/fluxes. Additional numerical assumptions are also made and are listed below.

2.2.4 Numerical Assumptions

(A.1) *The SGS correlation terms involving the diffusion coefficients and stress terms are neglected*: For example, the resolved viscous stress without the divergence term is expanded as,

$$\begin{aligned} \overline{2\mu S_{ij}} &= \overline{2(\tilde{\mu} + \mu'')(\widetilde{S_{ij}} + S''_{i,j})} \\ &= \overline{2\tilde{\mu} \widetilde{S_{i,j}}} + \overline{2\mu'' \widetilde{S_{i,j}}} + \overline{2\tilde{\mu} S''_{i,j}} + \overline{2\mu'' S''_{i,j}} \\ &\approx \overline{2\tilde{\mu} \widetilde{S_{i,j}}} \end{aligned} \quad (2.25)$$

This is a common assumption made in most of the LES codes and is justified in the high Reynold's number limit [47].

2.2 Fluid flow equations, assumptions and boundary conditions

(A.2) *Boussinesq approximation is valid*: The Boussinesq approximation stipulates that the turbulent flux follows a similar functional model as the molecular diffusion fluxes. In addition to this, this approximation is also based on the hypothesis of scale separation and local equilibrium [51]. The Boussinesq approximation is widely used in most of the LES codes available today even though experimental observations contrary to it have been reported [52].

(A.3) *The filtered chemical and radiative source terms are functions of the instantaneous, filtered flow variables only*: Similar to the assumption on SGS cross-correlation terms, the turbulent contribution to the chemical and radiative source term is neglected.

The above numerical assumptions are used in formulating the resolved and SGS stresses as explained in the following sections.

Filtered resolved fluxes

(F.1) The resolved/filtered viscous stress tensor is approximated as,

$$\begin{aligned}\overline{\tau_{ij}} &= \overline{2\mu \left(S_{ij} - \frac{1}{3} \delta_{ij} S_{ll} \right)} \\ &\approx 2\bar{\mu} \left(\tilde{S}_{ij} - \frac{1}{3} \delta_{ij} \tilde{S}_{ll} \right)\end{aligned}\tag{2.26}$$

Here S_{ij} refers to the symmetric part of the second-order velocity gradient tensor.

(F.2) The resolved filtered species diffusive flux is approximated as,

$$\overline{J_{i,k}} = -\rho \overline{\left(D_k \frac{W_k}{W} \frac{\partial X_k}{\partial x_i} - Y_k V_i^c \right)}\tag{2.27}$$

$$\approx -\bar{\rho} \left(\bar{D}_k \frac{W_k}{W} \frac{\partial \tilde{X}_k}{\partial x_i} - \tilde{Y}_k \tilde{V}_i^c \right)\tag{2.28}$$

(F.3) And the resolved filtered heat flux vector is approximated as,

$$\overline{q_i} = -\lambda \frac{\partial \overline{T}}{\partial x_i} + \sum_{k=1}^N \overline{J_{i,k} h_{s,k}}\tag{2.29}$$

$$\approx -\bar{\lambda} \frac{\partial \tilde{T}}{\partial x_i} + \sum_{k=1}^N \overline{J_{i,k} \tilde{h}_{s,k}}\tag{2.30}$$

where $h_{s,k}$ is the sensible enthalpy of species k .

2. GOVERNING EQUATIONS

SGS stresses and filtered source terms

(T.1) The SGS viscous stress tensor $\overline{\tau_{ij}^t}$ is defined as

$$\overline{\tau_{ij}^t} = -\bar{\rho} (\widetilde{u_i u_j} - \tilde{u}_i \tilde{u}_j) \quad (2.31)$$

Based on the Boussinesq assumption (A.2), this term is modeled as,

$$\overline{\tau_{ij}^t} = 2\bar{\rho}\nu_t \left(\widetilde{S_{ij}} - \frac{1}{3}\delta_{ij}\widetilde{S_{ll}} \right) \quad (2.32)$$

In the present study, the Sigma model [53] is used to evaluate the turbulent viscosity coefficient ν_t according to the relation,

$$\nu_t = (C_\sigma \Delta)^2 \frac{\sigma_3 (\sigma_1 - \sigma_2) (\sigma_2 - \sigma_3)}{\sigma_1^2} \quad (2.33)$$

The model constant C_σ is fixed as 1.5 and the filter characteristic length Δ is taken as the cube root of the nodal volume. σ_1, σ_2 and σ_3 are the singular values of the resolved velocity gradient tensor $\widetilde{S_{ij}}$. Sigma model uses the singular values of the velocity gradient tensor and generates zero turbulent viscosity for two-dimensional and axisymmetric flows. The model also replicates the cubic behavior of flow in near-wall regions.

(T.2) The SGS heat flux is given by the term,

$$\overline{q_i^t} = \bar{\rho} \left(\widetilde{u_i E} - \tilde{u}_i \tilde{E} \right) \quad (2.34)$$

and similar to the viscous flux is modeled as,

$$\overline{q_i^t} = -\lambda_t \frac{\partial \widetilde{T}}{\partial x_i} + \sum_{k=1}^N \overline{J_{i,k}^t} \widetilde{h_{s,k}} \quad (2.35)$$

where,

$$\lambda_t = \frac{\bar{\rho}\nu_t \overline{C_p}}{Pr^t} \quad (2.36)$$

Here Pr^t is the turbulent Prandtl number. Turbulent Prandtl number is a constant specified by the user. In the present study, the value of Pr^t is fixed as 0.6.

(T.3) The SGS species diffusion flux is given by,

$$\widetilde{J_{i,k}^t} = \bar{\rho} \left(\widetilde{u_i Y_k} - \tilde{u}_i \tilde{Y}_k \right) \quad (2.37)$$

2.2 Fluid flow equations, assumptions and boundary conditions

This flux is modeled as,

$$\overline{J_{i,k}^t} = -\bar{\rho} \left(D_k^t \frac{W_k}{W} \frac{\partial \tilde{X}_k}{\partial x_i} - \tilde{Y}_k \tilde{V}_i^{c,t} \right) \quad (2.38)$$

where the turbulent species diffusion coefficient D_k^t is obtained from,

$$D_k^t = \frac{\nu_t}{Sc_k^t} \quad (2.39)$$

Here Sc_k^t is the turbulent Schmidt number which is also specified by the user (a value of 0.6 is used in the present study).

2.2.5 Turbulent source terms

In the present study, the filtered chemical source terms are directly evaluated using the filtered values of the primitive variables and species mole concentrations. Hence, the reaction rates are calculated as,

$$\overline{Q}_j = K_{fj} \prod_{k=1}^N [\tilde{X}_k]^{\nu'_{kj}} - K_{rj} \prod_{k=1}^N [\tilde{X}_k]^{\nu''_{kj}} \quad (2.40)$$

and the species production rates are evaluated as,

$$\tilde{\dot{\omega}}_k = \sum_{j=1}^{N_r} \tilde{\dot{\omega}}_{kj} = W_k \sum_{j=1}^{N_r} \nu_{kj} \overline{Q}_j \quad (2.41)$$

The filtered value of the heat release rate due to combustion, $\overline{\dot{\omega}}_T$ is similarly expressed as a function of the resolved, instantaneous, species production rates as,

$$\tilde{\dot{\omega}}_T = \sum_{j=1}^{N_s} \Delta H_{fj}^0 \tilde{\dot{\omega}}_j \quad (2.42)$$

2.2.6 Boundary conditions

The furnace configuration under study has multiple inlets (through which air and fuel enters the domain), a single outlet through which the flue gases escape to the stacks, no-slip walls on the furnace and burner and a symmetry boundary. For the inlets and the outlet, Navier-Stokes Characteristic Boundary Conditions (NSCBC) are used. For the no-slip walls and the symmetry boundary condition a weak formulation is enforced. These boundary conditions are explained in the following sub-sections.

2. GOVERNING EQUATIONS

Mass flow inlets

Since fuel and air mass flow rates and their temperatures and composition are known, mass flow inlet boundary conditions are chosen. Here the mass flow rates \dot{m}_{fuel} , \dot{m}_{air} , temperature and species compositions are specified. To rightly resolve the acoustic and vorticity behavior of the flow, NSCBCs are used. In this method, the corrected wave amplitudes (strengths) at the boundary due to the imposed boundary condition are calculated as,

$$\left\{ \begin{array}{l} \text{strength (4)} = \frac{2K_{\rho U_n} \Delta t}{\rho(1-M_n)} ((\rho U_n)^t - (\rho U_n)) \\ \text{strength (2)} = K_{\rho U_t} \Delta t (0 - U_{t1}) \\ \text{strength(3)} = K_{\rho U_t} \Delta t (0 - U_{t2}) \\ \text{strength (5 + k)} = \rho K_Y \Delta t (Y_k^t - Y_k) \\ \text{strength (1)} = -\rho K_T \Delta t \frac{(T^t - T)}{T} \end{array} \right.$$

Here $\rho U_n^t, Y_k^t$ and T^t are the target mass flow rates, species mass fractions and temperature respectively. The tunable constants K are relaxation coefficients which act as high-frequency filters letting the high frequencies escape through the boundary while still retaining the average value of quantities to the specified target values.

Outflow

NSCBC based outflow condition is used in the present study to weakly enforce the outlet pressure. The imposition of pressure in a characteristic framework is tricky as a direct imposition of the pressure would make the boundary perfectly reflecting. On the other hand, imposing the wave strength to zero would make the boundary perfectly non-reflecting but will result in the outlet pressure drifting away from target values. Hence, the wave strength is calculated as,

$$\text{strength (4)} = 2 \frac{K_P \Delta t (P^t - P^n)}{\rho c} - (1 - \beta) \text{transv(4)} \quad (2.43)$$

Like the inlet boundary conditions mentioned before, K_P is the relaxation coefficient that determines the pressure imposition on the boundary. Setting $K_P = 0$ would render the boundary to be perfectly non-reflecting, while setting a high value would make the boundary increasingly reflecting.

No slip adiabatic walls

Since the furnace and burner wall temperatures are not known apriori and considering the computational cost associated with carrying out a conjugate heat transfer analysis, approximate boundary conditions are enforced on the walls. The no-slip boundary condition ensures that the velocity on the walls are zero.

The temperature gradient normal to the wall is also enforced to zero to make sure the walls are adiabatic. Since the walls are non-porous the species diffusive fluxes on the walls are also set to zero. Mathematically,

$$\vec{v} = 0 \tag{2.44}$$

$$\nabla p \cdot \vec{n} = 0$$

$$\nabla Y_k \cdot \vec{n} = 0$$

$$\nabla T \cdot \vec{n} = 0$$

Symmetry

In this thesis, only one-half of the full steam cracking furnace is simulated and hence a symmetric boundary condition is used. On the symmetry boundary, the following weak boundary conditions are enforced,

$$\nabla p \cdot \vec{n} = 0 \tag{2.45}$$

$$\nabla \mathbf{v} \cdot \vec{n} = 0 \tag{2.46}$$

$$\nabla(\rho Y_k) \cdot \vec{n} = 0 \tag{2.47}$$

Having described the physical and numerical governing equations, assumptions and boundary conditions used in this study, pertaining to fluid flow the same aspects for radiative transfer are detailed in the following section.

2.3 Radiative heat transfer

As in the previous section, the governing equations, physical & numerical assumptions and the boundary conditions of radiative transfer equations are described as follows.

2.3.1 Governing equations

The governing equation for radiative transfer is given below [54]:

$$\frac{1}{c} \frac{\partial I_\eta}{\partial t} + \frac{\partial I_\eta}{\partial s} = \kappa_\eta I_{b\eta} - \kappa_\eta I_\eta - \sigma_{s\eta} I_\eta + \frac{\sigma_{s\eta}}{4\pi} \int_{4\pi} I_\eta(\hat{\mathbf{s}}_i) \Phi_\eta(\hat{\mathbf{s}}_i, \hat{\mathbf{s}}) d\Omega_i \tag{2.48}$$

Following common notations, t and s refer to time and space coordinate respectively. The above equation solves for the spectral radiative intensity, I_η at a given spectral wavenumber η and expresses the transport of I_η in space and time subjected to mechanisms of absorption, emission and scatterings expressed by the terms on the right-hand side of Eq. 2.48. Here $I_{b\eta}$ refers to the Planck's

2. GOVERNING EQUATIONS

function and is related to the black body emissive power $E_{b\eta}$ given by the well known Planck's law,

$$E_{b\eta}(T, \eta) = \frac{2\pi hc_0^2 \eta^3}{n^2 [e^{hc_0\eta/nkT} - 1]} \quad (2.49)$$

Here h and k refer to the Planck's constant (with a value of 6.26×10^{-34} Js) and Boltzmann constant (with a value of 1.3807×10^{-23} J/K) respectively. c_0 is the speed of light in vacuum (with a value of 2.998×10^8 m/s) and n is the refractive index of the medium. For any black surface or diffuse medium, Eq. 2.50 relates the Planck's function to the spectral emissive power, $I_{b\eta}$.

$$I_{b\eta} = \frac{E_{b\eta}}{\pi} \quad (2.50)$$

The first term on the right-hand side of Eq. 2.48 is the contribution to radiative intensity due to the emission from the participating medium. The parameter κ is the linear absorption (or emission) coefficient. It is assumed that the emission from a volume of the participating medium is linearly proportional to the spectral intensity and the length of the medium considered. The second term refers to the absorption of spectral intensity by the medium and is assumed proportional the intensity and the length of the volume under study. The negative sign in front of the term implies the reduction in intensity due to absorption. The third term in the equation signifies the reduction in intensity due to scattering from the medium. Here, $\sigma_{s\eta}$ is the linear scattering coefficient. The loss in intensity due to scattering is also assumed linearly proportional to the intensity and the length of the volume of the participating medium. Φ_η is the scattering phase function and is the positive contribution to the intensity received in the given volume due to scattering from all directions. The scattering phase function is subjected to the normalization condition given by,

$$\frac{1}{4\pi} \int_{4\pi} \Phi_\eta(\hat{\mathbf{s}}_i, \hat{\mathbf{s}}) d\Omega \equiv 1 \quad (2.51)$$

Once the spectral intensity is solved using Eq. 2.48, the heat transfer due to radiation at the frequency η is given by

$$q_\eta \cdot \hat{\mathbf{n}} = \int_{4\pi} I_\eta \hat{\mathbf{n}} \cdot \hat{\mathbf{s}} d\Omega \quad (2.52)$$

The total heat transfer from all the frequencies in thermal radiation is then derived as,

$$q = \int_0^\infty q_\eta d\eta = \int_0^\infty \int_{4\pi} I_\eta(\hat{s}) \hat{s} d\Omega d\eta \quad (2.53)$$

Most often, the quantity of interest to fluid dynamicists is the amount of heat added or removed at a particular point in the flow due to radiation. This is estimated as the divergence of the heat flux vector. Integrating Eq. 2.48 over all solid angles, one obtains

$$\nabla \cdot q_\eta = \kappa_\eta \left(4\pi I_{b\eta} - \int_{4\pi} I_\eta d\Omega \right) = \kappa_\eta (4\pi I_{b\eta} - G_\eta) \quad (2.54)$$

G_η is defined as the spectral incident radiation and represents the energy density at a point in the participating medium due to radiation at a frequency η . The total heat flux is obtained by integrating Eq. 2.54 over all frequencies. One then obtains,

$$\nabla \cdot q = \nabla \cdot \int_0^\infty q_\eta d\eta = \int_0^\infty \kappa_\eta (4\pi I_{b\eta} - G_\eta) d\eta \quad (2.55)$$

2.3.2 Physical assumptions

The following assumptions are made in the derivation of RTE mentioned in Eq. 2.48.

- (A.1) The participating medium is homogenous
- (A.2) Effect of polarization is neglected
- (A.3) The medium is under local thermodynamic equilibrium
- (A.4) The medium has a constant refractive index n

In addition to the above assumptions inherent in the derivation Eq. 2.48, two additional assumptions are made in this study.

- (A.1) *Steady-state*, ($\frac{\partial I_\eta}{\partial t} = 0$) : This assumption is pretty valid as the time scales of flow is very large when compared to that of the speed of light.
- (A.2) *Effects due to scattering are neglected*: The size of ash, soot and vapor particles are smaller when compared to that of the wavelengths of thermal radiation. Hence, it is common [55],[56] to neglect the effect of scattering in combustion applications.

2. GOVERNING EQUATIONS

2.3.3 Boundary conditions

The following boundary conditions are used in the present study.

Diffusively emitting and reflecting walls

The walls of the steam cracking furnace in this study are modeled as diffusively emitting and reflecting. On such surfaces, the radiation intensity is modeled as,

$$I(\mathbf{r}_w, \hat{\mathbf{s}}) = \epsilon(\mathbf{r}_w) I_b(\mathbf{r}_w) + \frac{\rho(\mathbf{r}_w)}{\pi} \int_{\hat{\mathbf{n}} \cdot \hat{\mathbf{s}}' < 0} I(\mathbf{r}_w, \hat{\mathbf{s}}') |\hat{\mathbf{n}} \cdot \hat{\mathbf{s}}'| d\Omega' \quad (2.56)$$

Here, r_w and $\hat{\mathbf{s}}$ indicate the position vector of the wall and direction of the incoming intensity respectively. ϵ is the emissivity of the wall and ρ is the wall reflectivity related to the emissivity as, $\epsilon = 1 - \rho$.

Symmetry boundary condition

Since the domain includes a symmetric wall, the symmetry boundary condition is used for determining the incident and the outgoing intensities. For any surface with normal $\hat{\mathbf{n}}_f$ and the incident radiation direction $\hat{\mathbf{s}}_i$ the specularly reflected direction $\hat{\mathbf{s}}_r$ is given by,

$$\hat{\mathbf{s}}_r = 2(\hat{\mathbf{n}}_f \cdot \hat{\mathbf{s}}_i) \hat{\mathbf{n}}_f - \hat{\mathbf{s}}_i \quad (2.57)$$

A simplified approach in implementing the symmetry boundary is to enforce zero normal gradient for the incident radiation and to enforce the value of the incident radiation in the outgoing direction.

2.4 Conclusions

1. The governing equations of fluid flow are discussed and the physical assumptions used to simplify them are listed. The fuel-air mixture and the flue gases are treated as perfect gases. Constant Le and Sc numbers for each species are used in this study and the effects of Soret and Dufour are neglected. Gravitational force is included in the momentum and energy equations to reflect the effect of buoyancy.
2. LES governing equations are discussed along with the approximations used in calculating the filtered viscous stresses. Boussinesq hypothesis is invoked to model the SGS terms for the momentum, energy and species equations. Sigma model is used to model the SGS stresses in the momentum equation due to its low cost and its superior behavior in near-wall regions.

3. Radiative transfer equation used in this study is detailed. For the present study, the effect of scattering is neglected. The boundary conditions used in this study, namely diffusively reacting walls and symmetric boundary conditions are also explained.

Chapter 3

Numerical methods and their analysis

Contents

4.1	Introduction	84
4.2	Literature Survey	85
4.3	Objectives of this chapter	89
4.4	LESAULTS Method	89
4.5	Theoretical Computational Speedup	94
4.6	Design of LESAULTS method	97
4.7	Error Analysis	106
4.7.1	GSA of LESAULTS method	106
4.7.2	Application to LCDE	110
4.7.3	Validation of LESAULTS method	114
4.7.4	Order of accuracy	123
4.7.5	Conservation property of LESAULTS	124
4.8	Numerical Validation	126
4.8.1	2-Dimensional isentropic vortex convection	126
4.8.2	Flow past 3D circular cylinder	130
4.8.3	Sandia-D	133
4.9	Conclusions and Perspectives	142

Having described the governing equations of fluid flow, the physical & numerical assumptions and boundary conditions in the previous chapter, this chapter deals with the numerical methods used to solve these equations. The LES solver used in the present study is AVBP. AVBP is a predominantly MPI dependent, explicit time integration based hybrid Finite Volume (FV)-Finite Element (FE) solver that works on unstructured meshes. Compressible reactive, Navier-Stokes equations are solved in AVBP with the problem of combustion being addressed

using the species transport framework. The convective numerical schemes available in AVBP include purely FV schemes (Centered, Lax-Wendroff (LW)) and FE schemes (variants of Taylor-Galerkin schemes such as TTGC and TTG4A). Out of all these schemes in AVBP, LW and TTGC are the most widely used. While LW enjoys the advantage of low computational cost, TTGC benefits from its superior accuracy and resolution properties.

Although this chapter is included in this thesis with the objective of describing the numerical methods used in AVBP, emphasis is also made on the numerical analysis of two of these popular schemes used, namely LW and TTGC. There are three reasons why numerical analysis of schemes is discussed here. Firstly, such an analysis can highlight the numerical properties of these schemes and could be helpful in interpreting the obtained numerical solution. Secondly, the analysis of these schemes when applied to governing equations involving diffusion and source terms has not been carried out in the past. Hence this analysis highlights the effect of diffusion and chemical source terms (although in a simplified manner) on the numerical properties of the schemes. Finally, presenting the analysis in the chapter serves as a precursor to the following chapter where the same analysis is extended to study the LES acceleration methodology.

Keeping these objectives in mind, this chapter is organized as follows. Section 3.1 discusses the previous studies performed on the numerical analysis of schemes. This helps one in identifying the gaps in the research 'terrain' and in emphasizing the significance of the effort in this chapter. Based on the conclusions from this section, the objectives of this chapter are summarized in section 3.2. Before presenting the numerical analysis of the two schemes, it is necessary to describe their implementation in AVBP. This is done in section 3.3. The analysis of these numerical schemes when applied to the linear convection (LCE), linear convection-diffusion (LCDE) and linear convection-diffusion-reaction (LCDRE) equations are presented in section 3.4 followed by a summary of the conclusions from this chapter.

3.1 Literature survey

Analysis of numerical methods used in CFD has been a widely studied topic. The most popular among such methods is the Von-Neumann analysis. Von-Neumann analysis [57] originated at the Los Alamos Laboratory in the 1950s and was used initially to study the stability of the linear barotropic vorticity equation. This analysis involves expressing the numerical solution of periodic problems in terms of their Fourier frequencies and identifying the modes of the numerical

3. NUMERICAL METHODS AND THEIR ANALYSIS

difference equation that may potentially lead to instability. The second method for numerical analysis widely in use today is the Matrix Stability method [58]. In this method, the convective (and diffusive) operators when applied to the numerical approximations of PDEs are expressed in the form of a matrix. The effects of boundary conditions are also included in this matrix representation. The eigenvalues of this matrix then determine the stability of the numerical scheme studied. The third and the final method is the Global Spectral Analysis (GSA) [59]. This method analyses the numerical solution in the spectral space. The conditions for stability of the numerical scheme are analyzed by looking at the amplification factors obtained from GSA. In addition to the issue of stability, emphasis is also made on dispersion relation preservation- a critical aspect to be considered for high-performance computing solvers.

While all of the above analysis methods predict the numerical stability of schemes accurately, they differ from each other in their study of other numerical properties. This is explained as follows. The Von-Neumann method applies only to periodic problems. The effect of boundary closures cannot be studied using this method. Another shortcoming of this method is the assumption that the numerical solution follows the exact convection speed as that of the governing PDE. This is seldom true. The numerical phase and group velocity of the linear convection equation, for example, is scheme-dependent and varies based on the Courant-Friedrich-Lewy (CFL) number and the wavenumber of the solution. This assumption of Von-Neumann has been used to derive an evolution equation for the numerical error. This equation is incorrect as has been demonstrated in [60]. Similar to the convection speed, the other physical properties of the governing equations such as the diffusion coefficient (for the LCDE and LCDRE) and the reaction source term (for the LCDRE) also are not constants when solved numerically. This particular aspect has been highlighted in [61, 62]. The Matrix Method, on the other hand, provides information on the stability of schemes by looking at the spectral radii of the matrix formed from the numerical operators. If the spectral radius is larger than unity, then numerical instability is expected to occur during long time integration. Hence, this method predicts instability (only) after a considerable duration of time integration. Another major drawback suffered by the previously mentioned methods is the lack of information on the dispersion relation properties of schemes. Dispersion relation of a PDE refers to the expression relating to the spatio-temporal properties of the system in the spectral space. Any numerical method must be able to reproduce this relation numerically to the maximum extent possible. This particular aspect is very critical in high performance computing such as in DNS and LES. A stable

scheme does not necessarily ensure an accurate numerical solution. Instead, the numerical method should be able to accurately resolve the speed of propagation of information, diffusion of information and the production (or destruction) of information in addition to being stable. Hence, while choosing numerical schemes for LES or DNS solvers, one should ensure that the scheme should predict the right amplitude of the solution (dissipation), the right speed (dispersion) and the right diffusive (diffusion) properties of the governing PDE. Any scheme which satisfies these conditions is called a Dispersion Relation Preserving (DRP) scheme [63]. In contrast to the previously mentioned analysis methods, GSA addresses these properties too- it predicts not only the stability of the scheme but also the numerical dispersion, diffusion and source term properties of schemes (DRP properties). GSA also has the additional benefit of incorporating the effect of boundary closures on numerical schemes. Considering these advantages, in this study, GSA is used to carry out the numerical analysis. Owing to their popularity as mentioned previously, LW and TTGC are the numerical schemes chosen for the analysis.

Simulation of fluid flows involves the numerical solution of the governing partial differential equations (PDEs) subjected to certain levels of approximations. In the majority of the cases, the governing PDEs are non-linear in nature. The non-linearity of these PDEs makes the analysis of schemes used to solve them nearly impossible. Researchers then often resort to analyzing these schemes applied to prototypical linear PDEs. The question of the validity of such an analysis when extended to non-linear PDEs is open and often debatable. However, our vast experience in CFD has prompted us to believe that such analysis indeed holds true when extended to the non-linear PDEs to a fair degree of accuracy.

Most of the analyses of numerical schemes have been performed for the linear convection equation in the past. It is widely known that the stability limit for the LW scheme corresponds to the CFL number (N_c) being less than or equal to 1. Similar observation on the stability of the TTGC scheme has also been made in [64, 65]. The numerical analysis of the LCDE and LCDRE however, have not received much attention. The author in [66] studied the numerical stability of the linear convection-diffusion equation by analyzing the leading order truncation errors. The approach has then been applied to conclude on the stability of non-linear difference equations. In [67, 68], the authors used the matrix method to perform a similar study for central and upwind schemes applied to convection-diffusion equation. More generally, the Von Neumann analysis has been carried out in [69] for various time discretization methods and in [70] for the explicit central and upwind schemes. It has also been used in [71] to analyze six-point Pade

3. NUMERICAL METHODS AND THEIR ANALYSIS

type schemes. When it comes to a detailed account of the various methods used to study the stability of $1D$ convection-diffusion equation, readers are referred to [72] for further information.

Extensions to the multi-dimensional convection-diffusion equation are also available. In [73], authors study the stability of explicit time integration schemes using a matrix method with various boundary conditions and the Von-Neumann method for problems with periodic boundary conditions. In [74], the stability of Odd-Even Line Hopscotch (OELH) method is devised while solving the $2D$ convection-diffusion equation. Finally, [75] details the numerical properties of high-order compact schemes using GSA for the convection-diffusion equation.

On a few occasions, numerical analysis of schemes applied to LCDRE has also been performed. In [76], the authors developed a 2-step ADI scheme for solving the LCDRE equation. The unconditional stability of this scheme was then established using the Von-Neumann analysis. The phase error using this method is also reported. The method was validated using $1D$ and $2D$ LCDRE test cases. Recently in an article [77], the authors derived a non-linear stability criterion and applied it to analyse a discontinuous galerkin scheme for two different time integration approaches. The stability criteria that the authors developed are an extension of the classical Von-Neumann method by linearizing the convective term in the governing PDE. The applicability of this criteria was then demonstrated on simplified reactive Navier-Stokes equations. The authors in [78] developed a stabilized version of a mixed finite element method for the LCDRE. The stability and error analysis of this new method was carried out by defining a norm of the bilinear form expressed in the difference equation. In [79], a new scheme was developed for the non-linear LCDRE. The scheme is designed to ensure positivity of the dependent variables and the stability of the scheme was studied using Von-Neumann analysis after appropriate linearization of the governing non-linear LDRE.

The previous discussion highlights the following observations. Firstly, most of the studies in the past on numerical analysis have been performed on LCE. The numerical properties of schemes (LW and TTGC) have been well studied for this governing equation only. Secondly, the analysis of schemes for LCDE has been carried out with the prime focus being that of numerical stability. The diffusive and dispersive properties in the presence of diffusion have not been studied so far for LW and TTGC. Finally, analysis of schemes for LCRDE was mostly carried out for FE-type schemes for ascertaining stability limits. This study mentioned in this chapter is an attempt to address these shortcomings.

3.2 Objectives of this chapter

Based on the discussion in the previous section, the objectives of this chapter are listed as follows:

- (O.1) To introduce the framework of GSA. The advantages of GSA over other numerical analysis methods have been highlighted in the previous section. The introduction of GSA also serves as a prerequisite to Chapter 4 where the LES acceleration method is analyzed.
- (O.2) To study the numerical properties of LW and TTGC schemes as applied to LCDE and LCDRE.
- (O.3) To demonstrate the results from GSA using numerical tests.

3.3 Numerical methods in AVBP

As mentioned previously, AVBP is a massively parallel, cell-vertex based mixed FV-FE solver that works on unstructured meshes. The numerical formulation in AVBP belongs to a class of schemes called as Residual Distribution schemes (RD) and Fluctuation Splitting Schemes (FS). Due to the close proximity in the formulation to the FV based discretizations, it is easy to implement FE-based schemes in the solver and hence FE schemes such as TTGC and TTG4A are also available as numerical schemes in AVBP. AVBP schemes rely on cell topology to ensure the conservation of flow quantities while the flow properties are stored on the mesh nodes. This is quite different from the classical FV method of storing flow variables at cell centroids. The details of the implementation of this numerical scheme is presented as follows.

The compressible, Navier-Stokes (NS) equations in the conserved variable formulation are solved in AVBP. In the conservative form, the system of governing equations can be expressed as,

$$\frac{\partial U}{\partial t} + \frac{\partial F}{\partial x} = S \quad (3.1)$$

where U , F and S refer to the vector of conserved variables, numerical fluxes and source terms respectively. In AVBP, the conserved variables, as well as the primitive variables are stored at the cell vertices (used interchangeably as nodes). Based on the method of lines, the solution procedure is broadly split into two steps: (1) Residual calculation (2) Time integration and are explained as follows:

3. NUMERICAL METHODS AND THEIR ANALYSIS

- *Cell residual gather calculation:* In the first step, the cell residual defined at (a fictitious) cell centroid r_C is calculated using the Green-Gauss algorithm as given below. Here $|C|$ is the cell volume and F_h and dA refers to the numerical flux function and the area vector of the faces constituting the cell respectively. Since the primitive variables are already stored at the vertices of the cell, a simple trapezoidal rule is used to evaluate the surface integral. This operation is called the gather operation.

$$r_C = \frac{1}{|C|} \oint F_h \cdot dA \quad (3.2)$$

- *Cell residual scatter calculation:* As mentioned in the previous step, the cell residual is calculated at the cell centroid. This is redistributed to the cell vertices to obtain the node residual r_j by carrying out a volume-weighted average of cell residuals of all the cells that share the given node as given below.

$$r_j = \frac{1}{\mathcal{C}_j} \sum_{C \in \mathcal{D}_j} \mathcal{D}_{j,c} r_C |C| \quad (3.3)$$

Here, \mathcal{C}_j refers to the median-dual cell volume, $\mathcal{D}_{j,c}$ refers to the distribution matrix at the j^{th} node of cell C . This operation is shown in Fig. 3.1

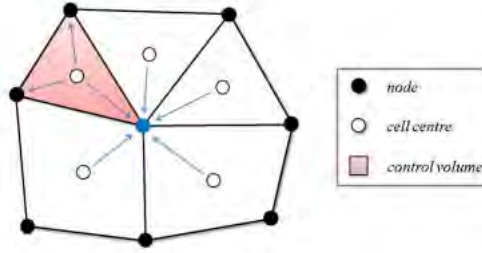


Figure 3.1: Scatter and gather operation in AVBP

- The last step involves time integration of the nodal residual integrated over the median-dual cell volume. Runge-Kutta (RK) time integration procedure is used for the time integration.

$$\int_{\mathcal{C}_j} \frac{d\mathbf{u}}{dt} dV \approx \frac{d\mathbf{u}_j}{dt} |\mathcal{C}_j| \quad (3.4)$$

For 1 and 2-step time integrations, the coefficients in the RK scheme is modified accordingly.

The calculation of the convective, diffusive and source term contribution to cell residual is explained briefly in the following paragraphs.

Convective flux residual

For the LW scheme which involves a single step time integration, the above mentioned steps result in the following algebraic equation for the vector of unknown variables u_j^{n+1} .

$$\frac{\mathbf{u}_j^{n+1} - \mathbf{u}_j^n}{\Delta t} = -\frac{1}{|\mathcal{C}_j|} \sum_{C \in \mathcal{D}_j} \frac{1}{n_v^C} \mathbf{r}_C^n |C| + \frac{\Delta t}{2d |\mathcal{C}_j|} \sum_{C \in \mathcal{D}_j} (\mathcal{A}_C \mathbf{r}_C)^n \cdot \mathbf{n}_{j,C} \quad (3.5)$$

$()^n$ and $()^{n+1}$ refer to properties at time levels at n and $n+1$ respectively. n_v^C is the number of vertices in cell C , d is the geometrical dimension of the problem and $\mathbf{n}_{j,C}$ is the normal at the j^{th} node of cell C .

Here, \mathcal{A}_C is the vector of flux jacobian tensors defined at the centroid of each cell.

A similar expression for the TTGC scheme, which comprises of 2-step time integration is as follows,

$$\mathbf{M} \frac{\mathbf{u}_j^{n+1} - \mathbf{u}_j^n}{\Delta t} = -\frac{1}{|\mathcal{C}_j|} \sum_{C \in \mathcal{D}_j} \frac{1}{n_v^C} \mathbf{r}_C^n |C| + \frac{\Delta t}{2d |\mathcal{C}_j|} \sum_{C \in \mathcal{D}_j} (\mathcal{A}_C \mathbf{r}_C)^n \cdot \mathbf{n}_{j,C} \quad (3.6)$$

The Equations. 3.5 and 3.6 are the same except for the mass matrix appearing on the left-hand side of Eqn. 3.6. Hence similar subroutines are used for calculating the residual contributions for LW and TTGC. However, TTGC involves the inversion of mass matrix \mathbf{M} to calculate the solution at time level $n + 1$. Numerically it is expensive to perform an exact inversion of the mass matrix and hence a two-pass Jacobi iteration is performed to obtain an approximate matrix inversion. Since TTGC involves two-time integrations along with an approximate mass matrix inversion, it is approximately 2-2.5 times costlier than the LW scheme.

Diffusive flux residual

The contributions to the node residual from the diffusive fluxes involve the surface integral of the viscous fluxes \mathbf{F}_j^v . This is calculated in AVBP as,

$$\nabla \cdot \mathbf{F}^v|_j = \frac{1}{d |\mathcal{C}_j|} \sum_{C \in \mathcal{D}_j} \mathbf{F}_{j,C}^v \cdot \mathbf{n}_{j,C} \quad (3.7)$$

The flux $\mathbf{F}_{j,C}^v$ is approximated to the viscous flux calculated using the cell centroid values. This way of calculating the viscous flux contribution involves the median-dual cell at node j and the stencil for this operation is shown in Figure 3.2.

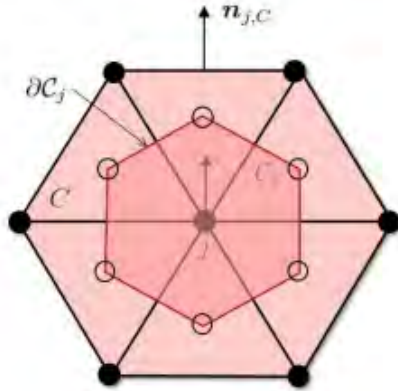


Figure 3.2: Stencil used in viscous flux calculation in AVBP

Source terms

The source term in the governing equations are evaluated using the values of primitive variables defined at node j as,

$$\int_{c_j} s d\nu = s_j |C_j| \quad (3.8)$$

While the residual contributions from diffusive fluxes are added at intermediate time steps (in multi-time integration schemes such as TTGC), the source terms are added to the residuals only at the final step of time integration.

3.4 Analysis of numerical schemes in AVBP

Having explained in brief the numerical schemes and their implementation in AVBP, in this section, their analysis using GSA is presented. This section is divided into three parts. Sections 3.4.1, 3.4.2 and 3.4.3 discuss the numerical analysis of LW and TTGC schemes applied to LCE, LCDE and LCDRE respectively. Each of these sections begins with a discussion on the theoretical properties of these PDEs followed by a discussion on the numerical dispersion relations. The application of these relations to LW and TTGC schemes are then discussed followed by interpretation of the results from GSA. Salient aspects of the properties are demonstrated using appropriate numerical tests.

3.4.1 1D Linear Convection Equation (LCE)

Theoretical analysis of 1D LCE

The 1D LCE is given by the equation,

$$\frac{\partial u}{\partial t} + c \frac{\partial u}{\partial x} = 0, \quad (3.9)$$

where $u(x, t)$ is the unknown dependent variable, $t \in [0, \infty)$ refers to time, $x \in [0, L]$ denotes space and c is a constant. For mathematical convenience and without losing generality, a periodic boundary condition is assumed at $x = 0$ and $x = L$. In order to obtain the physical dispersion relation, the unknown function u is expressed as its Fourier-Laplace transform given by,

$$u(x, t) = \int \int \bar{U}(k, \omega) e^{i(kx - \omega t)} dk d\omega, \quad (3.10)$$

In the above expression, $\bar{U}(k, \omega)$ is the Fourier-Laplace amplitude of function u . Substituting this relation in Eq. 3.9 the following dispersion relation is obtained.

$$\omega = c k \quad (3.11)$$

Here ω is the circular frequency and k is the wavenumber. Both of these quantities are real for the specific case of the linear convection equation considered. In order to obtain the exact solution, the Fourier transform of u is considered as below.

$$u(x, t) = \int \hat{U}(k, t) e^{i k x} dk, \quad (3.12)$$

Substituting this equation in Equation.3.9 one obtains the ordinary differential equation,

$$\frac{d\hat{U}}{dt} + i c k \hat{U} = 0. \quad (3.13)$$

the solution of which gives,

$$\hat{U}(k, t) = \hat{F}(k) e^{-i c k t}. \quad (3.14)$$

where $\hat{F}(k)$ is the Fourier transform of the initial solution $u(x, 0)$. Substituting this expression in Eqn. 3.12 one obtains,

$$u(x, t) = \int \bar{F}(k) e^{i k(x - c t)} dk, \quad (3.15)$$

This provides the very well-known solution of LCE wherein the initial solution is propagated at a speed c . The physical amplification factor, G_{phy} defined as the ratio of the Fourier amplitude between two times instance is given by,

3. NUMERICAL METHODS AND THEIR ANALYSIS

$$G_{phy} = \frac{\hat{U}(k, t + \Delta t)}{\hat{U}(k, t)} = e^{-i\omega\Delta t} = e^{-ikc\Delta t} \quad (3.16)$$

The absolute value of G_{phy} is equal to 1 implying that the input signal does not undergo any change in amplitude. The phase speed of the signal is given by

$$c_{phy} = \frac{\omega}{k} = c \quad (3.17)$$

and the group velocity, $V_{g,phy}$ is given by,

$$V_{g,phy} = \frac{d\omega}{dk} = c \quad (3.18)$$

The phase and group velocity are constant for the LCE considered here and independent of the wavenumber, k implying a non-dispersive system.

Numerical analysis of 1D LCE

Let us consider the numerical solution of the given LCE expressed in Eq. 3.9. Let u_i^n denote the numerical solution of the equation at the i^{th} node and at time level n . The location of the i^{th} node is given by $x_i = i h$ where h is the grid spacing. The current numerical time $t^n = n \Delta t$ where Δt is the time step used. The numerical value of u at time $n + 1$ is given by the general expression for explicit time integration schemes as,

$$u_i^{n+1} = S(u_{i-l}^n, u_{i-l+1}^n \dots u_{i+m}^n, u_{i-l}^{n-1}, u_{i-l+1}^{n-1} \dots u_{i+m}^{n-1}, \dots, u_{i-l}^{n-p}, u_{i-l+1}^{n-p} \dots u_{i+m}^{n-p}) \quad (3.19)$$

where l and m depend on the spatial stencil chosen and p depends on the temporal integration scheme.

The Fourier transform of the numerical solution at node j and time level n can be expressed as,

$$u_j^n = \int \hat{U}(k, t) e^{i k x_j} dk, \quad (3.20)$$

The Fourier transform of u_{j+l}^n then becomes using the phase shift property,

$$u_{j+l}^n = \int \hat{U}(k, t) e^{i k x_j} e^{i k l h} dk, \quad (3.21)$$

In analogy to the governing PDE, u_j^{n+1} is expressed as

$$u_j^{n+1} = \int G_{num} \hat{U}(k, t) e^{i k x_j} dk, \quad (3.22)$$

where G_{num} is the numerical amplification factor.

The numerical dispersion relation can then be expressed as,

3.4 Analysis of numerical schemes in AVBP

$$\omega_{num} = c_{num} k \quad (3.23)$$

Unlike the Von-Neumann analysis where the numerical phase speed is assumed the same as the physical phase speed, GSA accommodates the change in the phase speed observed numerically due to the nature of the scheme used. The numerical circular frequency will be a complex function when there are central difference terms occurring. The numerical phase angle β is given by,

$$\tan(\beta) = - \left(\frac{(G_{num})_{Imag}}{(G_{num})_{Real}} \right) \quad (3.24)$$

$(G_{num})_{Imag}$ and $(G_{num})_{Real}$ are the imaginary and real parts of the complex quantity G_{num} .

The numerical phase speed c_{num} is then obtained as,

$$c_{num} = \frac{\omega_{num}}{k} = \frac{\beta}{k \Delta t} \quad (3.25)$$

$$\frac{c_{num}}{c_{phy}} = \frac{\beta}{kh N_c} \quad (3.26)$$

where N_c is the Courant-Friedrich-Lewy (CFL) number defined by $N_c = c\Delta t/h$

The group velocity of the numerical solution $V_{g,num}$ is then calculated as,

$$V_{g,num} = \frac{\partial \omega_{num}}{\partial k} = \frac{1}{\Delta t} \frac{\partial \beta}{\partial k} \quad (3.27)$$

$$\frac{V_{g,num}}{V_{g,phy}} = \frac{\partial \beta}{N_c \partial kh} \quad (3.28)$$

The above-mentioned analysis is general for any numerical scheme. The application of this analysis to LW and TTGC schemes is provided in the following sections.

Application to LW and TTGC Schemes

The LW scheme when applied to the 1D LCE on a uniform grid with grid spacing h and time step Δt and CFL number N_c is given as follows:

$$u_j^{n+1} = u_j^n - \frac{N_c}{2}(u_{j+1}^n - u_{j-1}^n) + \frac{N_c^2}{2}(u_{j+1}^n - 2u_j^n + u_{j-1}^n), \quad (3.29)$$

Applying GSA as discussed previously to this stencil, gives the following relations for the numerical amplification factor (G_{LW}) for the LW scheme.

$$G_{LW} = 1 - i N_c \sin(kh) + [N_c^2 (\cos(kh) - 1)]. \quad (3.30)$$

3. NUMERICAL METHODS AND THEIR ANALYSIS

The relations for the numerical phase speed and group velocity then follow using the analysis shown before as,

$$\frac{c_{num}}{c} = \frac{1}{(kh)N_c} \tan^{-1} \left(\frac{N_c \sin(kh)}{1 + N_c^2(\cos(kh) - 1)} \right). \quad (3.31)$$

$$\frac{v_{g,num}}{c} = \left[\frac{\cos(kh) + N_c^2(1 - \cos(kh))}{(1 + N_c^2(\cos(kh) - 1))^2 + N_c^2 \sin^2(kh)} \right]. \quad (3.32)$$

The TTGC scheme is derived ([64]) similar to the LW scheme by employing Taylor series expansion of u with respect to time and substituting the first and second-order time derivatives using central spatial difference relations. The scheme is designed to involve two steps and when applied to LCE is given in the following form,

$$\begin{aligned} \tilde{u}^n &= u^n + \alpha_{TTGC} \Delta t u_t^n + \beta_{TTGC} \Delta t^2 u_{tt}^n \\ u^{n+1} &= u^n + \Delta t \tilde{u}_t^n + \gamma_{TTGC} \Delta t^2 u_{tt}^n \end{aligned} \quad (3.33)$$

where $\tilde{()}$ denotes the values of the numerical solution at the intermediate time step. $\alpha_{TTGC}, \beta_{TTGC}$ and γ_{TTGC} are tunable constants. Applying the Galerkin approach assuming P1 element formulation on Eq. 3.34 one obtains,

$$\frac{(\tilde{u}_{i+1}^n + 4\tilde{u}_i^n + \tilde{u}_{i-1}^n)}{6} = \frac{(u_{i+1}^n + 4u_i^n + u_{i-1}^n)}{6} - \alpha_{TTGC} N_c \frac{(u_{i+1}^n - u_{i-1}^n)}{2} \quad (3.34)$$

$$+ \beta_{TTGC} N_c^2 (u_{i+1}^n - 2u_i^n + u_{i-1}^n) \quad (3.35)$$

$$\frac{(u_{i+1}^n + 4u_i^n + u_{i-1}^n)}{6} = \frac{(u_{i+1}^n + 4u_i^n + u_{i-1}^n)}{6} - N_c \frac{(\tilde{u}_{i+1}^n - \tilde{u}_{i-1}^n)}{2} \quad (3.36)$$

$$+ \gamma_{TTGC} N_c^2 (u_{i+1}^n - 2u_i^n + u_{i-1}^n) \quad (3.37)$$

Applying GSA on the above stencil, one obtains the expressions for the numerical amplification factor for TTGC scheme G_{TTGC} , the phase speed and group velocity as given below.

$$G_{TTGC} = 1 + \gamma_{TTGC} N_c \hat{A} \hat{S} - \alpha_{TTGC} (\hat{A} \hat{L})^2 - i \hat{A} \hat{L} \left(1 + \beta_{TTGC} N_c \hat{A} \hat{S} \right) \quad (3.38)$$

$$\frac{c_{num}}{c} = -\frac{\theta}{(kh)N_c} \quad (3.39)$$

$$\frac{V_{g,num}}{c} = \frac{1}{N_c} \frac{\partial \theta}{\partial kh} \quad (3.40)$$

3.4 Analysis of numerical schemes in AVBP

Here, θ is the argument of the complex function G_{TTGC} . And the parameters in Eq. 3.40 are defined as,

$$\hat{A} = \frac{3 N_c}{(2 + \cos(kh))}, \quad (3.41)$$

$$\hat{S} = 2 (\cos(kh) - 1) \quad (3.42)$$

$$\hat{L} = \sin(kh) \quad (3.43)$$

Discussion on numerical properties

The results of the analysis are presented now. As mentioned previously, the exact solution of LCE propagates the initial solution undissipated with a phase and group velocity equal to c . Hence, any scheme used in high-performance computing codes should preserve the amplitude of the initial solution and propagate this solution with the right speed c . Hence, the three numerical properties (hereafter referred to as DRP properties) of schemes of interest to us are the numerical amplification factor $|G_{num}|$, the non-dimensional phase speed c_{num}/c and the non-dimensional group velocity $V_{g,num}/c$. These properties for the LW and TTGC schemes are plotted in Figure 3.3 as a function of kh (non-dimensional wavenumber) and N_c . To highlight how well these schemes preserve the exact dispersion relation, a tolerance of 1% is applied (shown as the gray region in the figure) on these properties.

It is observed from Figure 3.3 that the DRP regions for all the three properties, namely $|G_{num}|, c_{num}/c, V_{g,num}/c$, are larger for TTGC when compared to LW emphasizing the superior numerical performance of TTGC scheme. While for TTGC, 52% of the full $kh - N_c$ space is DRP (for G_{num}), only 37% is DRP in the case of LW. Similarly, the DRP regions of phase speed and group velocity for TTGC scheme is 36% and 25% respectively. The corresponding numbers for LW scheme are 15% and 8% only. It is also to be noted that while TTGC can resolve the exact group velocity of the solution up to a wavenumber of 0.75, LW can accomplish similar performance only up to $kh = 0.15$. It is also interesting to observe that there exist regions in the $kh - N_c$ plane where the numerical group velocity is negative. This would imply the solution traveling in the opposite direction to that of the exact solution. Such conditions are known as q-waves in literature. Typically these waves occur at high wavenumbers. For TTGC scheme, q-wave region is observed for $kh \geq 2.1$ while for the LW scheme q-waves are found to occur for $kh \geq 1.57$ showing that TTGC can resolve the right direction of group velocity much better than LW.

3. NUMERICAL METHODS AND THEIR ANALYSIS

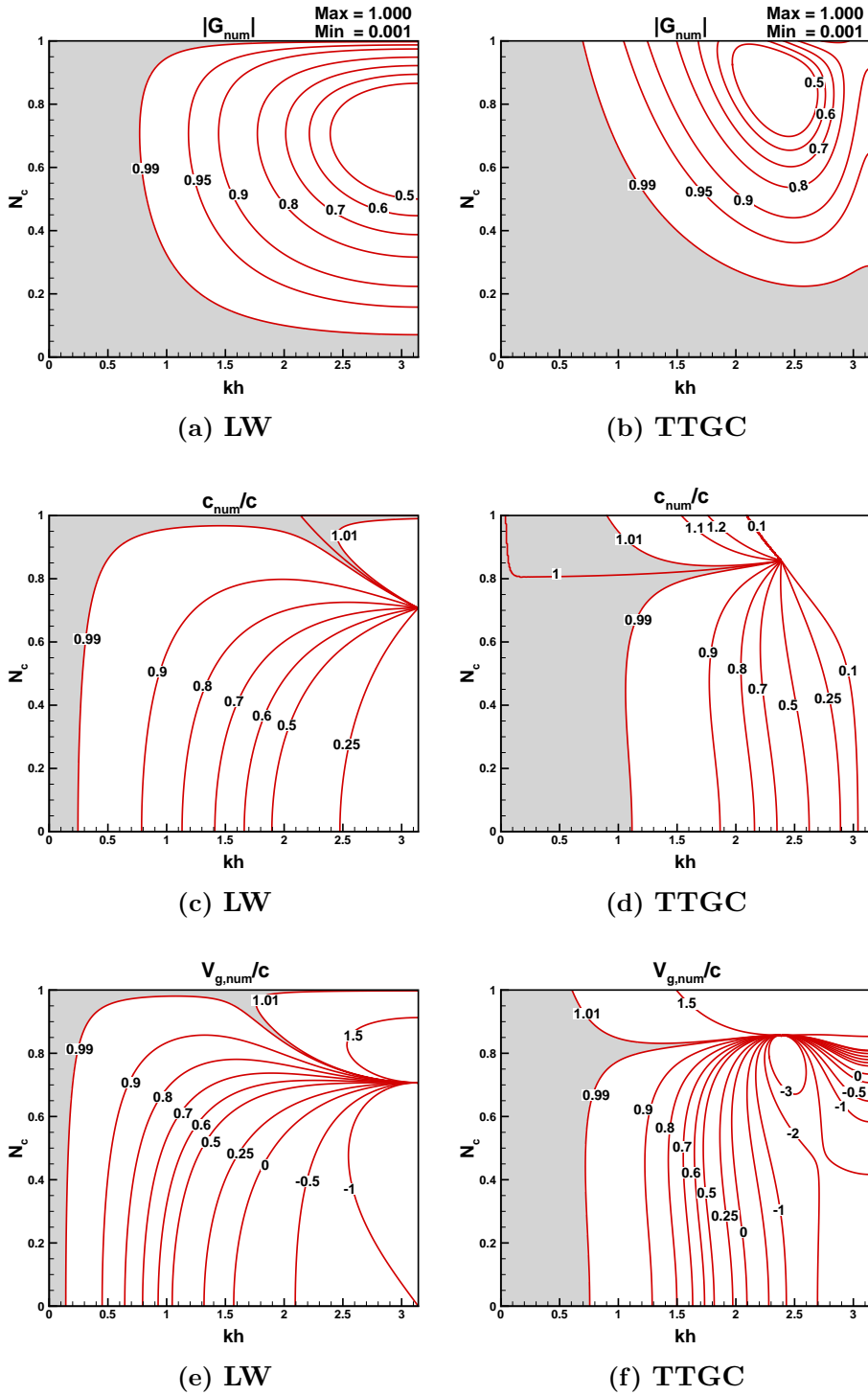


Figure 3.3: Dispersion relation properties for LW and TTGC scheme when applied to the 1D linear convection equation.

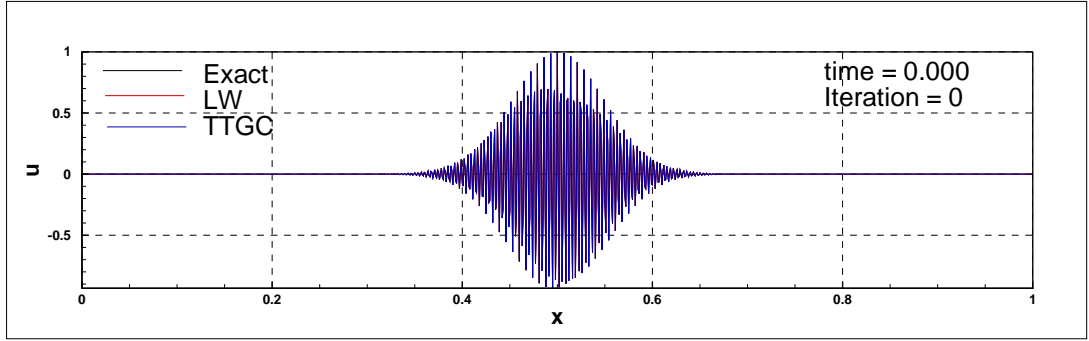
To demonstrate the q-wave phenomena and the performance of LW and TTGC at such conditions, a numerical solution of LCE is carried out using these schemes. The spatial domain $0 \leq x \leq 1$ is discretised using 1000 elements ($h = 0.001$). The initial solution provided is that of a wavepacket with a central wavenumber

3.4 Analysis of numerical schemes in AVBP

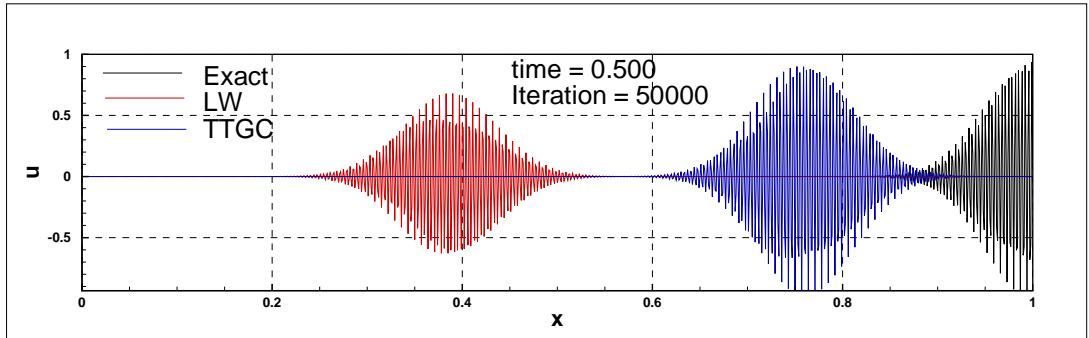
(k_0) corresponding to $k_0h = 1.8$ as shown in Figure 3.4 (a). The initial solution is provided by the following equation,

$$u(x, 0) = e^{-\alpha_0(x-x_0)^2} \sin(k_0x) \quad (3.44)$$

The value of α_0 used here is 0.05. CFL number, N_c used in this test is 0.01. The value of $V_{g,num}/c$ for LW and TTGC schemes obtained using GSA analysis and shown in Figures 3.3 (e) and (f) for the value of $kh = 1.8$ and $N_c = 0.01$ are -0.22 and 0.52 respectively. The numerical solution obtained using LW and TTGC schemes after 5000 iterations is shown in Figure 3.4 (b). The solution obtained using the LW scheme shows a damped initial solution that propagated upstream while the TTGC solution propagates the solution in the right direction although with an incorrect group velocity. The numerically observed group velocities are -0.221 and 0.518 respectively and are in an excellent match with the theoretically predicted values.



(a) $t = 0$



(b) $t = 0.5$

Figure 3.4: q-Waves observed in the solution of LCE using LW and TTGC schemes. $kh = 1.8$ and $N_c = 0.01$ values are used. The LW solution is can be observed to propagate upstream while TTGC scheme propagates at half the right speed.

3.4.2 1D Linear Convection-Diffusion Equation (LCDE)

Theoretical analysis of 1D LCDE

The 1D LCDE in one-dimensional space coordinate x and time t is given as,

$$\frac{\partial u}{\partial t} + c \frac{\partial u}{\partial x} = \alpha \frac{\partial^2 u}{\partial x^2}, \quad (3.45)$$

Here, c and α are real numbers and constants specifying respectively the convection speed (as shown in the following paragraphs) and diffusion coefficient. The spatial domain is defined as $0 \leq x \leq L$ and periodic boundary conditions are assumed at $x = 0$ and $x = L$. To calculate the physical dispersion properties of this equation, the dependent variable $u(x, t)$ is expressed in terms of its Fourier Transform given by Eqn. 3.10. Substitution of this expression in Eqn. 3.45 one obtains the exact dispersion relation for the LCDE as,

$$\omega = c k - i \alpha k^2. \quad (3.46)$$

When compared to the LCE, the dispersion relation of LCDE now accommodates a complex circular frequency ω .

The exact phase and group velocity for this PDE is obtained using as,

$$c_\varphi = \frac{\omega}{k} = c - i \alpha k, c_{phy} = Re(c_\varphi) = c \quad (3.47)$$

$$v_{g,\varphi} = \frac{\partial \omega}{\partial k} = c - 2 i \alpha k. V_{g,phy} = Re(V_{g,\varphi}) = c \quad (3.48)$$

The imaginary part is here a direct result of the energy damping as a function of time and contained in a wave k . The importance of the complex group velocity or the energy propagation speed is detailed in [75]. Note that both retrieved speeds are effectively complex functions due to the diffusion process taking place at the same time as convection.

Another way of looking at the above problem is to access the physical amplification factor: *i.e.* comparing the solution amplitude at two distinct time instants separated by Δt so that,

$$G_{phy} = \frac{\hat{U}(k, t + \Delta t)}{\hat{U}(k, t)} = e^{-\alpha k^2 \Delta t} e^{-i k c \Delta t} = e^{-i \omega \Delta t}. \quad (3.49)$$

For the problem at hand, G_{phy} solely depends on the speed at which information travels through the medium while it is diffused as expressed through Eq. (3.49).

Numerical analysis of 1D LCDE

Similar to the analysis done previously for 1D LCE, the numerical dispersion relation for the convection-diffusion equation can be formulated as,

$$\omega_{num} = c_{num} k - i \alpha_{num} k^2. \quad (3.50)$$

The numerical dispersion relation depends on the numerical phase speed (c_{num}) and the numerical diffusion coefficient (α_{num}). As emphasized earlier, ideally one desires these quantities to be equal to their physical counterparts but are seldom observed to be so in finite numerical computations. The expression for the numerical amplification factor can be obtained as,

$$G_{num} = e^{-i \omega_{num} \Delta t} \quad (3.51)$$

$$= e^{-i c_{num} k \Delta t - \alpha_{num} k^2 \Delta t} \quad (3.52)$$

The amplitude of the numerical amplification is then,

$$|G_{num}| = e^{-\alpha_{num} k^2 \Delta t} \quad (3.53)$$

The expressions for phase angle β , phase speed c_{num} and group velocity $V_{g,num}$ remain similar to the one for the convection equation but now is also a function of the Peclet number, $Pe = \alpha \Delta t / h^2$.

$$\beta = \tan^{-1} \left(\frac{-\text{Imag}(G_{num})}{\text{Real}(G_{num})} \right) \quad (3.54)$$

$$\frac{c_{num}}{c} = \frac{\beta}{(kh) N_c} \quad (3.55)$$

$$\frac{V_{g,num}}{V_{g,phy}} = \frac{1}{N_c} \frac{\partial \beta}{\partial (kh)} \quad (3.56)$$

$$(3.57)$$

Till now, the numerical properties derived are similar to the ones derived for LCE except for the fact that they are no more functions of kh and N_c alone, but also the Peclet number Pe . However, for the case of LCDE, in addition to the above DRP properties, one also needs to include the non-dimensional numerical diffusion coefficient which can be obtained from Eqn. 3.53 by taking the natural logarithm and can be expressed as,

$$\ln(|G_{num}|) = -\alpha_{num} k^2 \Delta t \quad (3.58)$$

$$\frac{\alpha_{num}}{\alpha} = \frac{-\ln(|G_{num}|)}{Pe (kh)^2} \quad (3.59)$$

3. NUMERICAL METHODS AND THEIR ANALYSIS

Application of GSA to LW applied to LCDE

The diffusion term in the LCDE is modeled using second-order central difference (CD_2) approximation in AVBP. The LW scheme for convection term and CD_2 approximation for diffusion term (together denoted as $LW - CD_2$) when applied to the 1D LCDE has the following stencil, at node j and time level n ,

$$u_j^{n+1} = u_j^n - \frac{N_c}{2}(u_{j+1}^n - u_{j-1}^n) + \frac{N_c^2}{2}(u_{j+1}^n - 2u_j^n + u_{j-1}^n) + Pe(u_{j+1}^n - 2u_j^n + u_{j-1}^n) \quad (3.60)$$

$$= u_j^n - \frac{N_c}{2}(u_{j+1}^n - u_{j-1}^n) + \varsigma(u_{j+1}^n - 2u_j^n + u_{j-1}^n) \quad (3.61)$$

where $\varsigma = N_c^2/2 + Pe$

Substituting the Fourier Transform for the numerical solution of u_j^n in the above equation, one obtains the expression for numerical amplification factor for the $LW - CD_2$ scheme as,

$$G_{LW-CD_2} = 1 - i N_c \sin(kh) + 2\varsigma(\cos(kh) - 1) \quad (3.62)$$

The numerical phase angle, β_{LW-CD_2} is then obtained as,

$$\beta_{LW-CD_2} = \tan^{-1} \left(\frac{N_c \sin(kh)}{1 + 2\varsigma(\cos(kh) - 1)} \right) \quad (3.63)$$

and the non-dimensional numerical phase speed and group velocity,

$$\frac{c_{num}}{c_{phy}} = \frac{c_{num}}{c} = \frac{\beta_{LW-CD_2}}{(kh) N_c} \quad (3.64)$$

$$\frac{V_{g,num}}{V_{g,phy}} = \frac{V_{g,num}}{c} = \frac{1}{N_c} \frac{\partial \beta_{LW-CD_2}}{\partial (kh)} \quad (3.65)$$

The numerical diffusion coefficient is calculated according to equation Eqn. 3.99.

$$\frac{\alpha_{num}}{\alpha} = \frac{-\ln(|G_{LW-CD_2}|)}{Pe (kh)^2} \quad (3.66)$$

Application of GSA to TTGC- CD_2

Similar to the $LW - CD_2$ scheme discussed in the previous subsection, the diffusive terms are modeled using second-order central difference terms in both the time integrations steps in TTGC. Then the stencil of TTGC applied to LCDE is

given as,

$$\frac{(\tilde{u}_{i+1}^n + 4\tilde{u}_i^n + \tilde{u}_{i-1}^n)}{6} = \frac{(u_{i+1}^n + 4u_i^n + u_{i-1}^n)}{6} - \alpha_{TTGC} N_c \frac{(u_{i+1}^n - u_{i-1}^n)}{2} \quad (3.67)$$

$$+ \beta_{TTGC} N_c^2 (u_{i+1}^n - 2u_i^n + u_{i-1}^n) + Pe (u_{i+1}^n - 2u_i^n + u_{i-1}^n) \quad (3.68)$$

$$\frac{(u_{i+1}^n + 4u_i^n + u_{i-1}^n)}{6} = \frac{(u_{i+1}^n + 4u_i^n + u_{i-1}^n)}{6} - N_c \frac{(\tilde{u}_{i+1}^n - \tilde{u}_{i-1}^n)}{2} \quad (3.69)$$

$$+ \gamma_{TTGC} N_c^2 (u_{i+1}^n - 2u_i^n + u_{i-1}^n) + Pe (u_{i+1}^n - 2u_i^n + u_{i-1}^n) \quad (3.70)$$

Application of GSA to TTGC scheme then yields the following expressions for $G_{num}, c_{num}, V_{g,num}$ and α_{num} .

$$G_{TTGC-CD_2} = 1 + \frac{\hat{A} \hat{S} \varsigma_2}{N_c} - \alpha_{TTGC} (\hat{A} \hat{L})^2 - i \hat{A} \hat{L} \left(1 + \frac{\hat{A} \hat{S} \varsigma_1}{N_c} \right) \quad (3.71)$$

$$\frac{c_{num}}{c} = -\frac{\theta}{(kh)N_c} \quad (3.72)$$

$$\frac{V_{g,num}}{c} = \frac{1}{N_c} \frac{\partial \theta}{\partial kh} \quad (3.73)$$

$$\frac{\alpha_{num}}{\alpha} = \frac{-\ln(|G_{TTGC-CD_2}|)}{Pe (kh)^2} \quad (3.74)$$

where the numerical phase angle β is now given as,

$$\tan(\beta) = -\left(\frac{\text{Imag}(G_{TTGC-CD_2})}{\text{Real}(G_{TTGC-CD_2})} \right) \quad (3.75)$$

Discussion on numerical properties for LCDE

The DRP properties of schemes when applied to LCDE now depend on the Peclet number Pe , in addition to kh and N_c as explained previously. The properties of these schemes are now explained in terms of dissipation, dispersion and diffusion in the following paragraphs.

Dissipation properties: The exact solution to LCDE no more preserves the amplitude of the initial solution. This can be observed from the expression for G_{phy} in Eqn. 3.49 and its dependence on the diffusion coefficient. Hence, to characterize the stability property of schemes, a new quantity G_{rel} is defined as, $G_{rel} = |G_{num}|/|G_{phy}|$. For an ideal numerical scheme, $G_{rel} = 1$ is desired. $G_{rel} < 1$ implies an over-damped solution while $G_{rel} > 1$ implies an under-damped one. $G_{rel} > 1$ does not necessarily imply numerical instability as the amplitude of the numerical solution can be greater than that of the exact solution even while

3. NUMERICAL METHODS AND THEIR ANALYSIS

being stable. In order to identify the unstable region, the condition $|G_{num}| > 1$ is appropriate.

The contours of G_{rel} as a function of kh and N_c for various values of Pe are shown in Figure 3.5 for the LW scheme and in Figure 3.6 for the TTGC scheme. The DRP region (identified as the region with 1% tolerance from the exact solution) is shown in gray. The unstable region defined by $G_{num} > 1$ is colored in orange. One observes that the effect of viscous dissipation is to decrease the stable region of the computations for both LW and TTGC schemes. While for small values of Pe ($Pe < 0.01$), the unstable regions are observed at high wavenumbers ($kh > 1.5$) and at N_c values close to 1, at high values of Pe ($Pe > 0.1$) unstable regions are clearly visible at lower values of N_c and kh . For the LW scheme, at $Pe = 0.5$, the unstable region extends across all values of N_c at high wavenumbers. This would imply that even if the numerical solution contains low-frequency content, (large flow structures in case of CFD), the background noise in the solution that typically occurs at high frequencies may get amplified and can finally lead to numerical instability. Hence $Pe = 0.5$ is the critical value of Pe beyond which stable computations are impossible. A similar value of Pe for the TTGC scheme is $Pe = 0.17$.

In order to illustrate this further, the results of a numerical test are illustrated in Figure 3.9. Here the numerical solution of LCDE is sought using LW-CD₂ scheme. The one-dimensional domain used in the test extends from $x = -50$ to $x = 50$ and is discretised using 1000 grid elements. The initial solution is that of a wavepacket similar to the one used in the previous section on LCE and centered around $kh = 1.8$ and initially located at $x = 0$. The Pe number chosen is 0.5 and the value of N_c is fixed as 0.4. The results from the numerical solution at various time instants are shown in Figure 3.7. From the DRP chart in Figure 3.5 one can find that the value of G_{rel} is 0.575 and hence an underdamped solution is predicted by GSA. This is indeed observed in frames (b) and (c) of Figure 3.7 where the numerical solution is gradually damped. At time $t = 5$, the numerical solution is found to be completely damped. However, after long time integration (at $t = 20.0$) spurious oscillations are observed in frame (d) of Figure 3.7. This is due to the amplification of the background numerical noise arising from round-off errors which appear at the Nyquist frequency ($kh = \pi$).

Dispersion properties: Since flow features, in general, occur in a wide range of wavenumbers, it is more worthwhile to look at non-dimensional group velocities rather than phase speed. Figures 3.8 and 3.9 shows the contours of $V_{g,num}/c$ for LW and TTGC schemes respectively. The DRP regions are shaded in gray while the q-wave regions are colored in orange. One can observe that at low values

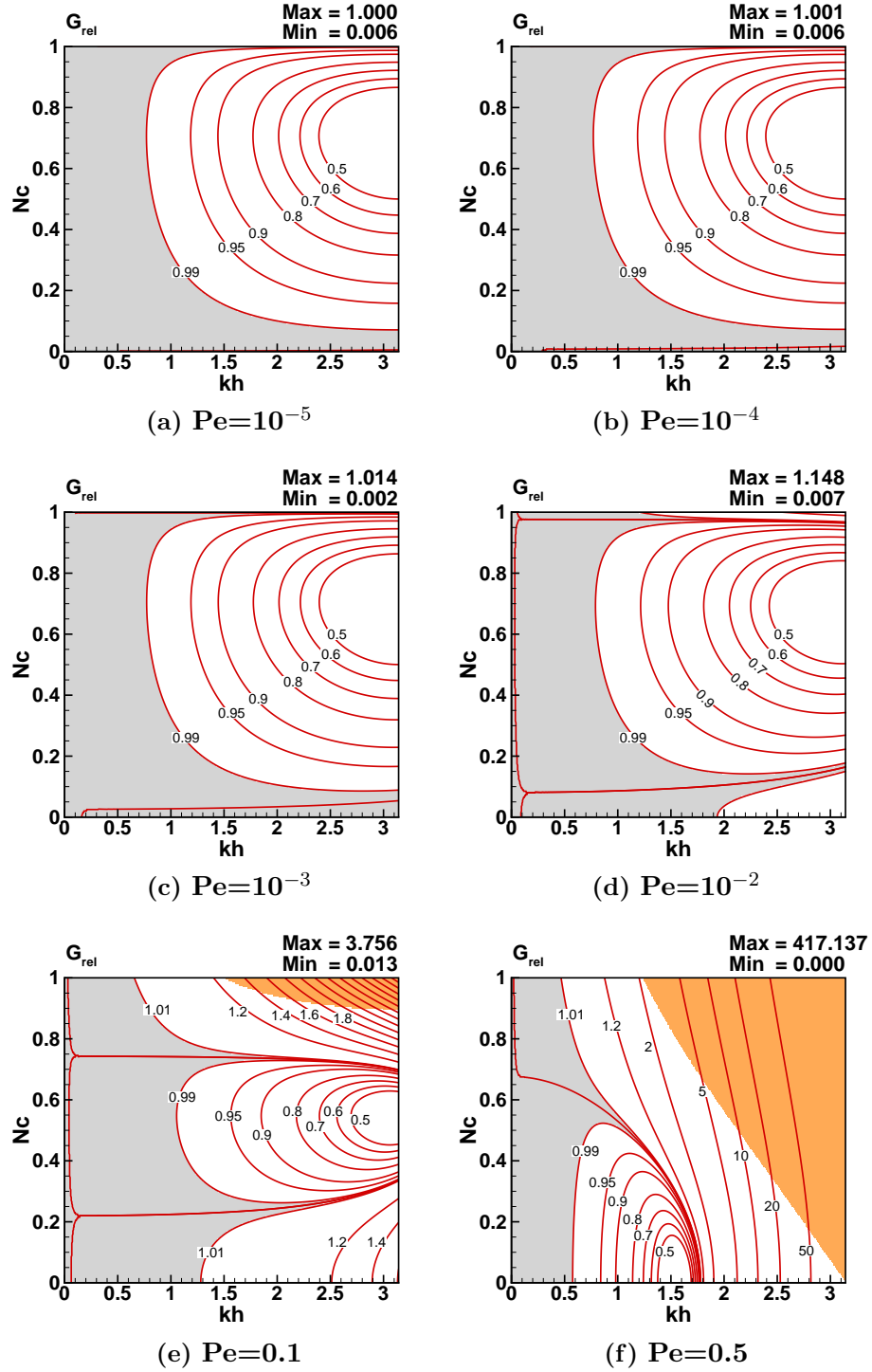


Figure 3.5: Contours of G_{rel} for LW scheme at various values of Pe

of Pe the effect of Pe on $V_{g,num}$ is less pronounced for both LW and TTGC schemes alike. At $Pe > 0.1$, the DRP regions increasingly keep shrinking and being limited to very low kh values. At $Pe > 0.25$ LW scheme does not exhibit any more q-wave phenomena while for TTGC, q-wave regions are present until $Pe = 0.17$ which is the limiting value of Pe for stable computations.

3. NUMERICAL METHODS AND THEIR ANALYSIS

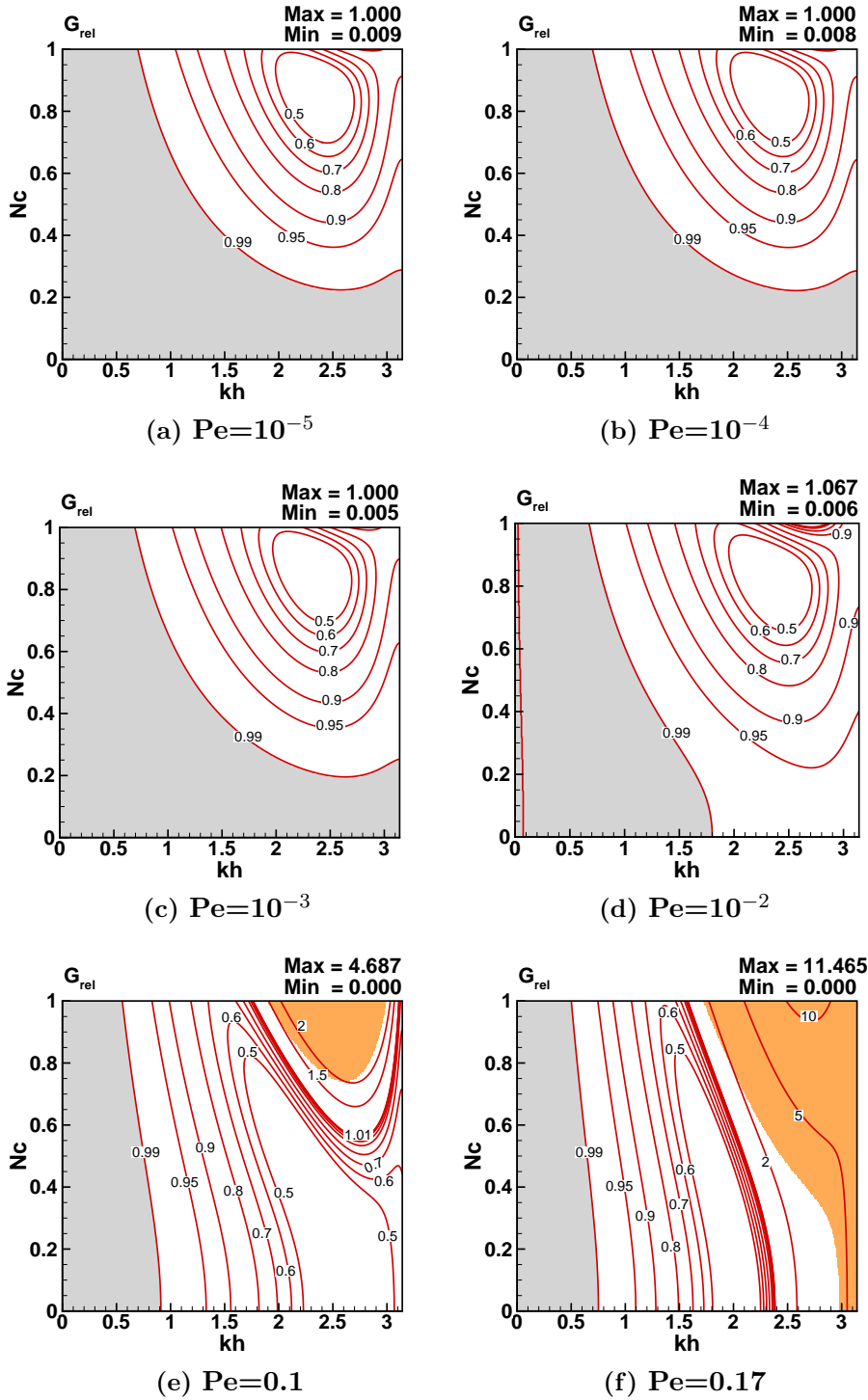


Figure 3.6: Contours of G_{rel} for TTGC scheme at various values of Pe

Diffusion properties: An additional property to be analysed for LCDE is the non-dimensional diffusion coefficient α_{num}/α . The contours of α_{num}/α for LW and TTGC schemes at various Pe are shown in Figures 3.10 and 3.11 respectively. As in the case of other DRP properties shown previously, the DRP regions are colored

3.4 Analysis of numerical schemes in AVBP

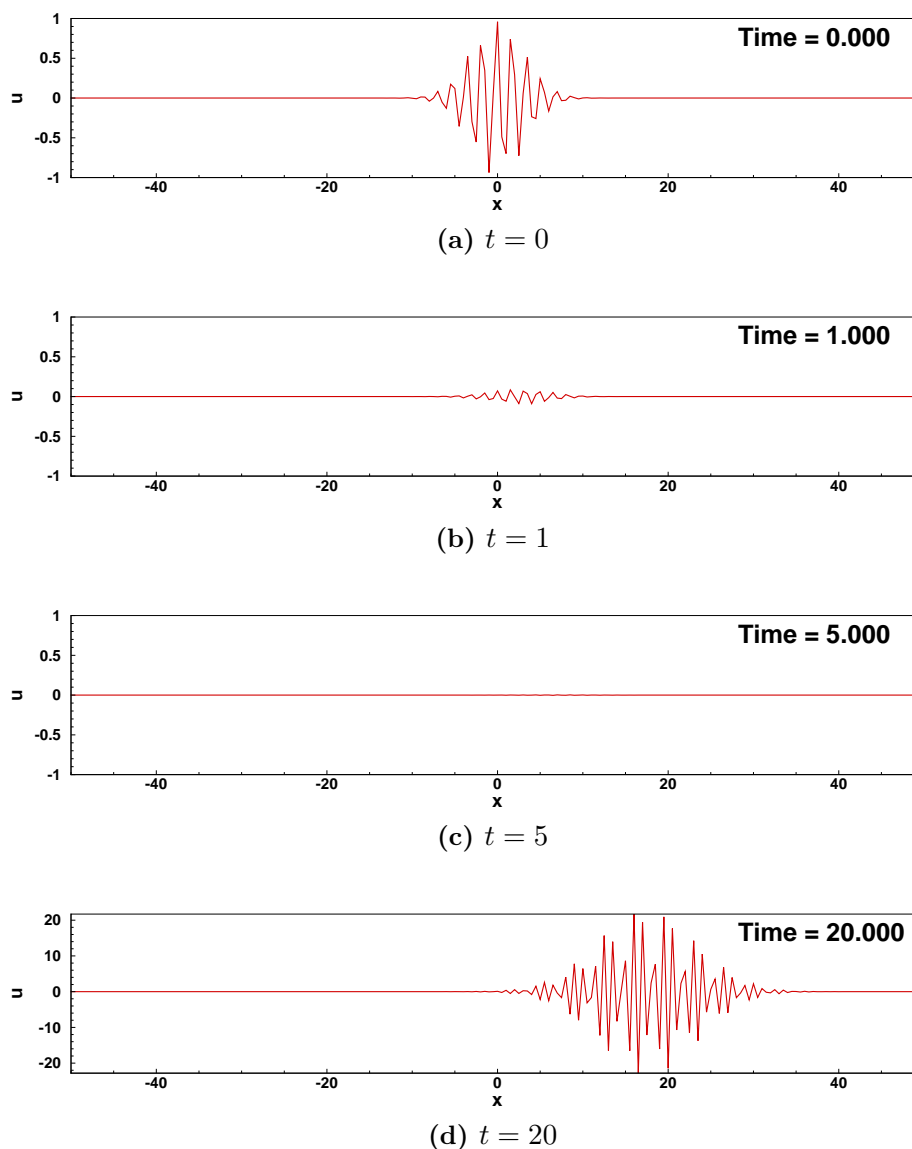


Figure 3.7: Numerical solution of LCDE with initial wavepacket solution. LW-CD₂ is used with $k_0h = 1.8$, $N_c = 0.01$, $Pe = 0.5$

in gray. At low values of Pe , the DRP regions for LW and TTGC are located very close to the origin ($kh = 0$ and $N_c = 0$). TTGC is found to resolve diffusion better than LW scheme. As Pe is increased, the DRP regions increases considerably for LW scheme than TTGC scheme. The presence of a negative diffusion coefficient is observed from $Pe = 0.1$ for both LW and TTGC schemes. Negative diffusion coefficients imply anti-diffusion and are clear indicators of impending numerical instability. It is also interesting to observe that the regions of anti-diffusion coincide with that of $|G_{num}| > 1$ shown in Figures 3.5 and 3.6. Hence, numerical instabilities for LCDE are nothing but manifestations of anti-diffusion at high wavenumbers.

3. NUMERICAL METHODS AND THEIR ANALYSIS

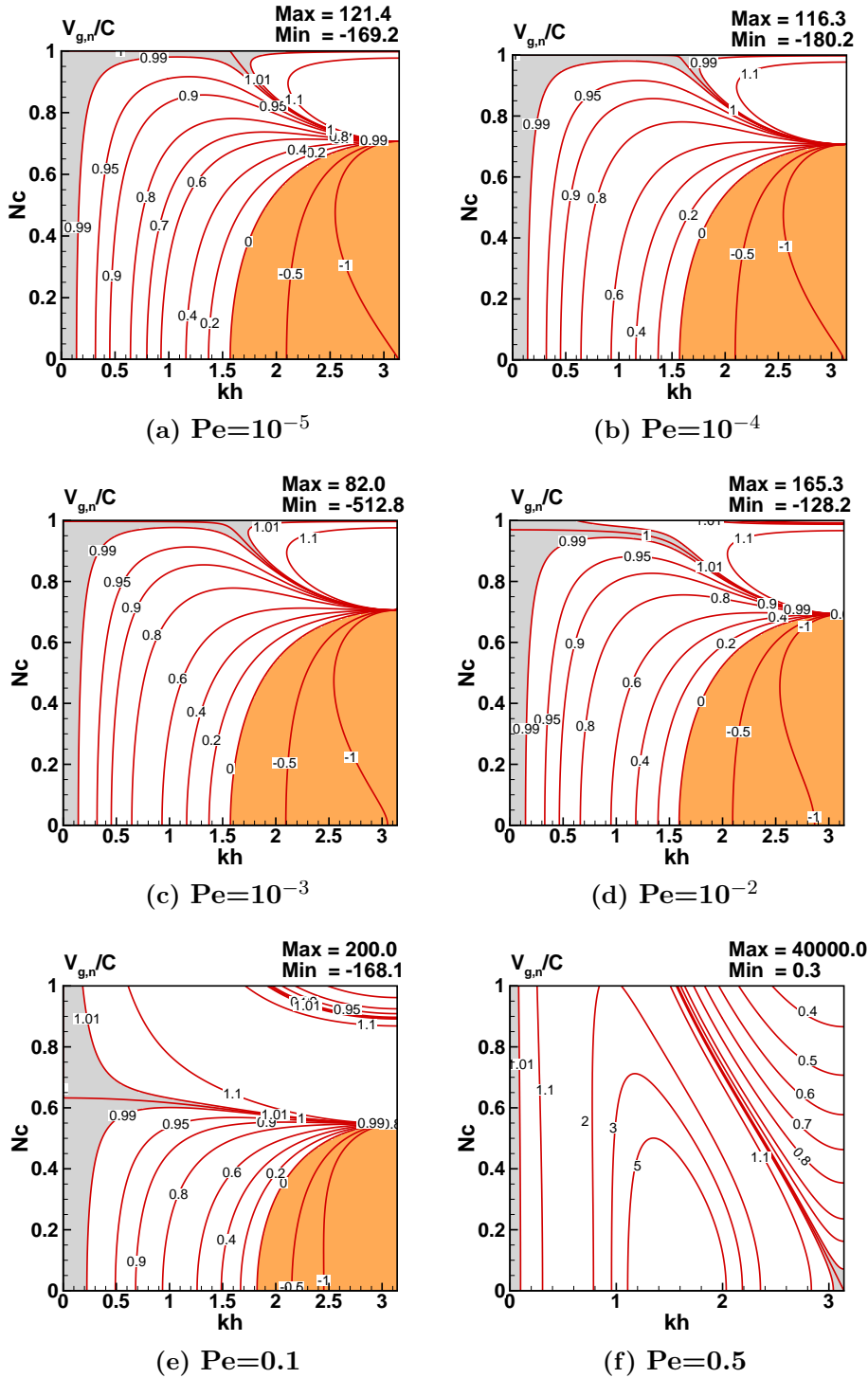


Figure 3.8: Contours of non-dimensionalised numerical group velocity $V_{g,n}/C$ for LW scheme at various values of Pe

In order to highlight this effect of α_{num}/α on the numerical solution yet another numerical test is performed. Similar to the previous numerical test, the LCDE is solved on the domain $0 \leq x \leq 1$. A wavepacket with the central spatial frequency corresponding to $kh = 1$ and located initially at $x = 0.5$ is provided

3.4 Analysis of numerical schemes in AVBP

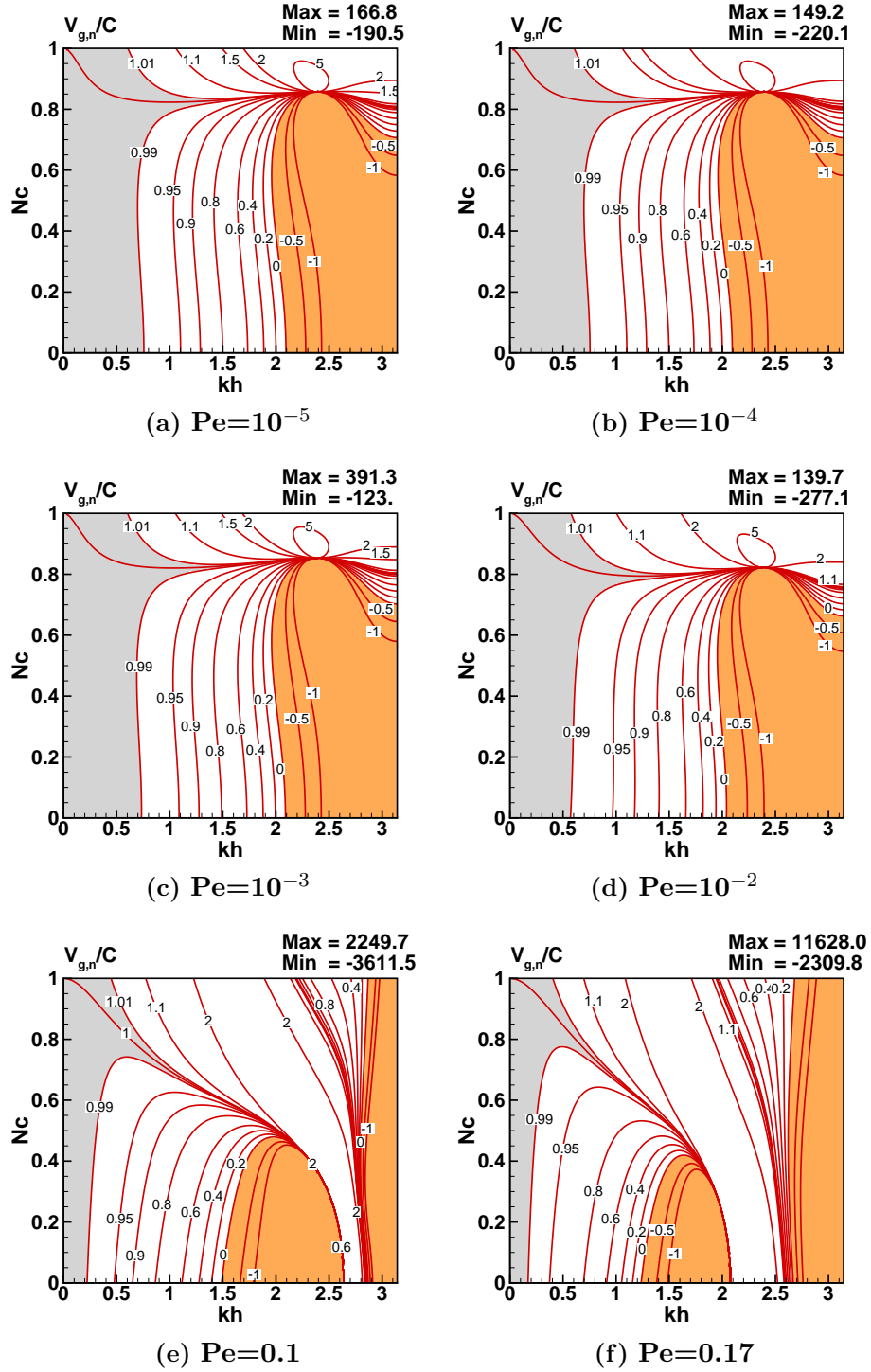


Figure 3.9: Contours of non-dimensionalised numerical group velocity $V_{g,n}/C$ for TTGC scheme at various values of Pe

as the initial solution. The value of Pe is fixed as 0.0001 and that of N_c as 0.35. LW-CD₂ scheme is used for the numerical solution. From the DRP property chart in Figure 3.11, for the specified values of kh , N_c and Pe , the value of $\alpha_{num}/\alpha = 10.5$ and that of $G_{rel} = 0.99$. Hence, the solution is predicted to be

3. NUMERICAL METHODS AND THEIR ANALYSIS

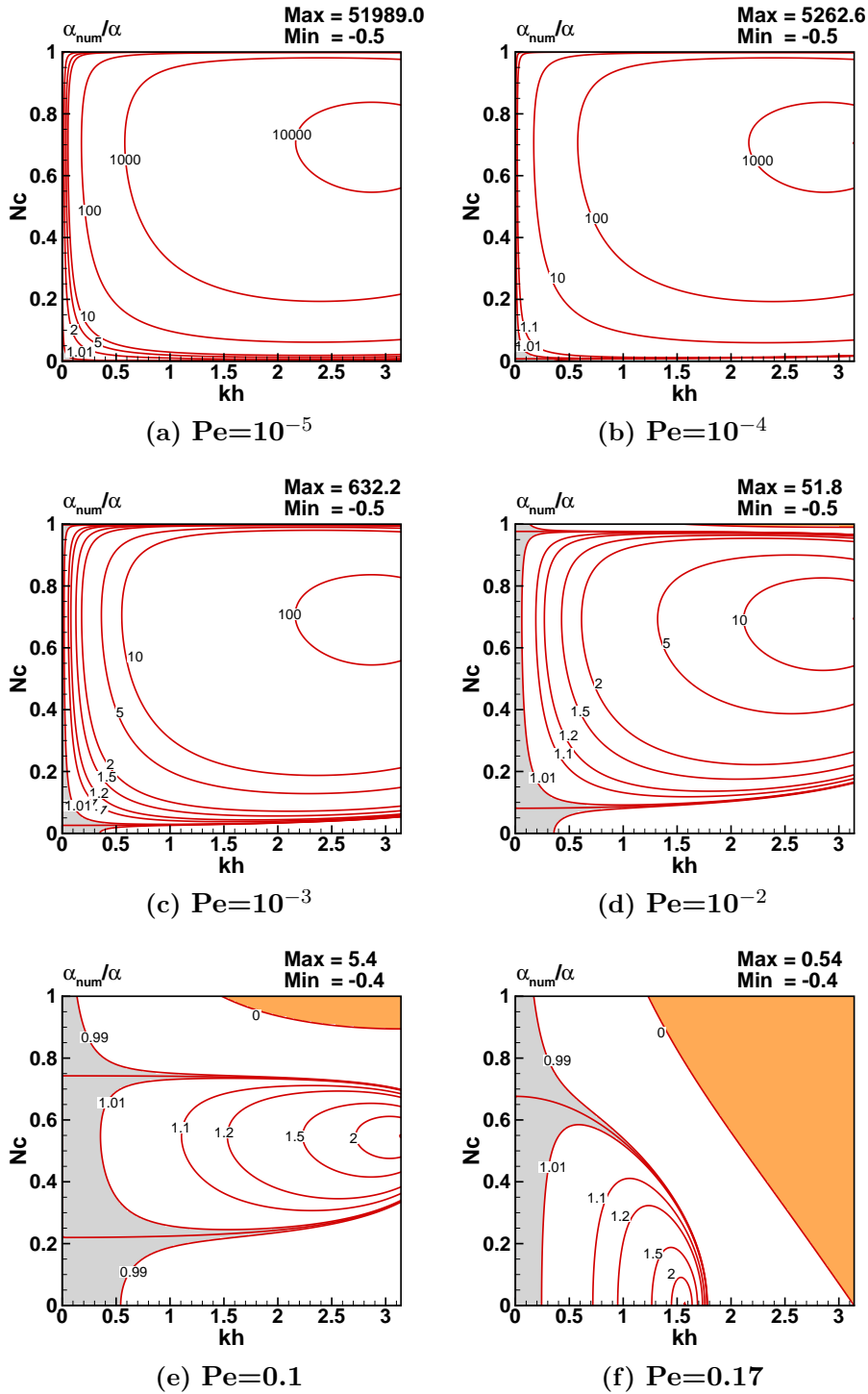


Figure 3.10: Contours of non-dimensionalised numerical diffusion coefficient α_{num}/α for LW-CD₂ scheme at various values of Pe

stable (since $G_{rel} < 1$). The numerical solution at time $t = 0.315$ is shown in Figure 3.12 (a). The damped numerical solution is clearly observable when compared to the exact solution (colored in black). Figure 3.12 (b) shows the exact solution for the same problem with the diffusion coefficient modified to $= 10.5$

3.4 Analysis of numerical schemes in AVBP

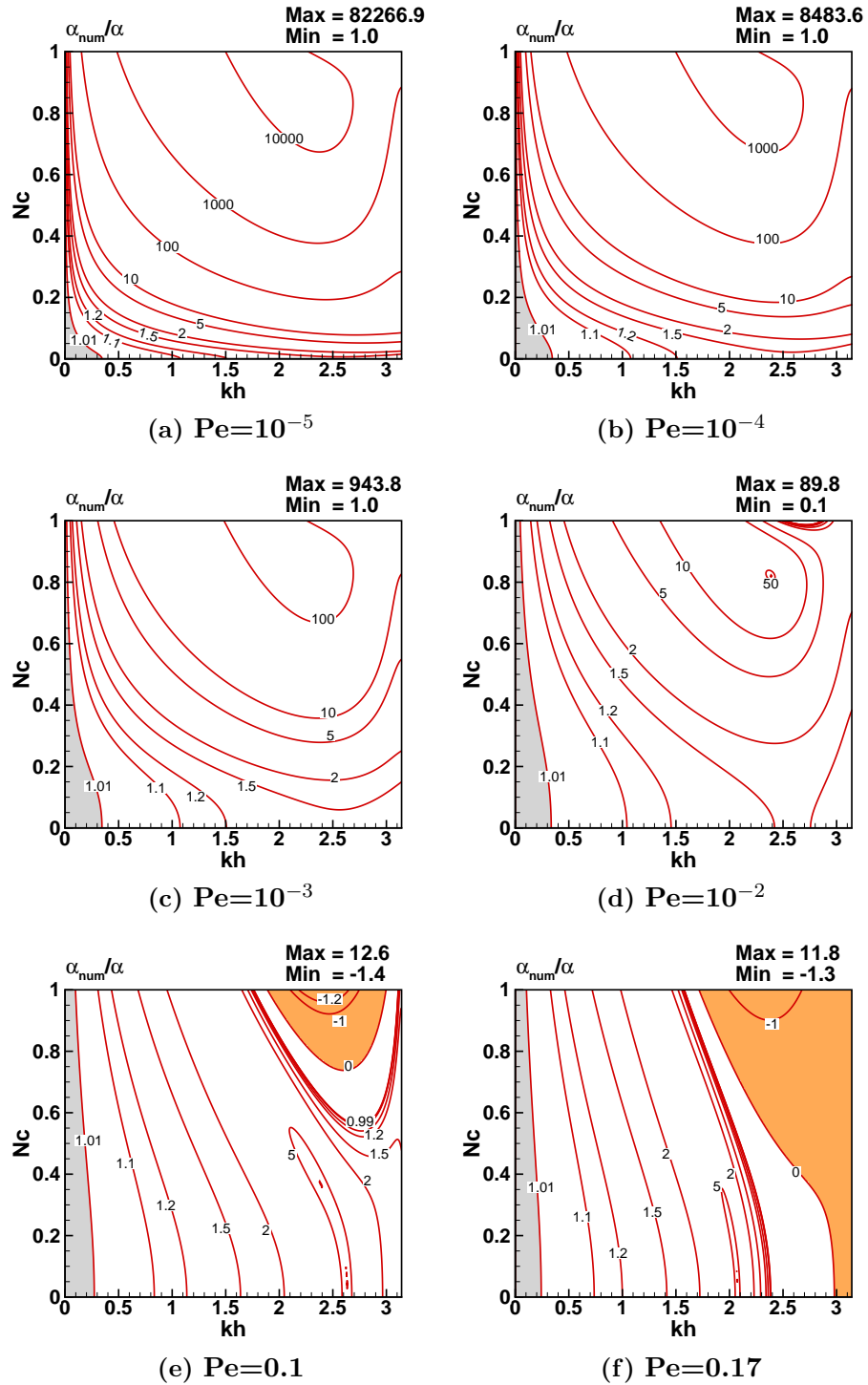
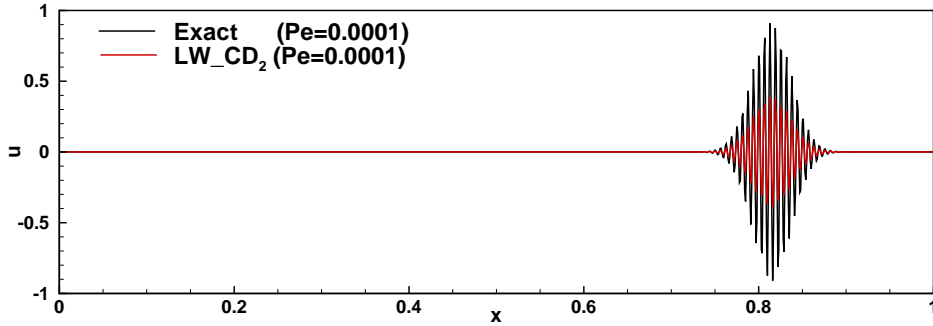


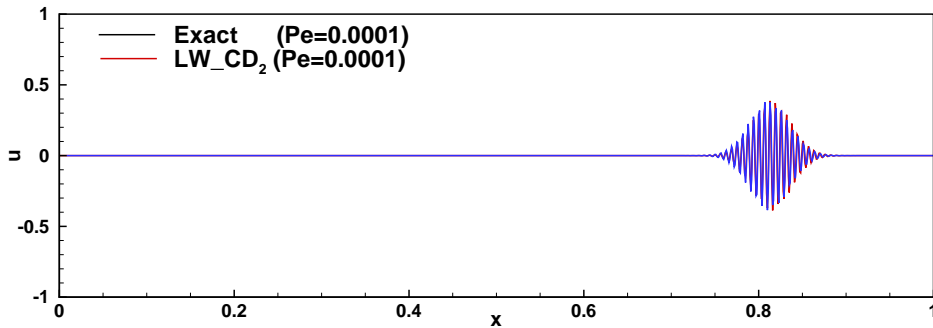
Figure 3.11: Contours of non-dimensionalised numerical diffusion coefficient α_{num}/α for TTGC-CD₂ scheme at various values of Pe

times the original diffusion coefficient α . The exact solution with this modified value of α is shown in frames (b) with a zoomed in view of the solution shown in Figure 3.12(c). The clear match between the exact solution with the modified diffusion coefficient and the numerical solution obtained using LW-CD₂ is clearly

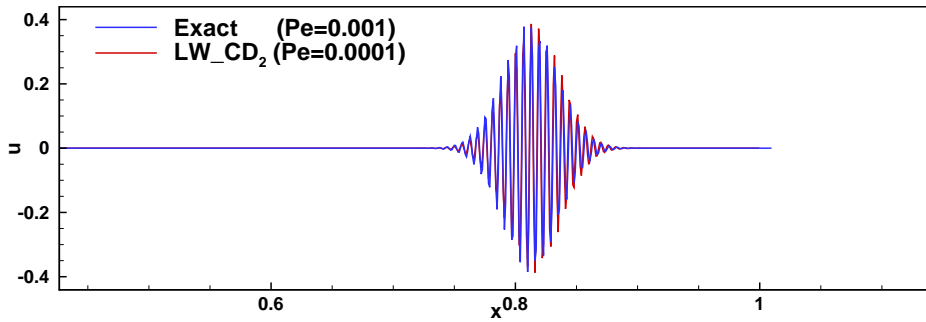
3. NUMERICAL METHODS AND THEIR ANALYSIS



(a) $t=0.315$



(b) $t=0.315$, exact solution with modified α



(c) Zoomed in view of exact solution with modified α

Figure 3.12: Numerical solution of 1D LCDE calculated using LW-CD₂ for a wavepacket with $kh = 1.0$ at time $t=0.315$. $Pe = 0.0001$ and $N_c = 0.35$

observable. This demonstrates the relevance of respecting the DRP property of schemes for high performance computing. This particular aspect can have significant role in diffusion dominated flow problems such as in diffusion flames where the mesh (kh) and time step (N_c) induced augmentation of diffusion coefficient can cause significant errors in predicting the flame properties such as heat release rate, temperature and length of diffusion flame as discussed in [80].

3.4.3 1D Linear Convection-Diffusion-Reaction Equation (LCDRE)

Theoretical analysis of 1D LCDRE

The 1D LCDRE in independent variables x and t is given by,

$$\frac{\partial u}{\partial t} + c \frac{\partial u}{\partial x} = \alpha \frac{\partial^2 u}{\partial x^2} + Su, \quad (3.76)$$

and is considered in this section. As in the case of LCDE, c and α are real constants and refer to the phase speed and diffusion coefficient respectively. The linear source term in the equation is given by Su where S is also a real constant.

By following the same analysis performed for LCDE, one obtains the dispersion relation for the above LCDRE as,

$$\omega = c k - i \alpha k^2 + i S \quad (3.77)$$

The phase speed and the group velocity is then obtained as,

$$c_\varphi = \frac{\omega}{k} = c - i \alpha k + i \frac{S}{k} \quad (3.78)$$

$$v_{g,\varphi} = \frac{\partial \omega}{\partial k} = c - 2 i \alpha k \quad (3.79)$$

As mentioned in the case of LCDE, the imaginary part of the phase and group velocity expressions given above contribute only in altering the signal amplitude. Hence, the actual speeds correspond to the real part of the above expressions.

The physical amplification factor for LCDRE is given by,

$$G_{phy} = e^{-i \omega \Delta t} \quad (3.80)$$

$$= e^{(-\alpha k^2 + S)\Delta t} e^{-i k c \Delta t} \quad (3.81)$$

and,

$$|G_{phy}| = e^{(-\alpha k^2 + S)\Delta t} \quad (3.82)$$

$$= e^{(-Pe (kh)^2 + Da N_c)} \quad (3.83)$$

where Pe, N_c have the same definitions as in the previous sections and $Da = Sh/c$ is the Damkohler number. From the above expression, it can be observed that contrary to the LCE and LCDE, the amplitude of the exact solution can either increase or decrease with time depending on whether $Da N_c > Pe(kh)^2$ or not.

3. NUMERICAL METHODS AND THEIR ANALYSIS

Numerical Analysis of 1D LCDRE

The numerical dispersion relation when cast in the form of,

$$\omega_{num} = c_{num} k - i \alpha_{num} k^2 + i S_{num} \quad (3.84)$$

gives the following expressions for G_{num} , c_{num}/c_{phy} and $V_{g,num}/V_{g,phy}$.

$$G_{num} = e^{-i \omega_{num} \Delta t} = e^{-i(c_{num} k - i \alpha_{num} k^2 + i S_{num}) \Delta t} \quad (3.85)$$

$$|G_{num}| = e^{(-\alpha_{num} k^2 + S_{num}) \Delta t} \quad (3.86)$$

$$\frac{c_{num}}{c} = \frac{\beta}{(kh) N_c} \quad (3.87)$$

$$\frac{V_{g,num}}{V_{g,phy}} = \frac{1}{N_c} \frac{\partial \beta}{\partial (kh)} \quad (3.88)$$

$$(3.89)$$

where β is the numerical phase angle which is given by Eq. 3.108

Taking the logarithm of Eq. 3.86, one obtains,

$$\ln(|G_{num}|) = -\frac{\alpha_{num}}{\alpha} Pe (kh)^2 + \frac{S_{num}}{S} Da N_c \quad (3.90)$$

The non-dimensional source term can then be expressed as,

$$\frac{S_{num}}{S} = \frac{\ln(|G_{num}|_{kh=0})}{Da N_c} \quad (3.91)$$

Substituting the above expression in Eq. 3.90, the expression for α_{num}/α can be obtained as,

$$\frac{\alpha_{num}}{\alpha} = \frac{[\ln(|G_{num}|_{kh=0}) - \ln(|G_{num}|)]}{Pe (kh)^2} \quad (3.92)$$

Application to LW

The GSA performed above for the LCDRE in the previous section is now applied to the LW-CD₂ scheme. In the presence of the source term, the LW-CD₂ scheme is modified as,

$$u_j^{n+1} = u_j^n - \frac{N_c}{2}(u_{j+1}^n - u_{j-1}^n) + \varsigma(u_{j+1}^n - 2u_j^n + u_{j-1}^n) + Da N_c u_j^n \quad (3.93)$$

where $\varsigma = N_c^2/2 + Pe$

By performing similar analysis as done before, one obtains the expression for numerical amplification factor as,

$$G_{LW-CD_2} = 1 - i N_c \sin(kh) + 2\varsigma(\cos(kh) - 1) + Da N_c \quad (3.94)$$

3.4 Analysis of numerical schemes in AVBP

The numerical phase angle, β_{LW-CD_2} is then calculated as,

$$\beta_{LW-CD_2} = \tan^{-1} \left(\frac{N_c \sin(kh)}{1 + 2\zeta(\cos(kh) - 1) + Da N_c} \right) \quad (3.95)$$

and the numerical phase speed and group velocity are derived as,

$$\frac{c_{num}}{c} = \frac{\beta_{LW-CD_2}}{(kh) N_c} \quad (3.96)$$

$$\frac{V_{g,num}}{V_{g,phy}} = \frac{V_{g,num}}{c} = \frac{1}{N_c} \frac{\partial \beta_{LW-CD_2}}{\partial (kh)} \quad (3.97)$$

The non-dimensional numerical diffusion coefficient for the LW-CD₂ is given by,

$$\frac{\alpha_{num}}{\alpha} = \frac{1 + Da N_c - \ln(|G_{LW-CD_2}|)}{Pe (kh)^2} \quad (3.98)$$

and the non-dimensional source term is,

$$\frac{S_{num}}{S} = \frac{1 + Da N_c}{Da N_c} \quad (3.99)$$

Application to TTGC

The TTGC scheme when applied to the LCDRE has the following stencil. It should be noted that the source term is added only in the second stage of time integration.

$$\frac{(\tilde{u}_{i+1}^n + 4\tilde{u}_i^n + \tilde{u}_{i-1}^n)}{6} = \frac{(u_{i+1}^n + 4u_i^n + u_{i-1}^n)}{6} - \alpha_{TTGC} N_c \frac{(u_{i+1}^n - u_{i-1}^n)}{2} \quad (3.100)$$

$$+ (\beta_{TTGC} N_c^2 + Pe) (u_{i+1}^n - 2u_i^n + u_{i-1}^n) \quad (3.101)$$

$$\frac{(u_{i+1}^n + 4u_i^n + u_{i-1}^n)}{6} = \frac{(u_{i+1}^n + 4u_i^n + u_{i-1}^n)}{6} - N_c \frac{(\tilde{u}_{i+1}^n - \tilde{u}_{i-1}^n)}{2} \quad (3.102)$$

$$+ (\gamma_{TTGC} N_c^2 + Pe) (u_{i+1}^n - 2u_i^n + u_{i-1}^n) + Da N_c u_j^n \quad (3.103)$$

The numerical properties of the TTGC scheme are then obtained as,

$$G_{TTGC-CD_2} = 1 + \frac{\hat{A} \hat{S} \zeta_2}{N_c} - \alpha_{TTGC} (\hat{A} \hat{L})^2 - i \hat{A} \hat{L} \left(1 + \frac{\hat{A} \hat{S} \zeta_1}{N_c} \right) + Da N_c \quad (3.104)$$

$$\frac{c_{num}}{c} = \frac{\beta}{(kh) N_c} \quad (3.105)$$

$$\frac{V_{g,num}}{c} = \frac{1}{N_c} \frac{\partial \beta}{\partial kh} \quad (3.106)$$

$$\frac{\alpha_{num}}{\alpha} = \frac{-\ln(|G_{TTGC-CD_2}|)}{Pe (kh)^2} \quad (3.107)$$

where the numerical phase angle β is now given as,

$$\tan(\beta) = - \left(\frac{\text{Imag}(G_{TTGC-CD_2})}{\text{Real}(G_{TTGC-CD_2})} \right) \quad (3.108)$$

3. NUMERICAL METHODS AND THEIR ANALYSIS

Discussion on numerical properties for LCDRE

Dissipation and stability properties:

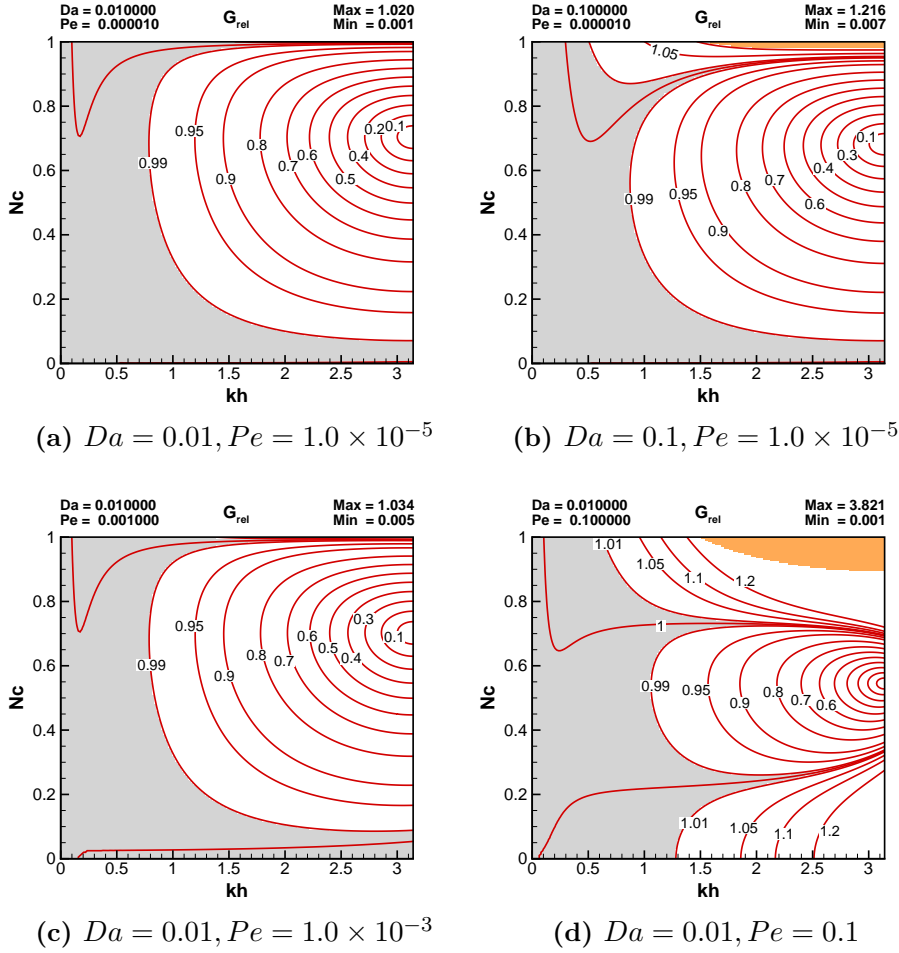


Figure 3.13: Contours of G_{rel} for various values of Da and Pe computed for the LW scheme

Unlike LCDE where the effect of physical diffusion is to dampen the amplitude of the solution, in LCDRE the initial solution may get attenuated or amplified with time depending on the sign of the source term used. Hence, to study the dissipation properties of the numerical schemes one needs to look at the G_{rel} values (same as defined for LCDE). Similar to the discussion on LCDE, $G_{rel} > 1$ implies an underdamped solution whereas $G_{rel} < 1$ refers to an overdamped solution. To highlight the effect of Da and Pe on the numerical properties, we focus the discussion on negative source term values. In this case, one would expect the solution amplitude to be damped over time. Figure 3.13 shows the contours of G_{rel} for the LW scheme, in the $kh - Nc$ plane for various Pe and Da numbers. Figure 3.13 (a) shows the G_{rel} values for a very low value ($Pe = 10^{-5}$

3.4 Analysis of numerical schemes in AVBP

of Pe number and Da number ($Da = 0.01$). The contours look very similar to that of the LCDE equation discussed in the previous section for this value of Da . When the Da value is increased to 0.1 while keeping the Pe number the same, one observes the presence of unstable regions at high kh and N_c values. This can be observed in sub-figure (b) of the same figure. For increasing Da , the DRP region is progressively reduced for the same value of Pe . Hence, increasing the Da number brings in numerical instability at high kh and N_c values. The effect of Pe can also be studied from sub-figures (c) and (d). It can be noted that for low Da and with higher Pe numbers, the G_{rel} contours follow a similar pattern as in the case of LCDE. A similar trend is also observed for the TTGC scheme, however, no perceivable regions of instability are observed at higher Da as can be seen from Figure 3.14.

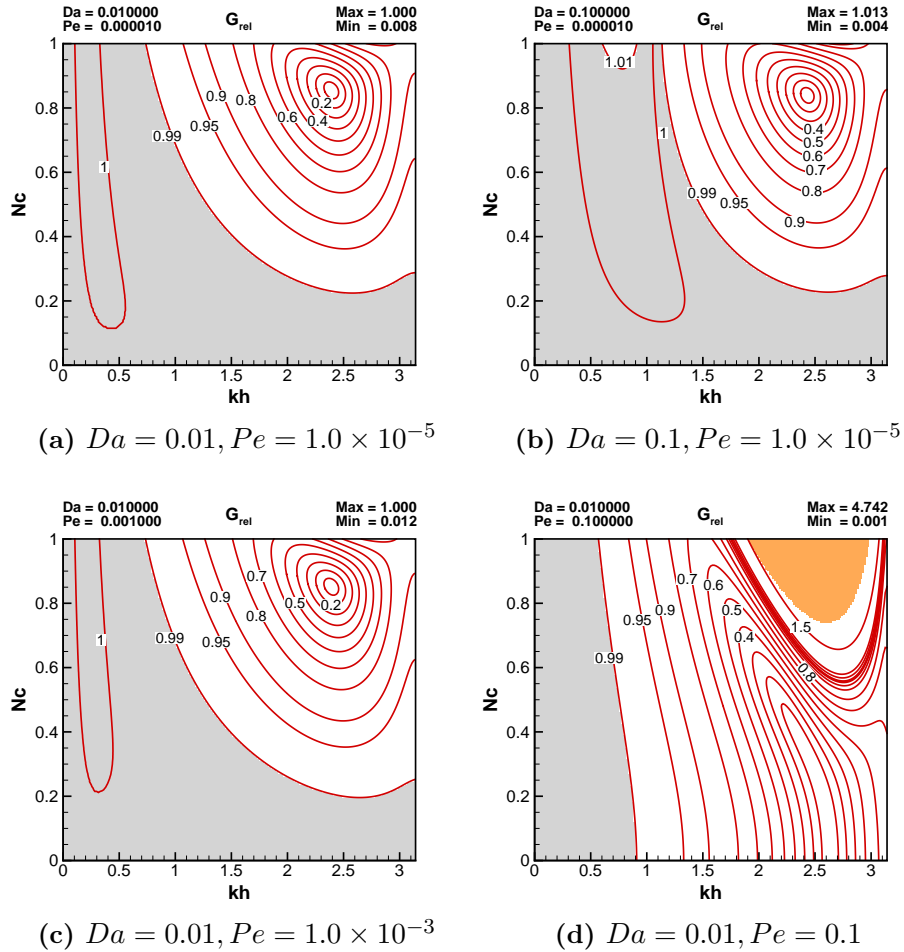


Figure 3.14: Contours of G_{rel} for various values of Da calculated for LW (left column) and TTGC (right column) schemes. The Pe value used is 10^{-5} .

By performing a sweep through all the kh values, one can create a stability

3. NUMERICAL METHODS AND THEIR ANALYSIS

map for both the schemes as a function of N_c , Pe and Da . For negative source terms S , the stability map is identified by considering an iso-surface of $G_{num} = 1$ and is shown in Figures 3.15. Two revealing observations can be made: firstly, the maximum value of N_c that can be used for stable computations decreases with increasing Da . For the LW scheme, this limiting value of N_c is observed to be 0.7 while the similar value for TTGC is 0.8. Secondly, at low values of N_c , the limiting value of Pe remains unchanged while varying Da . The limiting value of Pe remain unaltered (as in the case of LCDE) at 0.5 and 0.17 for LW and TTGC schemes respectively.

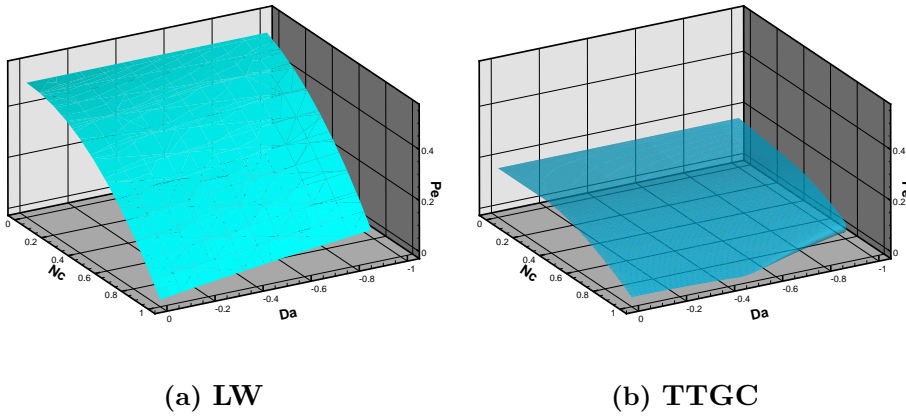


Figure 3.15: Iso-surface of $|G_{num}| = 1$ in the $Da - N_c - Pe$ space for the LCDRE equation for (a) LW (b) TTGC

Dispersive properties: To study the dispersive properties of the schemes for LCDRE, the contours of $V_{g,num}/c$ are plotted in Figure 3.16 for both LW and TTGC at $Pe = 1.0 \times 10^{-5}$. This value of Pe is chosen since the topic of interest is high Reynolds number flows. Similar to the observations on G_{rel} discussed before, $V_{g,num}/c$ show variations in their behavior with increasing Da for both LW and TTGC schemes. When Da is increased from 0.01 to 0.1, the DRP regions are reduced and confined to very low kh and N_c values. The q-wave regions are clearly visible in the plots however show negligible changes with increasing Da for both the schemes. This underlines the need to use very low N_c values while running reactive flow simulations not just due to stability reasons, but also to capture propagation phenomena such as flame speeds, accurately.

Diffusive properties The numerical diffusive properties of LCDRE for both the schemes are plotted in Figure 3.17. Even though the contours of α_{num}/α are similar to that observed for LCDE, the DRP regions are observed to be limited to very low values of N_c and kh only. This is further reduced as the Da is increased

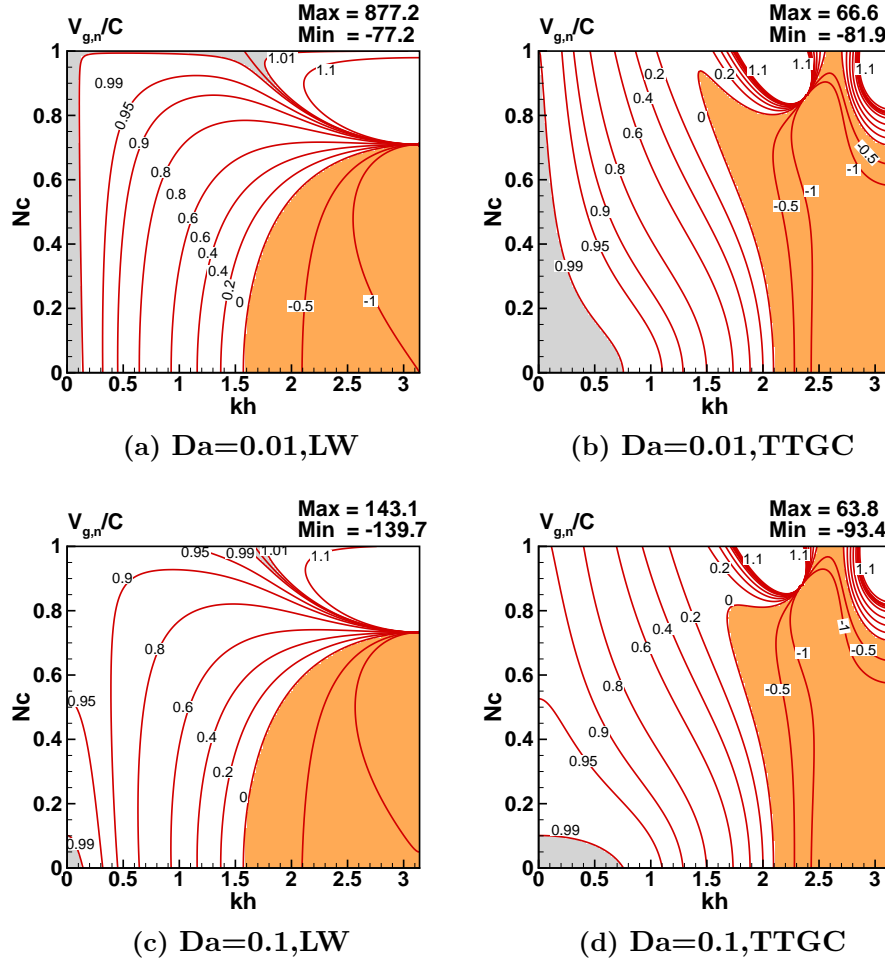


Figure 3.16: Contours of $V_{g,num}/c$ for various values of Da calculated for LW (left column) and TTGC (right column) schemes. The Pe value used is 10^{-5} .

for both the schemes, as can be observed from the figure. The significance of this property for diffusion flows is already highlighted in the previous section. The present analysis reemphasizes the finding that the presence of reaction source terms further restricts the DRP zones of this property. Hence, while simulation diffusion dominated reactive flows, one needs to use extremely fine values of time step and grid sizes. The extent to which this is religiously followed in practical numerical computations is something every CFD user needs to be aware of.

3.5 Conclusions

The following conclusions are made from the analysis performed in this chapter.

- (C.1) The framework of GSA is introduced using three prototypical, one-dimensional linear PDEs. The theoretical properties of these equations are derived and

3. NUMERICAL METHODS AND THEIR ANALYSIS

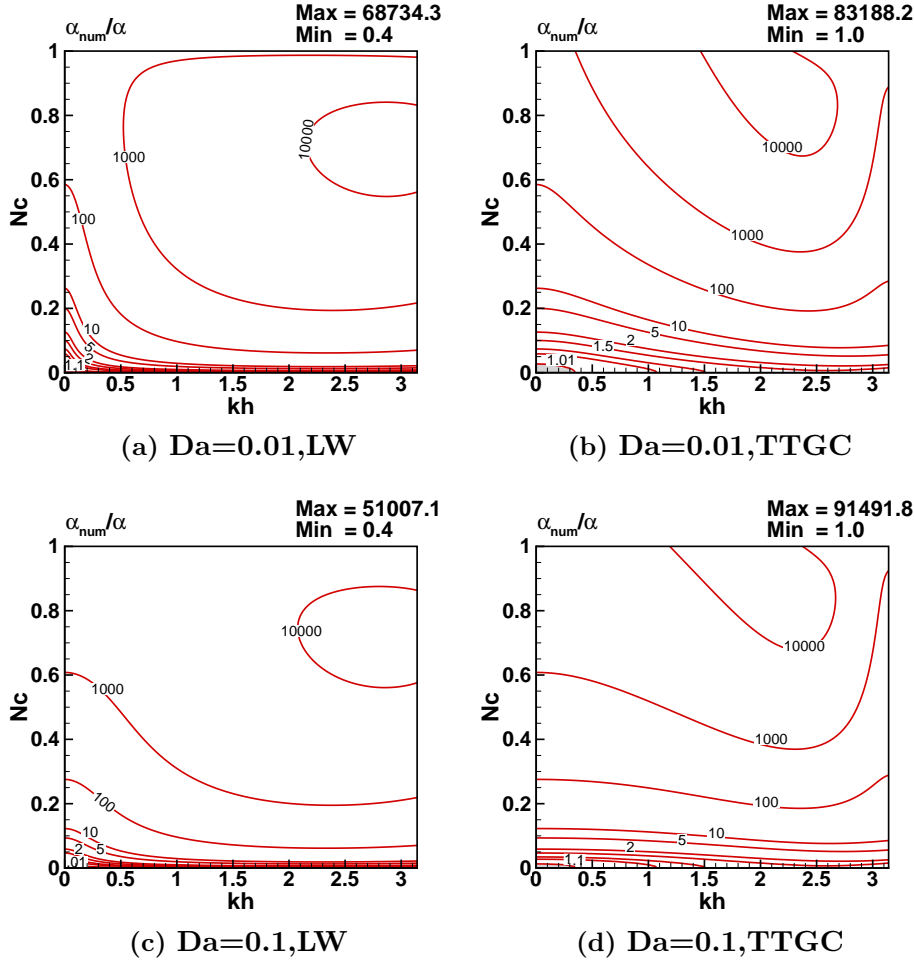


Figure 3.17: Contours of α_{num}/α for various values of Da calculated for LW (left column) and TTGC (right column) schemes. The Pe value used is 10^{-5} .

the significance of the dispersion relation is highlighted. The corresponding numerical properties and the numerical dispersion relations are derived and these relations are applied specifically to study the LW and TTGC schemes. The concept of DRP in terms of dissipation, dispersive and diffusive properties are discussed.

- (C.2) The GSA for the 1D LCE reveals the superior DRP property of TTGC when compared to LW. TTGC is observed to resolve the solution more accurately (52% of $kh - N_c$ space) than LW (37%). Also, TTGC resolves the group velocity accurately over a wide range of $kh - N_c$ space when compared to LW. The negative group velocity region for the LW scheme starts at $kh = 1.57$ while the similar kh value for TTGC is 2.1. Hence, the region of q-wave is further high in the range of kh values for TTGC when compared to LW. LW on the other hand enjoys very good DRP properties

at $N_c = 1$ for all values of kh hence explaining its popularity in the CFD community.

- (C.3) Analysis for LCDE demonstrates the counterintuitive effect of physical dissipation on numerical stability. For non-zero Pe , the stability of both the schemes is found to be impaired initially at high N_c and kh values. As Pe is increased, the region of instability in the $kh - N_c$ space is found to increase at high kh values. Both the schemes demonstrate a critical value of Pe number at which this region of instability extends over the entire range of N_c values and at high kh values. The critical Pe number for LW is found to occur to $Pe = 0.5$ while for TTGC it is $Pe = 0.17$. The dispersive property of both the schemes is also found to deteriorate at higher Pe values. Surprisingly LW scheme no more exhibits q-wave behavior for $Pe > 0.25$ while it is present all throughout stable computations for TTGC scheme. Of all the numerical properties, the numerical diffusive property is found to be the most restrictive and limits kh to very low value for DRP. With increasing Pe values, the DRP properties are also found to improve. The presence of anti-diffusion is also observed at higher Pe values and at high wavenumbers.
- (C.4) The effect of Da is to further increase the instability and to reduce the DRP region of both the schemes for a given value of Pe . For low values of Da , its effect is not so much pronounced while for $Da > 0.1$ clear regions of instability are observed in the $kh - N_c$ space. The dispersive and the diffusive properties also show similar trends for both the schemes, with the DRP regions deteriorating at higher values of Da and Pe .

Chapter 4

Development and analysis of LESAULTS method

Contents

5.1	Introduction	148
5.2	Literature survey	149
5.3	Objectives of this chapter	156
5.4	A comparison of methane-air combustion mechanisms	157
5.5	Chemical mechanism reduction using ARCANE	162
5.5.1	DRG with error propagation (DRGEP)	162
5.5.2	Chemical lumping	163
5.5.3	QSS Assumption	163
5.5.4	Thermal and Transport properties	164
5.6	Validation of reduced mechanism	165
5.6.1	Validation using 1DUP flames	165
5.6.2	Validation using IDT	167
5.6.3	Validation using 1DCD flames	168
5.6.4	Application to a 3-dimensional laminar flame	170
5.7	Conclusions	176

4.1 Introduction

In the previous chapter, the numerical methodology and GSA of two of the most popular numerical schemes used in AVBP are presented. These schemes have been thoroughly validated for two and three-dimensional, reactive and non-reactive flow problems and has been widely used for more than two decades ([81]). However, the explicit nature of time integration procedure in AVBP renders these schemes inefficient for multiscale, multiphysics flow problems and hence

requires alternate, new methods to accelerate LES computations. In this chapter, a novel method developed to accelerate LES computations-LESAULTS (acronym for **LES Acceleration Using Local Time Stepping**) is described.

This chapter is organised as follows. The limitation of explicit time integration methods due to stability requirement, the concomitant numerical stiffness and the numerical methods developed in the past to tackle this problem of numerical stiffness are presented in Section 4.2. Towards the end of this section, explanation is also provided as to why the author chose to develop the LESAULTS method described in this chapter. This section also sets the stage for defining the objectives of this chapter which are listed in Section 4.3. Following this, the LESAULTS methodology is described in detail in Section 4.4. As already stated, the sole objective of developing LESAULTS method is to speed up LES computations without compromising the accuracy of existing schemes. Hence, the theoretical speed up limit attainable using this method is derived in Section 4.5. This is followed by the error analysis of LESAULTS method using GSA in Section 4.7 and its numerical validation in Section 4.8. The conclusions drawn and perspectives are summarized in the last Section 4.9.

4.2 Literature Survey

The only drawback that refrains the CFD-Steam Cracking community from using LES in their design processes is the high computational costs associated with LES in comparison to RANS. While this is partly because of the fine grid resolution demanded by LES computations, the major limitation arises from the restriction on the maximum allowable time step that can be used for time integration of the unsteady LES governing equations. The maximum allowable time step is determined by stability requirements of the numerical scheme in use, popularly known as the CFL criterion. As explained in the previous chapter, such a time step restriction is mandatory if the scheme has to be stable and even more restrictive if it has to be DRP as demonstrated through numerical property charts in the previous chapter.

Many studies have been carried out in the past to address the challenges due to time step restriction in CFD solvers. A common approach is to use implicit and implicit-explicit (IMEX) time integration schemes. In implicit schemes, the residual at time level n in the governing PDE is numerically expressed as a function of flow variables at the $(n + 1)^{\text{th}}$ time level. From Von-Neumann stability analysis, many authors have concluded that this method gives unconditional stability and that large values of N_c can be used in such computations. It goes without saying

4. DEVELOPMENT AND ANALYSIS OF LESAULTS METHOD

that such a 'theoretical unconditional stability' comes at increased computational cost. The numerical solution at the $(n + 1)^{\text{th}}$ time step is expressed implicitly as a function of the solution at n^{th} time level (and hence the name implicit method). This demands the solution of a system of linear algebraic equations for the updated solution using direct or iterative solvers thereby increasing the computational cost. The solution of the system of linear equations also negatively impacts the parallelizability of the solver. Additionally, the unconditional numerical stability is seldom achieved in practical computations. In [82], the authors have carried out LES simulations of turbulent channel flow and have concluded that the ratio of the time step and cell characteristic length should not be more than 2-3 thus limiting the maximum allowable time step that can be chosen even in implicit schemes. Another criticism against implicit methods is its poor numerical resolution properties when compared to explicit schemes. In [83], authors have carried out DNS of transitional flow over a flat plate with monochromatic wall excitation using implicit and explicit schemes. Their study concluded that even though the implicit scheme used in their analysis enjoyed neutral stability, it was unable to predict the spatio-temporal wave front which is typically observed in flows en route to turbulence. IMEX methods perform even worse since in addition to the above mentioned reasons, the interface between the implicit and explicit time integration zones could act as regions of sources of erroneous, numerically induced wave packets.

In the case of explicit time integration schemes, the solution at the $(n + 1)^{\text{th}}$ time level depends only on the current and previous (in the case of multi-step, explicit schemes) time levels. Hence, this class of schemes do not require complicated matrix inversion procedure and are computationally cheap. They also enjoy the benefit of efficient parallelisability and excellent accuracy and resolution properties. The major drawback explicit schemes suffer is due to the much restrictive stability criteria that determines the maximum available time step that can be used for time integration. Many modifications of explicit schemes, with the objective of surmounting this stability criteria have been developed in the past and can be broadly classified as Asynchronous local time stepping schemes, Multirate schemes and Domain Decomposition based local time stepping schemes.

A crude version of the current asynchronous local time stepping schemes were used in the past to accelerate convergence of Euler equations towards steady state solution. In such attempts, the interest is to arrive at the final steady solution irrespective of the accuracy of the transient solution. For the same reason, such schemes cannot be used in LES computations as the objective is to compute the unsteady governing equations in a time accurate manner. Recently,

an asynchronous local time stepping scheme [84] was developed for such unsteady equations using the 'discrete-event simulation' methodology. In this method, a timestamp is associated with each computational cell in the domain based on a predicted "event" based on the governing PDE. This step is followed by an event processing step where the cell with the smallest time stamp is time integrated using the maximum allowable time step in that cell. This is in turn followed by an event synchronization step where the cell neighboring the smallest timestamp cell is updated and flux interfaces are corrected. Finally an event scheduling step is initiated where the time stamp and the residual of the cell is recalculated. These procedures are repeated for all cells in the domain to calculate the unsteady solution. The authors have proved the stability of this method and demonstrated its application to 1D convection-diffusion-reaction equation. In [85, 86, 87, 88] the authors have extended this approach by applying local N_c as refreshing time stamps and demonstrated the method for gas discharge problems. In another study [89], the authors have devised another local time stepping strategy using first order upwind schemes. The issue of conservation is addressed in this work by carrying out flux interpolation at cell interfaces with different local time steps. In their work, the authors have demonstrated the applicability of this methodology to aeroacoustic problems.

Adaptive mesh refinement (AMR) methods fall into the category of both asynchronous time stepping methods as well as multirate schemes. AMR schemes were introduced into the CFD community through the pioneering work of Berger [90]. In their work, which used block structured meshes, the global mesh comprises of a 'parent' coarse mesh and a number of 'children' fine meshes overlapping with the parent mesh. Local time step is used to time integrate the finer children meshes. Hence, in effect, this method works on both spatial and temporal adaptivity. The parent mesh solution values located inside the child mesh are then obtained by volume weighted averaging of the finer children mesh solution located inside the parent mesh. The flux values at the parent-children interface are also calculated by interpolating solution values from the child mesh and time integration is performed using explicit methods. This method of Berger was then modified to include global conservation in [91]. In [92, 93, 94, 95], the authors extended the AMR approach to solve incompressible Navier-Stokes equations using projection methods. In another attempt [96], the same approach was extended to study two-phase flows with level set and surface tension methods.

In multirate time integration schemes, multiple time steps are present in the computational domain and each time step is devoted to a group of contiguously located cells. The time steps are chosen such that they are integral multiples of

4. DEVELOPMENT AND ANALYSIS OF LESAULTS METHOD

the smallest time step in the domain. One of the early attempts at multirate schemes is the work of Osher and Sanders [97]. The authors established a locally varying time step for forward Euler time integration schemes for various flux functions. However, their schemes were first order accurate in space and time. The authors in [98] extended this work to second order schemes in space and time. However, their scheme is not mass conservative. Similar second order schemes were also developed in [99, 100]. These schemes, like the one designed by Dawson, are found to be non-conservative in nature. Extension of these methods to third order [101] and fourth order accuracy [102, 103] also has been carried out recently.

Domain decomposition methods using local time stepping work on similar lines as multirate schemes, the only difference being that the full computational domain is divided into multiple overlapping sub-domains with each sub-domain being time integrated using a time step specific to that particular sub-domain. Similar to multirate schemes, each time step in the sub-domain is chosen as an integral multiple of the smallest of the time steps in all sub-domains. This approach has been used in [104] to model realistic cardiac tissue models. The application of this method to CFD is discussed in [105]. In this work, the authors have developed a domain decomposition based local time stepping method for various explicit numerical schemes. This method is then applied to the LES of a 2-dimensional jet flow as a validation exercise. The same method has been applied to the LES of plume from a rocket nozzle in [106].

In summary, multiple approaches have been devised to tackle the challenge of reducing computational cost arising from numerical stiffness in LES. Although implicit methods guarantee 'theoretical stability' for high CFL numbers, the maximum N_c value that can be often used is restricted in LES. The computational cost of matrix inversions and poor numerical resolution are also demonstrated drawbacks of implicit methods. On the other hand, explicit methods have good resolution properties and parallelizability but suffer from stringent stability conditions. Asynchronous time stepping methods, used to improve this stability restriction, have been attempted in the past but their applicability to LES is still not demonstrated. Multirate schemes and AMR schemes are often limited to structured block grids. Domain decomposition methods on the other hand, are applicable to unstructured grids and have the advantages enjoyed by multirate schemes. Hence, in this study, an extension of the domain decomposition method of [105] is proposed. The LES solver AVBP, has in-built capability to deal with overset grids [107] which makes the adoption of this method all the more attractive.

4.3 Objectives of this chapter

As mentioned in the introduction, the objective of this chapter is to explain the development of LESAULTS methodology. Keeping in mind, the state of the art in LES acceleration methods discussed in the previous section, the objectives of this chapter are listed as follows:

- (A.1) *To describe the novel LES acceleration method-LESAULTS and the principles of its operation*
- (A.2) *To derive the theoretical speed up limit attainable using LESAULTS*
- (A.3) *To describe the design of LESAULTS methodology*
- (A.4) *To analyze the error incurred due to local time stepping in LESAULTS method and the effect of various numerical parameters on the accuracy of LESAULTS method when compared to the conventional solver*
- (A.5) *To apply LESAULTS method to LES equations and to establish the proof of speed up using numerical tests*

4.4 LESAULTS Method

As an example, consider the flow emanating from a jet into quiescent surroundings as shown in Figure 4.1 (a). LES of such a flow phenomena would require fine mesh cells in regions inside the jet and near the shear layers located just downstream of the jet orifice to resolve the spatial and temporal flow dynamics in these regions. Due to the presence of these fine mesh cells, an explicit LES solver would demand a small time step in such regions. On the other hand, locations farther downstream of the jet represent regions where the mixing of the jet with quiescent fluid is complete. In such regions, a fine mesh is not required as the turbulent statistics would be more or less spatially uniform and devoid of steep gradients. Hence coarser mesh cells could be used here. In conventional explicit LES solvers, the time step dictated by the smallest cell in the domain is used for time integration in the entire domain. This makes the LES computations in this manner an 'over kill' and hence inefficient.

The LESAULTS approach to solve the same flow phenomena is demonstrated in Figure 4.1(b). Here the computational domain is divided into two overlapping sub-domains (colored in red and blue respectively) with the overlapped region colored in orange. The mesh in these two sub-domains are distributed among

4. DEVELOPMENT AND ANALYSIS OF LESAULTS METHOD

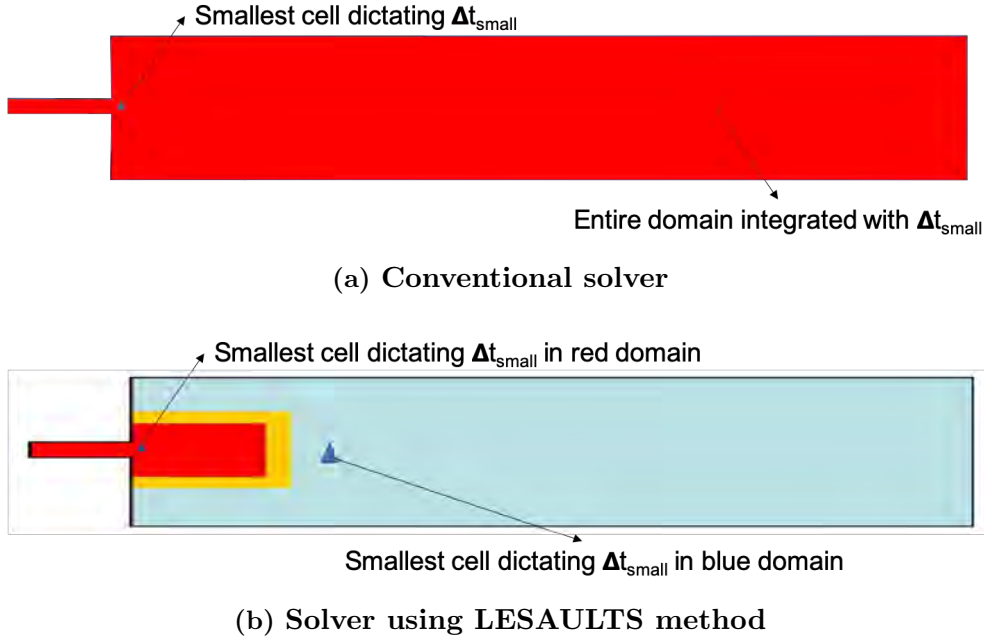


Figure 4.1: Schematic showing time step in LES using (a) Conventional LES solver (b) LESAULTS method based LES solver

different computing cores in a 'Multiple Data Multiple Algorithm' framework. Starting from the same flow time t^n and a smooth initial condition, each of these sub-domains is time integrated independent of the other using the smallest time step pertaining to that particular sub-domain. It is to be noted that the time steps used for time integration are specifically chosen such that the larger time step (Δt_{large} , used in blue domain) is an integral multiple of the smaller time step (Δt_{small} , used in red domain). It should also be noted that during the intermediate time integration steps, an approximate boundary condition is used at the interface boundaries located in each of the overlapped sub-domains. Different number of time integrations are performed in each of the sub-domains independently until they arrive at the nearest common flow time t^{n+1} (equal to the least common multiple of both the time steps). At this stage, both the sub-domains have slightly different solutions of the governing PDE obtained from time integration using different time steps. In the overlapped zone, two sets of solutions (corresponding to the two sub-domains) exist at any given spatial location. Once both the sub-domains reach a common flow time, the solution in the overlapped zone is calculated as a function of the two sets of available solutions at time level t^{n+1} . This requires the exchange of flow information between the computing cores operating on the overlapped zone. Once the solution in the overlapped zone is computed, the above steps are repeated continuously in the LES solution procedure. The speed up in LESAULTS computations is obtained by properly

distributing the computational load among the computing processors.

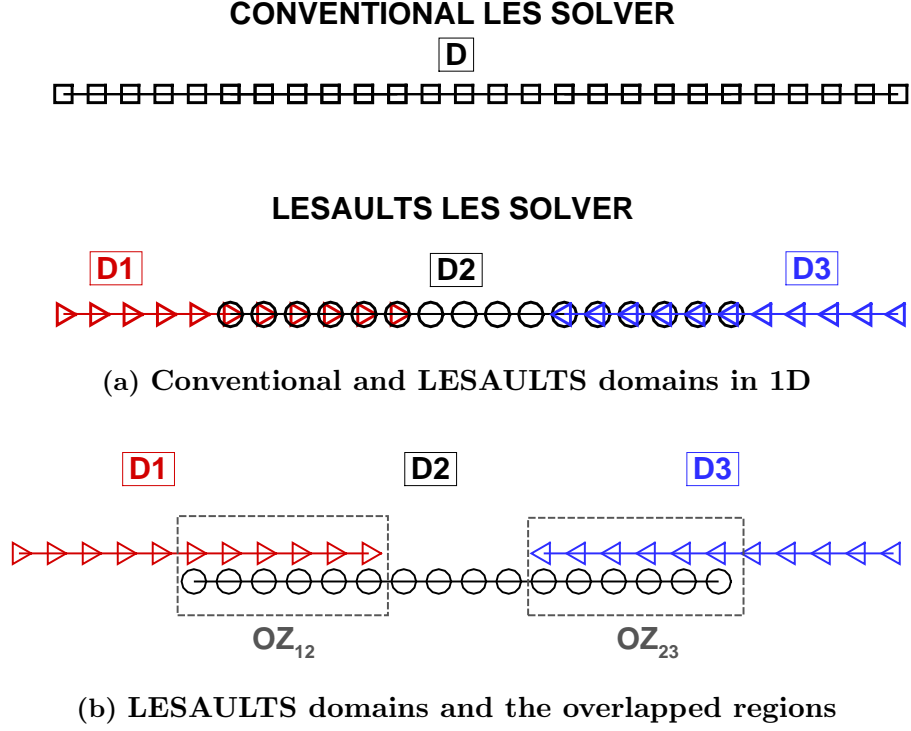


Figure 4.2: Schematic of conventional and LESAULTS method applied to a 1D domain. (a) single domain used in conventional solver and sub-domains used in LESAULTS method. (b) An exaggerated view of overlapped zones

In order to explicate this concept further, LESAULTS method applied to a one-dimensional domain is shown in Figure 4.2. Consider the one dimensional domain D (colored in black) shown in Figure 4.2(a) used in computing the solution using the conventional explicit solver. For the sake of simplicity, it is assumed that the domain D is discretised using N number of uniform grid points shown as square symbols in the sub-figures. In LESAULTS methods, the domain D is decomposed into three overlapping sub-domains- D_1, D_2 and D_3 such that $D = D_1 \cup D_2 \cup D_3$ as shown in the same sub-figure. The overlapped zones between the sub-domains are named as OZ_{12} and OZ_{13} such that $OZ_{12} = D_1 \cap D_2$ and $OZ_{23} = D_2 \cap D_3$. Let the number of nodes in the sub-domains D_1, D_2 and D_3 be N_1, N_2 and N_3 respectively. These numbers include the number of nodes present in the overlapped zones as well. Let the number of nodes in OZ_{12} and OZ_{23} be N_{12} and N_{13} respectively. To make a fair comparison between the conventional method and LESAULTS method, let the same uniform mesh size used to discretise domain D be used in the case of all sub-domains as well. It is also ensured that the nodes of the two sub-domain meshes in the overlapped zones have

4. DEVELOPMENT AND ANALYSIS OF LESAULTS METHOD

Subdomain, i	Number of nodes, N_i	Time step, Δt_i	Number of inter- mediate integra- tions, $R_{\delta t, i}$
D1	N_1	Δt_1	$\max(\Delta t_i)/\Delta t_1$
D2	N_2	Δt_2	$\max(\Delta t_i)/\Delta t_2$
D3	N_3	Δt_3	$\max(\Delta t_i)/\Delta t_3$
OZ12	N_{12}	$\Delta t_{12}=\max(\Delta t_1, \Delta t_2)$	$\max(\Delta t_i)/\Delta t_{12}$
OZ23	N_{23}	$\Delta t_{23}=\max(\Delta t_2, \Delta t_3)$	$\max(\Delta t_i)/\Delta t_{23}$

Table 4.1: Table showing the sub-domains, time steps and the number of intermediate time integration steps for the LESAULTS configuration shown in Figure 4.2

an exact node-to-node conformance in their physical location as well. Although not mandatory, this assumption is enforced since the meshes are stationary and so that the interpolation errors could be minimised. Hence, out of the total number of nodes in the overlapped zones OZ12 and OZ23 (N_{12} and N_{13} respectively), half of them belong to either of the sub-domains constituting the overlapped zones. Let the time steps in each of the sub-domains D1, D2 and D3 be Δt_1 , Δt_2 and Δt_3 respectively. It is evident that the grid sizes in the overlapped regions OZ12 and OZ23 are such that they respect the stability criteria for the larger among the time steps pertaining to the sub-domains constituting the overlapped zones. These details are shown in Table 4.1 for clarity. Here $R_{\delta t, i}$ denotes the number of time integrations the sub-domain i undergoes before all the flow times in each of the sub-domains reach the next possible common value.

The time integration methodology in LESAULTS method comprises of two stages namely, (i) intermediate time integration stage and (ii) solution synchronization stage. A schematic of these stages are shown in Figure 4.3. At the beginning of the time integration procedure, all the sub-domains are initialised at time level t^n . Initial solution is enforced among all the subdomains and the uniqueness of solution at the overlapped zone is ensured. Once this is assured, intermediate time integrations between time levels t^n and t^{n+1} are performed. Here each sub-domain is integrated in time independently of the other, using the time step pertaining to that sub-domain. For the particular configuration shown in Figure 4.3, D1 is integrated using time step Δt_1 , D2 using Δt_2 and D3 using Δt_3 . It is obvious that during this stage, the boundary condition at each of the interface boundary is unknown. To tackle this shortcoming, the boundary values at the domain interfaces in the overlapped region is kept the same as their values at time level t^n (Dirichlet boundary condition). The intermediate time integration step is completed once each of the sub-domains completes $R_{\delta t}$ number of

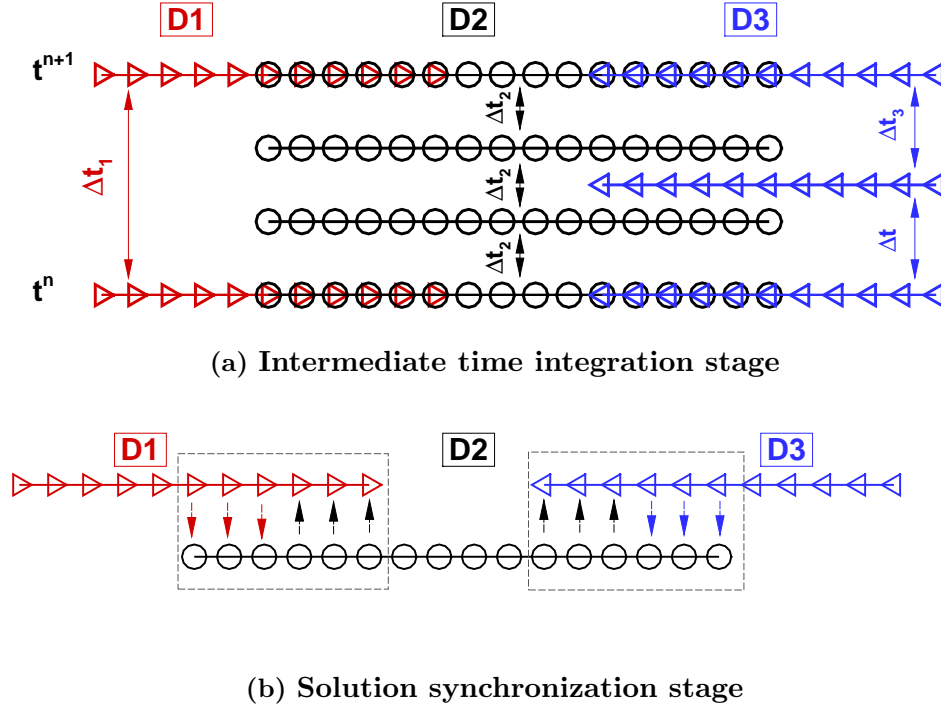


Figure 4.3: Various stages in the LESAULTS method (a) Intermediate time integration stage (b) Solution synchronization stage

independent time integrations. This corresponds, for this particular example, in sub-domain D_1 performing 1 time integration and D_2 and D_3 performing 3 and 2 time integrations respectively. This completes the intermediate time integration stage.

By the end of this stage, one obtains a unique solution set for each of the sub-domain obtained after time integration using the time step pertaining to that sub-domain. Two sets of solutions (that are slightly different due to the different time steps used) are available in the overlapped zones-OZ12 and OZ23, each one corresponding to the sub-domain to which the mesh node belongs to. This multiplicity of solutions at the same time and spatial location needs to be avoided in computations. In addition to this, the solution values near the domain interfaces where the Dirichlet boundary conditions (mentioned in the previous paragraph) are enforced are corrupted due to the approximate nature of the boundary condition used. These values need to be corrected before proceeding with further time integrations. These corrections are performed in the solution synchronization stage. In this stage, the solution values at the overlapped zones are made unique and calculated as a unique value from the two available solution sets available at a given spatial location. The objective of this solution synchronization stage is to minimize the errors accumulated in the overlapped zones and to ensure unique-

4. DEVELOPMENT AND ANALYSIS OF LESAULTS METHOD

ness of solution. This completes one stage of the LESAULTS method. The above two steps are repeated to solve for the unsteady solution of governing equations in LESAULTS method.

This completes a preliminary description of the LESAULTS method thereby addressing Objective (A.1). Further details of the implementation of this method is described along with error analysis in the Section 4.6. But before moving to that section it is imperative to explain how the speed up in LES computations is obtained using LESAULTS method and to derive the theoretical estimates of the maximum speed up attainable using this method. This is discussed in the following section.

4.5 Theoretical Computational Speedup

The speed-up obtained using LESAULTS method is defined as the ratio of the computational time taken by the conventional explicit solver to that taken using LESAULTS method for integrating through the same flow time, for the same number of computational degrees of freedom (nodes in the mesh) and using the same number of computational cores. Hence, speed-up S_{th} is expressed as,

$$Speedup, S_{th} = \frac{T_{c,CONV}}{T_{c,LESAULTS}} \quad (4.1)$$

In the above expression, $T_{c,CONV}$ and $T_{c,LESAULTS}$ are the computational times taken by the conventional LES solver and LESAULTS method based solver respectively.

For the sub-domain $D1$ (in the configuration explained in the previous section) comprising of N_1 number of nodes and a time step Δt_1 and for which C_1 number of computing cores are dedicated, the computational time ($T_{c,1}$) associated with one intermediate time integration is given by,

$$T_{c,1} \propto \frac{N_1}{C_1} \quad (4.2)$$

$$T_{c,1} = \kappa \frac{N_1}{C_1} \quad (4.3)$$

$$(4.4)$$

where κ is a constant of proportionality. Since $D1$ performs $R_{\delta t,1}$ number of intermediate time integrations before solution synchronization, the total computational time taken to update solution from time level t^n to t^{n+1} is given by,

$$T_{c,1} = \kappa R_{\delta t,1} \frac{N_1}{C_1} \quad (4.5)$$

4.5 Theoretical Computational Speedup

Similarly, for the domains D2 and D3 the computational times are obtained as,

$$T_{c,2} = \kappa R_{\delta t,2} \frac{N_2}{C_2} \quad (4.6)$$

$$T_{c,3} = \kappa R_{\delta t,3} \frac{N_3}{C_3} \quad (4.7)$$

Here C_2 and C_3 are the number of computing cores dedicated to $D2$ and $D3$ respectively. For proper load balancing between the computing cores, it is desirable to have

$$T_{c,1} = T_{c,2} = T_{c,3} = T_{c,LESAULTS} \quad (4.8)$$

This provides the expression for the appropriate number of cores to be dedicated to each sub-domain as,

$$C_1 = \frac{R_{\delta t,1} N_1}{(R_{\delta t,1} N_1 + R_{\delta t,2} N_2 + R_{\delta t,3} N_3)} (C_{tot}) \quad (4.9)$$

$$C_2 = \frac{R_{\delta t,2} N_2}{(R_{\delta t,1} N_1 + R_{\delta t,2} N_2 + R_{\delta t,3} N_3)} (C_{tot}) \quad (4.10)$$

$$C_3 = \frac{R_{\delta t,3} N_3}{(R_{\delta t,1} N_1 + R_{\delta t,2} N_2 + R_{\delta t,3} N_3)} (C_{tot}) \quad (4.11)$$

where $C_{tot} = C_1 + C_2 + C_3$ is the total number of computing cores used. Similarly, for a conventional LES solver, the time taken to update solution from time level t^n to t^{n+1} , $T_{c,CONV}$ is given as,

$$T_{c,CONV} = \kappa \max(R_{\delta t,i}) \frac{N_1 + N_2 + N_3 - 0.5 (N_{12} + N_{23})}{C_{tot}} \quad (4.12)$$

The presence of the term $\max(R_{\delta t,i})$ in the above expression is because the conventional solver is time integrated using the smallest time step in the entire domain and hence performs the same number of intermediate time integrations as the sub-domain with the smallest time step used in LESAULTS configuration.

Hence, the theoretical speed up S_{th} is obtained by substituting equations 4.12 and 4.8 in Equation 4.1.

$$S_{th} = \frac{T_{c,conv}}{T_{c,LESAULTS}} = \max(R_{\delta t,i}) \frac{N_1 + N_2 + N_3 - (N_{12} + N_{23})}{R_{\delta t_1} N_1 + R_{\delta t_2} N_2 + R_{\delta t_3} N_3} \quad (4.13)$$

In general, for a LESAULTS configuration with N_{sub} number of subdomains and C_{tot} number of computing cores, the above expression can be extended as,

$$S_{th} = \max(R_{\delta t,i}) \frac{(\sum_{i=1}^{N_{sub}} N_i - (\sum_{j=1}^{N_{sub}} \sum_{i=1}^{N_{sub}} N_{ij})/2)}{\sum_{i=1}^{N_{sub}} R_{\delta t_i} N_i} \quad (4.14)$$

4. DEVELOPMENT AND ANALYSIS OF LESAULTS METHOD

N_{ij} denotes the number of nodes in the overlapped zones between sub-domains i and j .

The optimum number of cores dedicated to sub-domain i is given by,

$$C_i = \frac{R_{\delta t,i} N_i}{\sum_{i=1}^{N_{sub}} R_{\delta t,i} N_i} (C_{tot}) \quad (4.15)$$

It can be observed that the speed up S_{th} is maximum when $max(R_{\delta t,i})$ is large along with low values of N_i for sub-domains with $R_{\delta t,i} > 1$. It is also to be emphasized that the number of nodes in the overlapped regions should be kept as low as possible to achieve the maximum speed up.

To elucidate the significance of the above expression, we consider a two sub-domain configuration with the larger sub-domain containing the larger number (N_1) of nodes having an $R_{\delta t,1}$ value of 1 and the smaller sub-domain containing N_2 number of nodes ($N_2 \ll N_1$). Then, S_{th} can be expressed as a function of the node number ratio, R_n defined as the ratio of number of nodes in the larger sub-domain to that in the smaller sub-domain (N_1/N_2) and $R_{\delta t} = R_{\delta t,2}$ as,

$$S_{th} = R_{\delta t} \frac{(R_n + 1)}{(R_n + R_{\delta t})} \quad (4.16)$$

The variation of S_{th} with R_n and $R_{\delta t}$ is plotted in Figure 4.4.

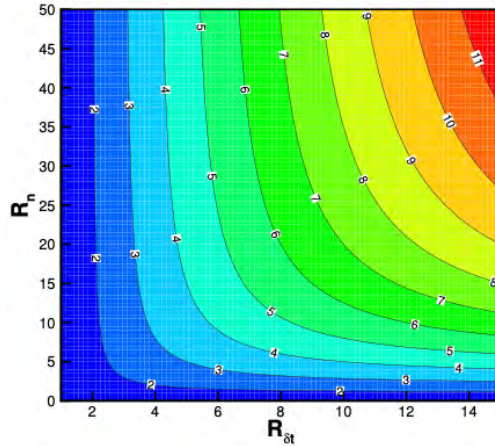


Figure 4.4: Contours of S_{th} as a function of R_n and $R_{\delta t}$ for a two sub-domain decomposition

It is observed from Figure 4.4 that the speed up obtained is maximum for high values of R_n and $R_{\delta t}$ implying that a high speed up is obtained when a high value of $R_{\delta t}$ is used in the sub-domain with the smallest time step containing a small number of nodes. Hence, LESAULTS method is efficient in LES computations when the limiting time step is dictated only by a very small number of cells in the computational domain. In this Section the theoretical speed up attainable using LESAULTS has been derived and hence Objective (A.2) is addressed.

4.6 Design of LESAULTS method

As explained in Section 4.4, the LESAULTS method works on local time stepping in multiple overlapping sub-domains. While the time integration procedure in the non-overlapping zones is rather straight forward, special attention needs to be given on how to define the solution values in the overlapped zones. The design of LESAULTS method is carried out by ensuring the following two points.

- The solution in the overlapped zone is unique. In other words, two nodes in the overlapped zones that share the same physical location should have the same solution at same time after the solution synchronization stage.
- The error due to local time stepping in the overlapped zone is minimized to the extent possible ensuring minimum length of overlapped zone for maximum speed up.

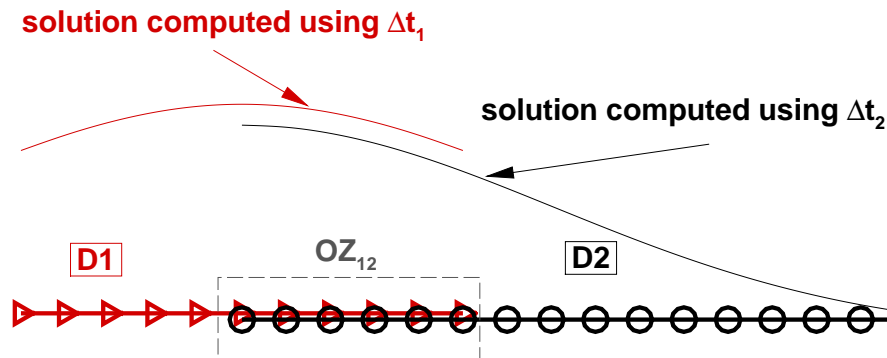


Figure 4.5: Solution in the two sub-domains and in the overlapped zone after the intermediate time integration stage

To explain the procedure of finding the solution in the overlapped zone, a two sub-domain configuration as shown in Figure 4.5 is used. Here the sub-domains $D1$ and $D2$ are discretised using the same mesh size and uses two different time steps for time integration as discussed in Section 4.4. The presence of overlapped zones using two different time steps can result in two sets of solutions after the intermediate time integration stages. This is shown by the red and black curves in Figure 4.5 although in an exaggerated manner.

In the following analysis, the following notation is used: ${}_l u_j^n$ is used to denote any quantity u at the j^{th} node in the l^{th} sub-domain at time level n . Using this

4. DEVELOPMENT AND ANALYSIS OF LESAULTS METHOD

notation, any two coincident nodes in the overlapping zone OZ12 with node ' j ' belonging to D1 and node ' k ' belonging to D2, the following expression for the x-coordinate holds,

$${}_1x_j^{n+1} = {}_2x_k^{n+1} \quad (4.17)$$

Then the computed solution u in the overlapped zone, after the intermediate time integration stage in general is given by,

$${}_1u_j^{n+1} \neq {}_2u_k^{n+1} \quad (4.18)$$

The difference in the computed solutions arise because of the different time steps used in the intermediate time integration stage as mentioned before. This needs to be corrected and a unique value of solution is to be fixed. This is performed in two steps.

In the first step, a corrected solution $u_{i,j-corr}^{n+1}$ is calculated using both the values of solution sets $({}_1u_j^{n+1}, {}_2u_k^{n+1})$ such that,

$$u_{i,j-corr}^{n+1} = f({}_1u_j^{n+1}, {}_2u_k^{n+1}) \quad (4.19)$$

An easy choice for such a function $f({}_1u_j^{n+1}, {}_2u_k^{n+1})$ is the weighted average of the two solutions given by,

$$u_{i,j-corr}^{n+1} = (1 - \alpha_c) {}_1u_j^{n+1} + \alpha_c {}_2u_k^{n+1} \quad (4.20)$$

where α_c is a weighing function dependent on the x-coordinate in the overlapped zone and $0 \leq \alpha_c \leq 1$ such that it smoothly varies from 0 in D1 to a value of 1 in D2. This would ensure a smooth transition of the solution from D1 to D2. There could be many choices for defining the spatial variation of α_c such that a smooth transition of the corrected solution $u_{i,j-corr}$ is obtained. Such a choice is shown by the blue curve in Figure 4.6 and would look attractive for 1D LESAULTS configurations. However, when applied to geometrically complicated 3D configurations, this would require costly algorithms to evaluate α_c as function of distance from interface boundaries. Hence, in this study we use a simplified functional dependence given by the Heaviside function as shown by the green curve in the same Figure.

In the first step of the synchronization stage, the corrected solution value is obtained as,

$$u_{i,j-corr}^{n+1} = (1 - H(x = x_p)) {}_1u_i^{n+1} + H(x = x_p) {}_2u_j^{n+1} \quad (4.21)$$

$$(4.22)$$

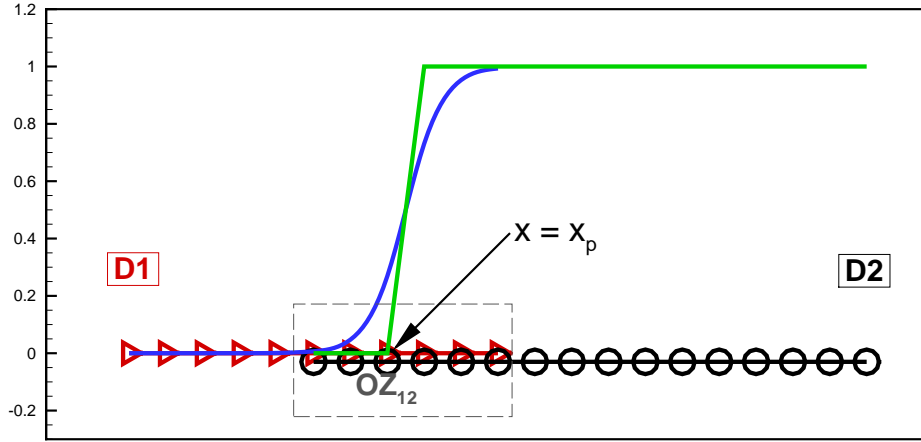


Figure 4.6: Variation of the weighing function α_c along the overlapped zone

In other words,

$$u_{i,j-corr}^{n+1} = \begin{cases} {}_1u_j^{n+1}, & \text{if } x < x_p \\ {}_2u_k^{n+1}, & \text{if } x \geq x_p \end{cases} \quad (4.23)$$

where $H(x = x_p)$ is the Heaviside function defined at $x = x_p$.

This corrected solution value is enforced to the coincident nodes in the second and final step of the solution synchronization stage.

$${}_1u_j^{n+1} = {}_2u_k^{n+1} = u_{i,j-corr}^{n+1} \quad (4.24)$$

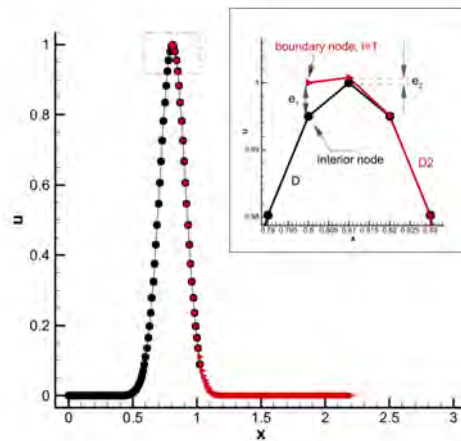


Figure 4.7: Schematic of error at boundary nodes after intermediate time integrations

It now remains to find out the location $x = x_p$ at which the Heaviside function is to be centered. x_p should be chosen subject to the condition that length of

4. DEVELOPMENT AND ANALYSIS OF LESAULTS METHOD

the overlapped zone should be minimal. To find out the optimum value of x_p , the following analysis is performed. Our ultimate goal is to find out how much the error due to the Dirichlet boundary condition propagates from the interface boundary into the interior of the sub-domain. The value of x_p is chosen where the value of this error is zero (or minimal) and depends on the number of intermediate time integrations performed and the numerical scheme used.

We consider a two domain configuration as shown in Figure 4.7. For the sake of clarity, the solution in sub-domain D1 is not shown as the conclusion obtained for sub-domain D2 should be applicable to D1 as well. The black and the red curves indicate solutions computed using conventional and LESAULTS method respectively after $R_{\delta t}$ time integrations. It should be noted that both the domains (D and D2) have the same grid size h and time step δt_s and the solutions were initially identical and coincident with each other. The differences in the computed solutions in D2 after $R_{\delta t}$ time integration is due to the approximate boundary condition used in domain D2 during the intermediate time integrations. The technique to find x_p here is to find the node nearest to the boundary where the error (shown as e1 and e2 in the figure) is minimum (or if possible zero). Then the Heaviside function can be centered at that node and the corrected value of the solution can be interpolated from the other sub-domain sharing the overlapped zone.

Now, an analysis to evaluate the error at the near boundary nodes is detailed. For any spatial scheme, the numerical solution procedure in sub-domain D2 can be expressed as,

$$[A]_2 \{u\}^{n+\Delta t_s} = [B]_2 \{u\}^n \quad (4.25)$$

or,

$${}_2\{u\}^{n+\Delta t_s} = [C]_2 \{u\}^n \quad (4.26)$$

where,

$$(4.27)$$

where $[A]$ is the coefficient matrix of the particular numerical scheme under consideration. For the LW scheme, $[A]$ is an identity matrix. For the TTGC scheme, which is spatially implicit, the matrix $[A]$ is tridiagonal in nature. $[B]$ is a matrix representing the flux residual computed using the scheme. After $R_{\delta t}$ intermediate time integrations, the solution at time level t^{n+1} is given by,

$${}_2\{u\}^{n+1} = [C]^{R\delta t} {}_2\{u\}^n \quad (4.28)$$

At any particular node i in the sub-domain D2, the above equation can be written as,

$${}_2u_i^{n+1} = \sum_{j=1}^{N_2} C_{ij}^{R\delta t} {}_2u_j^n \quad (4.29)$$

Here, $C_{ij}^{R\delta t}$ refers to the $(i, j)^{th}$ element in the matrix $[C]^{R\delta t}$.

It is to be noted that since Dirichlet boundary conditions are used at node 1 in sub-domain 2, $C_{11} = 1$ and $C_{1j} = 0$ for $j = 2, 3..N_2$ where N_2 is the total number of nodes in D2. Expressing the solution ${}_2u_j^n$ in terms of its Fourier transform one obtains,

$${}_2u_i^{n+1} = \sum_{j=1}^{N_2} C_{ij}^{R\delta t} \int \hat{U}(k, t) e^{ikx_j} dk \quad (4.30)$$

$$= \int \sum_{j=1}^{N_2} C_{ij}^{R\delta t} \hat{U}(k, t) e^{ikx_j} dk \quad (4.31)$$

$$= \int \sum_{j=1}^{N_2} C_{ij}^{R\delta t} \hat{U}(k, t) e^{ikx_i} e^{ik(x_j-x_i)} dk \quad (4.32)$$

$$= \int \sum_{j=1}^{N_2} C_{ij}^{R\delta t} e^{ik(j-i)h} \hat{U}(k, t) e^{ikx_i} dk \quad (4.33)$$

$$= \int \sum_{j=1}^{N_2} C_{ij}^{R\delta t} P_{ji} \hat{U}(k, t) e^{ikx_i} dk \quad (4.34)$$

where $\hat{U}(k, t)$ is the Fourier amplitude of the signal u^n .

The matrix P represents a projection operator that projects from spectral space (k) to real number space (x) such that any element (j, i) of matrix P is given by $P_{ji} = e^{ikh(j-i)}$. Comparing Eq. 4.34 with the equation expressing the amplification factor, one can conclude that the amplification factor projected to node i is given by,

$${}_2G_i^{R\delta t} = \sum_{j=1}^{N_2} C_{ij}^{R\delta t} P_{ji} \quad (4.35)$$

It is emphasized that ${}_2G_i$ is the amplification factor at node i and is in general not the same as derived in the previous chapter. Near the boundary nodes,

4. DEVELOPMENT AND ANALYSIS OF LESAULTS METHOD

the value of ${}_2G_i$ will be different (based on the boundary closure scheme) from that evaluated for a periodic domain described in Chapter 3. As one moves farther away from boundary nodes towards the interior nodes, the amplification factor shall approach the value predicted using periodic assumption derived in Chapter 3. This particular aspect has been mentioned in [108].

Hence the error at the boundary node in sub-domain D2 (marked as e_1 in Figure 4.7) is defined as $e_1 = {}_2u_1^{n+1} - {}_c u_k^{n+1}$ where ${}_c u_k$ refers to the solution computed using conventional method in domain D and k represents the node in domain D that is coincident with that of node 1 in domain D2. Similarly, for any near boundary node i , the error e_i can be expressed as,

$${}_2e_i = {}_2u_i^{n+1} - {}_c u_k^{n+1} \text{ such that} \quad (4.36)$$

$${}_2x_i = {}_c x_k \quad (4.37)$$

Expressing ${}_2u_i^{n+1}$ and ${}_c u_k^{n+1}$ using their Fourier transform one obtains,

$${}_2e_i = \int [{}_2G_i^{R\delta t} - {}_c G_{int}^{R\delta t}] U(k, t) e^{ikx_k} dk \quad (4.38)$$

Here, it is safe to assume that the node k in Domain D is sufficiently far from boundaries of domain D and hence the expression for the amplification factor at node k is same as the one evaluated for a periodic domain denoted as ${}_c G_{int}^{R\delta t}$ in Eq. 4.38. The value of amplification factor at node i , ${}_2G_i^{R\delta t}$ is evaluated for any particular numerical scheme using Eq. 4.35.

The magnitude of the error ${}_2e_i$ is given as $\epsilon_{bnd,i} = |{}_2G_i^{R\delta t} - {}_c G_{int}^{R\delta t}|$ and is a function of the non-dimensional wavenumber kh , CFL number N_c and the node number, i . To find out the value of $x = x_p$ at which the Heaviside function is to be anchored, the value of $\epsilon_{bnd,i}$ is calculated at various nodes near the boundaries using expression 4.38 and the node j at which $\epsilon_{bnd,j}$ is minimal (preferably zero) at a given value of $R\delta t$ and for a given scheme is sought.

For the present study, the value of $\epsilon_{bnd,i}$ is calculated by considering the linear convection equation as the governing PDE and for the LW and TTGC schemes. The number of nodes, N_2 is taken as 100. This is sufficient enough to ensure that amplification factor at any interior node approaches the corresponding value calculated for a periodic domain. The matrix $[C]$ is computed for LW and TTGC schemes. For the LW scheme, the calculation of $[C]$ is straight forward and is essentially the residual values calculated at every node. For the original TTGC scheme, $[A]$ is tridiagonal in nature and the calculation of $[C]$ is computationally intensive. In the AVBP implementation of TTGC, an approximate 2-step Jacobi method is used to invert the $[A]$ matrix. The details of this Jacobi method is

provided in [64]. In the present study, this approximate Jacobi method is used to calculate the $[C]$ matrix in Eq. 4.35.

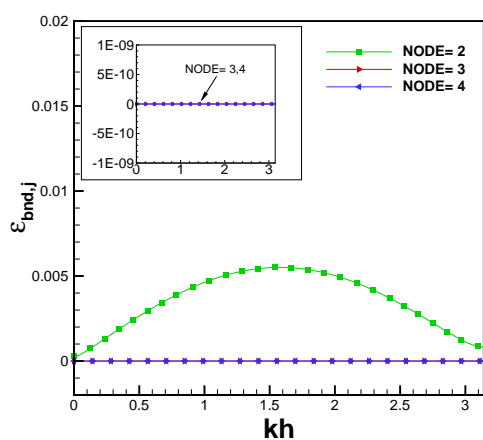
Figure 4.8 shows the value of $\epsilon_{bnd,i}$ plotted at various nodes near the interface boundary for values of $R_{\delta t} = 2, 5, 10$. The value of $N_c = 0.1$ is used and $\epsilon_{bnd,i}$ is calculated and plotted across all wavenumbers. One can observe that the value of $\epsilon_{bnd,i}$ is maximum at the near the boundary nodes (node number=2,3) and reduces as one moves to nodes in the interior of the domain, for both the LW and TTGC schemes. For $R_{\delta t} = 2$ and LW scheme, node 2 produces a maximum error of 0.005 while all the nodes in the interior produce zero error. For the TTGC scheme, absolute zero error is difficult to be obtained due to the implicit nature of the scheme. The error $\epsilon_{bnd,i}$ at node 5 is plotted in the inset in Figure 4.8(b) and is found to be of the order 10^{-5} . Similarly, for other values of $R_{\delta t}$, it is observed that the error induced by TTGC scheme is higher than that for LW scheme at the same node. This is due to the spatially implicit nature of the TTGC scheme due to which the error due to the approximate boundary condition is propagated farther into the interior of the domain.

In general, it is observed that for the LW scheme, the error falls to absolute zero after the node number $i = R_{\delta t} + 1$ (here $i=1$ is the boundary node, $i=2$ is the near boundary node etc.). This is observed from Figure 4.9 where the nearest boundary node at which the maximum error is less than a specified cutoff value is plotted. For the LW scheme, the error is identically zero for any node $i > R_{\delta t} + 1$. This is because of the spatially local stencil used in the LW scheme. For the TTGC scheme, an absolute zero error is difficult to obtain due to the spatially implicit nature of the scheme as mentioned before. Depending on the cut-off error value chosen, the nearest node at which the maximum error is below the specified cut-off value varies. It should also be noted that this particular plot of TTGC is for $N_c = 0.1$. At higher N_c values this value of node number could differ. As a rule of thumb, we propose the node number to be chosen as $2 \times R_{\delta t} + 1$. This would ensure that the error is minimal (although not zero) and at the same time keep the size of overlapped zone short. This particular rule is used in the numerical tests performed which are explained in Section 4.8 and is found to provide accurate results.

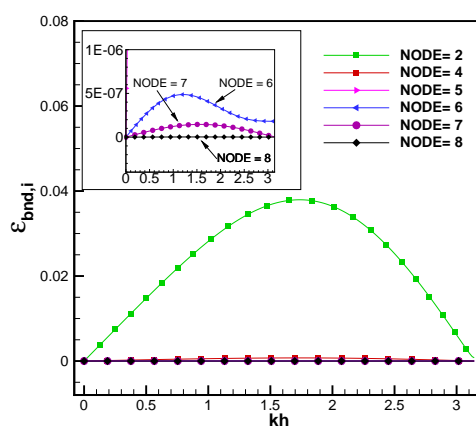
The conclusions from the previous paragraph can be applied to sub-domain D1 as well. Hence, for the overlapped zone OZ_{12} , the optimum number of cells to be used with LW scheme is $R_{\delta t,1} + R_{\delta t,2} + 1$. The corresponding number for TTGC scheme is $2(R_{\delta t,1} + R_{\delta t,2}) + 1$.

Hence, from the prior analysis, the following conclusions are made about the design of LESAULTS method.

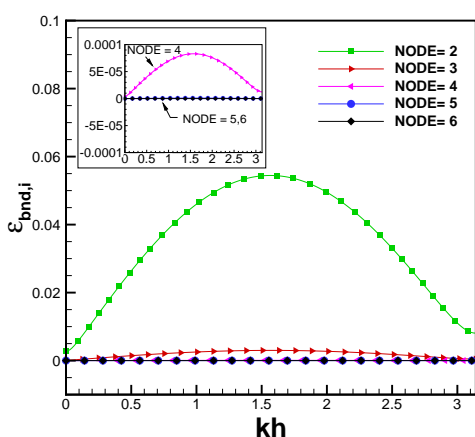
4. DEVELOPMENT AND ANALYSIS OF LESAULTS METHOD



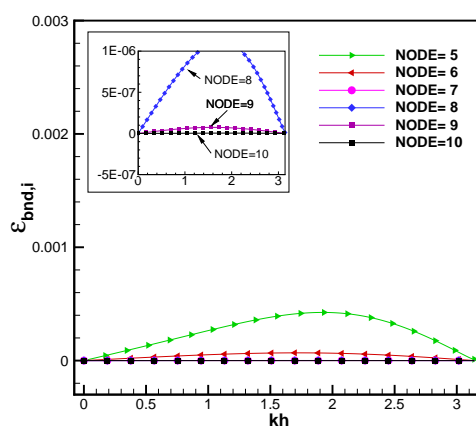
(a) LW scheme, $R_{\delta t} = 2$



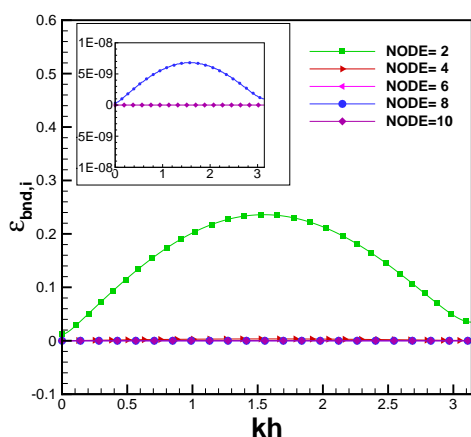
(b) TTGC scheme, $R_{\delta t} = 2$



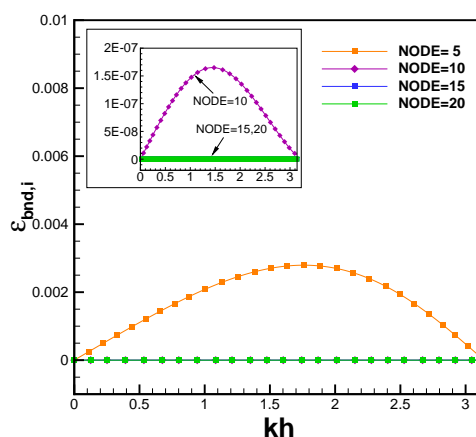
(c) LW scheme, $R_{\delta t} = 5$



(d) TTGC scheme, $R_{\delta t} = 5$



(e) LW scheme, $R_{\delta t} = 10$



(f) TTGC scheme, $R_{\delta t} = 10$

Figure 4.8: Variation of $\epsilon_{bnd,i}$ as a function of kh at $N_c = 0.1$ for various nodes near the boundary.

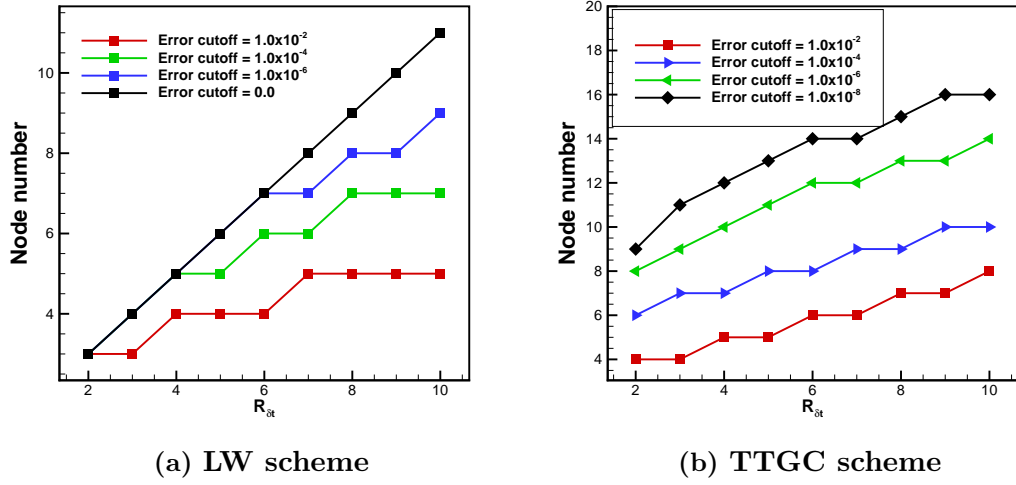


Figure 4.9: Node number at which the maximum error is less than or equal to cutoff error plotted for various $R_{\delta t}$ values

- The presence of overlapped zone in LESAULTS method is absolutely necessary to reduce the error due to local time stepping
- The solution value in the overlapped zone is obtained using the weighted average of the solution values obtained in the sub-domains constituting the overlapped zone computed using the two time steps
- For the sake of simplicity, the weighing function (α_c) is chosen as a Heaviside function. The value at which the function is anchored, $x = x_p$ depends on the numerical scheme used and the value of $R_{\delta t}$ in the sub-domain.
- For LW scheme, the value of x_p corresponds to the spatial location of the $(R_{\delta t} + 1)^{th}$ node where the node numbering starting from the boundary node towards the interior. Similarly for the TTGC scheme, this node number corresponds to $2 \times R_{\delta t} + 1$.
- Extending the above rule to both the sub-domains sharing an overlapped zone, the total length of the overlapped zone OZ_{ij} corresponds to $R_{\delta t,i} + R_{\delta t,j} + 1$ for LW scheme and $2 \times (R_{\delta t,i} + R_{\delta t,j}) + 1$ for the TTGC scheme.

Having derived the various factors determining the design of LESAULTS method, the error analysis of the method is presented in the following section.

4.7 Error Analysis

Definition of error: The numerical schemes available in AVBP have been well validated and the GSA of LW and TTGC schemes applied to three prototypical linear PDEs have been presented in the previous chapter as well. Although the prime objective of LESAULTS method is to speed up LES computations, it needs to be ensured that the errors generated using local time stepping is analysed and a quantitative information on the error is derived. Since AVBP (and the schemes used in AVBP) have been well studied and validated, it is meaningful to study the error arising from LESAULTS with respect to the conventional solver results rather than the exact solution as the philosophy used here is to design a method that is as accurate and yet faster than the conventional AVBP solver.

Hence, the error due to LESAULTS method in sub-domain i is defined as

$${}_i\epsilon = {}_i u - {}_c u \quad (4.39)$$

where ${}_i u$ and ${}_c u$ are the solutions obtained in the sub-domain i using LESAULTS method and the solution obtained using conventional LESAULTS solver respectively.

4.7.1 GSA of LESAULTS method

In order to analyze the error arising from LESAULTS, GSA of LESAULTS method for the linear convection equation (LCE) is discussed as follows. Consider the LCE in independent variables x and t and with a constant phase speed c defined as,

$$\frac{\partial u}{\partial t} + c \frac{\partial u}{\partial x} = 0, \quad (4.40)$$

in the spatial domain $0 \leq x \leq L$.

When using the conventional solver, the governing LCE is solved in the domain D shown in Figure 4.10. Domain D is discretised using linear elements of length h . Let the small time step chosen while solving the LCE in D be ${}_c \Delta t = \Delta t_s$ and the corresponding CFL number be ${}_c N_c = c \Delta t_s / h$.

When using the LESAULTS method, the same governing PDE is solved in a two sub-domain configuration shown in the same Figure. Here the domain D used in the conventional method is divided into two overlapping sub-domains D1 and D2. Similar to the previous discussion, the overlapped zone between D1 and D2 is also observed in the Figure. For the sake of analysis, the same

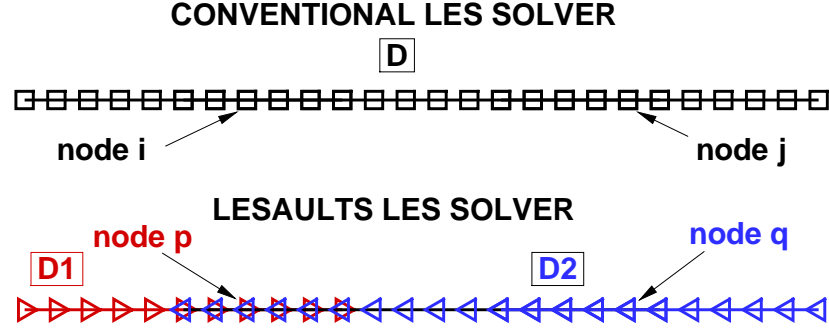


Figure 4.10: 1D domains used to solve 1D LCE

uniform mesh size h is used for discretising domain D1 and D2 including the overlapped zone. To demonstrate the error analysis of LESAULTS method, let the time step used in D1 be the same as that used in the conventional solver. Hence ${}_1\Delta t = \Delta t_s$. Similarly let the time used in D2 be ${}_2\Delta t = \Delta t_l = R_{\delta t}\Delta t_s$. Let the corresponding CFL numbers be denoted by ${}_1N_c$ and ${}_2N_c$ respectively where ${}_2N_c = R_{\delta t}{}_1N_c$. Hence, for this configuration, D1 undergoes $R_{\delta t}$ intermediate time integration steps while D2 undergoes 1 time integration step before the solution synchronization stage.

The numerical solution at the node number i in Domain D (shown in Figure) and at time level t^n is expressed using its one-dimensional Fourier transform as,

$${}_c u_j^n = \int \hat{U}(k, t) e^{i k x_j} dk, \quad (4.41)$$

The numerical solution at time level t^{n+1} (after $R_{\delta t}$ time steps) is given by,

$${}_c u_i^{n+1} = \int G^{R_{\delta t}}(kh, {}_c N_c) \hat{U}(k, t) e^{i k x_i} dk, \quad (4.42)$$

where $G^{R_{\delta t}}(kh, {}_c N_c)$ is the amplification factor after $R_{\delta t}$ time steps.

Similarly, the solution at a coincident node (node p in Figure) in sub-domain D1 at time level t^{n+1} is given by,

$${}_1 u_p^{n+1} = \int G^{R_{\delta t}}(kh, {}_1 N_c) \hat{U}(k, t) e^{i k x_p} dk, \quad (4.43)$$

Here, it is assumed that node p is located upstream of the node at which the Heaviside function α_c is anchored. As mentioned in the previous section, by selecting the right value of function α_c , the error from boundary closure is minimised and hence the amplification factor values used in the above expressions are that of the interior nodes derived in Chapter 3.

4. DEVELOPMENT AND ANALYSIS OF LESAULTS METHOD

Since sub-domain D2 undergoes only 1 intermediate time integration step, the solution at any node q in D2 is given by,

$${}_2u_q^{n+1} = \int G(kh, {}_2N_c) \hat{U}(k, t) e^{ikx_q} dk, \quad (4.44)$$

Similarly, at the corresponding node j in Domain D, the solution is expressed as,

$${}_c u_j^{n+1} = \int G^{R\delta t}(kh, {}_cN_c) U(k, t) e^{ikx_j} dk, \quad (4.45)$$

The error due to LESAULTS at node p in sub-domain D1 is given by,

$$\epsilon_p = {}_1u_p^{n+1} - {}_c u_i^{n+1}, \quad (4.46)$$

Substituting Equations 4.43 and 4.42 in 4.46 one obtains,

$$\epsilon_p = \int [G^{R\delta t}(kh, {}_1N_c) - G^{R\delta t}(kh, {}_cN_c)] \hat{U}(k, t) e^{ikx_i} dk \quad (4.47)$$

Since ${}_1N_c = {}_cN_c$, the error ϵ_p is identically zero. This expression is valid for all nodes in D1 except the nodes at which the weighing function α_c discussed in the previous section is non-zero.

Similarly the error at the node q in D2 is given by,

$$\epsilon_q = \int [G(kh, {}_2N_c) - G^{R\delta t}(kh, {}_cN_c)] \hat{U}(k, t) e^{ikx_q} dk \quad (4.48)$$

It is to be noted that the error at node q, ϵ_q is not equal to zero since the CFL numbers in sub-domain D2 and domain D are different. The magnitude of the first term in the above integral is a measure of the dissipative error and is given by,

$$\epsilon_G = |G(kh, {}_2N_c) - G^{R\delta t}(kh, {}_cN_c)| \quad (4.49)$$

The error in phase speed and the group velocity are then given by,

$$\epsilon_{CN} = \frac{({}_2C_{num}^{n+1} - {}_cC_{num}^{n+1})}{c} \quad (4.50)$$

$$\epsilon_{Vgn} = \frac{({}_2V_{g,num}^{n+1} - {}_cV_{g,num}^{n+1})}{c} \quad (4.51)$$

where ${}_2C_{num}$ and ${}_cC_{num}$ are the phase speeds and ${}_2V_{g,num}$ and ${}_cV_{g,num}$ are the group velocities and are functions of the kh and N_c and for any numerical scheme. These expressions have been derived in the previous chapter and are given by Equations 3.26 and 3.28.

Figure 4.11 shows a schematic of the spatial variation of error ϵ_G , ϵ_{CN} , ϵ_{Vgn} along the sub-domains D1 and D2. The spatial variation of the weighing (Heaviside) function is also shown in the Figure. The location at which the Heaviside

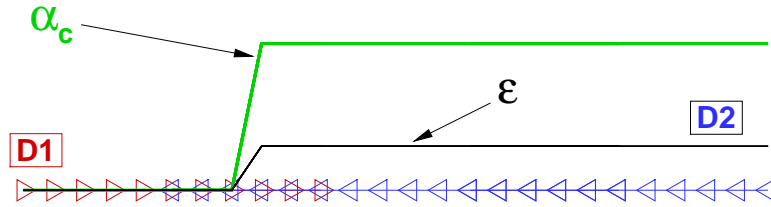


Figure 4.11: Weighing function α_c and the error ϵ in the sub-domains while using LESAULTS method

function is anchored has already been discussed in the previous section. The above analysis shows that the error in sub-domain D1 is zero for all nodes upstream of $\alpha_c = 1$. The errors in D2 on the other hand are provided by expressions 4.49 and 4.51.

Analysis of errors due to LW and TTGC

The above expressions for dissipative, phase and dispersive errors are now calculated using Equations 4.49 and 4.51 using the expressions derived from Chapter 3 for $R_{\delta t}$ values of 2, 5 and 10.

The plots of ϵ_G in the $kh - N_c$ plane for LW and TTGC schemes are shown in Figure 4.12. In the Figure, N_c refers to the largest value of CFL used in either of the sub-domains. The region where the dissipative error ϵ_G is less than 1% is colored in gray. It can be observed that for LW scheme with $R_{\delta t} = 2$, LESAULTS scheme is able to resolve the solution amplitude within 1% error for all frequencies of wavenumbers upto an N_c value of 0.1. The corresponding value of N_c for TTGC scheme for $R_{\delta t} = 2$ is 0.25. Similarly LW scheme is able to resolve (within an error of 1%) wavenumbers corresponding to $kh < 0.5$ for all values of N_c used. The corresponding value for TTGC scheme is $kh = 0.75$. This would imply that if one expects high frequency waves (such as in shear layers) in overlapped zones, then it is advisable to keep the CFL number less than 0.1 for LW scheme and less than 0.25 for TTGC scheme. If the overlapped zone is devoid of any such high frequency events then any of stable CFL number can be used. With increasing values of $R_{\delta t}$, the dissipation error region is observed to shrink gradually as can be observed from the Figure.

The phase speed error obtained with LESAULTS using LW and TTGC scheme is shown in Figure 4.13. Similar to the plots of ϵ_G , the region with less than 1% error is colored in gray. It is observed that for the LW scheme, the phase speed

4. DEVELOPMENT AND ANALYSIS OF LESAULTS METHOD

is captured accurately for all wavenumbers for $N_c < 0.17$ while for the TTGC scheme a higher N_c value ($N_c = 0.25$) could be used for the same error limit of 1%. Similarly, any stable value of N_c could be used to resolve the phase speed of any input signal with a spatial frequency with $kh < 0.4$. TTGC scheme on the other hand, can resolve wavenumbers upto a value of 0.6 with any value of N_c . Similar to the observation for ϵ_G , the error region for the phase speed shrinks progressively with increasing values of $R_{\delta t}$.

Similar observations can also be made about the dispersive error, as shown in Figure 4.14. The dispersive errors are much restrictive when compared to the phase errors for both LW and TTGC schemes with low frequency waves ($kh < 0.3$) resolvable for all stable values of N_c for both LW and TTGC schemes. The favorable error region in the plots are also observed to shrink with increasing values of $R_{\delta t}$.

4.7.2 Application to LCDE

The previous analysis performed for LCE can be extended to the LCDE equation given by,

$$\frac{\partial u}{\partial t} + c \frac{\partial u}{\partial x} = \alpha \frac{\partial^2 u}{\partial x^2}, \quad (4.52)$$

Following the same spectral analysis discussed in the previous section, the dissipation error for the 2 sub-domain configuration mentioned previously can be obtained as,

$$\epsilon_G = |G(kh, {}_2N_c, {}_2Pe) - G^{R_{\delta t}}(kh, {}_cN_c, {}_cPe)| \quad (4.53)$$

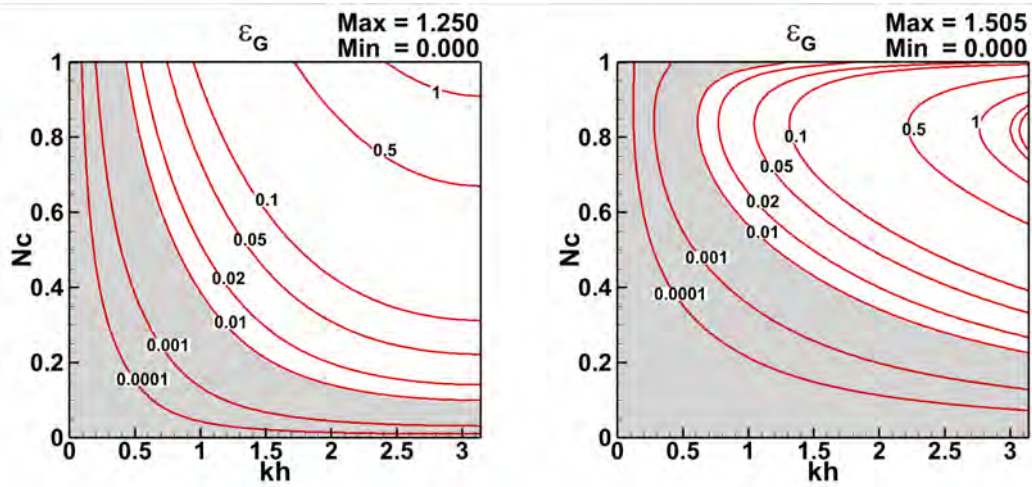
It should be noted that the Peclet numbers defined as $Pe = \alpha \Delta t / h^2$ are different for each of the sub-domains considered depending on the time step used. The error in phase speed and the group velocity are given by,

$$\epsilon_{CN} = \frac{({}_2C_{num}^{n+1} - {}_cC_{num}^{n+1})}{c} \quad (4.54)$$

$$\epsilon_{Vgn} = \frac{({}_2V_{g,num}^{n+1} - {}_cV_{g,num}^{n+1})}{c} \quad (4.55)$$

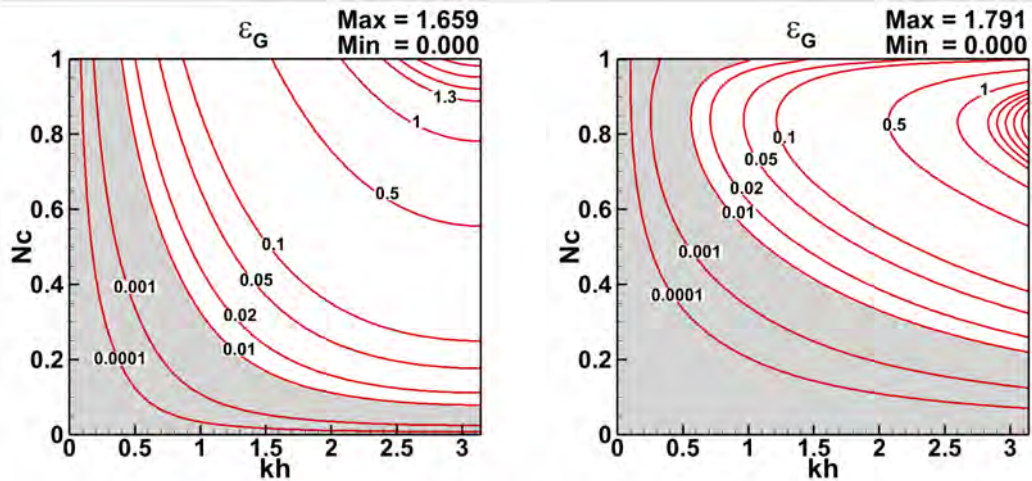
with C_{num} and $V_{g,num}$ now being a function of Pe in addition to kh and N_c as in the case of LCE.

The application of the above expressions to LW and TTGC schemes is performed and the dissipation error, ϵ_G for LW and TTGC schemes for various values of Pe ($Pe=10^{-5}, 10^{-3}$ and 10^{-1}) and $R_{\delta t}$ values of 2, 5 and 10 are shown in Figures 4.15, 4.16 and 4.17 respectively. For low values of Pe (high Reynolds numbers), no perceivable change (when compared to the LCE results discussed



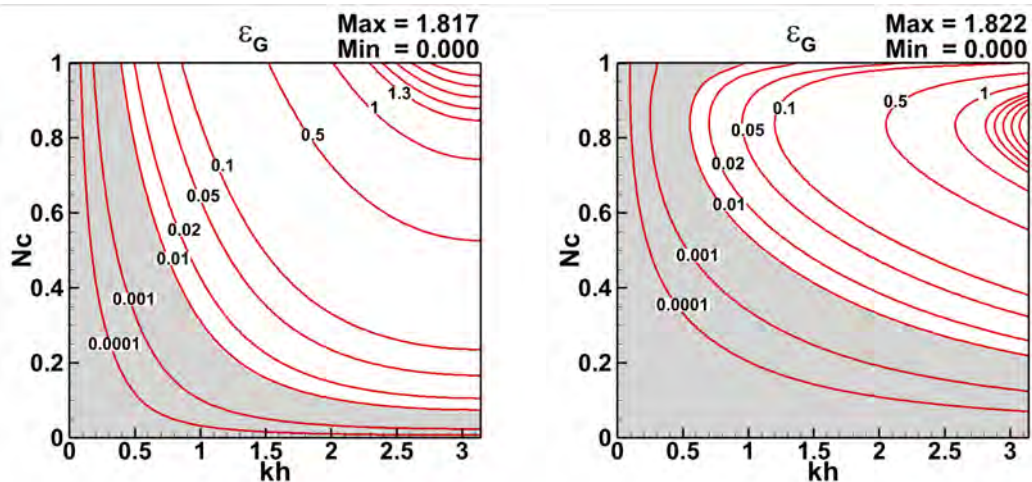
(a) LW, $R_{\delta t} = 2$

(b) TTGC, $R_{\delta t} = 2$



(c) LW, $R_{\delta t} = 5$

(d) TTGC, $R_{\delta t} = 5$

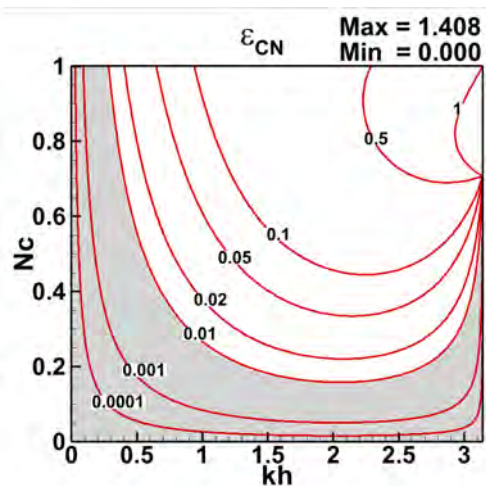


(e) LW, $R_{\delta t} = 10$

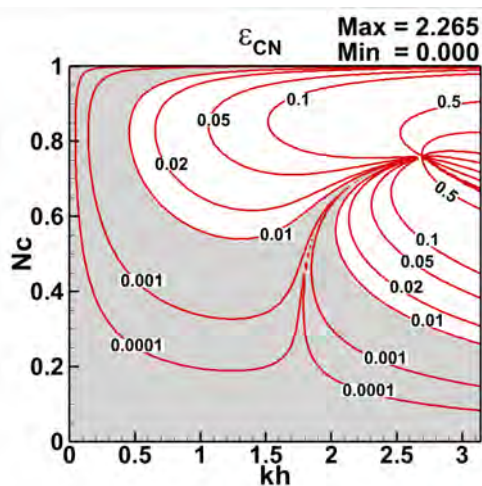
(f) TTGC, $R_{\delta t} = 10$

Figure 4.12: Contours of ϵ_G for LW and TTGC schemes at various values of $R_{\delta t}$

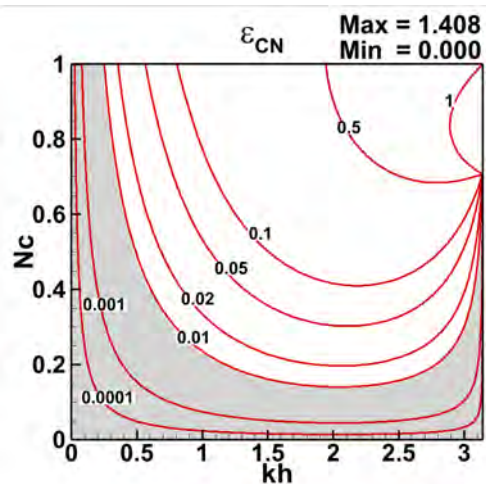
4. DEVELOPMENT AND ANALYSIS OF LESAULTS METHOD



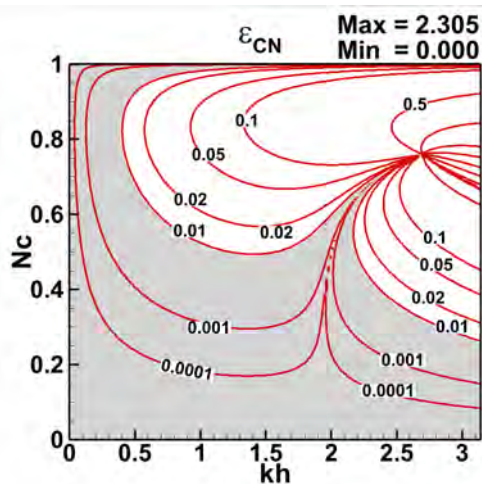
(a) $LW, R_{\delta t} = 2$



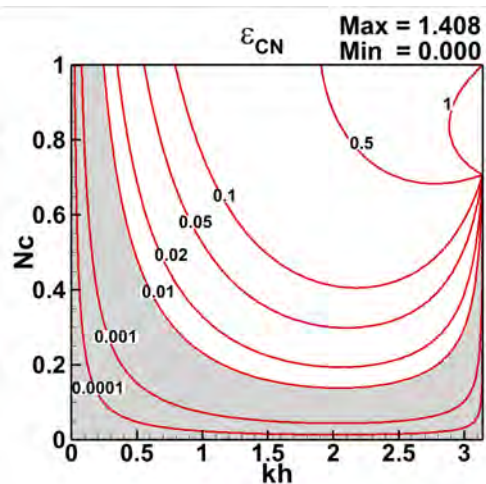
(b) $TTGC, R_{\delta t} = 2$



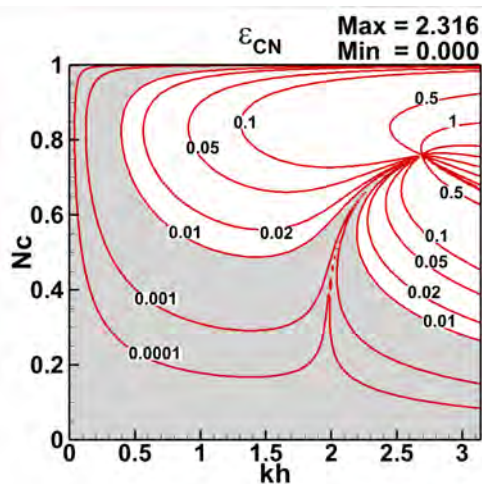
(c) $LW, R_{\delta t} = 5$



(d) $TTGC, R_{\delta t} = 5$



(e) $LW, R_{\delta t} = 10$



(f) $TTGC, R_{\delta t} = 10$

Figure 4.13: Contours of ϵ_{CN} for LW and TTGC schemes at various values of $R_{\delta t}$

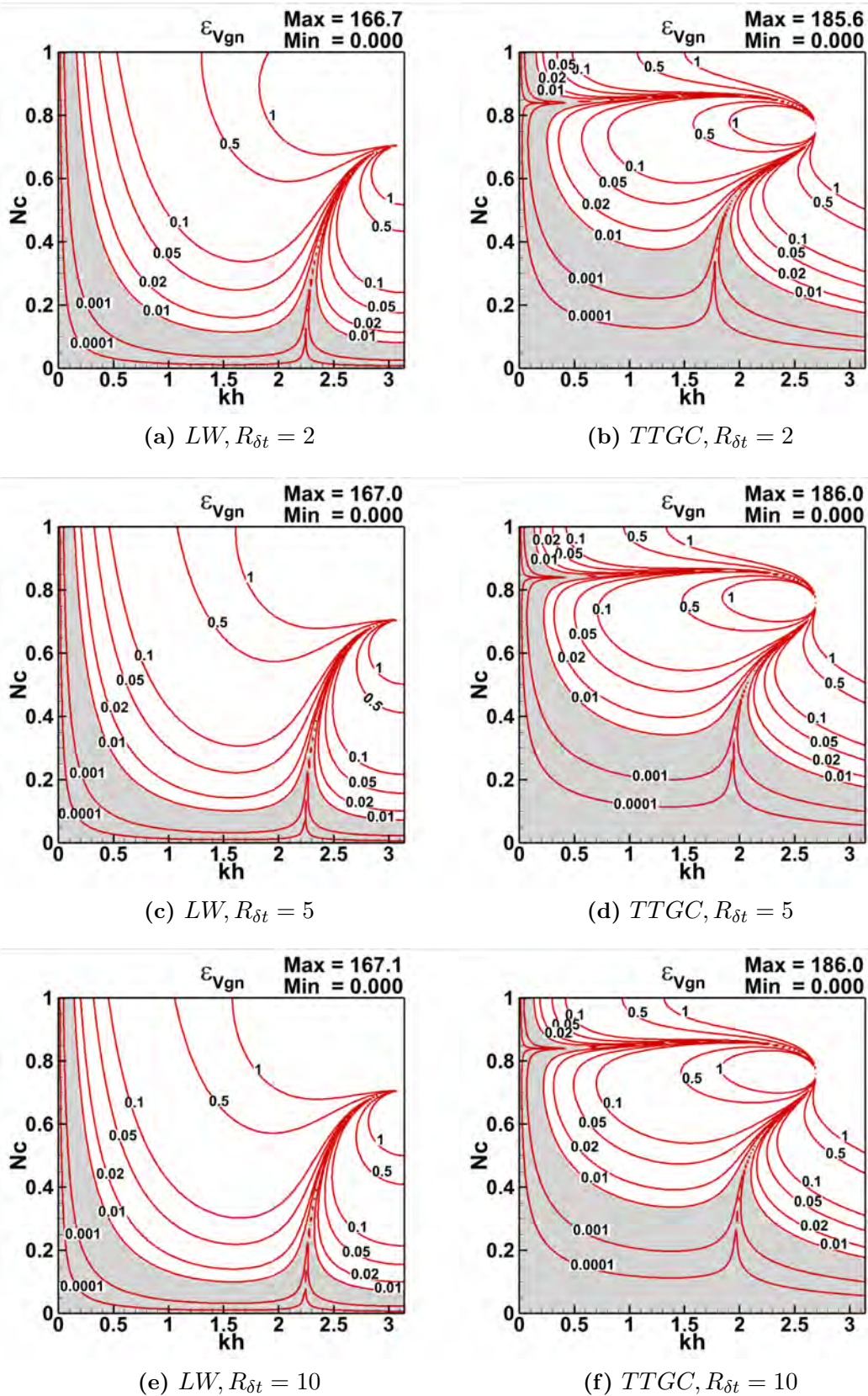


Figure 4.14: Contours of ϵ_{Vgn} for LW and TTGC schemes at various values of $R_{\delta t}$

4. DEVELOPMENT AND ANALYSIS OF LESAULTS METHOD

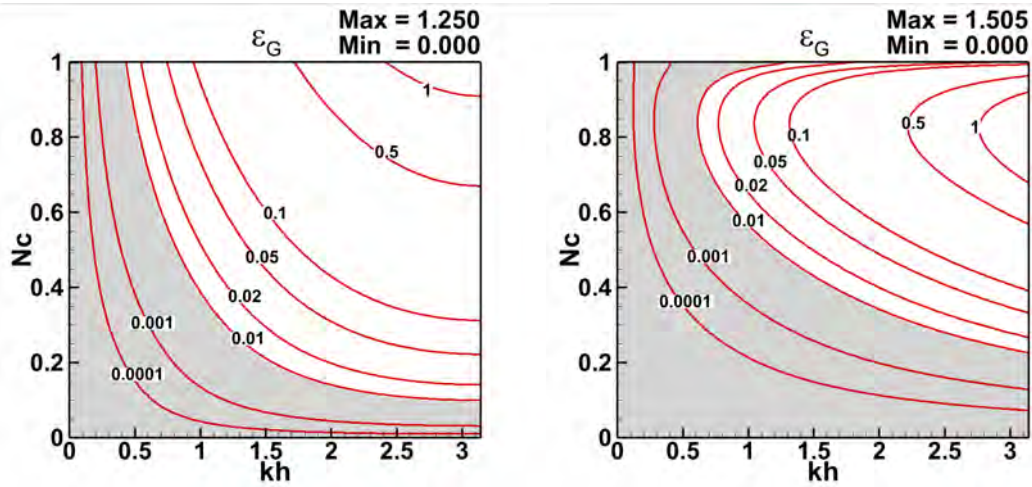
in the previous section) in the dissipation error plots is observed between different values of $R_{\delta t}$. Hence, this further underlines the suitability of employing LESAULTS method for LES applications which are typically simulated for high Reynolds number flows. For $Pe=0.1$ (low Reynolds number), different trends are observed between LW and TTGC. While for LW scheme, LESAULTS method permits the accurate calculation of the solution for very low frequencies only ($kh < 0.5$, although for high N_c values), for the TTGC scheme all permissible wavenumbers could be solved accurately (with less than 1% error) for value of $N_c < 0.2$. With increasing values of $R_{\delta t}$, the favorable error region is observed to shrink marginally for LW and TTGC schemes and for all Pe values.

Similar to the discussion on dissipation error ϵ_G , dispersive errors for the LCDE equation using LW and TTGC schemes are shown in Figures 4.18, 4.19 and 4.20 for $R_{\delta t}$ values 2,5 and 10 respectively. No appreciable difference in the error region is observed for low values of Pe ($Pe=10^{-5}$ and 10^{-3}) when compared to the LCE results. For higher Pe values ($Pe=0.1$), the dispersive error is minimal for $kh < 0.2$ for the LW scheme. For the TTGC scheme, all wavenumbers could be calculated accurately although the value of maximum N_c value that could be used is restricted ($N_c < 0.1$).

4.7.3 Validation of LESAULTS method

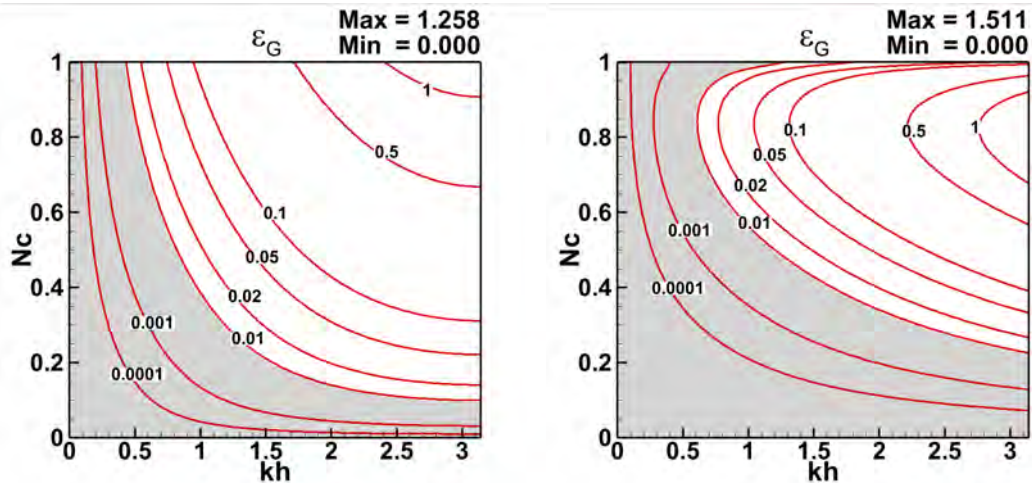
In this section, the previously mentioned analysis is validated using numerical tests. The governing PDE chosen is the LCE with unit phase speed, c and in a domain extending from $x = 0$ to $x = 3$. For applying the LESAULTS method, the domain is divided into three sub-domains-D1, D2 and D3 as shown in Figure 4.21(a). All three sub-domains are discretised using a constant meshing size, $h = 0.01$. The CFL numbers in the sub-domains D1, D2 and D3 are $N_{c,1}, N_{c,2}$ and $N_{c,3}$ respectively such that $N_{c,1} = N_{c,3} = 10 \times N_{c,2}$ ($R_{\delta t} = 10$). The size of the overlapped zones is determined using the recommended size as mentioned in the previous section. The initial solution provided is that of a wavepacket shown in Figure 4.21(a). The wavepacket is centered at $x = 0.5$ with the non-dimensional central wavenumber $kh = 0.5$.

A total of four numerical tests are carried out, the details of which are provided in Table 4.2. In all the tests, the same value of $R_{\delta t} = 10$ is used since this is a considerably large value. For each numerical scheme, two tests are carried out: one using a high value of $N_{c,1} = N_{c,3} = 0.5$ (cases 1 and 3) and the remaining two test cases with a lower value of $N_{c,1} = N_{c,3} = 0.05$ (cases 2 and 4). The values



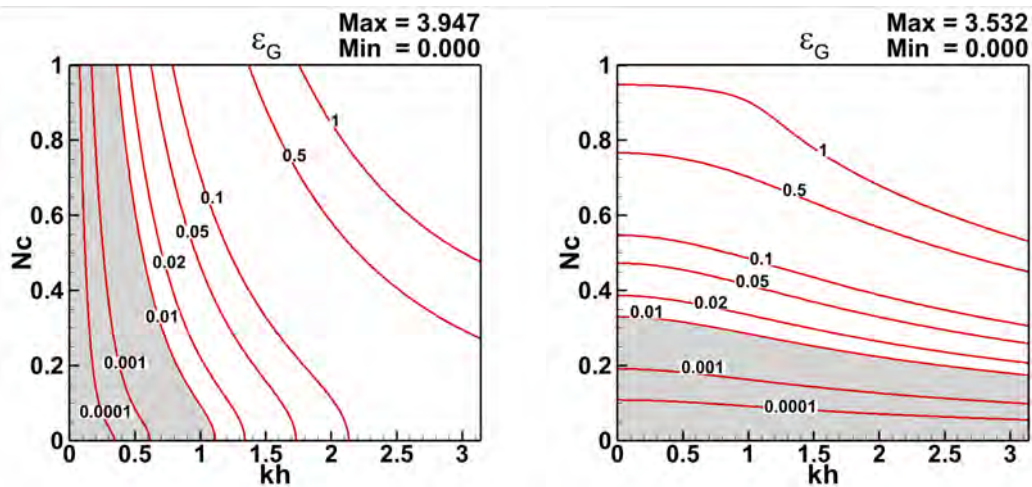
(a) LW, $Pe=10^{-5}$

(b) TTGC, $Pe=10^{-5}$



(c) LW, $Pe=10^{-3}$

(d) TTGC, $Pe=10^{-3}$



(e) LW, $Pe=0.1$

(f) TTGC, $Pe=0.1$

Figure 4.15: Contours of ϵ_G for LW and TTGC schemes at various values of Pe and $R_{\delta t} = 2$

4. DEVELOPMENT AND ANALYSIS OF LESAULTS METHOD

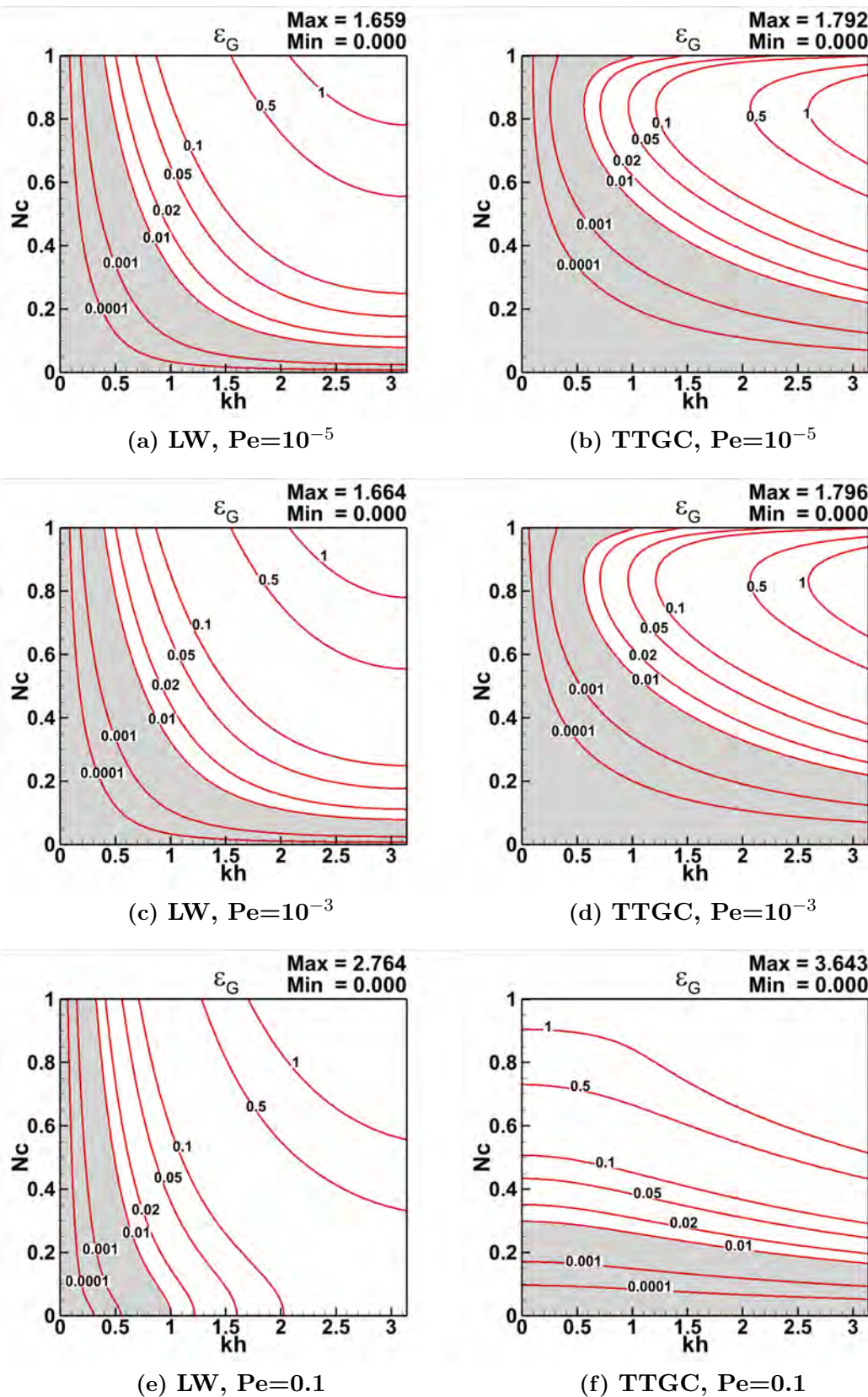


Figure 4.16: Contours of ϵ_G for LW and TTGC schemes at various values of Pe and $R_{\delta t} = 5$

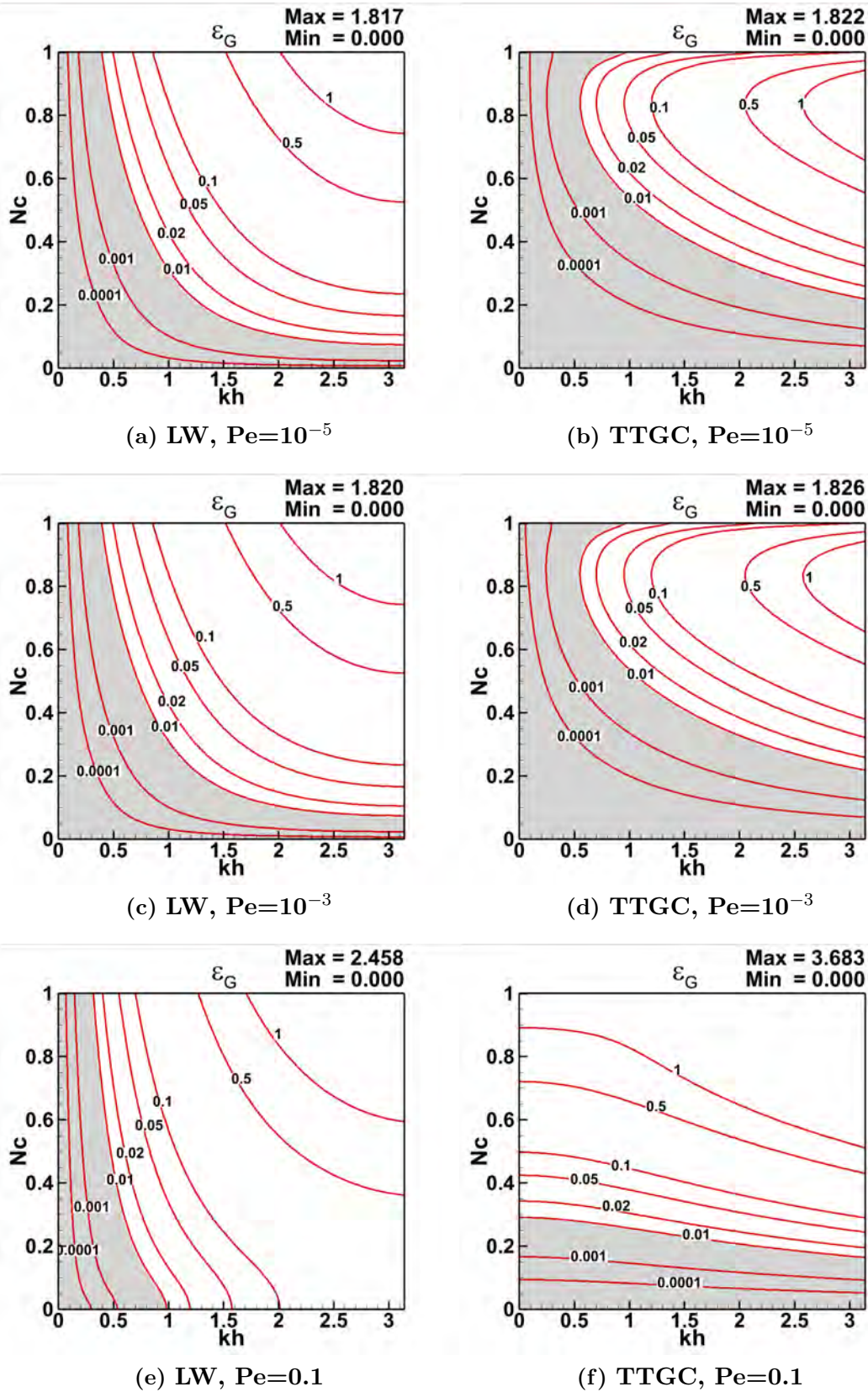


Figure 4.17: Contours of ϵ_G for LW and TTGC schemes at various values of Pe and $R_{\delta t} = 10$

4. DEVELOPMENT AND ANALYSIS OF LESAULTS METHOD

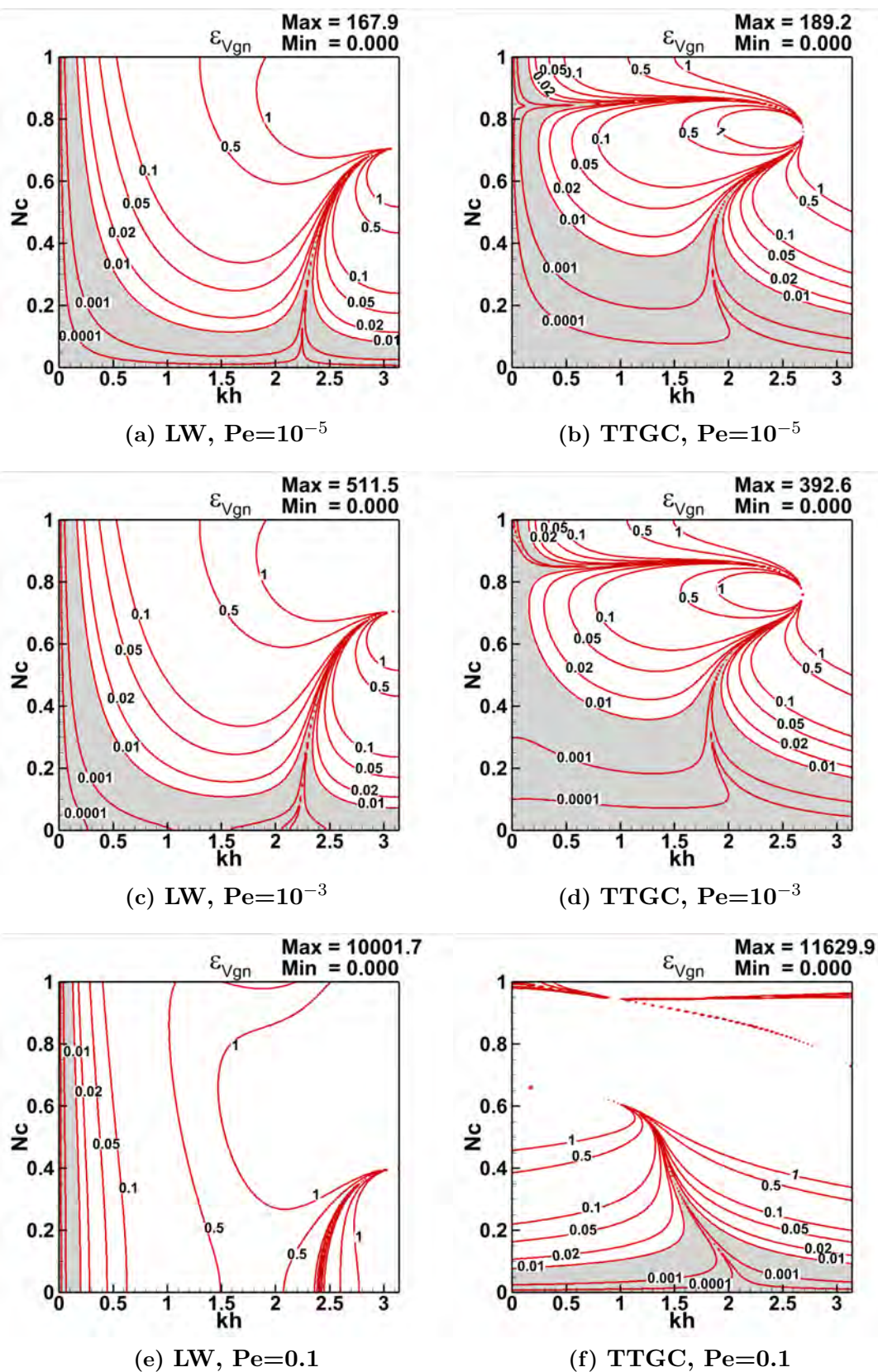
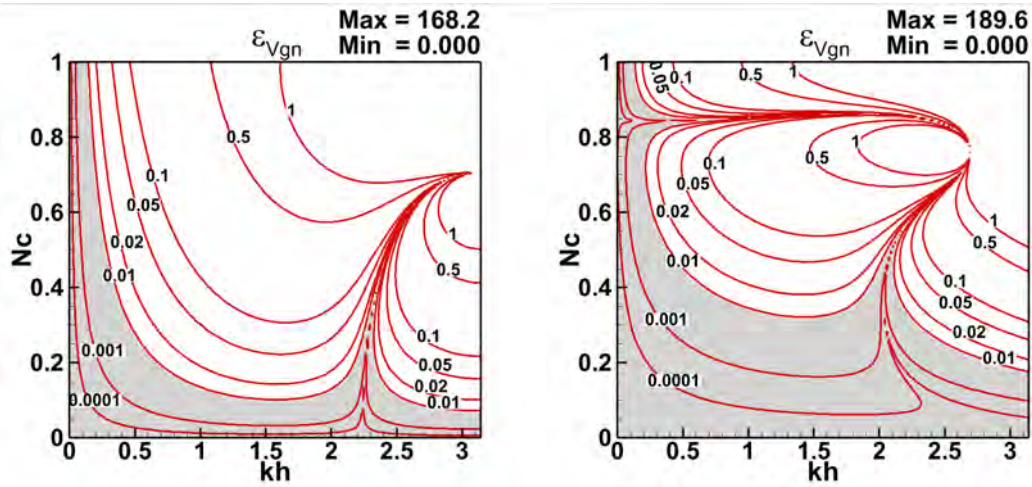
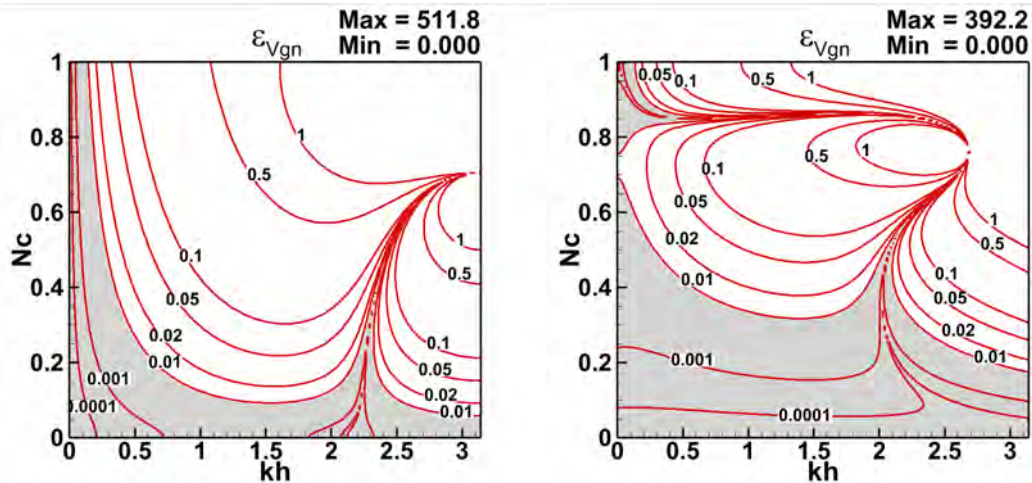


Figure 4.18: Contours of ϵ_{Vgn} for LW and TTGC schemes at various values of Pe and $R_{\delta t} = 2$



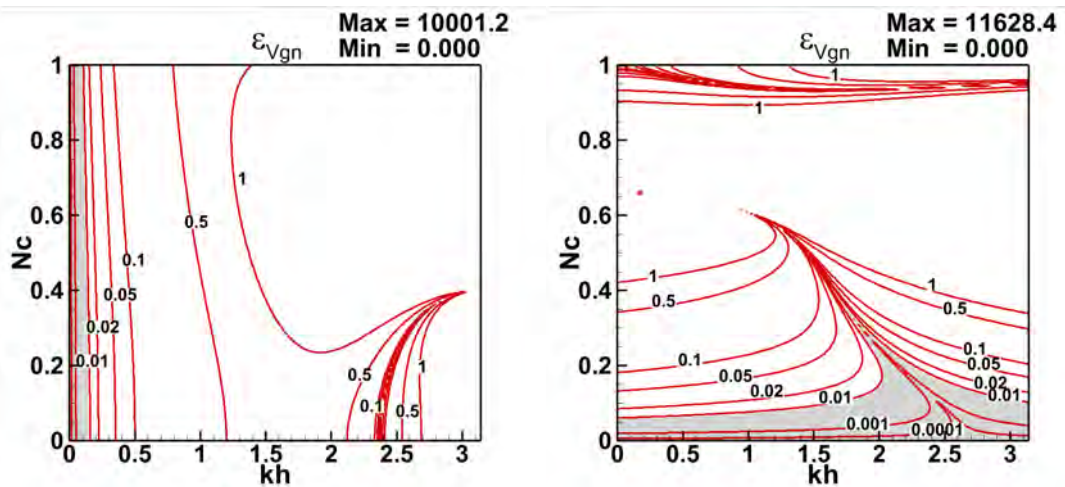
(a) LW, $Pe=10^{-5}$

(b) TTGC, $Pe=10^{-5}$



(c) LW, $Pe=10^{-3}$

(d) TTGC, $Pe=10^{-3}$



(e) LW, $Pe=0.1$

(f) TTGC, $Pe=0.1$

Figure 4.19: Contours of ϵ_{Vgn} for LW and TTGC schemes at various values of Pe and $R_{\delta t} = 5$

4. DEVELOPMENT AND ANALYSIS OF LESAULTS METHOD

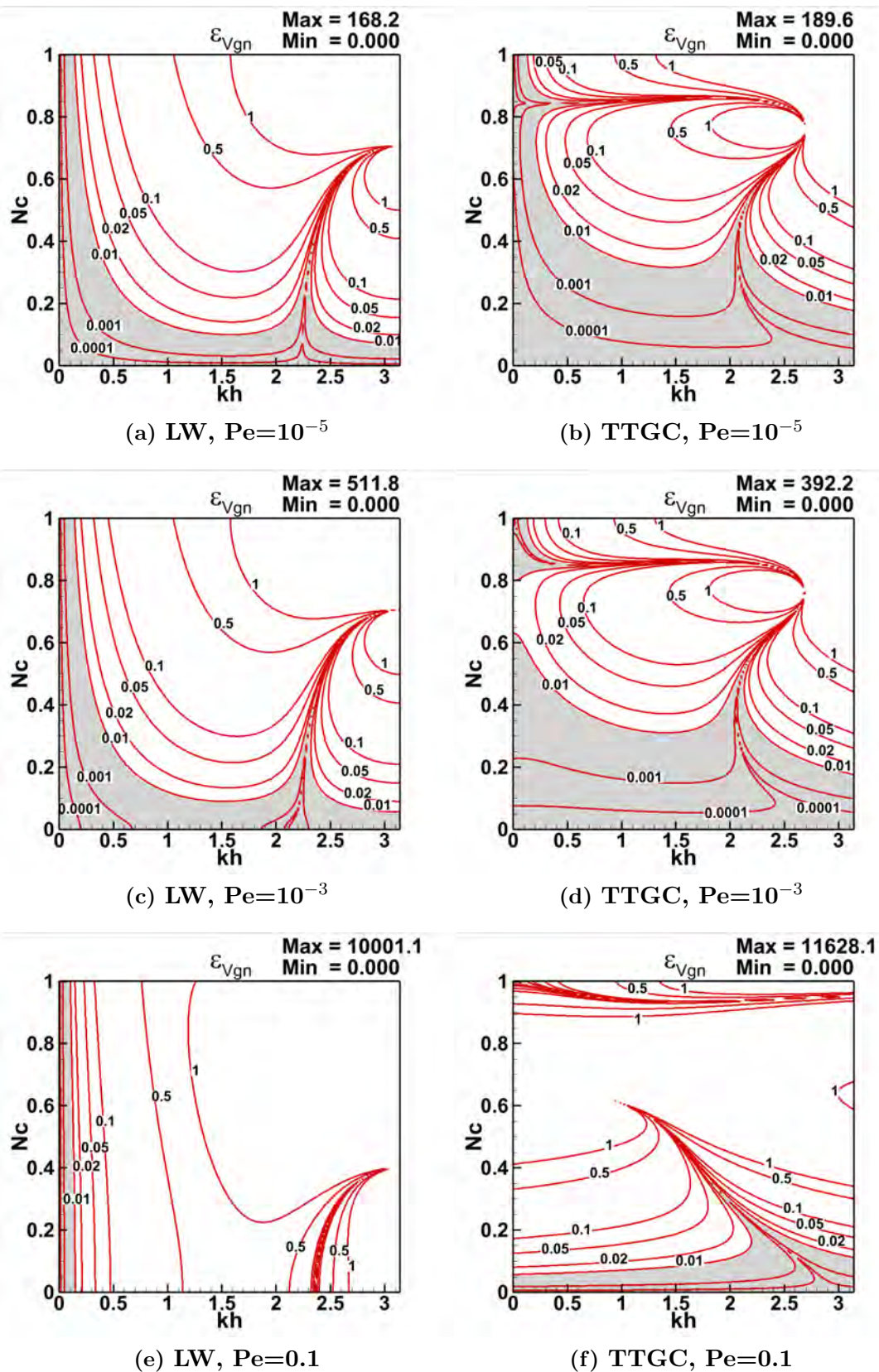


Figure 4.20: Contours of ϵ_{Vgn} for LW and TTGC schemes at various values of Pe and $R_{\delta t} = 10$

Case No	Scheme	$N_{c,1} = N_{c,3}$	$N_{c,2}$	ϵ_G	ϵ_{Vgn}
1	LW	0.50	0.050	2.9×10^{-3}	3.28×10^{-2}
2	LW	0.05	0.005	1.7×10^{-5}	3.35×10^{-4}
3	TTGC	0.50	0.050	8.1×10^{-4}	1.45×10^{-2}
3	TTGC	0.05	0.005	2.8×10^{-8}	9.37×10^{-7}

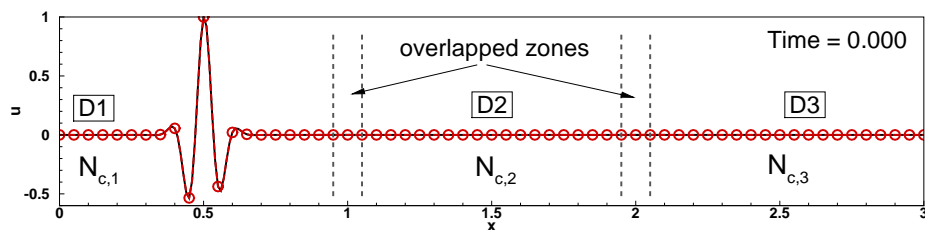
Table 4.2: Numerical tests performed using LESAULTS method for the LCE. ϵ_G and ϵ_{Vgn} values provided are from GSA analysis

of the dissipation and dispersion errors obtained from the GSA elucidated in the previous sections are also provided in the Table.

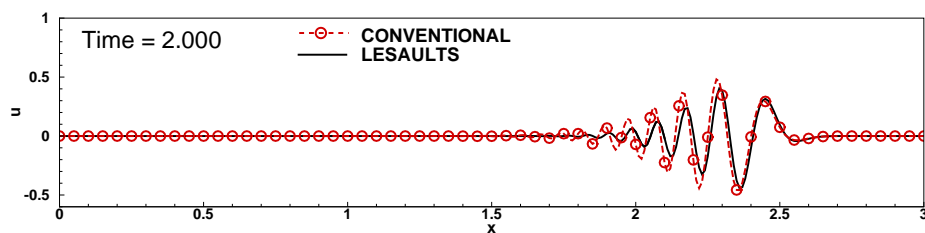
From the GSA analysis performed previously, it is observed that the dissipation error is close to two orders larger for case 1 (with $N_{c,1} = N_{c,3} = 0.5$) when compared to case 2 with $N_{c,1} = N_{c,3} = 0.05$. Hence, it is expected that for the given numerical combination of $kh, N_c, R_{\delta t}$ case 1 will be prone to more dissipation error (error in amplitude of the signal) than case 3. Similarly when comparing the LW and TTGC schemes for the same value of $N_{c,1} = N_{c,3} = 0.5$, GSA predicts higher error for the LW scheme (case 1) when compared to TTGC scheme (case 3). It is also observed that the dispersion error ϵ_{Vgn} is reduced by 2 orders of magnitude for the LW scheme and 4 orders of magnitude when $N_{c,1} = N_{c,3}$ is reduced from 0.5 to 0.05.

All cases (1-4) are computed till time $t = 2$ and the results are plotted in Figure 4.21. The red lines denote the conventional solver solution while the black lines are the solutions obtained using LESAULTS method. For Cases 1 and 2 using the LW scheme, the distortion of the initial wavepacket solution can be observed. This is due to the poorer DRP properties of LW scheme discussed in the previous chapter. When comparing the solutions obtained using LW scheme (cases 1 and 2), case 1 shows considerable difference between the computed solutions using conventional and LESAULTS method when compared to case 2. This is inline with the predictions from GSA. For the TTGC scheme, the amplitude and shape of the initial wavepacket is well preserved highlighting the superior DRP properties of TTGC scheme. When comparing the solutions obtained using TTGC scheme (cases 3 and 4), the solutions are in good agreement with each other even for the high N_c test case (Case 3). For the lower N_c case with TTGC (case 4), the match between the solutions is excellent. This set of tests ascertain the validity of GSA as well as the conclusions that has been drawn about the LESAULTS method discussed before.

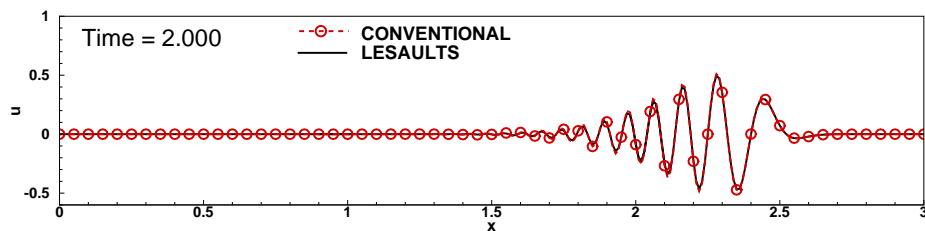
4. DEVELOPMENT AND ANALYSIS OF LESAULTS METHOD



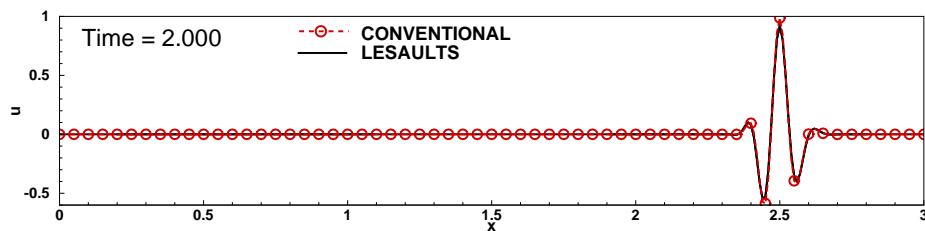
(a) LESAULTS configuration and initial solution



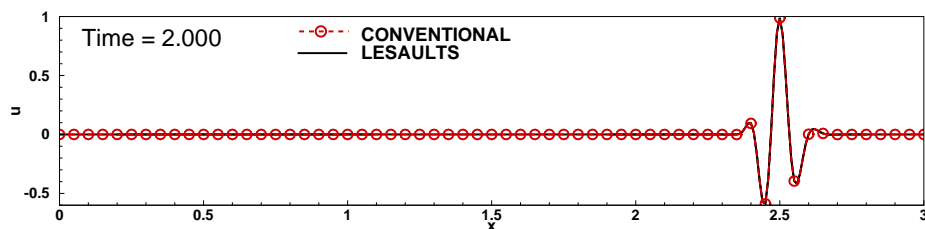
(b) LW, $N_{c,1} = N_{c,3} = 10$ $N_{c,2} = 0.5$



(c) LW, $N_{c,1} = N_{c,3} = 10$ $N_{c,2} = 0.05$



(d) TTGC, $N_{c,1} = N_{c,3} = 10$ $N_{c,2} = 0.5$



(e) TTGC, $N_{c,1} = N_{c,3} = 10$ $N_{c,2} = 0.05$

Figure 4.21: LESAULTS method applied to the solution of LCE. The initial solution is provided as a wavepacket centered at $x = 0.5$ and $kh = 0.5$

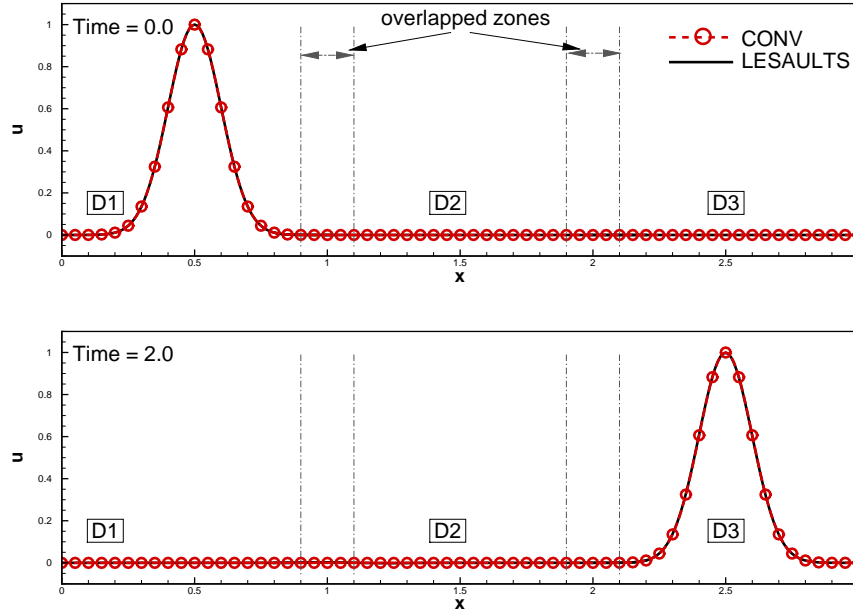


Figure 4.22: LESAULTS approach used to solve the test case with initial solution of Gaussian curve using TTGC scheme.

4.7.4 Order of accuracy

It is pivotal to demonstrate that the order of the numerical schemes is preserved when using LESAULTS method. To demonstrate this, numerical tests using LCE as the governing PDE are carried out similar to the previous section.

The spatial domain for the numerical tests are kept same as that in the previous section. In the present test cases, the grid sizes are varied. Tests are performed using conventional and LESAULTS method, for both LW and TTGC schemes and with grid spacing $h = 0.1, 0.01, 0.001$ and 0.0001 . The CFL number in domains D1 and D3 are kept as 0.1 ($N_{c,1} = N_{c,3} = 0.1$) and the value of $R_{\delta t,2}$ is set as 10 ($N_{c,2} = 0.01$) in all the test cases. The initial solution is provided in the form of a Gaussian curve centered at $x = 0.5$. All the tests are performed till time $t = 2$ is reached.

The conventional and LESAULTS solutions at the initial and final times computed using TTGC scheme with a mesh size of 0.01 is shown in Figure 4.22. Since the objective is to assess the order of accuracy using LESAULTS method, a metric for error $Error_{\text{inf}}$ is defined as follows,

$$Error_{\text{inf}} = \frac{\max(u - u_{\text{exact}})}{\max(u_{\text{exact}})} \quad (4.56)$$

where u and u_{exact} are the computed and exact solutions of LCE for the given initial solution respectively. This error norm is evaluated at the last iteration.

4. DEVELOPMENT AND ANALYSIS OF LESAULTS METHOD

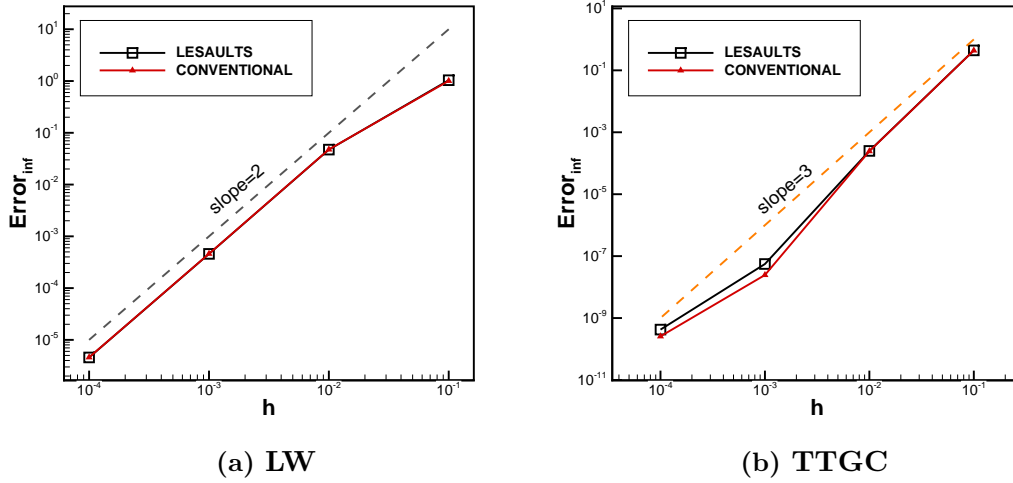


Figure 4.23: Error calculated for various mesh size h using LW and TTGC schemes for $R_{\delta t} = 10$

The computed error norm $Error_{inf}$ for various grid sizes is shown in Figure 4.23(a) for the LW scheme and in Figure 4.23(b) for the TTGC scheme. It is observed that the error obtained using LESAULTS method is in very close proximity to that obtained using the conventional solver. This is inline with the GSA analysis and its numerical validation presented in the previous section. The order of accuracy as shown by the slope of the curve demonstrates that the second order spatial accuracy of LW and third order spatial accuracy of TTGC is exactly reproduced using LESAULTS as well. Hence, through these numerical experiments, it is demonstrated that the order of the schemes are well preserved when LESAULTS method is used.

4.7.5 Conservation property of LESAULTS

One of the main drawbacks of all local time stepping schemes is their inability to strictly conserve quantities. These schemes are not purely conservative in nature and the same applies to LESAULTS method as well. In order to study the conservation properties of LESAULTS method, we consider a two sub-domain LESAULTS configuration used to solve 1D LCE and the corresponding conventional solver configuration as shown in Figure 4.24. The CFL number used in the domains D and D1 (${}_cN_c$ and ${}_1N_c$) are equal while the CFL number in D2 is large (${}_2N_c = R_{\delta t} {}_cN_c$). The overlapped zone in the LESAULTS configuration is shown as ω_L and the similar zone in the conventional solver domain is denoted as ω_C in the Figure.

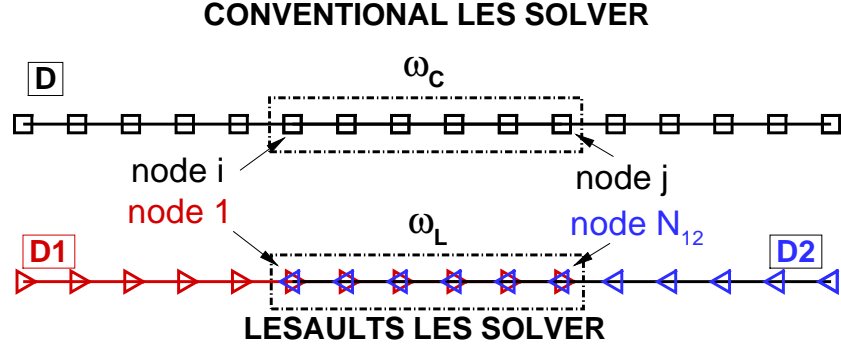


Figure 4.24: Conventional and a two-domain LESAULTS decomposition on a 1-D domain. ω_C and ω_L denote overlapped zones.

Integrating the LCE (given by Eq. 4.40) in space in the domain ω_c and after numerical evaluating the flux residual at the cell faces one obtains,

$$\frac{d}{dt} \int_{\omega_c} u d\omega = c [{}_c u_i - {}_c u_j] \quad (4.57)$$

Similarly, when the same integration is performed for the LESAULTS configuration over the overlapped region ω_L the following expression is obtained,

$$\frac{d}{dt} \int_{\omega_L} u d\omega = c [{}_1 u_1 - {}_2 u_{N_{12}}] \quad (4.58)$$

Subtracting Equation 4.57 from 4.58 one obtains,

$$\frac{d}{dt} \int_{\omega_L} u d\omega - \frac{d}{dt} \int_{\omega_c} u d\omega = c ({}_1 u_1 - {}_c u_i) - ({}_2 u_{N_{12}} - {}_c u_j) \quad (4.59)$$

Since the conventional LES solver (in the present study, AVBP) is designed to be conservative in nature, the second integral in Eq. 4.59 drops to zero under steady state conditions. Since ${}_c N_c = {}_1 N_c$ and the grid sizes in domain D and D1 are equal, it is proven in Section 4.7.1 that ${}_1 u_1 = {}_c u_i$. Hence the error due in conservation is given by $({}_2 u_{N_{12}} - {}_c u_j)$. Applying spectral analysis one can observe that this term is exactly the same as the dissipation error ϵ_G derived in Section 4.7.1 when analyzed in the spectral space. Hence the discussions on the dissipation errors provided in Section 4.7.1 holds valid for the error in conservation as well. It has been concluded in the analysis on dissipation errors earlier, that the dissipation error is minimal for low values of kh and N_c . Hence, the error in conservation is minimal when computations are carried out for low values of N_c and in locations where small values of kh are observed.

4.8 Numerical Validation

The analysis and its validation presented in the previous sections have been performed for linear governing PDEs. The objective of this section is to extend the validation presented previously to 2-D and 3-D non-linear Euler and Navier-Stokes equations. It is also worth noting that in the previous analysis the grid size in all the sub-domains were assumed to be constant. This is rarely the case in practical computations where the grid is spatially non-uniform. This effect of grid non-uniformity is also studied through numerical tests, in this section. Finally, the performance of LESAULTS method, when used with different types of cell elements (triangular and quadrilateral for 2-D, hexahedral and tetrahedral for 3-D) is also analysed.

To study the above mentioned aspects, the following numerical experiments are carried out. The 2-D dimensional isentropic vortex convection problem is the first of the numerical experiments. This 2-D test case is chosen to study the effect of cell topology as well as the effect of uniform and non-uniform meshes. Simulations are carried out using both quadrilateral and triangular elements for values of $R_{\delta t} = 2, 5, 10$. The meshes in these experiments are kept uniform as well as non-uniform and the effect of varying mesh is also analysed. The second numerical experiment is the incompressible flow past a 3D cylinder. This test case is chosen to demonstrate the applicability of LESAULTS method for 3-D, transitional flow problems. Hexahedral elements are used in this experiment and the value of $R_{\delta t}$ used is 5. The third and the final numerical experiment is performed using the Sandia-D flame. This test case demonstrates the LESAULTS method for reactive-turbulent flames. Tetrahedral elements are used in this experiment with the value of $R_{\delta t}$ chosen as 4. Through the above mentioned three numerical experiments, the applicability of LESAULTS method for a wide class of flow problems with different numerical settings is demonstrated.

4.8.1 2-Dimensional isentropic vortex convection

2D isentropic vortex convection is a typical CFD test case used to validate flow solvers. In this test case, an isentropic vortex is superposed on uniform flow of an inviscid fluid. This test case is used to validate the numerical methods for capturing the right convection speed and amplitude of the vortex. For the present study a rectangular domain with length 1.4 and height 0.6224 m is chosen. An isentropic, Rankine vortex of strength 0.01556 and radius 0.1 m units centered at $(x = 0.0778m, y = 0.3112m)$ is superimposed on a uniform flow with velocity of 100 m/s. The top and bottom boundary conditions are made translationally

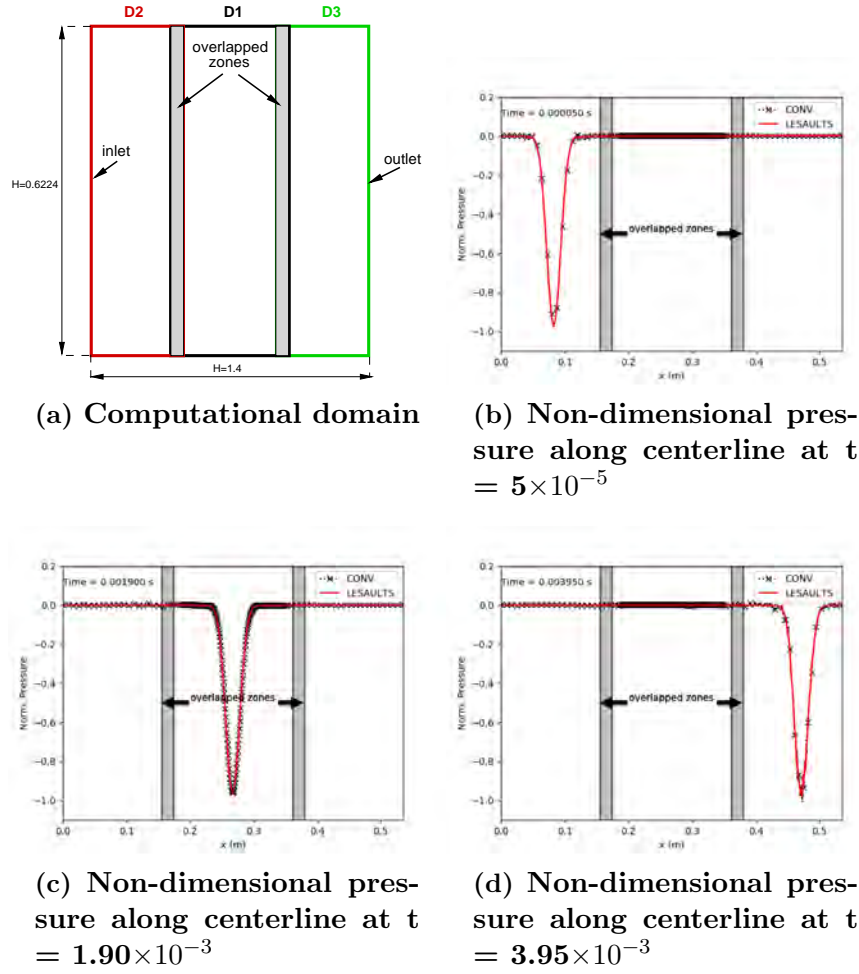


Figure 4.25: (a) Computational domain used in 2d COVO test case, (b,c,d) Non-dimensional pressure along the centerline at various time instants. Solution shown is that of Case 8

periodic. The left face is provided a characteristic inlet boundary condition and the right face is given a characteristic outflow boundary condition.

Simulations are performed using both conventional and LESAULTS methods. For the conventional solver, a single domain of dimensions mentioned previously is used. For the LESAULTS method, the computational domain is divided in the longitudinal direction into three overlapping sub-domains as shown in Figure 4.25. The sub-domain D1 is time integrated with a smaller time step and the remaining two sub-domains use equal large time step. This is designed so to demonstrate the LESAULTS method’s applicability to resolve convection from a higher time step region to a lower time step region and vice-versa.

The objective of this exercise is to study the effect of varying mesh sizes and element types on the LESAULTS method. Hence, multiple sets of test cases are simulated to study the effect of these parameters on the accuracy of LESAULTS method. These various test cases are described in Table 4.3. To have a fair

4. DEVELOPMENT AND ANALYSIS OF LESAULTS METHOD

Case No	Scheme	$\Delta t_2 = \Delta t_3$	Δt_1	Ele Type	Mesh Distribution
1	LW	1.0×10^{-6}	$\Delta t_2 / (R_{\delta t} = 2, 5, 10)$	Quad	Uniform
2	LW	1.0×10^{-6}	$\Delta t_2 / (R_{\delta t} = 2, 5, 10)$	Tri	Uniform
3	TTGC	1.0×10^{-6}	$\Delta t_2 / (R_{\delta t} = 2, 5, 10)$	Quad	Uniform
4	TTGC	1.0×10^{-6}	$\Delta t_2 / (R_{\delta t} = 2, 5, 10)$	Tri	Uniform
5	LW	1.0×10^{-6}	$\Delta t_2 / (R_{\delta t} = 2, 5, 10)$	Quad	Varying
6	LW	1.0×10^{-6}	$\Delta t_2 / (R_{\delta t} = 2, 5, 10)$	Tri	Varying
7	TTGC	1.0×10^{-6}	$\Delta t_2 / (R_{\delta t} = 2, 5, 10)$	Quad	Varying
8	TTGC	1.0×10^{-6}	$\Delta t_2 / (R_{\delta t} = 2, 5, 10)$	Tri	Varying

Table 4.3: Numerical experiments performed using 2-D isentropic vortex convection test case

comparison with the LESAULTS method, the conventional method is carried out with the smaller time step used in D1. To quantify the error with LESAULTS method, the following error definition is used.

$$\epsilon_{covo} = \max \left(\frac{p_{LESAULTS} - p_{CONV}}{p_{CONV}} \right) \quad (4.60)$$

where p is the pressure at any point in the domain and ϵ_{covo} is computed as the maximum of among all points in the domain at all computed times. Both the simulations (using conventional and LESAULTS) are solved using the same number of computational cores with the core distribution obtained from Eq. 4.11.

Actual computational speed up

Even though this test case is not an apt test case that truly demands the application of LESAULTS method, the theoretical and actual speed up obtained during simulations are reported in Table 4.4. The theoretical speed up is calculated using Eq. 4.14. In the reported values, the number of nodes in the overlapped zones are not taken into consideration and are hence approximate in nature. The actual speed up S_{act} is based on the time required for two successive computations. The LESAULTS efficiency $\eta_{LESAULTS}$ defined as $\eta_{LESAULTS} = S_{act}/S_{th}$ where S_{th} is given by Eq. 4.14 and gives an indication of how well LESAULTS method works is also provided in the Table. For the sake of brevity, the speed up values are reported only for the extreme case where ($R_{\delta t,1} = 10$) and for uniform grid distribution. Similar speed up values are obtained for other simulations as well.

Element type	Scheme	$R_{\delta t,1}$	N_1	N_2	N_3	S_{th}	S_{act}	$\eta_{LESAULTS}$
Quad	LW	10	50125	40501	40501	2.25	2.21	98%
Quad	TTGC	10	58947	40501	40501	2.09	1.92	92%
Tri	LW	10	51634	47409	47180	2.39	2.21	92%
Tri	TTGC	10	50125	40501	40501	2.31	2.09	90%

Table 4.4: Numerical experiments performed using isentropic vortex convection test case

It can be observed that in real computations, speed up close to the theoretical limits are indeed obtained ($\eta_{LESAULTS} = 90\%$), thereby emphasizing the benefit of using LESAULTS method.

Effect of mesh element type

To study the effect of mesh element type, simulations are carried out using quadrilateral and triangular mesh elements using LW and TTGC schemes. In this section we consider uniform mesh distribution (Cases 1-4) in Table 4.3. The same size of quadrilateral and triangular elements have been used and inviscid flow solver is used to perform simulations. The simulations are performed till the vortex convects through the outflow boundary. The profile of normalized pressure at a horizontal plane passing through the vortex center at various time instants is shown in Figures Fig:LESAULTS $_{C_{ovo_a}omains(c)}$ and (d) .

The error computed for the simulation with quadrilateral and triangular elements are shown in Figure 4.26(a) for $R_{\delta t}$ values of 2,5 and 10. The error with respect to the conventional solver is seen to increase with increasing value of $R_{\delta t}$ for all element types. The increase in error with $R_{\delta t}$ is seen to be higher for triangular elements when compared to quadrilateral elements. It is also observed that the error associated with TTGC scheme is lesser than LW scheme.

Effect of variable mesh sizes

In these test cases, the mesh size used in domain D1 is reduced by a factor equal to the value of $R_{\delta t}$ so that the cell CFL number N_c is kept approximately uniform in all sub domains. Similar to the previous exercise, simulations are carried out for $R_{\delta t}$ values of 2,5 and 10. The error calculated for these test cases using quadrilateral and triangular elements are shown in Figure 4.26(b). The error is found to be lower for quadrilateral cells than triangular cells due to better resolution properties of quad elements. Similarly, the error is also found to be

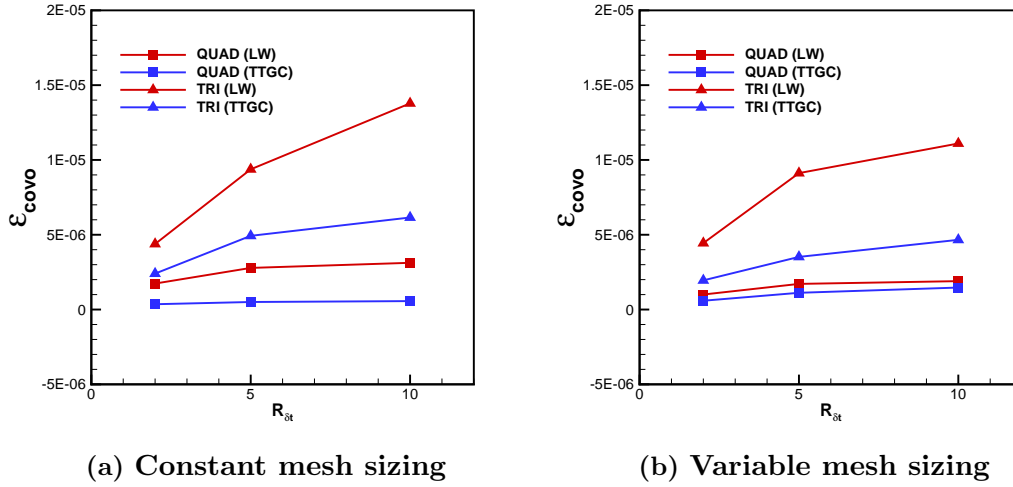


Figure 4.26: Error ϵ_{covo} calculated for (a) Uniform mesh spacing (b) Variable mesh spacing

lower for TTGC scheme when compared to LW ascertaining its superior numerical properties.

4.8.2 Flow past 3D circular cylinder

In this section, validation of the LESAULTS method for the 3-dimensional, incompressible, transitional flow past a circular cylinder at Reynolds number 3900 is described. In terms of the nature of turbulence present, this test case falls under the lower subcritical range of flow where the flow is essentially laminar beyond separation and turbulence is generated at the shear layers in the wake. This is a typical test case used to validate DNS ([109, 110]), LES ([111]) and RANS ([112, 113]) solvers with experimental data on the mean and rms values of velocity and pressure and the details of the measurement technique discussed in [114, 115].

This flow test case is modeled using a circular cylinder of diameter $D = 0.1$ m and a span length equal to π times the diameter (πD) kept laterally facing a uniform incompressible flow of velocity 0.61 m/s. The computational domain used to model the test case is shown in Figure 4.27(a). The cylinder is placed in a cylindrical computational domain of diameter $30D$. The end faces of the cylinder intersects the lateral faces of the computational domain such that end wall effects are neglected. The upstream semi-cylindrical boundary of the outer domain is modeled as an inlet while outflow boundary conditions are enforced on the downstream side of the cylinder. Similar to the previous test case,

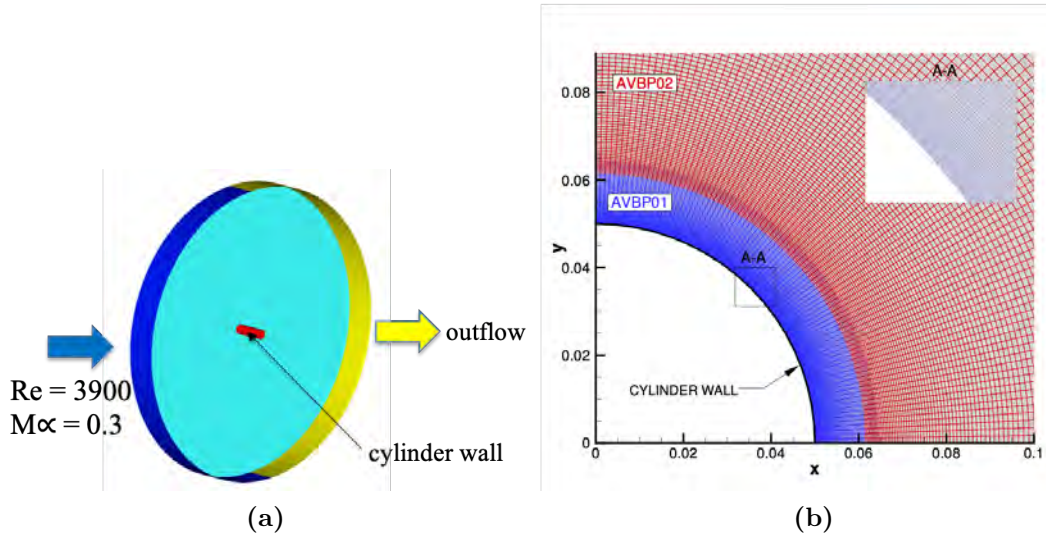


Figure 4.27: (a) Computational domain and boundary conditions used to solve the 3D flow past a circular cylinder. (b) Zoomed view on the LESAULTS partitioning

NSCBC based inlet and outlet boundary conditions are used in this study. The target pressure at the outflow boundary is specified as atmospheric pressure. The lateral faces of the computational domain are modeled as transitionally periodic to avoid end wall effects. The cylindrical wall is modeled as no-slip and adiabatic and no specific wall treatment is used. Air is used as the fluid for simulation and the viscosity of air is calculated using Sutherland's law. Since the flow is near isothermal, the viscosity is maintained nearly constant. The incoming flow velocity of 0.61 m/s along with the chosen length scale (D) ensures that the Reynold's number for the simulation is 3900.

As in the previous test case, two sets of simulations (corresponding to the conventional and LESAULTS solver) are performed. The mesh uses hexahedral cells using an 'O-type' grid configuration. It is for this reason that hexahedral grid cells are used since tetrahedral based LES computations of this case would require a huge number of mesh cells considering also the fact that no wall models are used. For properly resolving the fine scale turbulent structures generated near the cylinder wall, extremely fine cells are used in the near wall region. The boundary layer thickness on the cylinder at an angle of 80 degrees to the incoming flow is estimated as $0.0476D$ as mentioned in [116]. The wall-normal dimension of the mesh cell size is chosen such that this boundary layer thickness is resolved using 80 cells. The cylindrical wall surface is discretized using 360 elements in the circumferential direction and 40 cells in the span-wise direction respectively. Due to the fine nature of mesh cells near the wall, the time step in the domain is

4. DEVELOPMENT AND ANALYSIS OF LESAULTS METHOD

Element type	Scheme	$R_{\delta t,1}$	N_1	N_2	S_{th}	S_{act}	$\eta_{LESAULTS}$
Hexa	LW	5	900360	2922480	2.57	2.37	92%

Table 4.5: Theoretical and actual speed up obtained for the LES of 3D flow past a cylinder

restricted to a very small value. While using the conventional solver, this small time step value induces stiffness and makes the computation exorbitantly high.

For performing the LESAULTS simulation, the computational domain is divided into two sub-domains AVBP01 and AVBP02 as shown in Figure 4.27(b). Here AVBP01 is the domain that houses the cylinder wall and consists of 60 cells in the radial direction. This is the sub-domain with the fine cells requiring small time step. AVBP02 consists of the remaining portion of the computational domain and can accommodate a larger timestep.

LES with the conventional explicit solver is also performed for comparing the results of that obtained using LESAULTS method. Here a single computational domain is used, obtained by merging the mesh generated for the LESAULTS method. Hence it is emphasized that the grids used in LESAULTS and conventional simulations have an exact node-node spatial correspondence.

The simulations are performed using LW scheme for both the cases (conventional and LESAULTS) and the Sigma SGS model is used for turbulent closure. For the conventional simulation, a time step of 2.0×10^{-7} sec. is used for the entire sub-domain. For the LESAULTS method, the same time step is used in AVBP01 while a time step of 1.0×10^{-6} sec is used in AVBP02. Hence the value of $R_{\delta t}$ used for this simulation is 5. The number of nodes and the time steps used in the simulations are listed in Table Tab:Speedup_{3DC}. *Flowsimulationsareperformedforduration(inflowtime), wiseaveraginginadditiontotimeaveragingisalsoperformedonthe flowquantities.*

Actual computational speed up

It is interesting to compare the theoretical speed-up obtained using Eq. 4.14 with that of the speed-up obtained in practice. Table 4.5 shows the number of nodes in the sub-domains and the $R_{\delta t}$ used in the simulation. The theoretical speed-up calculated using Eq. 4.14 is 2.57 for this exercise. To compute the real speed-up, the average physical time taken per time step is noted for LESAULTS and conventional solver executions and the speed-up value is computed using Eq. 4.1. A good agreement is found between the theoretical and actual speed-up values with the LESAULTS efficiency being 92%.

Comparison of results obtained using conventional and LESAULTS method

The results obtained using LESAULTS and conventional solvers are presented in Figures(4.28, 4.29, 4.30, 4.31, 4.32). The lateral variation of the mean longitudinal and lateral velocity components at various downstream planes ($x/d=1,1.54,2.02,4,7$ and 10) are plotted in Figures 4.28 and 4.29. Both the quantities are non-dimensionalised using the freestream velocity values and are plotted against the non-dimensional y -coordinate. It is observed that the LW scheme is able to predict the mean longitudinal velocity pretty accurately. The excellent match between the LESAULTS and conventional solver results can also be noted at all downstream planes.

Similar observation is also observed for the non-dimensional, mean lateral velocity shown in Figure 4.29. Discrepancies are observed in the computed values when compared to measurements even though the computed values match the trends. This observation has been made in previous studies as well [109, 115]. However, excellent match is seen between the conventional and LESAULTS results underlining the accuracy of LESAULTS method in reproducing the conventional solver results.

Similar to the mean quantities, the first order turbulent statistical quantities are plotted in Figures(4.30, 4.31, 4.32). The rms of the longitudinal velocity non-dimensionalised by freestream velocity as a function of non-dimensional y -coordinate is plotted in Figure 4.30. Overall trends of the experimental measurements is found be reproduced using LW scheme. Small deviations of the computed values from measurements in the near downstream planes is observed. This could be due to the excess dissipation of the LW scheme. However, a good match between LESAULTS and conventional results are observed at all downstream planes.

Similar observations can also be made about the v -rms and uv -rms plots shown in Figures 4.31 and 4.32. An overall good match between the LESAULTS and conventional results are observed.

4.8.3 Sandia-D

The flame D of Sandia is a widely studied partially premixed, turbulent flame with detailed measurements of temperature, mixture fraction and species profiles available. This flame is chosen as a test case to demonstrate the applicability of LESAULTS method to turbulent reactive flow cases using tetrahedral meshes.

4. DEVELOPMENT AND ANALYSIS OF LESAULTS METHOD

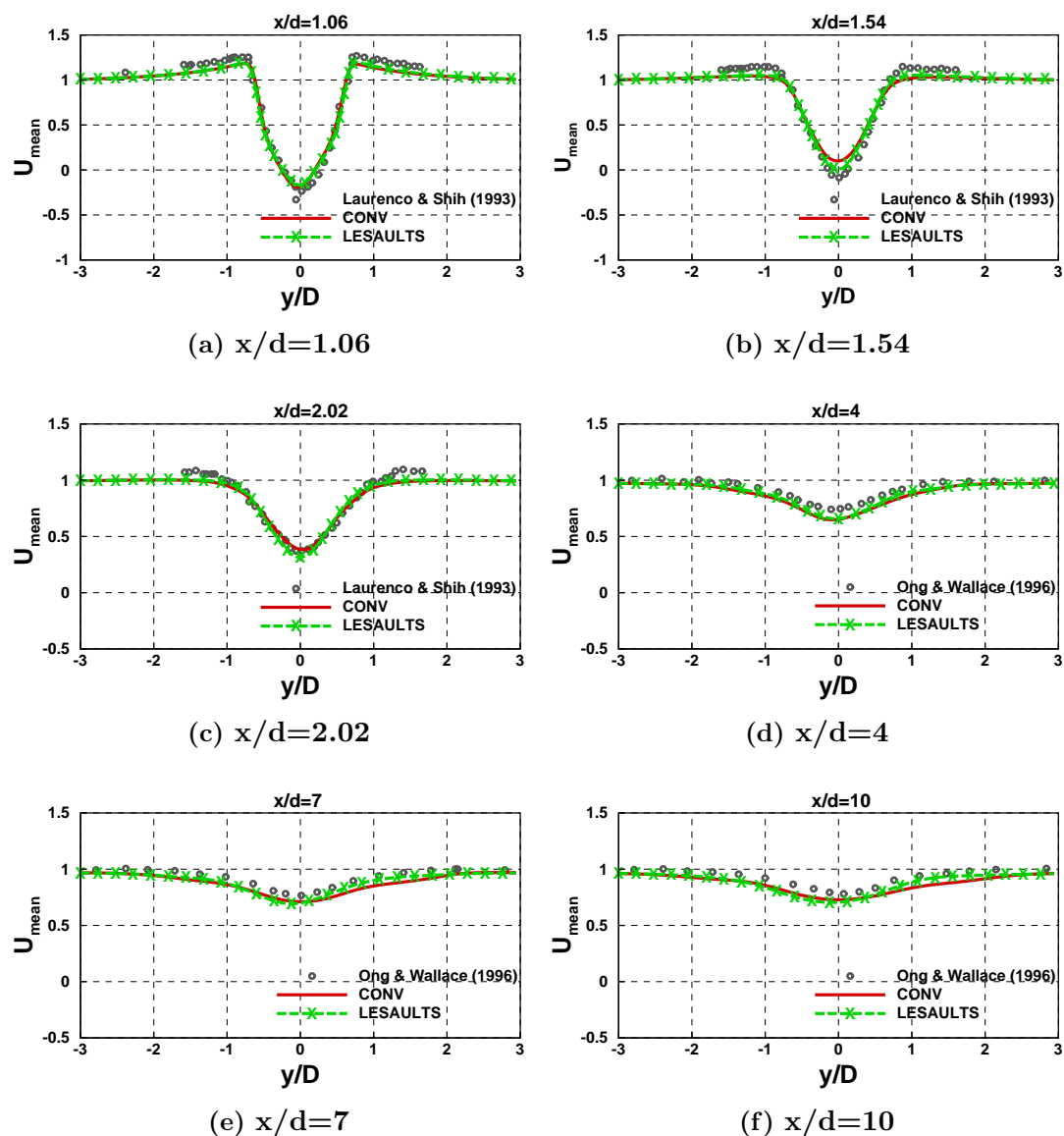


Figure 4.28: Variation of non-dimensional mean longitudinal velocity along non-dimensional y -coordinate at longitudinal planes calculated using conventional and LESAULTS method

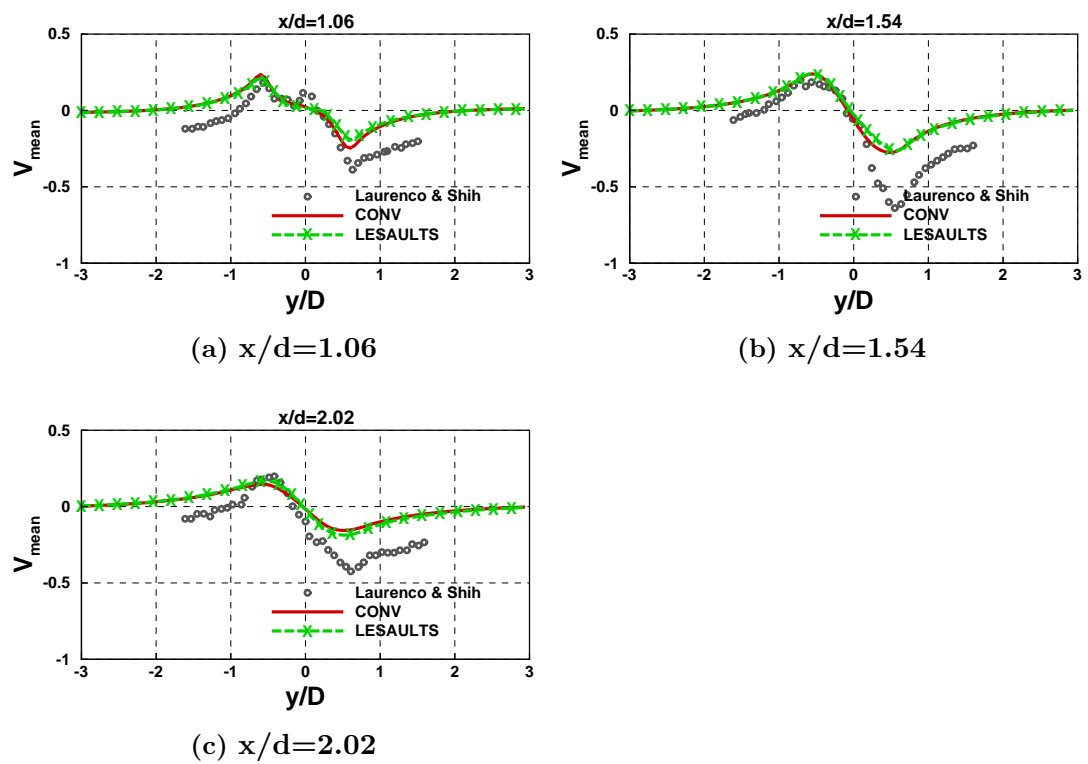


Figure 4.29: Variation of non-dimensional mean lateral velocity along non-dimensional y -coordinate at longitudinal planes calculated using conventional and LESAULTS method

4. DEVELOPMENT AND ANALYSIS OF LESAULTS METHOD

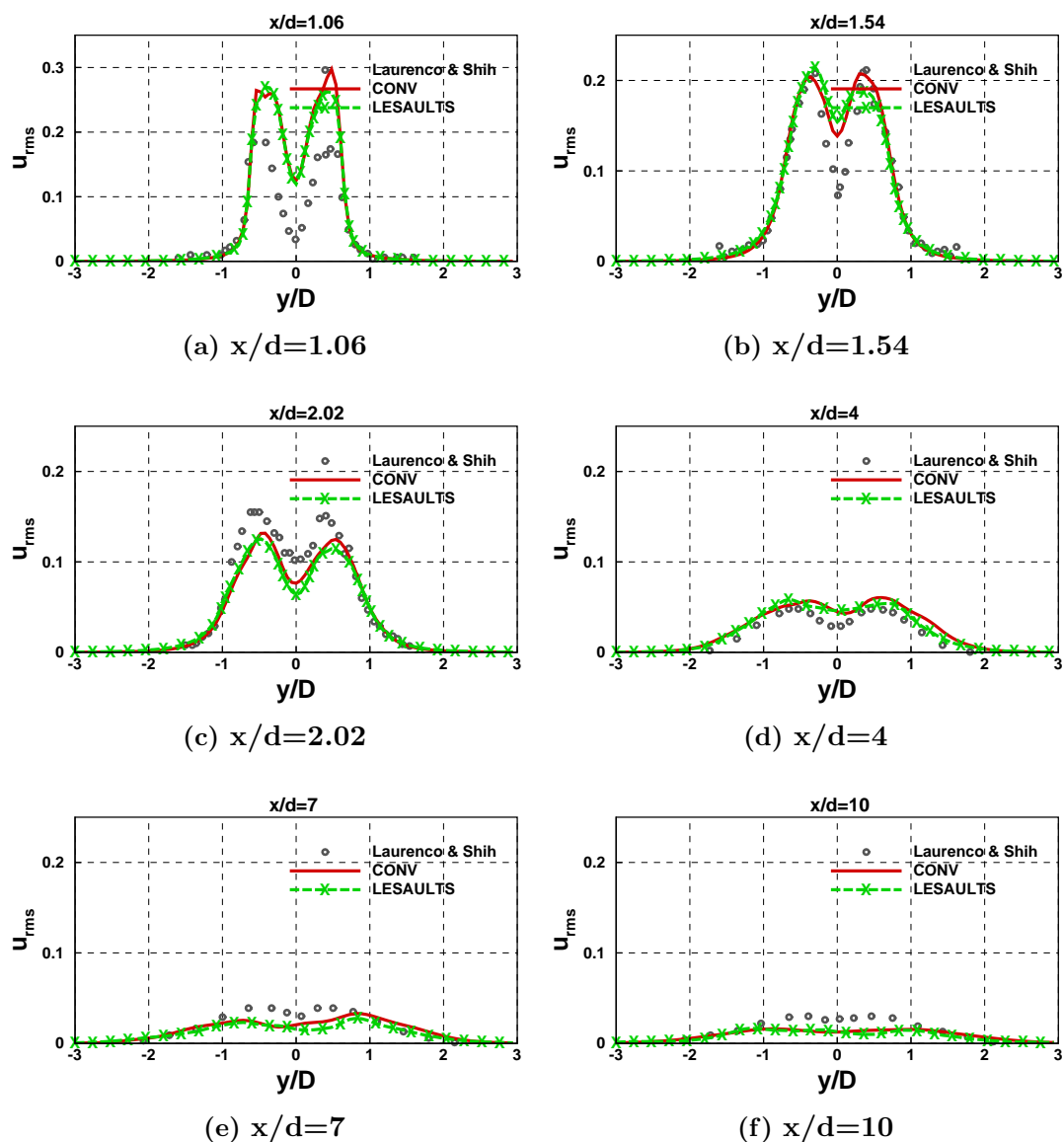


Figure 4.30: Variation of non-dimensional U_{rms} along non-dimensional y -coordinate at longitudinal planes calculated using conventional and LESAULTS method

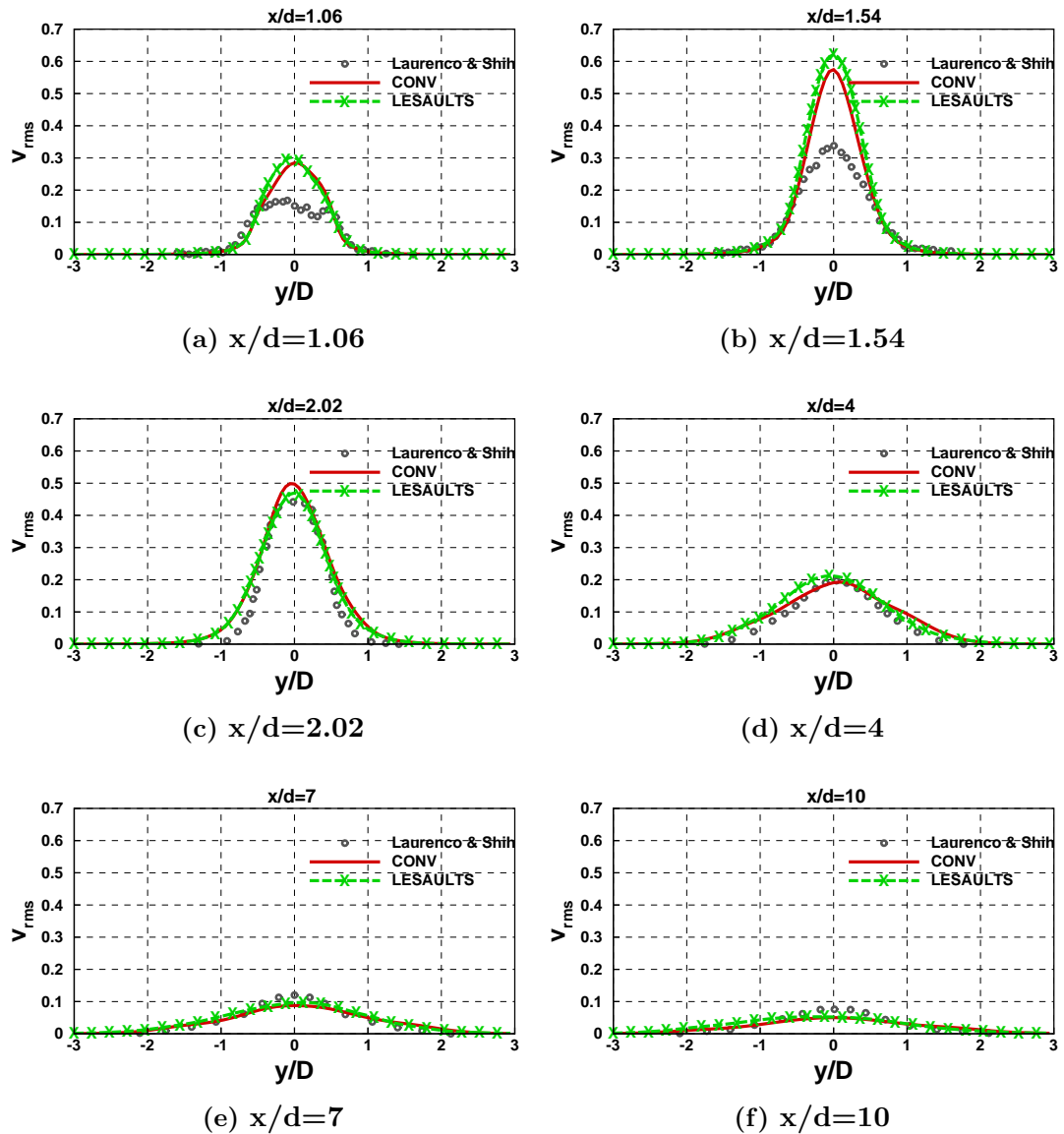


Figure 4.31: Variation of non-dimensional V_{rms} along non-dimensional y -coordinate at longitudinal planes calculated using conventional and LESAULTS method

4. DEVELOPMENT AND ANALYSIS OF LESAULTS METHOD

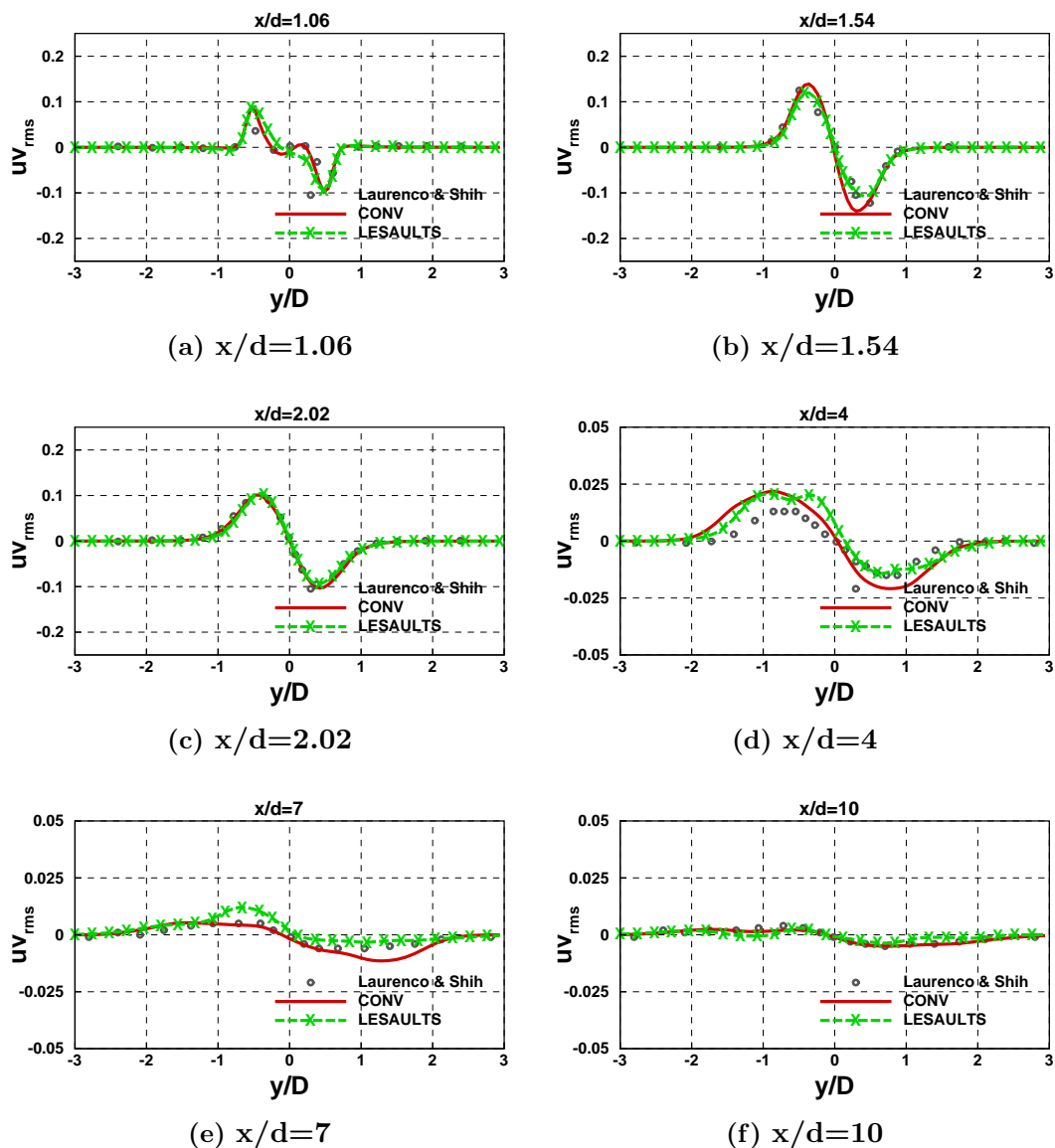
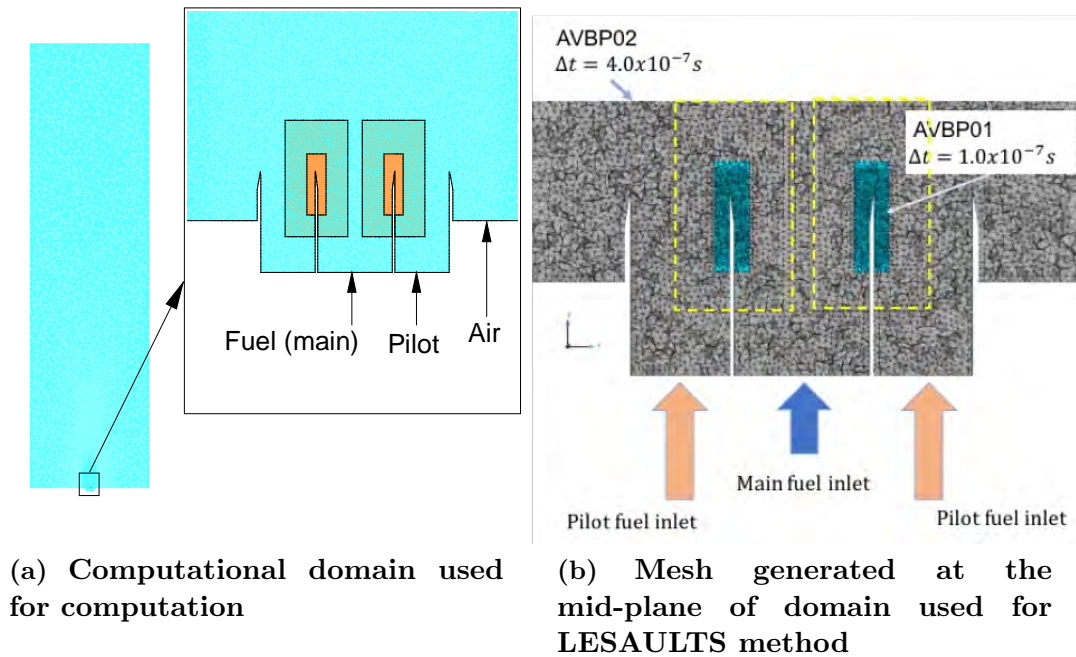


Figure 4.32: Variation of non-dimensional UV_{rms} along non-dimensional y -coordinate at longitudinal planes calculated using conventional and LESAULTS method



(a) Computational domain used for computation

(b) Mesh generated at the mid-plane of domain used for LESAULTS method

Figure 4.33: Computational domain and mesh generated for the Sandia-D flame using LESAULTS method

The domain for studying the flame is shown in Figure 4.33. The experimental set up used in the flame consists of a fuel jet emanating out of a cylindrical pipe with an inner diameter of 7.2mm. The partially premixed fuel consists of 25% methane diluted in air at room temperature. The bulk velocity of the fuel jet is 49.9 m/s. The fuel jet is surrounded by a cylindrical pilot flame produced by the combustion of methane in air at an equivalence ratio of 0.77 and at a temperature of 1880 K. Coflow air at temperature of 298 K and a bulk velocity 0.9 m/s serves as the oxidizer for sustaining combustion. Available experimental measurements include mean and rms values of temperature and radial profiles such as major species such as CH₄, O₂, CO₂, CO and NO.

The computational domain used to perform LES of the Sandia-D flame using conventional LES solver is shown in Figure 4.33(a). A cylinder of length 1.08 m and 0.288 m in diameter is used as the computational domain. The fuel and the pilot inlet boundaries are provided one diameter upstream of the jet orifice. The long domain length is necessary to capture the flame length and the plume accurately. Tetrahedral grid is generated inside the domain. A fine mesh is used to resolve the regions near the jet exit and the rims. From previous studies ([117]), it is observed that very fine mesh is required near the rim region and in regions upstream to the rims. This is required to ensure the flame stabilization mechanism is resolved well. Hence very fine cells are used in this region as shown

4. DEVELOPMENT AND ANALYSIS OF LESAULTS METHOD

in Figure 4.33(b). A cross section of the grid generated is shown in the same figure.

Since it is required to resolve the lip region with very fine cells, the limiting time steps are observed in this region. The large length of the domain (extending to 1.08m) also makes the computations using conventional method costly. Keeping this in mind, for the LESAULTS method, a two sub-domain configuration as shown in Figure 4.33(b) is used. The sub-domain AVBP01 comprises of the fine cells where time steps are small. The rest of the domain is included in sub-domain AVBP02. The overlapped zone between AVBP01 and AVBP02 is marked as enclosed by the yellow dotted lines in the Figure 4.33(b).

It is further emphasized that the same grid is used for the LES solution for both the conventional and LESAULTS method solution procedures. This is done by generating the mesh using a multi-zone computational domain in the grid generation tool CENTAUR. While the sub-domains are retained for the LESAULTS grids, for the conventional solution methodology the multizone grids are united to form a single grid with an exact node-node spatial correspondence with the LESAULTS grid mentioned.

The maximum allowable time step that can be used for the conventional LES solution method is 1.0×10^{-7} sec. For the LESAULTS method the same value of time step is used in sub-domain AVBP01. For AVBP02, a time step of 4.0×10^{-7} sec is used. Hence the $R_{\delta t}$ value for the LESAULTS method is 4. Such a knowledge of the typical time step used in conventional LES solver was available from a previous available study ([117]). This indeed allowed the careful choice of defining the geometry of the overlapped zone. It is ensured that the number of cells in the overlapped zone from one interface boundary normal to the other is 6 (=4+1+1) as mentioned in Section 4.6.

Since the objective of this exercise is to validate the LESAULTS methodology, a simple 2-step mechanism for methane combustion consisting of 6 species ([118]) is used in this study. Transport properties of this mechanism is based on a unit Le number assumption with the gas mixture viscosity calculated using Sutherlands law. The thermodynamic properties of the mixture is calculated using values from the Jannaf tables.

As mentioned previously, considering the lower computational cost, LW scheme is used in both the LES computations. The artificial viscosity model of Colin is used to stabilize the computations by damping inadvertent high frequency errors in computations. The SGS model used is that of Sigma. Turbulent Prandtl and Schmidt numbers are fixed as 0.6 each.

Element type	Scheme	$R_{\delta t,1}$	N_1	N_2	S_{th}	S_{act}	$\eta_{LESAULTS}$
Tetra	LW	4	240738	940311	2.28	2.05	90%

Table 4.6: Theoretical and actual speed up obtained for the LES of 3D flow past a cylinder

The boundary conditions are modeled in the following manner. At the fuel inlet, a turbulent velocity profile with the specified volume flow rate, temperature and species mass fractions are specified. Artificial turbulence injection at the fuel inlet is performed with a turbulent intensity of 2%. To model the pilot flame, adiabatic species composition and temperature corresponding to the equivalence ratio of the pilot flame is specified. The axial inlet velocity is specified as 11.4 m/s. Similarly, axial velocity and temperature of air is enforced at the coflow air inlet boundary. At the outlet, a characteristic based outflow boundary is specified with the target outlet pressure fixed to that of the ambient atmosphere.

LES computations using the conventional and LESAULTS method is carried out on the in-house high performance computing (HPC) machines Nemo. 360 computing cores are used for the conventional LES solution while 202 and 158 (total of 360) cores respectively are used for sub-domains AVBP01 and AVBP02 in the LESAULTS method. The core distribution among AVBP01 and AVBP02 is obtained using equation 4.16 in Section 4.5. LES computations are performed for a total duration of 8 flow through times (FTT) with time averaging performed for the last 5 FTTs to calculate the mean and rms values.

Actual computational speed up

Similar to that reported for the previous test case, the theoretical and actual speed-up values obtained for this exercise are reported in Table 4.6 along with the number of nodes in each sub-domain and the value of $R_{\delta t}$. A very good agreement is obtained between these values indicating the efficiency of the LESAULTS method in achieving speed-up in computations.

Comparison of results obtained using conventional and LESAULTS method

LES of the Sandia-D flame has been performed previously in [119] using very fine mesh and an analytically reduced chemical mechanism. Excellent match between computed and experimental results have been reported. However, the objective of the present exercise is to validate the LESAULTS method with respect to the conventional solver and to prove that a speed-up is achieved using

4. DEVELOPMENT AND ANALYSIS OF LESAULTS METHOD

LESAULTS without incurring any loss to the accuracy of the solution. Hence, a coarse mesh and a global chemical mechanism has been used in this study to keep the overall computational cost of this exercise low. The objective here is not to compare the computed results with experimental dataset which has hitherto been demonstrated in [119] but rather to compare LESAULTS results with that of the conventional solver. Hence, in the results shown in this section, experimental data values are not plotted.

The results obtained using conventional and LESAULTS method are shown in Figures(4.34, 4.35, 4.36). The radial profiles of the time-averaged temperature at three planes downstream of the fuel jet exit are shown in Figure 4.34. The three downstream planes are shown in the Figure correspond to $x/d=1,15$ and 45 . The mean quantities are calculated by a circumferential averaging of the already time averaged quantity. An excellent match is observed between the conventional and LESAULTS results of the mean temperature profiles. The rms temperatures are profiles at these planes are plotted in Figures 4.34 (b),(c) and (d). The rms values also exhibit excellent match between the LESAULTS and conventional methods.

Similar to the temperature plots, profiles of mean mixture fraction and species profiles of CH_4 , CO and CO_2 are also plotted in Figures(4.35 and 4.36). Similar to the observations made about temperature, excellent match is also observed for the mixture fraction and species profiles asserting the LESAULTS method's ability to reproduce turbulent statistical quantities.

4.9 Conclusions and Perspectives

The LESAULTS methods used to accelerate LES computations is described in this section. The theoretical speed up attained is derived and it is noted that the method is suited best for problems where a small number of cells restrict the maximum allowable time step used in explicit solvers. The treatment of solution at the overlapped zone is then described and its optimum length is derived for LW and TTGC schemes. Spectral analysis of this method showed minimal/no appreciable error for low wavenumbers, CFL number and Pe numbers. The method was then validated using 3 test cases- each of them demonstrating the accuracy of the LESAULTS method in capturing the first and second order turbulent statistics of flow.

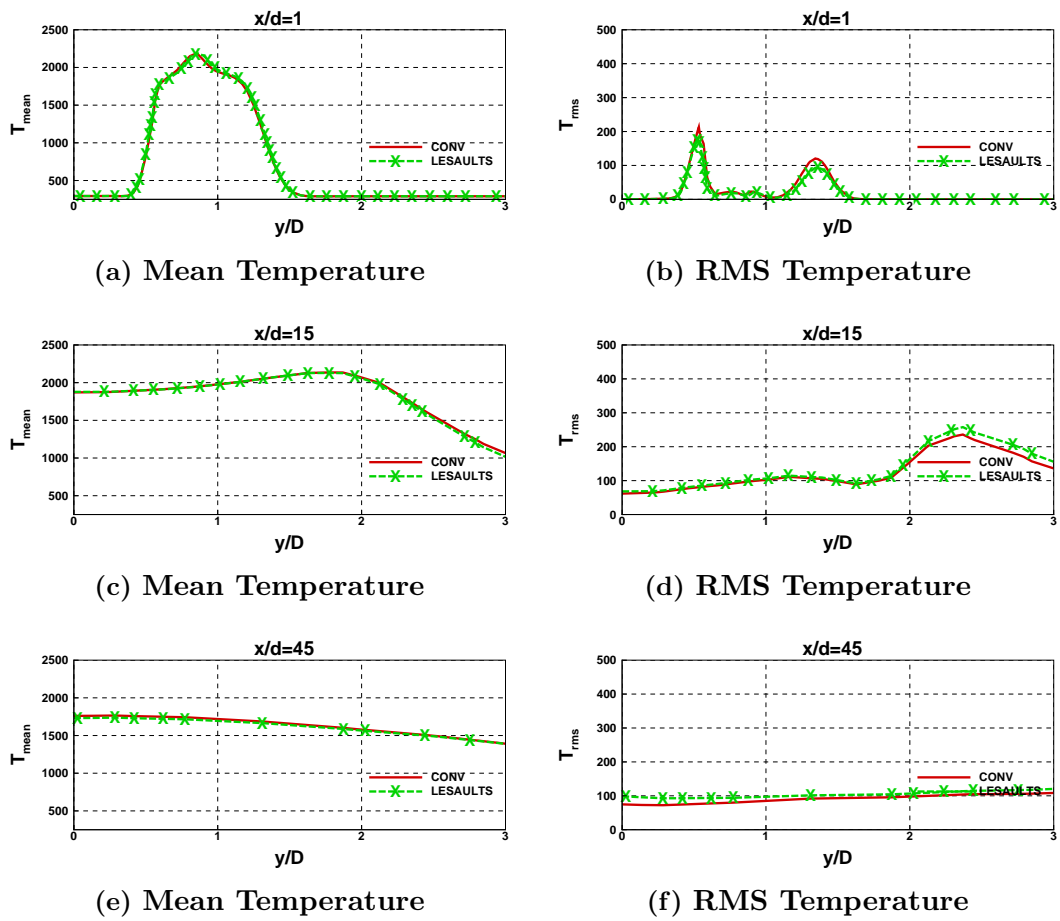
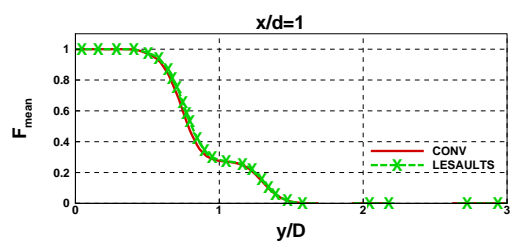
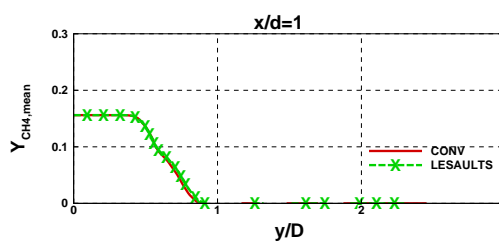


Figure 4.34: Radial profiles of mean and rms temperatures plotted at axial downstream planes

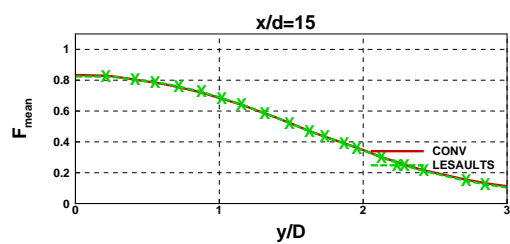
4. DEVELOPMENT AND ANALYSIS OF LESAULTS METHOD



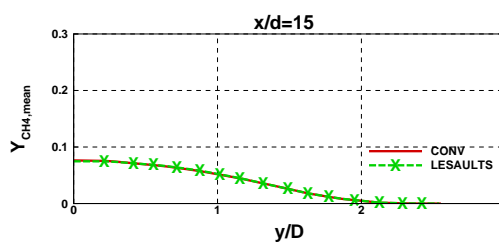
(a) Mean Mixture Fraction



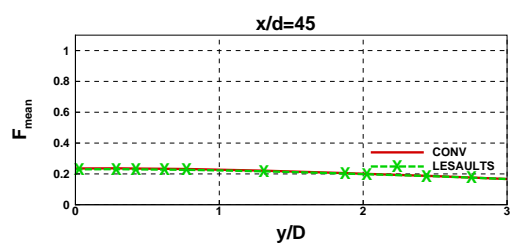
(b) Mean CH4 mass fraction



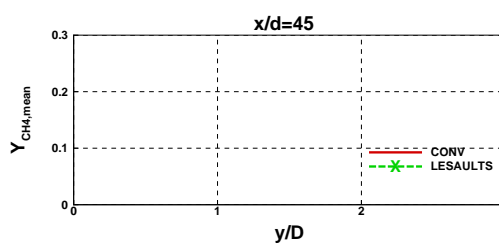
(c) Mean Mixture Fraction



(d) Mean CH4 mass fraction



(e) Mean Mixture Fraction



(f) Mean CH4 mass fraction

Figure 4.35: Radial profiles of mean mixture fraction and CH4 mass fraction plotted at axial downstream planes

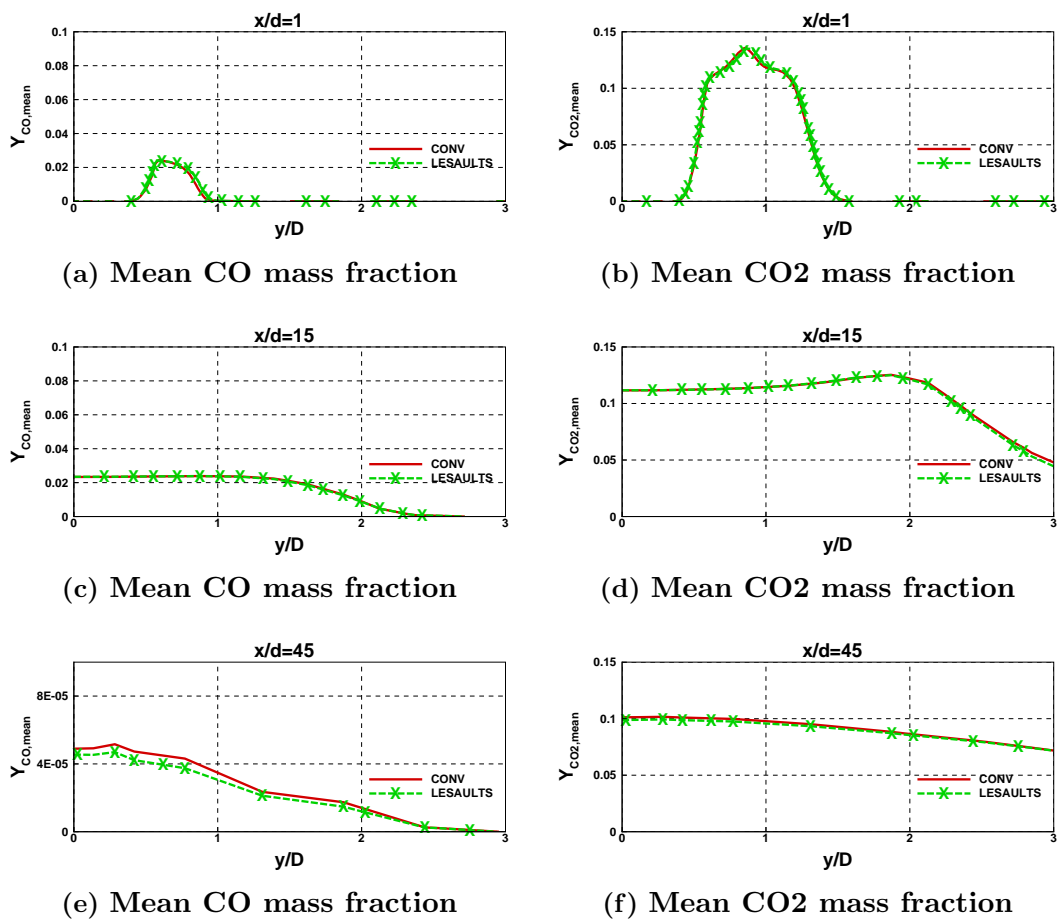


Figure 4.36: Radial profiles of CO and CO₂ mass fraction plotted at axial downstream planes

Part II

**Application to Furnace
Simulation**

In this part of the thesis, the chemical kinetic modeling methodology, radiation heat transfer modeling and the final application of all the sub-models in simulating the reacting flow inside the furnace is detailed.

Accurate prediction of combustion in the furnace implies accurate prediction of the global flame shape, local flame structure and flame characteristics such as heat release, flame speed and species distribution in space and time. This demands a sufficiently detailed chemical kinetic model along with accurate transport and thermodynamical properties. The way this is modeled in this thesis is detailed in Chapter 5.

Radiative heat transfer is the most important mode of heat transfer in furnace applications. The details of the radiative transfer equation solver used in this study is discussed in Chapter 6. The coupling procedure of the radiative solver with the LES solver along with the LESAULTS method requires special attention and is also discussed in the same Chapter. The concept of coupling is demonstrated and validated using a canonical, axi-symmetric, methane-air jet diffusion flame.

The final application of the previously mentioned sub-models in studying the reactive flow in the furnace is detailed in Chapter ,7. This is followed by a section on the overall conclusions and perspectives of this thesis.

Chapter 5

Analytical chemical mechanism reduction

Contents

6.1	Introduction	178
6.2	Literature Survey	179
6.3	PRISSMA RTE Solver	181
6.3.1	Angular discretisation	182
6.3.2	Spatial discretisation	183
6.3.3	Spectral discretisation	184
6.4	LESAULTS-PRISSMA Coupling Strategy	185
6.5	Validation of LESAULTS-PRISSMA Coupled solver	189
6.6	Conclusions	194

5.1 Introduction

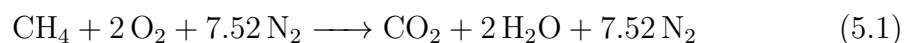
Chemical kinetic modeling in high accuracy flow simulations has always been a battleground between conflicting requirements and demands. Today, accurate reproduction of reactive flow phenomena observed in experiments is possible using DNS and LES when used with detailed chemical mechanisms. However, such simulations are limited to geometrically simple flame configurations. Simulations of reactive flow in engineering configurations are still not possible with detailed chemical mechanisms due to the high computational cost involved. Hence, researchers depend on simplifying assumptions that either reduce the complexity of the detailed mechanism by reducing the number of species and reactions involved or by invoking assumptions that reduce the overall dimensionality of the

chemical system described by the detailed mechanism by projecting it on lower-dimensional manifolds. In this chapter, the approach used to model the chemical kinetics in the LES of the steam cracking furnace is detailed.

This chapter is organized as follows. An introduction to chemical kinetic modeling, the various chemical mechanisms available today that describe lower (C1-C4) hydrocarbon combustion and the various methods to incorporate chemical kinetics in LES solvers are discussed in Section 5.2. In this thesis, the approach taken is that of solving the full set of species transport equations in order to accurately capture finite rate chemistry effects. This necessitates the reduction of the detailed mechanism. The analytical reduction methods are also explained in Section 5.2. This is followed by a comparative study (described in Section 5.4) of the various detailed mechanisms available today and their accuracy in predicting key combustion properties of methane-air flames. The most accurate detailed mechanism based on this study is chosen for analytical mechanism reduction. The details of the analytical reduction process are given in Section 5.5. The validation of the obtained reduced mechanism for 1D and 3D configurations are described in Section 5.6. The chapter ends by listing the conclusions from the above-mentioned exercises.

5.2 Literature survey

The combustion of methane in air can be described globally through a deceptively simple reaction written as,



However, it is well known that in reality, the above global reaction occurs through a number of elementary reactions involving major, minor and intermediate species and radicals. Even for simple alkanes such as methane and ethane, the number of species and reactions involved range in hundreds. For higher hydrocarbons, the number of species and reactions would further increase to a few thousands. The branch of chemical kinetic modeling involves the mathematical description of how a given mixture of species interact with each other through a series of reactions to form final product species at a specific temperature and pressure. This branch is not limited to combustion alone but also in diverse fields such as atmospheric modeling, chemical vapor deposition, petroleum processing and in biochemistry. Central to this branch is the science of modeling the species production and/or consumption rates as functions of temperature, pressure and

5. ANALYTICAL CHEMICAL MECHANISM REDUCTION

composition of the reacting fluid mixture. For simple reactors, this is mathematically expressed through ordinary differential equations the solution of which is often obtained through numerical methods.

A chemical kinetic mechanism forms the basis of kinetic modeling and is essentially a dataset comprising of species, their associated thermodynamic properties (heat of formation, specific heat and entropy as a function of temperature) and transport properties along with a group of elementary, reversible or irreversible reactions describing how the species involved in a reaction interact to produce/consume other species. The rate at which each reaction progresses is given through the law of mass action. The rate constant for the forward chemical reaction is expressed in the Arrhenius form and the same for the reverse reaction is often calculated by invoking the equilibrium assumption. A kinetic mechanism file contains details of the species and the reactions involved along with expressions for calculating the thermodynamic and transport properties. A number of tools for solving canonical 0D and 1D chemical reactors such as Chemkin [120], Cantera [121], Flamemaster [122], Opensmoke [123] and DETCHEM [124] using these kinetic mechanism files are already available and in popular use today.

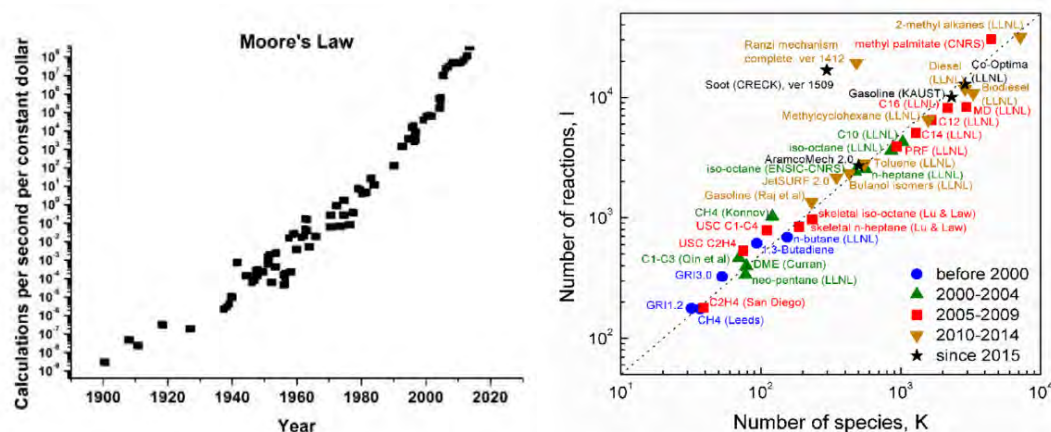
Design of mechanisms used to be a black art, with considerable involvement of intuition and rules of thumb. Some of these aspects have been reviewed by many authors in the past. For example, in [125], the authors review the state of the art in chemical mechanism design related to light hydrocarbon fuels, nitrogen chemistry and soot formation pathways. Computer based design of mechanisms was attempted later as detailed in [126, 127, 128] while the authors in [129] used a solution mapping method to obtain mechanisms based on optimized input parameters. Now a popular method of mechanism design, the authors in [129] describe an optimization and a solution mapping method applied to a large scale dynamic system. The responses of the system to a set of input parameters are expressed through algebraic expressions and are used to obtain a detailed mechanism with an optimized set of input parameters. More recently, Simmie [130] reviews the development of various detailed chemical mechanisms describing lower hydrocarbon fuel combustion along with the experiments used to validate these mechanisms. Theoretical chemistry also has started playing an important role in mechanism development of late. An excellent review of the recent advances made in this field is given in [131].

The early attempts at chemical mechanism design dealt with the modeling of ozone [132] and hydrazine decomposition [133]. This was followed by design of mechanisms describing hydrogen and later for methane [134]. Westbrook and Dryer in their seminal work [135], emphasized the hierarchical development of mechanisms wherein mechanisms involving higher hydrocarbons should contain sub-mechanisms describing lower hydrocarbons and the H₂/O₂ chemical system. This was followed by the work of Warnatz [136] identifying new pathways in methane combustion involving methyl recombination that produce unsaturated compounds such as ethene and ethyne. This work emphasized on the need to consider pathways of methane pyrolysis at high temperature conditions. Methane mechanisms were also developed in parallel by other researchers such as [137, 138, 139, 140], the culmination of which resulted in the various versions of the Gas Research Institute (GRI) mechanisms [141]. The GRI mechanisms gained wide popularity due to their wide range of applicability as well as its free online availability. Similar to the GRI mechanisms, mechanisms were also developed by other research teams such as the San Diego Mechanism [142], University of Southern California (USC) mechanism [143], Jetsurf [144], CRECK [145] and Aramco [146]. A compilation of the species and reactions involved in lower hydrocarbon combustion are reviewed and evaluated in [147, 148, 149, 150, 151, 152] for reference.

Apart from the description of reactions between species and their rate expressions, kinetic modeling also involves formulating and book keeping the thermodynamical properties of the species involved. The NIST webbook which compiles the thermodynamic properties of species from literature is available online [153] and so is the library of thermodynamic properties of ideal gas and condensed phase materials by Burcat and Goos [154]. The ATCT tables [155] records the most latest and accurate data on the heat of formation of species.

Over the last couple of decades, chemical kinetic mechanisms used to describe combustion have grown both in their complexity and in the number of species and reactions describing them. Westbrook et al., in their article [156] compared Moore's law that predicted the doubling of computing power every 18 months with the increase in the number of species (due to increase in computing power) involved in mechanisms which were later illustrated in [157]. Figure 5.1 (a) shows the increase in computing power over the last century. The increase in mechanism size (in terms of the number of species and reactions) can be seen in Figure 5.1 (b).

5. ANALYTICAL CHEMICAL MECHANISM REDUCTION



(a) Increase in computing power in the last century ([156])

(b) Number of species and reactions in recent detailed chemical mechanisms ([157])

Figure 5.1: Increase in computing power (a) and chemical mechanism size (b) in the past decades

The incorporation of chemical kinetic mechanisms in high accuracy CFD (such as LES and DNS) codes involve multiple challenges. Firstly, the number of species necessary to describe combustion occurring in a system can range from a dozen to a couple of hundreds depending upon the hydrocarbon fuel used. In order to resolve every, fine detail of the chemical dynamics of the system one needs to solve one transport equation for each species present in the mixture. This would necessitate the solution of more than 50 transport equations even for a simple fuel such as methane, at each point in the numerical grid and at each time instant. This places a huge burden on the computational cost for simulations. Although DNS of simplified geometries are possible using this approach, its applicability to engineering flow problems is still impractical. The second challenge arises due to the non-linearity and the large fluctuations of flow variables in turbulent flows. Fluctuations to the order of 25% in species mass fractions and hundreds of Kelvins in temperature are not uncommon in turbulent reactive flows. In the Arrhenius form of the chemical rate expressions, the species production/consumption rates are highly non-linear functions of species concentrations and temperature. This non-linear behavior when coupled with the high turbulent fluctuations pose challenges in the way source terms are to be treated in CFD solvers. The third and final challenge is associated with the multiple spatial and temporal scales associated with reactive flows. Turbulence and chemistry impose very small spatial and temporal scales in the flow which need to be resolved for accurate computations. The disparities in spatial and temporal scales imposed

by turbulence and chemistry can augment the stiffness associated in solving NS equations numerically.

To tackle the before mentioned challenges associated with chemistry and its interaction with turbulent flow, many approaches are devised. One of the oldest and computationally cheaper approach is to use a global mechanism describing the combustion of fuel with oxidizer [158]. The global mechanisms are derived from skeletal mechanisms by invoking the quasi-steady state (QSS) and partial equilibrium assumptions (PEA) assumptions. The rate constants for the reactions in these mechanism are 'tuned' to match well with experimental data on key flame quantities of interest such as the flame speed and the flame temperature. These mechanisms typically consist of 5-6 species and 2-4 reactions thereby making the solution of the species transport equations computationally amenable. However, it goes without saying that no reliable information on chemical phenomena such as ignition, quenching or emission production can be obtained using this method.

A second method in use today is the tabulated chemistry approach. Tabulated chemistry is often associated with the flamelet assumption where the turbulent flame brush is assumed to be comprising of a number of local laminar flame elements called flamelets. The high dimensionality of the chemical mechanism is reduced by assuming that the species composition falls into a very low dimensional manifold in the species composition space. The Intrinsic Low-Dimensional Manifold (ILDM) method developed by Pope and Maas [159, 160] is such a tabulated chemistry approach. This method relies on the fact that a system consisting of multiple species starts approaching a common trajectory in the species space after a particular time even when the system is started from different initial conditions. Hence, the trajectory that the system traces in the species space can be described with the help of a few variables such as the progress variable or mixture fraction thereby reducing the overall dimension of the problem in hand. Transport equations for progress variable (and/or mixture fraction) are solved and the thermochemical values at each point in the domain is obtained from precomputed tabulated values obtained from simulations of simple reactors and flames. The method works well for high temperature, near-equilibrium combustion applications. However, its applicability to low-temperature applications such as in ignition or quenching is not encouraging. Oijen and Goey [161] modified the ILDM approach to include low temperature effects by combining the flamelet and the manifold approaches. A similar approach was also developed independently by Gicquel [162] by developing manifolds from laminar one-dimensional

5. ANALYTICAL CHEMICAL MECHANISM REDUCTION

premixed flames. Yet another improved tabulated chemistry approach (ISAT) by Yang and Pope [163, 164] works on calculating these chemical tables on the fly as the simulation progresses and computing the flame structure using these tables.

The third and final approach of incorporating chemical kinetics in CFD simulations is to use the species transport framework in conjunction with analytically reduced chemistry. Over the last couple of decades, the computational capability available for CFD computations have increased dramatically, making the solution of species transport equations for reduced chemical mechanisms computationally amenable. This approach, although costlier than the tabulated chemistry methods, enjoys the advantages arising from the absence of restrictive assumptions mentioned previously. The use of this approach has been detailed and validated in [165, 166, 167]. Central to this approach is the derivation of the reduced mechanism analytically from a detailed mechanism.

Many methods are available today to reduce detailed mechanisms by selectively eliminating species and reactions which are not relevant to the current study and are briefly described as follows.

Sensitivity analysis

Sensitivity analysis is a prominent chemical reduction method and works by investigating the differences in the response of a system when known perturbations are provided to one or more of its inputs. This method helps in identifying the set of input parameters that play a dominant role in determining output variability. Using this information, species and reactions which are found not to affect key combustion properties can be eliminated from the detailed mechanism. Different methods of calculating chemical sensitivities exist. Sensitivity can be calculated either locally by studying the solution variation at a particular point in space or time or globally by studying the effects of input variation on key global flame parameters in the whole computational domain. Sensitivity can also be calculated for either a single output parameter or for a group of output parameters. The most common sensitivities studied are the local concentration sensitivity, local rate of production sensitivity and the jacobian sensitivity. A review on sensitivity analysis methods can be seen in [168, 169, 170, 171].

Principal Component Analysis (PCA)

PCA [172, 173, 174] makes use of sensitivity analysis and is often employed in the chemical reduction process. The method relies on defining an objective response

function depending on the species concentration sensitivity matrix. This function when expanded using the Taylor series and approximated to first-order terms gives rise to expressions involving species concentrations and reaction coefficients only. The eigenvalues of this function then give the change in the response function due to changes in the principal component. Hence, by defining a cut-off value for the eigenvalue, the reaction space can be divided into an influential and a non-influential part. The non-influential part does not affect the solution appreciably and hence can be removed from the mechanism hence reducing it.

Chemical lumping

Another technique for species reduction is through chemical lumping. In this method, a group of species is 'lumped' and considered as a single pseudo species which is kinetically equivalent to the original mechanism. The effect of the other species concentration on the lumped species kinetics is specifically modeled and the lumped species concentration is treated as a linear combination of the original species. This method is in general used to lump isomers as described in [175, 176].

Directed Relational Graph (DRG)

DRG is a graph-based method used in mechanism reduction. Here, each species of the detailed mechanism is considered a node in a graph and the arrow pointing from a species A to another species B is a measure of the contribution of species A in the formation of species B as shown by the schematic in Figure 5.2.

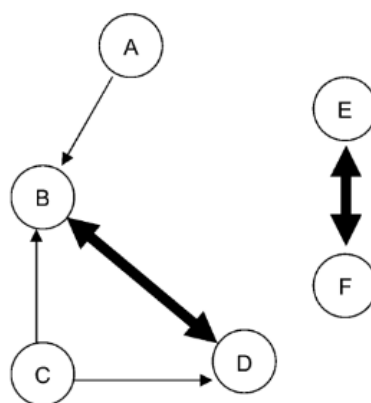


Figure 5.2: Schematic of DRG applied to species in a chemical mechanism

Using this graph, starting from species A, one can identify all the paths that lead to the formation of species B. By eliminating the reactions and species in the weakest paths that contribute minimally to the formation of species B the

5. ANALYTICAL CHEMICAL MECHANISM REDUCTION

mechanism can be reduced. Several expressions for evaluating the DRG can be found in the literature. Lu & Law used the following expression for defining the DRG,

$$r_{AB} = \frac{\sum_{0 < j < m} |\nu_{A,j} Q_j \delta_B^j|}{\sum_{0 < j < m} |\nu_{A,j} Q_j|} \quad (5.2)$$

Here, $\nu_{A,j}$ is the stoichiometric coefficient of species A in reaction j and the summation runs over all the reactions. Further modifications to this expression have been suggested by other researchers and the details of such modifications are presented in Section 5.5.

Quasi Steady State Assumption (QSSA)

The QSS assumption [177] is a method to identify species based on the time scales of their formation. This method is used to identify species that have a net rate of production close to zero. Invoking this assumption helps one to express the concentrations of such species in terms of algebraic expressions involving other species concentrations. Computationally, QSS species identification is carried out using either computational singular perturbation or using Level of Importance (LoI) methods.

Partial Equilibrium Assumption (PEA)

PEA method works similar to the QSSA and has been used to reduce skeletal mechanisms. By identifying and invoking partial equilibrium on reactions, the concentration of certain species can be expressed as algebraic relation involving other species concentrations thereby avoiding the solution of such species through transport equations.

5.3 Objectives of this chapter

The objectives of this chapter are listed as follows.

- (O.1) To compare various chemical mechanisms available today describing C1-C4 combustion and to down select the best mechanism describing natural gas combustion to be later used in the LES of the steam cracking furnace
- (O.2) To perform the analytical reduction of the detailed mechanism chosen from (O.1).
- (O.3) To validate the reduced mechanism obtained from (O.2) with the original detailed mechanism applied to 0D, 1D and 3D flame configurations

5.4 A comparison of methane-air combustion mechanisms

A brief discussion on the detailed mechanisms available today that describe C1-C4 hydrocarbon combustion has been provided in the introduction of this chapter. In this section, a comparison of four of the most popular mechanisms available today is made with experimentally available measurement data. The four mechanisms chosen for this comparative study are:

- Gas Research Institute GRI2.11 mechanism
- Gas Research Institute GRI3.0 mechanism
- CRECK mechanism (hereafter called as POLIMI mechanism)
- University of California San-Diego (hereafter called UCSD mechanism)

The number of species and reactions in the above mechanisms are listed in Table 5.1.

Mechanism	No. of species	No. of reactions
GRI 2.11	49	279
GRI 3.0	53	325
POLIMI	151	2357
UCSD	68	310

Table 5.1: The detailed mechanisms used in this comparative study and the number of species and reactions in them

The objective of this study is to compare the accuracy of these mechanisms in predicting the key global flame properties in simplified flame configurations. The 1D unstretched, freely propagating premixed (1DUP) flame, 1D counter-flow diffusion (1DCD) flame and the ignition delay time in iso-choric reaction experiments are the target flame configurations used for the comparison. The details of these studies are elucidated in the following sections.

Validation using 1D unstretched, freely propagating, premixed (1DUP) flame

The unstretched, laminar flame speed (S_L) is an important property of a fuel/oxidizer mixture and has been a subject of wide study for decades. Specifically for the methane- air mixture, a lot of experimental measurements have been performed in the past ([178, 179, 180, 181]) using techniques such as the bunsen burner

5. ANALYTICAL CHEMICAL MECHANISM REDUCTION

method, the heat flux method and the spherical flame method. To assess and compare the above mentioned detailed mechanisms, numerical computations of the freely propagating, unstretched, 1D premixed flames in methane-air mixtures are performed using the chemical analysis tool CANTERA [121]. The equivalence ratios in the computations are varied from 0.6 to 1.6. The temperature and pressure of the premixed unburnt methane-air mixture is fixed at 298 K and 1 Atmosphere respectively for comparison with available experimental data. The computations are performed on a 1D domain of length 2 cm. CANTERA solves the steady-state, 1D N-S and species transport equations on an adaptive grid to obtain the steady solution within user specified absolute and relative tolerance values. The thermal properties of the species are expressed as functions of temperature using NASA polynomials and are specified in the mechanism file and the thermal properties of the mixture are calculated using the mixing rule. Mixture averaged transport properties (viscosity, diffusion coefficients and heat conduction coefficients) are used for the simulations, with Soret and Dufour effects neglected. Figure 5.3(a) shows the computed and measured (in symbols) flame speed values as a function of equivalence ratio ϕ . It is observed that all four mechanisms predict the laminar flame speeds pretty accurately. All three mechanisms, namely GRI2.11, GRI3 and UCSD predict the same flame speed at lean conditions while POLIMI predicts relatively lower values. At stoichiometry GRI2.11 and GRI3.0 mechanisms are observed to over predict the experimental flame speed values while POLIMI mechanism predicts it fairly accurately. Under rich conditions, POLIMI slightly overpredicts computed flame speed while GRI mechanisms predict it well. In general, UCSD mechanism tends to underpredict flame speed values in stoichiometric and rich conditions. The maximum flame speed computed using POLIMI mechanism is observed to be on the slightly higher side when compared to the other mechanisms. It is to be stressed that all the four mechanisms predict flame speed well within the limits of uncertainties in measurements and this exercise in itself is inconclusive to down select a single mechanism for reduction.

Validation using ignition delay times (IDT)

Ignition delay time is another key characteristic of a fuel-oxidizer mixture and is used in studies to validate chemical mechanisms. In this study, the ignition delay time of methane-air mixture at three different equivalence ratios ($\phi = 0.5, 1, 2$) and at atmospheric pressure is calculated using all the above four mechanisms. The experimental data from shock tube measurements at these specified conditions are available for validation in [182]. The numerical ignition delay times

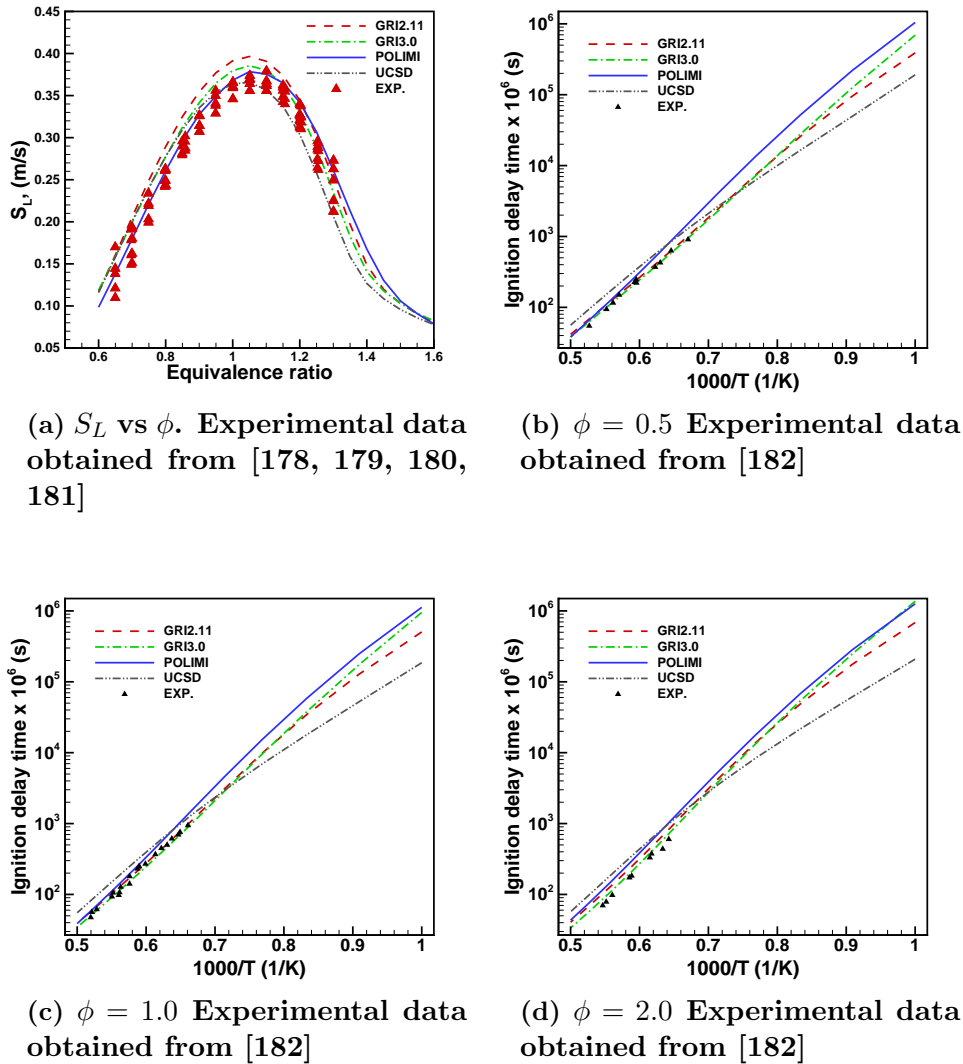
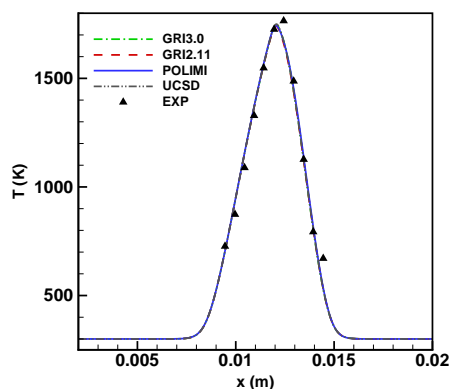


Figure 5.3: Computed and measured values of (a) laminar flame speed (S_L) at various equivalence ratios (ϕ) (b,c,d) Ignition delay time for three different equivalence ratios

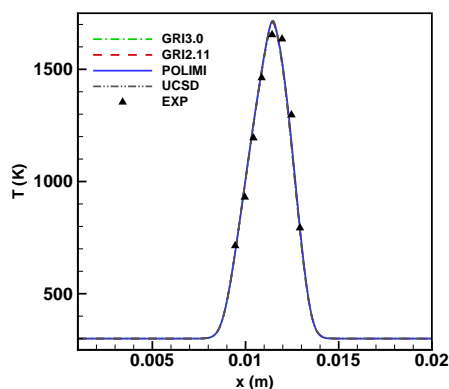
are calculated using CANTERA. The ignition delay time is calculated based on the time when OH species concentration is found to be at its peak. They are calculated for a series of temperature values of the mixture ranging from 1000 K to 2000 K. The results of the computations are shown along with the experimentally measured values (shown as symbols) for $\phi = 0.5, 1, 2$ in Figure 5.3. The ignition delay time predicted using GRI mechanisms and POLIMI are close to each other for all temperatures, whereas the UCSD mechanism predicts lower ignition delay time for temperatures less than 1500 K. Ignition delay times are predicted very accurately with the GRI mechanisms while reasonably good predictions are obtained with POLIMI for all the equivalence ratio considered. The

5. ANALYTICAL CHEMICAL MECHANISM REDUCTION

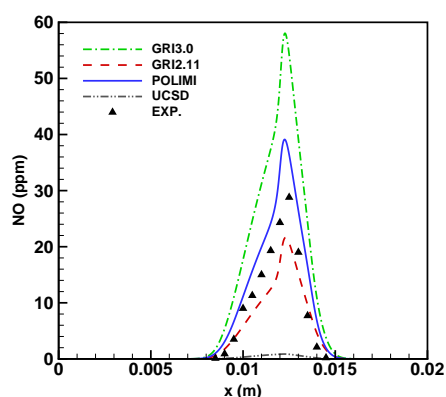
UCSD mechanism computes slightly higher ignition delay times at higher temperature and lower ignition delay times at lower temperatures when compared to measurements and the other three mechanisms.



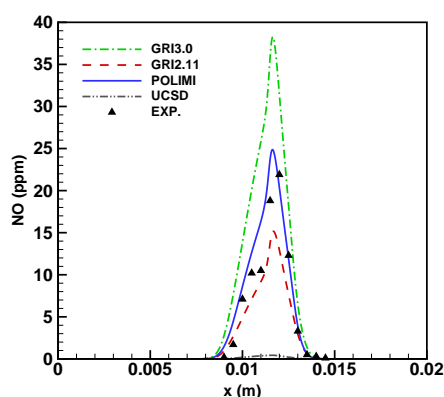
(a) Temperature for strain rate=20s. Experimental data obtained from [183]



(b) Temperature for strain rate=35s. Experimental data obtained from [183]



(c) NO for strain rate=20s. Experimental data obtained from [183]



(d) NO for strain rate=35s. Experimental data obtained from [183]

Figure 5.4: Computed and measured (a,b) temperature profiles for strain rates of 20,35 respectively (c,d) NO profiles for strain rates of 20,35 respectively

Validation using counter-flow diffusion (1DCD) flames

The mechanisms are now compared with measured data for the 1D counter-flow diffusion flame. For this purpose, the experimental dataset obtained using Laser Induced Florescence (LIF) in [183] is used. The fuel stream consists of 25% of CH_4 and 75% N_2 . Air is used as the oxidizer. Counter-flow flames are generated

5.4 A comparison of methane-air combustion mechanisms

for two values of strain rates (20 and 35 sec^{-1} respectively). The experimental measurement consists of the axial (centerline) profiles of temperature and NO mole fraction. Like the previous examples, the counter-flow diffusion flame computations are performed again using the tool CANTERA. The fuel and oxidizer composition at the respective inlets are enforced to the experimentally used values and the mass flow rates are chosen such that the above mentioned strain rates are attained. The results of the computations are shown in Figure 5.4. Figure 5.4 (a) and (b) shows the measured and computed axial temperature profiles for the two strain rates computed. All the mechanisms predict exactly the same temperature profiles. The computed and the measured temperature profiles are also in excellent agreement with each other. Figure 5.4 (c) and (d) show the computed and measured NO mole fraction along the flame axis. Discrepancies in the computed NO mole fraction profiles are observed between all the four mechanisms. The UCSD predictions are found to be considerably lower and inaccurate. The GRI 3.0 mechanism overpredicts NO for both the strain rates computed. This trend is anticipated and is a known deficiency with the GRI mechanisms due to their inclusion of HCN sub-mechanism [119] instead of the now well understood NCN pathway [184]. POLIMI mechanism on the other hand, includes the NCN pathway in the prompt NO mechanism and hence a better agreement with experimental values is observed.

From the previously mentioned exercises, the following conclusions can be made. Firstly, for the 1D premixed flame, all the four mechanisms compute the laminar flame speed fairly accurately. UCSD mechanism predicts lower flame speed in general while POLIMI and GRI mechanisms predict them better. Secondly, ignition delay times are predicted accurately by the GRI mechanisms while good agreement is obtained with POLIMI mechanism. UCSD mechanism predictions are observed to be slightly higher at higher temperatures. Finally, in the case of NO emission prediction in counter-flow diffusion flames, the NCN pathway of prompt mechanism which are not included in the other three mechanisms and thereby predicts NO formation much better when compared to the other mechanisms.

Considering the above conclusions, POLIMI mechanism is down selected for analytical reduction before being used in the LES simulation. This addresses objective (O.1) mentioned in Section 5.3. The aspects of analytical reduction of the POLIMI mechanism is explained in the following section.

5.5 Chemical mechanism reduction using AR-CANE

Analytical reduction of POLIMI mechanism is carried out using the tool AR-CANE [185]. Reduction in AR-CANE is carried out using the following three steps.

- Species and reaction reduction using DRGEP
- Species reduction using chemical lumping
- Species reduction using Quasi-Steady State (QSS) Assumption

The above methods are applied on the detailed mechanism in a sequential manner. For identifying and retaining only the important species and reactions, a set of global target flame quantities and reactor configurations need to be defined first. In this study, two sets of target flames are chosen.

The first target reactor is the freely propagating premixed flame while the second reactor is the iso-choric reactor. For the first reactor, the target flame quantities defined are the laminar flame speed and the exit values of mass fractions for major (CH_4 , CO_2 , CO , H_2O) and minor (NO , N_2O , NH_3 , NCN , HCN , N) species. The reduction error, defined as the difference between the target flame quantity obtained using the reduced mechanism and the detailed mechanism, is fixed at 5% for the laminar flame speed and major species mass fractions and 10% for the minor species mass fractions. Three operating points were decided for carrying out the premixed flame calculations corresponding to equivalence ratios of 0.7, 1.0 and 1.4 respectively. The temperature and pressure of the premixed gas is fixed at 298 K and 1 Atmosphere respectively.

For the second target reactor a 0D iso-choric reactor is chosen, the target flame quantity chosen is the ignition delay time. Target reactor computations are performed at the same equivalence ratio used in the premixed flame calculations namely, 0.7, 1.0 and 1.4. Similar to the premixed flame target reactor, the reduction error for the second reactor configuration is defined on ignition delay time. The cut-off value of this error is fixed at 50%.

5.5.1 DRG with error propagation (DRGEP)

The expression used for identifying and removing irrelevant species in DRG method is already mentioned in Eq. 5.2. However, this expression does not take into account species which contribute equally to the production and consumption

of a specified species. Hence a modification to Eq. 5.2 is suggested as for defining the DRG parameter between species A and B as,

$$r_{AB}^* = \frac{\left| \sum_{0 < j < m} \nu_{A,j} Q_j \delta_B^j \right|}{\max(P_A, C_A)} \quad (5.3)$$

where P_A and C_A are the production and consumption of species A. This modified expression now takes into effect the species which get consumed quickly in reactions. However, a deficiency of this expression is that it does not consider the indirect paths of formation of species B from species A. To take into account the effect of direct and indirect path through which species A contributes to species B, the following modified expression (DRGEP) is used,

$$r_{AB,p} = \min_{1 < i < n-1} r_{S_i S_{i+1}}^* \quad (5.4)$$

Here S_1 denotes species A, S_n denotes species B and S_i denotes all the intermediate species in the path taken to reach species B from A. The global DRG coefficient is then taken as the maximum of all the coefficients obtained for the various paths computed.

When the above DRGEP step is executed on the POLIMI mechanism, 109 species are discarded resulting in a skeletal mechanism consisting of 42 species and 335 reactions.

5.5.2 Chemical lumping

For the POLIMI mechanism, no species are identified as suitable candidates for chemical lumping.

5.5.3 QSS Assumption

Using the QSS assumption, the number of species are further reduced to 23 and the number of reactions to 295. The final reduced mechanism hence consists of 23 transported species and 19 QSS species with 295 reactions.

The various stages in the reduction process of POLIMI is summarized as a schematic in Figure 5.5.

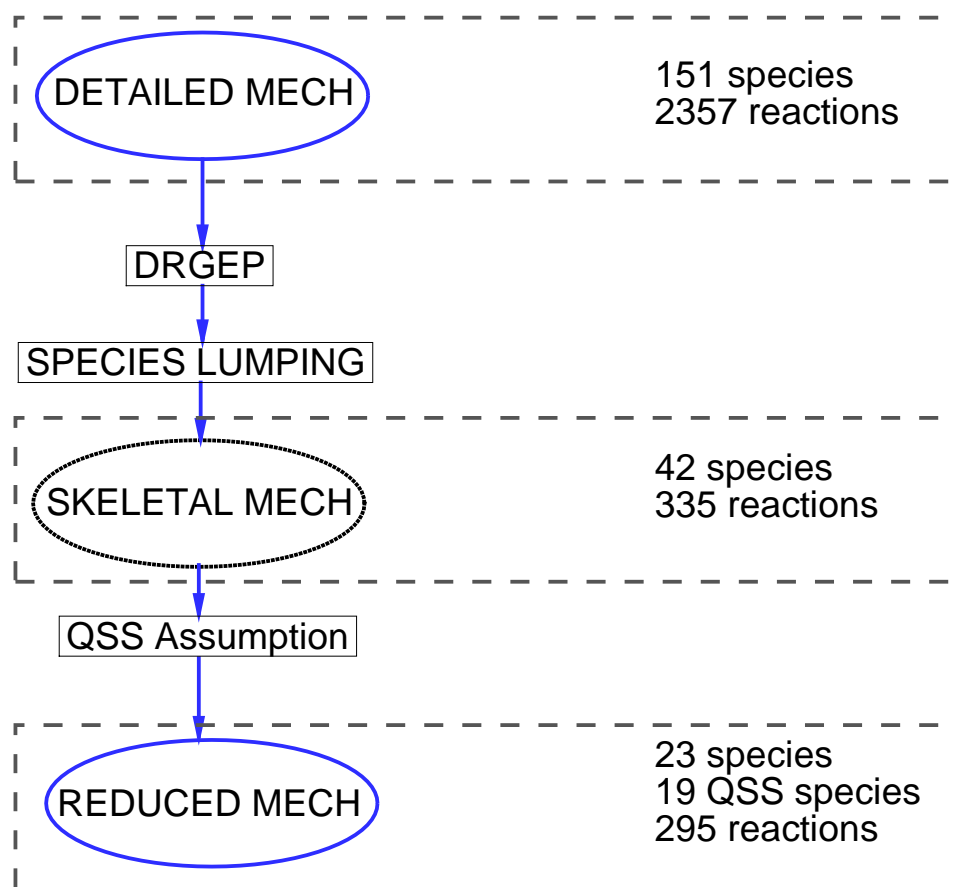


Figure 5.5: A schematic of the chemical mechanism reduction process applied to POLIMI mechanism used in this study

5.5.4 Thermal and Transport properties

The reduction process used in ARCANE detailed above does not alter the thermal properties (specific heat, heats of formation and entropy) of species and the mixture. Hence the thermal properties of the reduced mechanism remain the same as that of the detailed POLIMI mechanism.

The reduced mechanism is derived to be ultimately used in the LES solver AVBP. Since AVBP uses constant Schmidt (for each species) and Prandtl (for the mixture) numbers, the modeling of transport properties during reduction needs special attention. To derive the transport properties of the reduced mechanism, 1D laminar flame computations are performed for equivalence ratios ranging from 0.6 to 1.6 and an optimization procedure is executed to arrive at the Schmidt number of each species and Prandtl number of mixture that yield the most accurate results for the equivalence ratios considered.

At the end of this optimization process, a power law for viscosity for the gas

mixture is suggested. The reference temperature and the viscosity coefficients obtained from the procedure are respectively 1666.7 K and 0.6459. The transported species and their Schmidt numbers are provided in Appendix A.

This completes the description of the analytical mechanism reduction process and objective (O.2) is thereby addressed.

5.6 Validation of reduced mechanism

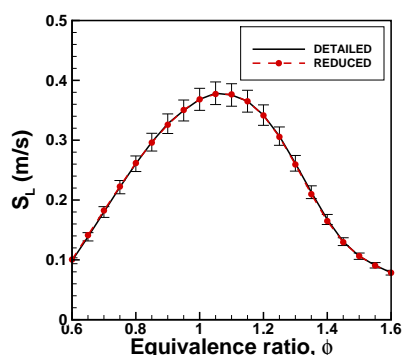
Once the POLIMI mechanism is reduced analytically, validation of the reduced mechanism so obtained is carried out. For this purpose, 0D and 1D reactor computations are carried out using CANTERA. Since the POLIMI mechanism has already been compared and validated with experimental data in Section 5.4, in this section the reduced mechanism is compared with the detailed mechanism only and not with measurement data. The objective is to ensure that the reduced mechanism is able to reproduce both local as well as global flame properties of the detailed mechanism to the best extent possible.

5.6.1 Validation using 1DUP flames

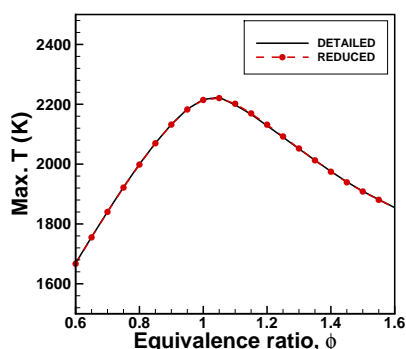
1D unstretched, laminar premixed flame computations are performed using CANTERA for both the detailed and the reduced mechanisms with methane-air as the fuel-air mixture. The transport properties of the reduced mechanism are that mentioned in the previous section with constant Schmidt and Prandtl numbers enforced. Simulations are carried out for equivalence ratios ranging from 0.6 to 1.6. The temperature and pressure of the premixed methane-air mixture is set at 298 K and 1 Atmosphere respectively.

To better analyze and compare the results, both global and local solutions are looked at. The results of global flame properties obtained from the computations are shown in Figure 5.6. The laminar flame speeds at various equivalence ratios computed using the detailed POLIMI mechanism and the reduced mechanism are shown in Figure 5.6(a). Excellent agreement is observed between both the mechanisms across all the equivalence ratios computed. The peak temperature in the laminar flame as a function of equivalence ratio is shown in Figure 5.6(b). The maximum difference in the peak temperature is observed to be less than 5K across all ϕ values. Similarly, the spatially integrated production rates of CO, CO₂, H₂O and NO for various equivalence ratios are shown in Figures 5.6(c,d,e and f) respectively. The reduced mechanism predicts the CO and NO production rates within 10% deviation from the detailed mechanism. The production rates of H₂O and CO₂ also show similar agreement with the detailed mechanism.

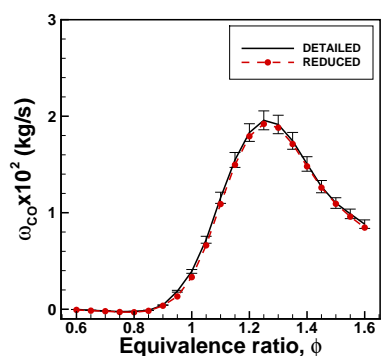
5. ANALYTICAL CHEMICAL MECHANISM REDUCTION



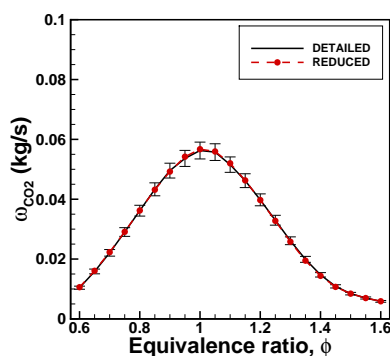
(a) S_L vs ϕ . Error bars correspond to $\pm 5\%$



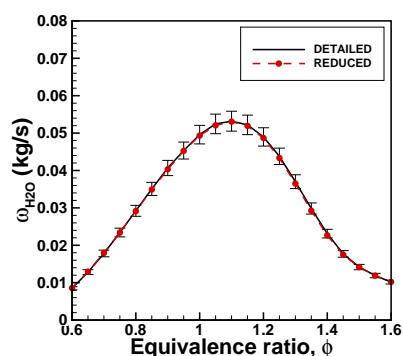
(b) T_{max} vs ϕ . Error bars correspond to $\pm 5K$



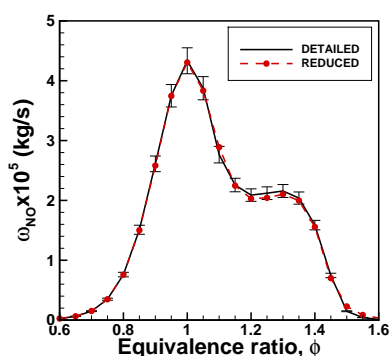
(c) CO vs ϕ . Error bars correspond to $\pm 10\%$



(d) CO_2 vs ϕ . Error bars correspond to $\pm 10\%$



(e) H_2O vs ϕ . Error bars correspond to $\pm 10\%$



(f) NO vs ϕ . Error bars correspond to $\pm 10\%$

Figure 5.6: Global properties of 1D laminar unstretched premixed flame computed using detailed and reduced mechanism for various values of ϕ . Error bars are plotted with respect to detailed mechanism

The spatial profiles of temperature and species mass fractions in the 1D premixed flames computed at equivalence ratios, $\phi = 0.6, 1, 1.4$ are shown in Fig-

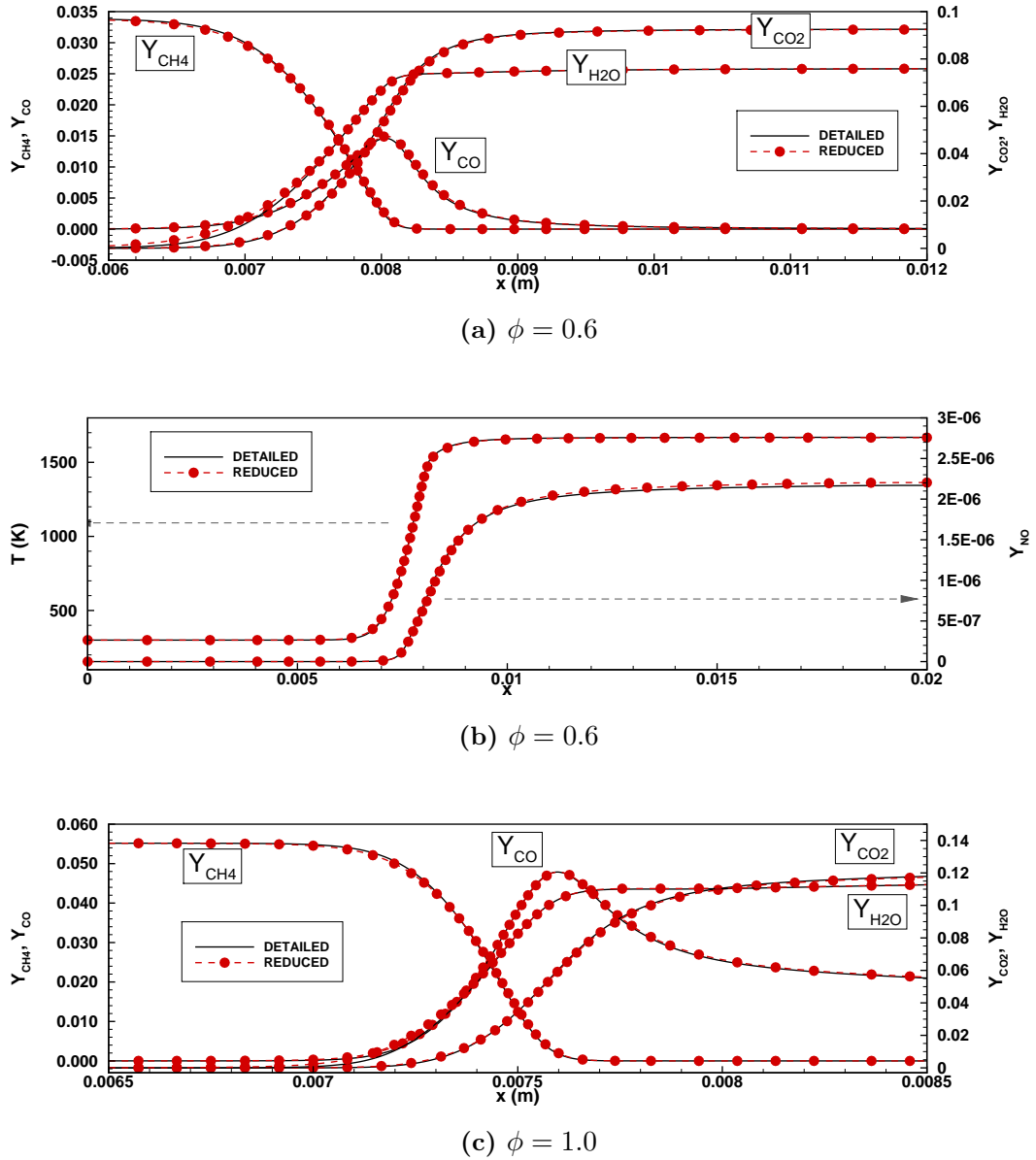


Figure 5.7: Spatial profiles of species and temperature in an 1D, un-stretched laminar premixed flame computed using detailed and reduced POLIMI mechanism

ures 5.7 and 5.8. An excellent agreement in the spatial variation of these quantities is observed between both the mechanisms.

5.6.2 Validation using IDT

0D iso-choric reactor is used to evaluate the ignition delay time computations of CH_4 -Air mixture using the detailed and reduced mechanism. Computations are performed using CANTERA for three values of equivalence ratios ($\phi = 0.7, 1, 1.4$) and at Atmospheric pressure. The results of the computations are shown in

5. ANALYTICAL CHEMICAL MECHANISM REDUCTION

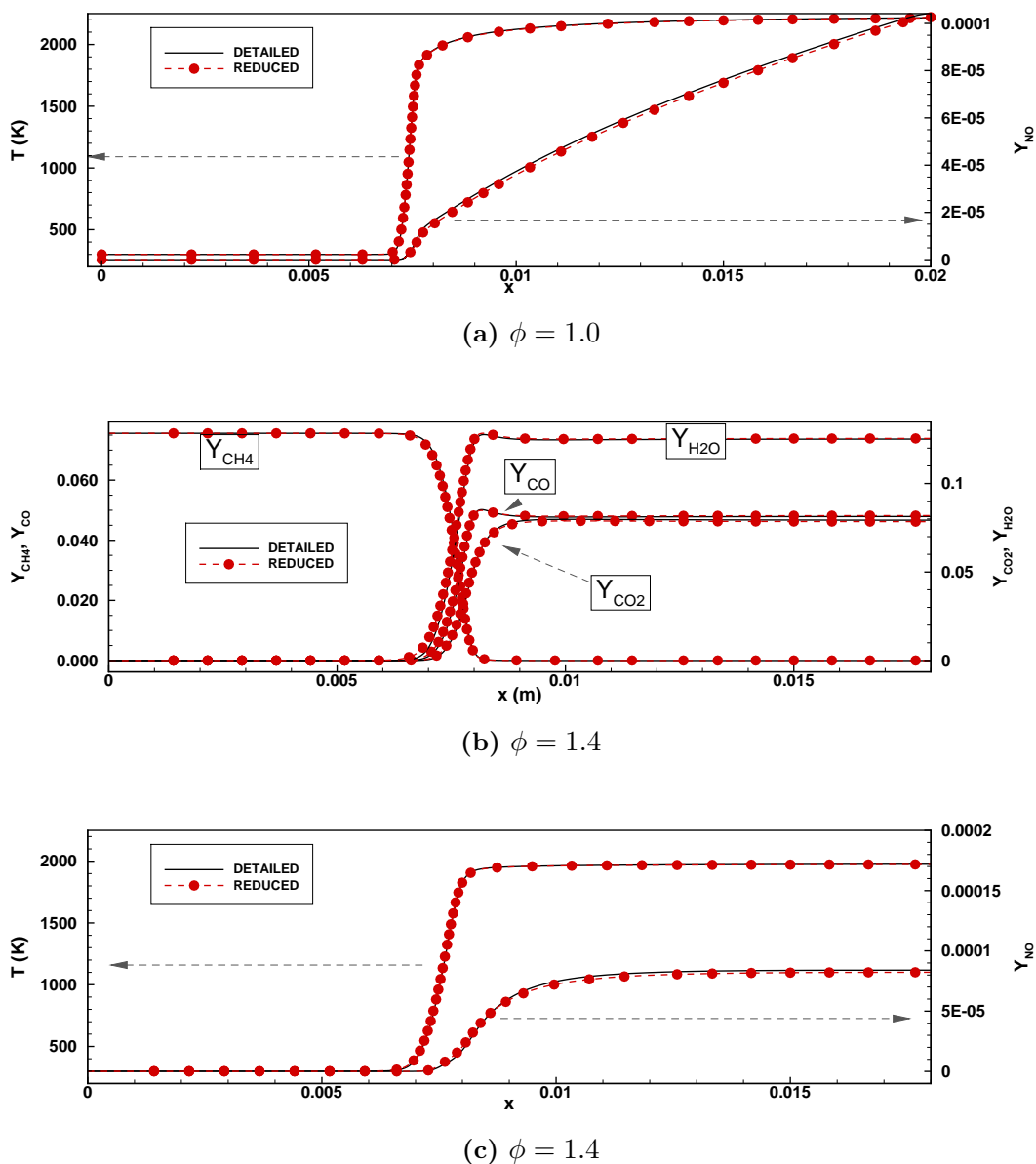


Figure 5.8: Spatial profiles of species and temperature in a 1D, unstretched laminar premixed flame computed using detailed and reduced POLIMI mechanism

Figure 5.9. Very good agreement is obtained between both the mechanisms for all equivalence ratios for the gas mixture temperature greater than 1400 K. At lower temperature, the differences in the ignition delay time predictions increase with discrepancy being significant at $T=1000\text{K}$.

5.6.3 Validation using 1DCD flames

Similar to the 1D premixed flame computations performed previously, comparison of the detailed and reduced mechanisms are carried out for 1D counter-flow

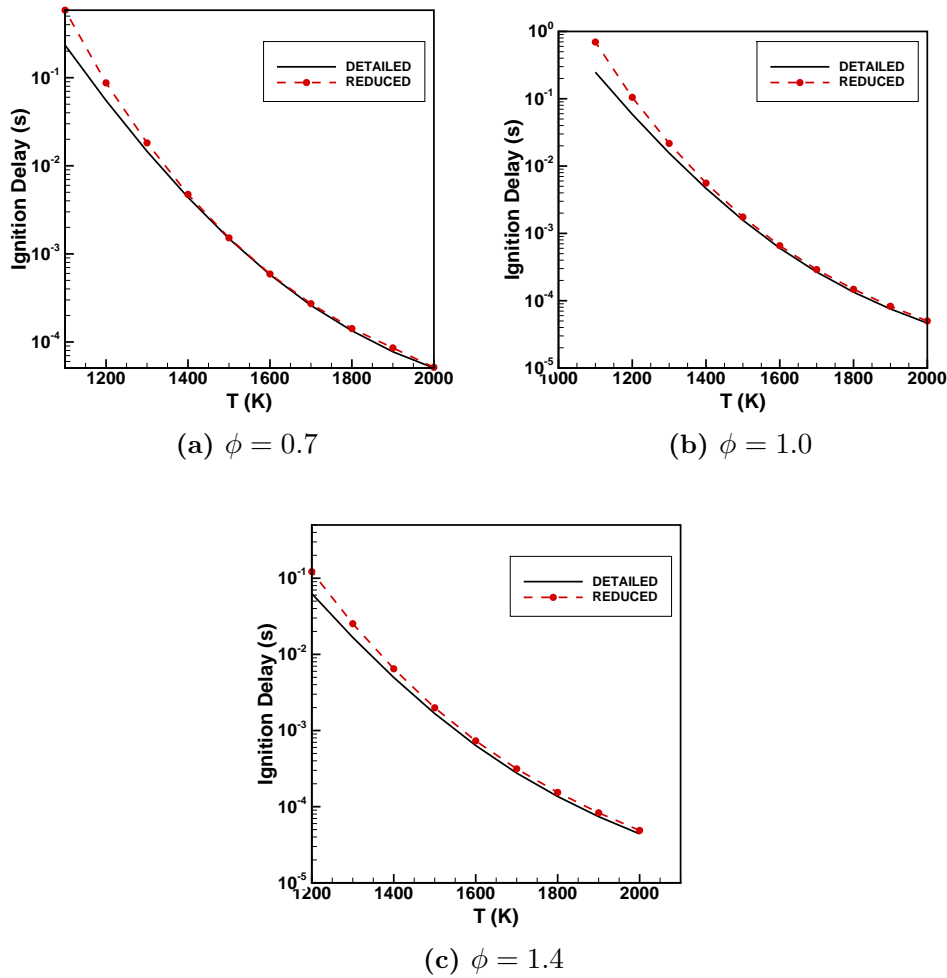


Figure 5.9: Comparison of detailed and reduced mechanism for ignition delay time computations

diffusion flames as well as using CANTERA. The fuel stream consists of pure CH_4 and oxidizer stream is Air. The temperature of both the streams are maintained at 298 K. The pressure is set to 1 Atmosphere. Simulations are carried out for strain rates varying from 25 sec^{-1} to 300 sec^{-1} . The strain rate definition used here is that of Magre et.al. [186] defined as the sum of the fuel and oxidizer stream velocity magnitudes divided by the length of the domain. It should be emphasized here that the counter-flow diffusion flame is not used as a target flame in the reduction process owing to the high computational cost and issues of convergence.

The results of the counter-flow diffusion flame computations are shown in Figures 5.10 and 5.11. Figures 5.10 show the variation of the global flame properties with strain rate computed using the two mechanisms. The difference in the peak temperature in the flame is within $\pm 10 \text{ K}$ across all strain rates. Similarly, the

5. ANALYTICAL CHEMICAL MECHANISM REDUCTION

species production rates integrated over the flame domain is found to be within $\pm 10\%$ when computed using the reduced mechanism. This is evident from Figures 5.10(c,d,e,f) that show the integrated production rates of CO, CO₂, H₂O and NO respectively. While the differences in integrated production rates of CO, CO₂ and H₂O are less than $\pm 5\%$, it is less than 10% for NO. Similarly, the spatial profiles of species mass fractions at two extreme values of strain rates (i.e. 25sec^{-1} and 250sec^{-1} respectively) used in the computations are shown in Figure 5.11. Just like in the premixed flame, excellent match is found between the species spatial profiles computed using both the mechanisms at both the strain rates.

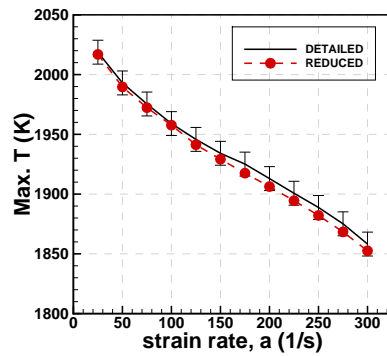
5.6.4 Application to a 3-dimensional laminar flame

In the previous subsection, the reduced mechanism is compared to the detailed mechanism for canonical 0D and 1D flame computations using CANTERA. Before employing the reduced mechanism to the LES of steam cracking furnace, it is desirable to validate the mechanism on a 3-dimensional laminar flame configuration.

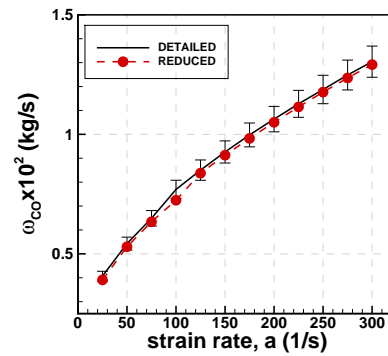
For this purpose, a laminar, jet diffusion flame with methane (diluted with nitrogen) as the fuel and air as the oxidizer is chosen. The experimental setup of this jet flame consists of a cylindrical fuel pipe of inner diameter 8 mm and thickness 1 mm is placed concentrically inside a co-flow cylindrical pipe that supplies air. A schematic of the experimental flame configuration is shown in Figure 5.12(a). The co-flow air is first supplied to a settling chamber filled with quartz beads that makes the coflow air velocity profile uniform. The resulting uniform air stream exits from the settling chamber through perforated plates. The fuel and co-flow pipe combination is kept inside a quartz enclosure to simulate a confined flame inside the combustion chamber. Measurements of radial profiles of temperature and major species (CH₄, CO, CO₂, O₂, H₂O and H₂) mole fractions are available at three axial planes located downstream (at 8 mm, 12 mm and 20 mm respectively) of the fuel exit plane. Further details of the experimental setup can be found in [187, 188]. The fuel and oxidizer inlet properties are provided in Table 5.6.4

	Flow properties	Fuel inlet	Oxidizer inlet
	Mean velocity (m/s)	0.065	0.155
	Temperature (K)	298	298
[h]	N ₂ (mole fraction)	0.51	0.79
	O ₂ (mole fraction)	0.00	0.21
	CH ₄ (mole fraction)	0.49	0.00

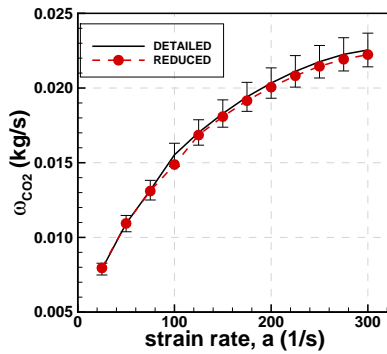
5.6 Validation of reduced mechanism



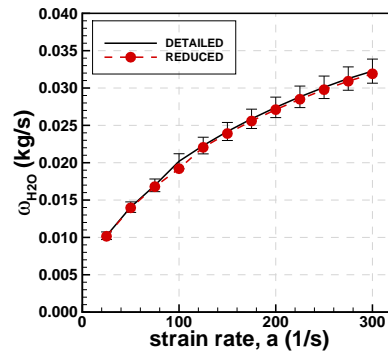
(a) Max. temperature. Error bars correspond to $\pm 10K$



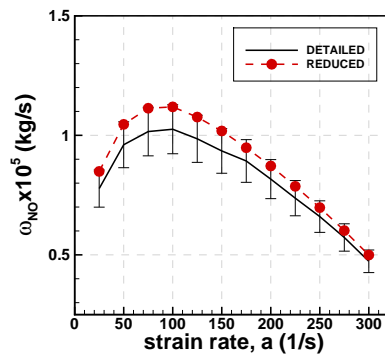
(b) Integrated CO production rate. Error bars correspond to $\pm 5\%$



(c) Integrated CO₂ production rate. Error bars correspond to $\pm 5\%$



(d) Integrated H₂O production rate. Error bars correspond to $\pm 5\%$



(e) Integrated NO production rate. Error bars correspond to $\pm 10\%$

Figure 5.10: Global diffusion flame properties computed using detailed and reduced mechanisms. Error bars are plotted with respect to the detailed mechanism

5. ANALYTICAL CHEMICAL MECHANISM REDUCTION

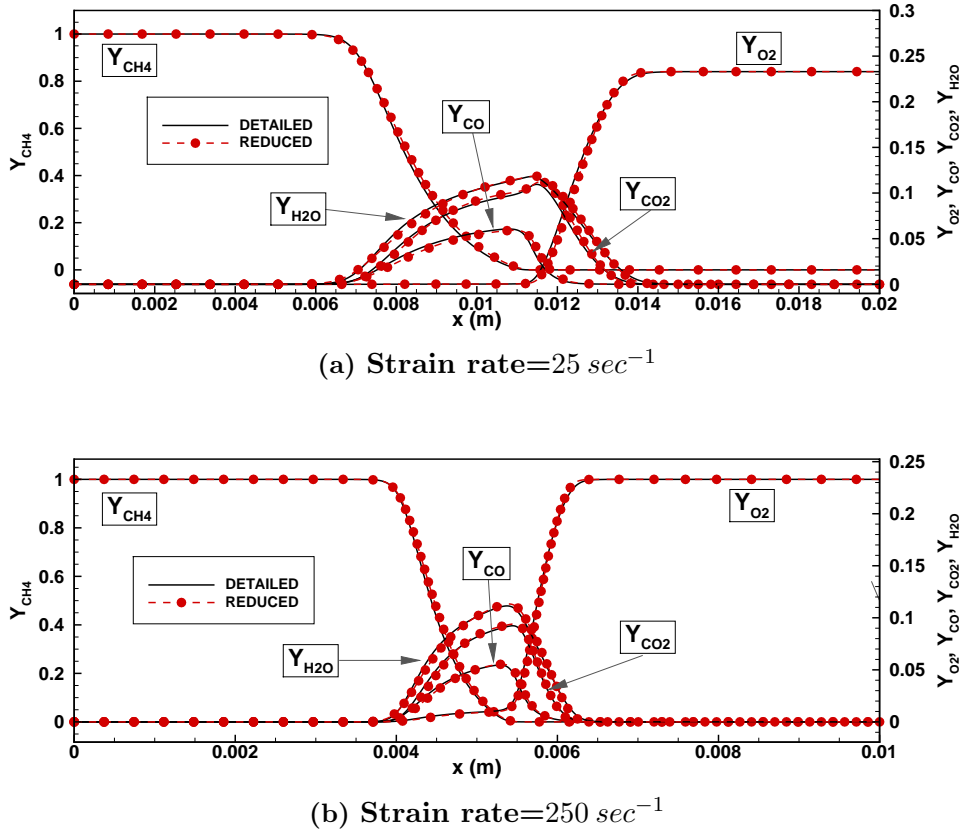


Figure 5.11: Spatial profiles of major species mass fractions at two different strain rates

The computational domain used for the numerical simulation consists of a cylinder of outer diameter 60mm and length 100 mm. A schematic of the computational domain is shown in Figure 5.12(b). The fuel inlet is modeled as a circular face of radius equal to that of the fuel pipe (4 mm). The remaining part of the face of the cylinder is considered the co-flow inlet as shown in the figure. The fuel travels inside the fuel pipe for a distance of 10 mm before interacting with the coflow air. Tetrahedral cells are used for mesh generation in the simulation. The smallest cells are located near the fuel rim where mesh elements of characteristic length 0.05 mm is used. To resolve the flame structure efficiently, fine mesh cells of size (0.1mm) are used in the fuel jet region up to a length of 30 mm downstream of the fuel jet exit.

The fuel consists of 49% CH_4 and 51% N_2 by volume and is supplied to the chamber at a temperature of 298 K. A parabolic velocity profile with a bulk velocity of 0.065 m/s is enforced at the fuel inlet. At the co-flow boundary, a uniform velocity profile for air is provided with a bulk velocity of 0.155 m/s and at temperature 298 K. Both the fuel and air inlets are modeled using the NSCBC

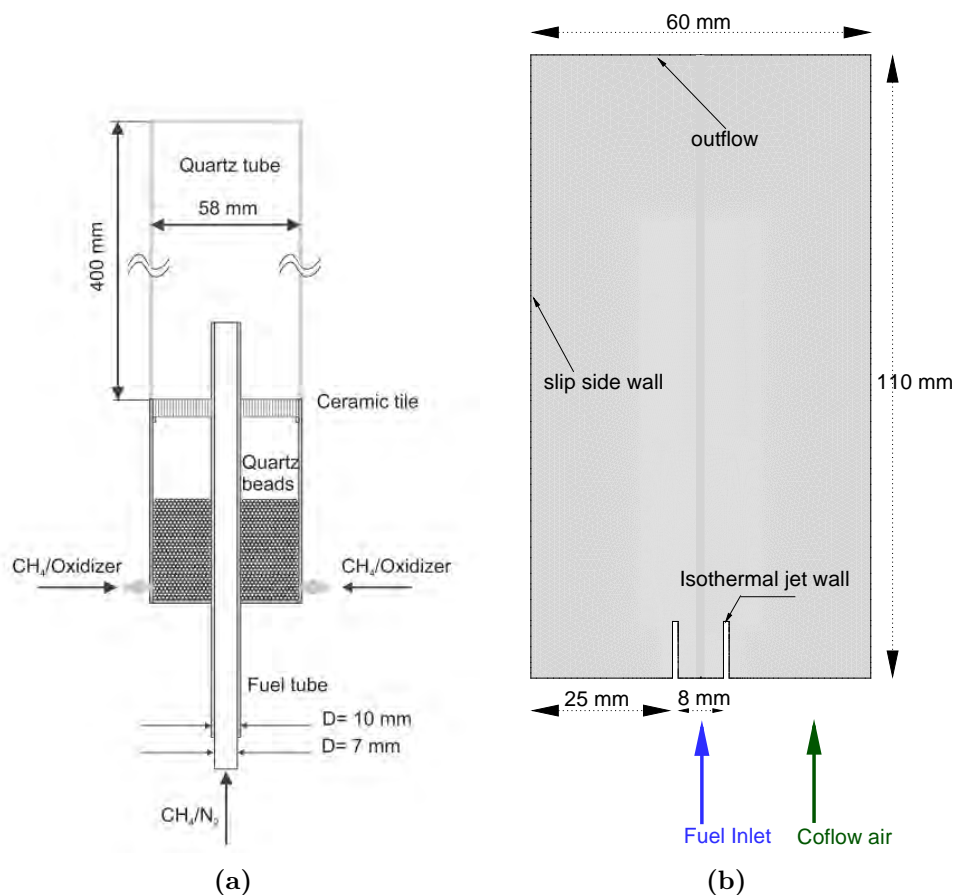


Figure 5.12: Schematic of the (a) experimental flame configuration (b) computational domain used in this study

boundary conditions. The fuel jet wall is modeled as an isothermal wall with the temperature of the metal fixed as 298 K. The side-walls are treated as adiabatic and as free slip. Atmospheric pressure is kept as the target pressure at the outflow boundary condition.

The reduced mechanism is used to simulate combustion with the transport properties as mentioned in Section 5.6.1. The effect of radiative heat transfer is modeled by invoking the optically thin assumption. The Planck mean absorption coefficient of major species (CH_4 , CO , CO_2 and H_2O) are provided as functions of temperature using 4th order polynomials.

Simulation is carried out for a flow time of 10 sec. The steady, radial profiles of major species mole fractions at the three axial planes ($z=\text{constant}$ planes) located 8 mm, 12 mm and 20 mm downstream respectively are shown in Figures 5.13. The methane profiles at $Z=8$ mm and $Z=12$ mm show excellent match with measured values shown by symbols. Similarly, excellent match is also observed for the profiles of O_2 mole fractions. At $Z=20$ mm, CH_4 is consumed

5. ANALYTICAL CHEMICAL MECHANISM REDUCTION

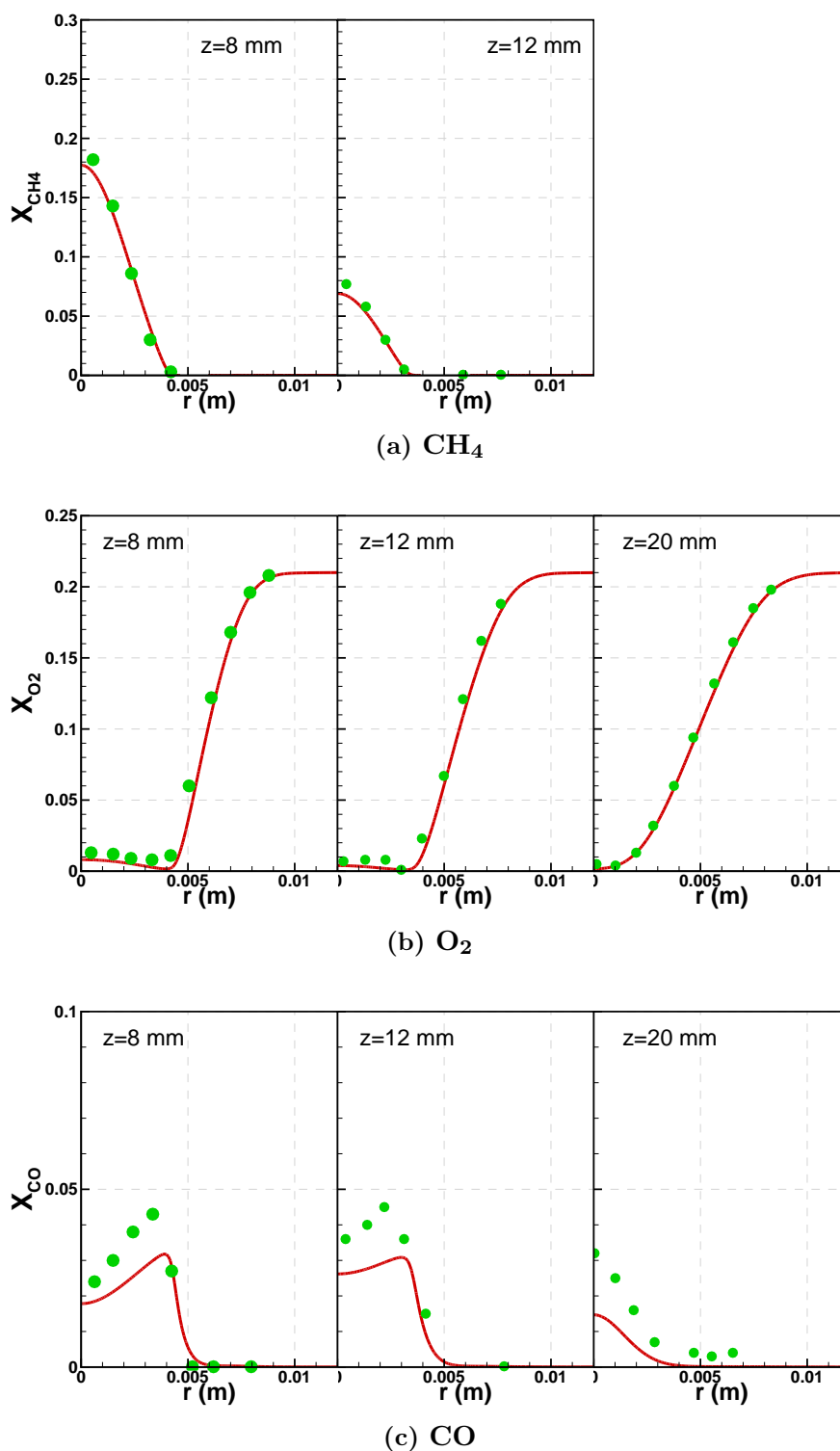


Figure 5.13: Radial profiles of CH_4 , O_2 and CO mole fractions plotted at axial downstream planes

completely as is evident from the O_2 profiles showing 0 at the fuel axis. CO_2 profiles are also predicted accurately by the simulations while mole fractions of H_2O are slightly overpredicted towards the fuel stream. CO and H_2 profiles are

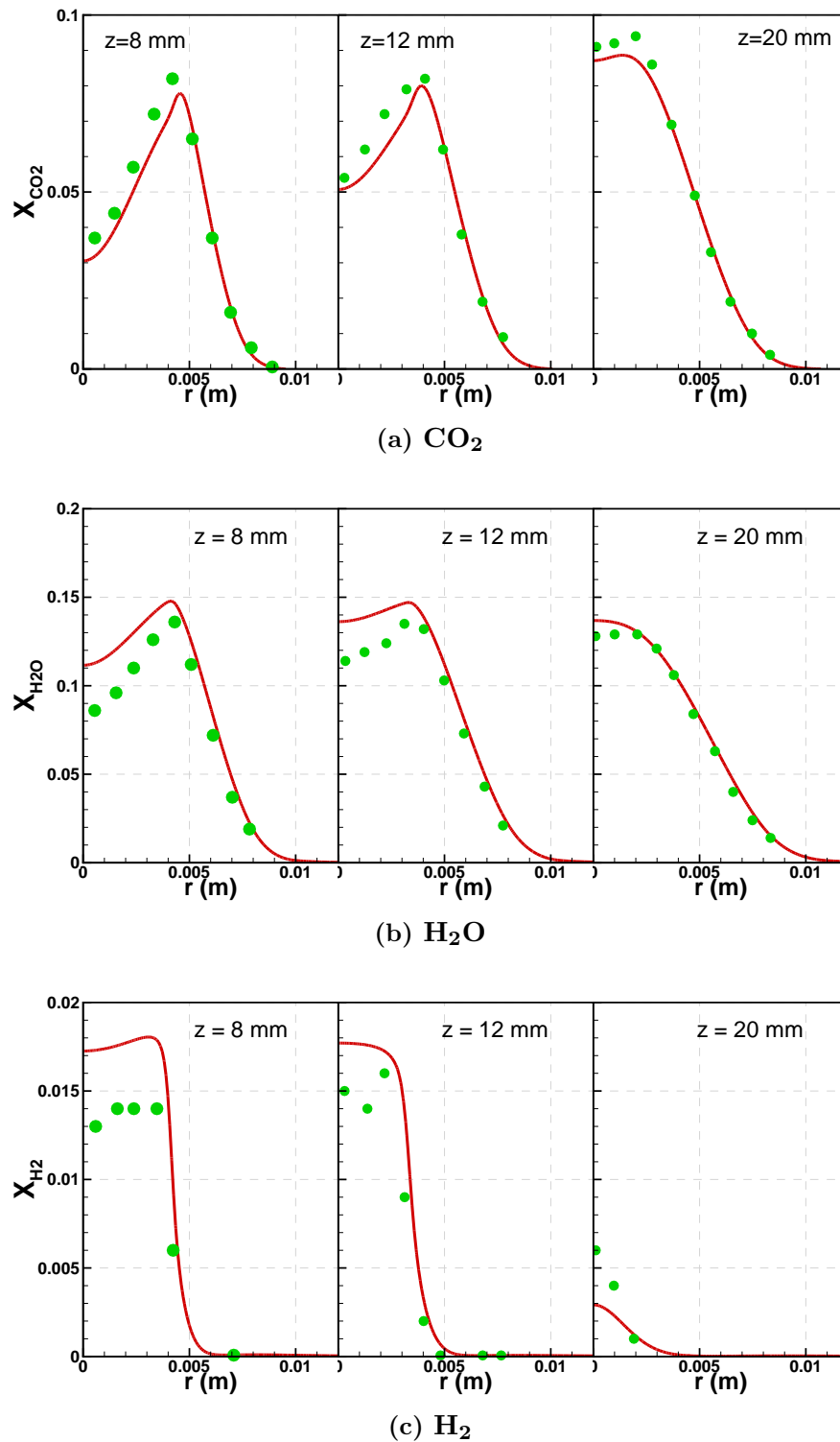


Figure 5.14: Radial profiles of CO_2 , H_2O and H_2 mole fractions plotted at axial downstream planes

also reproduced with fairly good agreement with data. The minor differences between the experimental measurements and numerical simulations could be due to the experimental uncertainties in measurements as explained by the authors

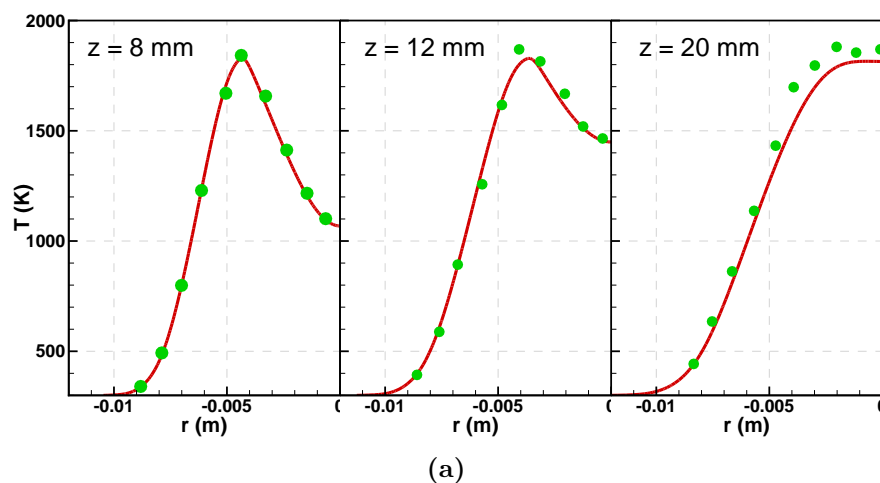


Figure 5.15: Radial profiles of temperature plotted at axial downstream planes

in [188].

With the exercises mentioned in this section, the reduced mechanism is validated with respect to the detailed mechanism for 0D, 1D and 3D flame configurations. Hence, this section addresses the objective (O.3) mentioned in Section 5.3.

5.7 Conclusions

The following conclusions are made from this Chapter.

- A comparative study of four popular, detailed mechanisms is performed using 0D iso-choric reactors and 1D premixed and diffusion flames. Comparison with available experimental data showed that all mechanisms predict laminar flame speed within levels of measurement uncertainty. Ignition delay time predictions of GRI mechanisms and POLIMI mechanism have a good match with available shock tube measurements. NO measurements for counter-flow diffusion flame match relatively better with POLIMI mechanism. The NCN pathway for prompt NO sub-mechanism is absent in other mechanisms which give incorrect results for NO concentration. Owing to a better resolution of NO profiles, POLIMI mechanism is chosen for further reduction and use in the LES simulation.
- Analytical reduction of POLIMI mechanism is carried out using the in-house chemical mechanism reduction tool ARCANE. Reduction is carried out using DRGEP followed by QSS assumption based species and reaction

methods. Transport properties of the reduced mechanism is obtained by optimizing their values for 1D premixed flames.

- The reduced mechanism is compared with the detailed mechanism for the 0D and 1D flames. Laminar flame speed values obtained using reduced mechanism are observed to be within 5% difference when compared to detailed mechanism. Peak temperature differences between the mechanisms are found to be within $\pm 10K$. All species of interest are observed to be accurately reproduced within an accuracy of $\pm 10\%$ by the reduced mechanism. The reduced mechanism is also used to simulate a laminar jet diffusion flame with $\text{CH}_4 + \text{N}_2$ as the fuel. The computed and measured radial species mole fraction profiles show excellent agreement to each other thereby underlining the accuracy of the reduced mechanism in retaining the original flame structure.

Chapter 6

Modeling radiative heat transfer effects

Contents

7.1	Test Furnace Configurations	197
7.2	Geometric modeling	199
7.2.1	Computational Domain	199
7.2.2	Boundary conditions	200
7.3	Grid generation	201
7.4	Computational settings	203
7.5	Results	204
7.6	Conclusions	212

6.1 Introduction

In this chapter, the framework for the incorporation of radiative heat transfer effects into LES simulation is described. Of particular interest is the coupling of the LESAULTS approach based LES solver with the RTE solver, PRISSMA and the computational gain obtained using this coupling. In Section 6.2, the state-of-the-art in the field of numerical radiative heat transfer analysis is discussed. This is followed by a description of the in-house RTE solver PRISSMA in Section 6.3. The computational benefit of coupling the LESAULTS method with the PRISSMA solver is discussed in Section 6.4. This approach is validated using a laminar jet diffusion flame, the results of which are presented in Section 6.5. Finally, conclusions from this chapter are summarized in Section 6.6.

6.2 Literature Survey

The significance of the incorporation of radiative heat transfer effects in combustion simulations is increasingly being appreciated over the years. Nevertheless, it would not be an understatement to mention that the field of radiative heat transfer analysis in combustion applications is still a fertile pasture for numerical and experimental research. The research efforts can hence be broadly classified into experimental and numerical. Experimental research predominantly focuses on the prediction of spectral properties such as the refractive indices [189, 190, 191] and absorption coefficients [192], soot emissions [193], flame extinctions at microgravity [194], on the properties of pool fires [195] and about flames in combustors [196].

On the other hand, the modeling efforts on the numerical side can be broadly classified into three fields. The first class of studies focuses on modeling the spectral properties of gases and their mixtures. Currently, there are many approaches to modeling the spectral properties depending on the desired level of accuracy and computational cost that is incurred. The line-by-line (LBL) method [197] relies on integrating the RTE in the spectral space considering the variation of the spectral properties at each frequency in the full spectrum. This would consist of millions of frequencies and hence this method is computationally costly and renders it almost impossible to be used in conjunction with CFD applications of engineering interests. The second method is the Narrow Band (NB) method, which is getting considerable attention in recent times. There are two types of NB methods: namely the statistical method and the correlated k-method. The statistical Narrow Band (SNB) method provides the spectral transmissivity over a narrow band of frequencies in the spectrum and is pretty accurate. However, it suffers from two main drawbacks. The first drawback is its inability to be used with any differential RTE solvers such as Discrete Ordinate Method (DOM), Finite Volume Method (FVM) or P1 methods without bringing in additional assumptions. Hence this method can be used as it is only with ray tracing methods. The second drawback is that the effect of scattering cannot be modeled unless a Monte-carlo based method is used, thereby making the solver computationally costly. The correlated k-distribution (NBCK) based method, on the other hand, does not suffer from any such deficiencies as it directly calculates the absorption coefficient and hence can be used with any of the RTE solvers. The third method of spectral modeling is that of the wide band models (WBM) where a constant black body intensity is assumed over wider bands of frequencies, hence making it less accurate than NB models. The fourth method, namely the full spectrum

6. MODELING RADIATIVE HEAT TRANSFER EFFECTS

correlated K method (FSCK) method works on reordering the absorption coefficients over the full spectrum thereby making the integration in wavenumber space computationally cheaper and efficient. Finally, global models such as the Weighted Sum of Gray Gas (WSGG) model are computationally cheaper than all of the previously mentioned models and can be used with any type of RTE solvers. The WSGG model works on replacing the non-gray gases with gray gases with their spectral properties computed independently. The spectral line based WSGG (SLW) model is an improvement over the classical WSGG model where absorption coefficients are reordered into a smooth monotonically increasing function making the integration in frequency space easier.

The second class of research is directed towards the numerical solution of the RTE. A lot of methods of solution for the RTE exist as described in [54]. Ray tracing and Monte-Carlo based methods (MCM) can be used to calculate quasi-exact solution and are considered the best methods available and are often used in benchmarking other numerical solution methods. In the case of MCM, estimates of the error associated to the solution can also be obtained. The above two methods can be applied conceptually to include all possible complexities and to couple them with CFD solvers. However, the cost associated with these methods are too high to be used in CFD application currently. Approximate methods of solution of RTE also exist such as the Zonal methods, DOM, Discrete Transfer Method and the method of spherical harmonics. Zonal methods are an extension of the surface exchange methods and include the effect of participating medium by assuming the domain to be sub-divided into smaller, iso-thermal sub-domains. These methods are computationally cheap and have been used extensively in the past for example, to simulate combustion and radiative losses inside furnaces [38]. The DOM method works on discretising the angular space into angular sub-domains and approximating the quadrature using precalculated weights. DOM although sensitive to the spatial discretisation and the ray effect, is shown that when used with the S4 and LC11 quadratures, provides solution with accuracy levels close to that of MCM.

The third and final research frontier is that of tackling the turbulence-radiation interaction (TRI) problems. The considerable fluctuations in temperature and species concentrations occurring in combustion applications arising from turbulence can have a significant impact on the radiation properties and heat transfer characteristics. An excellent review of numerical studies on TRI is provided in [198]. In [199], the authors studied the turbulence-radiation interaction in two-dimensional acetylene-air planar flames. An FVM approach in conjunction with DOM is used while only absorption of combustible gases is considered. In [200],

DOM is used to study the radiative effects inside a gas turbine combustor using a gray gas model. A DOM solver is used to solve the RTE in PRECCINSTA burner in [201]. The SNBcK gas model is used in this study. LES and DOM is coupled and coupled solver is applied to simulate a bluff-body stabilized flame in [202]. The authors of the study concluded that radiation plays an important role in determining the flame stabilization mechanism even though the heat loss through radiation is only a percentage of the total heat released from the flame. More recently, the authors in [203] extended the same approach to study the same flame and performed a comparative study of the various band integration models.

In this study, the work of [203] is extended to perform LES of the steam cracking furnace. However, the LES solver used in this study employs the LESAULTS method detailed in Chapter 4. Before discussing the details of the coupling between the LESAULTS solver and the radiative solver-PRISSMA as provided in Section 6.4, a brief overview of the PRISSMA solver is provided in the following section.

6.3 PRISSMA RTE Solver

The solver name PRISSMA [204] is an acronym for **P**arallel **R**adIative **S**olver with **S**pectral integration on **M**ulticomponent medi**A**. The code is jointly developed by CERFACS and EMAC and is primarily intended for combustion applications. PRISSMA is a parallel RTE solver and works on the discrete ordinate method for all cell element types.

As mentioned in Chapter 2, the governing RTE is given as,

$$\begin{aligned} \frac{dI}{ds} &= \hat{\mathbf{s}} \cdot \nabla I(\mathbf{r}, \hat{\mathbf{s}}) \\ &= \kappa(\mathbf{r})I_b(\mathbf{r}) - \beta(\mathbf{r})I(\mathbf{r}, \hat{\mathbf{s}}) + \frac{\sigma_s(\mathbf{r})}{4\pi} \int_{4\pi} I(\mathbf{r}, \hat{\mathbf{s}}') \Phi(\mathbf{r}, \hat{\mathbf{s}}', \hat{\mathbf{s}}) d\Omega' \end{aligned} \quad (6.1)$$

Here, I refers to the total radiation intensity, \mathbf{s} and \mathbf{r} refer to the direction of the radiation and the position vector of the point under consideration respectively. κ, β and σ_s are the emission, extinction and scattering coefficients. Φ is the scattering phase function and I_b is the black body radiation intensity.

The boundary condition for the total intensity at any diffusive boundary is given by,

$$I(\mathbf{r}, \hat{\mathbf{s}}) = \epsilon(\mathbf{r}) I_b(\mathbf{r}) + \frac{\rho(\mathbf{r})}{\pi} \int_{\hat{\mathbf{A}} \cdot \hat{\mathbf{s}}' < 0} I(\mathbf{r}, \hat{\mathbf{s}}') \left| \hat{\mathbf{i}} \cdot \hat{\mathbf{s}}' \right| d\Omega' \quad (6.2)$$

6. MODELING RADIATIVE HEAT TRANSFER EFFECTS

ϵ and ρ are the emissivity and the reflectivity at the boundary surface.

In the DOM, the governing RTE is discretised and solved for n discrete directions $s_i, i = 1, 2..n$. Hence the governing RTE is discretised in these directions as

$$\hat{\mathbf{s}}_i \cdot \nabla I(\mathbf{r}, \hat{\mathbf{s}}_i) = \kappa(\mathbf{r})I_b(\mathbf{r}) - \beta(\mathbf{r})I(\mathbf{r}, \hat{\mathbf{s}}_i) + \frac{\sigma_s(\mathbf{r})}{4\pi} \sum_{j=1}^{N_{dir}} w_j I(\mathbf{r}, \hat{\mathbf{s}}_j) \Phi(\mathbf{r}, \hat{\mathbf{s}}_i, \hat{\mathbf{s}}_j), \quad i = 1, 2, \dots, n \quad (6.3)$$

In combustion applications, the presence of soot particles and fuel droplets can contribute to both in and out scattering effects. However, these effects are negligible and hence neglected in PRISSMA solver. The RTE then solved using DOM are given by,

$$\hat{\mathbf{s}}_i \cdot \nabla I(\mathbf{r}, \hat{\mathbf{s}}_i) = \kappa(\mathbf{r})I_b(\mathbf{r}) - \beta(\mathbf{r})I(\mathbf{r}, \hat{\mathbf{s}}_i), \quad i = 1, 2, \dots, N_{dir} \quad (6.4)$$

Once the above equations are solved for the radiation intensities at every point, the radiative heat transfer at any point in the domain is obtained as,

$$\mathbf{q} \cdot \hat{\mathbf{n}}(\mathbf{r}_w) = \epsilon(\mathbf{r}_w) [\pi I_b(\mathbf{r}_w) - H(\mathbf{r}_w)] \quad (6.5)$$

The divergence of the above heat transfer function is the source term in the energy equation of fluid flows and is given by,

$$S_r = \nabla \cdot \mathbf{q} = \kappa(4\pi I_b - G) \quad (6.6)$$

Where the incident radiation term G in the above equation is given by the relation,

$$G = \int_{4\pi} I(\mathbf{s}_i) d\Omega \quad (6.7)$$

6.3.1 Angular discretisation

In DOM, the angular integrals in Eqs. 6.1 and 6.7 are calculated using numerical quadratures given by,

$$\int_{4\pi} f(\hat{\mathbf{s}}) d\Omega \simeq \sum_{i=1}^{N_{dir}} w_i f(\hat{\mathbf{s}}_i) \quad (6.8)$$

w_i refers to the directional quadrature weight associated with direction s_i . N_{dir} is the total number of discrete directions considered for the analysis. The

directional weights w_i are also subjected to the following compatibility conditions,

$$\begin{aligned}
 \int_{4\pi} d\Omega &= 4\pi = \sum_{i=1}^{N_{dir}} w_i, \\
 \int_{4\pi} \hat{\mathbf{s}} d\Omega &= \mathbf{0} = \sum_{i=1}^{N_{dir}} w_i \hat{\mathbf{s}}_i \\
 \int_{4\pi} \hat{\mathbf{s}} \hat{\mathbf{s}} d\Omega &= \frac{4\pi}{3} \delta = \sum_{i=1}^{N_{dir}} w_i \hat{\mathbf{s}}_i \hat{\mathbf{s}}_i,
 \end{aligned} \tag{6.9}$$

Different angular discretisations exist in the literature such as the LC_{11} quadrature, S_N quadrature, T_N quadrature and the polar and azimuthal quadratures. The number of directions in LC_{11} quadrature is 96 and is generally considered to be the most accurate among the above-mentioned methods [205, 206]. For the S_N quadrature, the number of directions $N_{dir} = N(N+2)$ where N is the quadrature order. Similarly for the T_N quadrature, the number of directions is $N_{dir} = N^2$. In PRISSMA solver, S_N quadrature is used. The effect of the quadrature order on the solution accuracy was studied in [207] and it is observed that a reasonably good solution is obtained with $N = 4$. Hence, in this study, a fourth-order angular quadrature is used.

6.3.2 Spatial discretisation

The finite volume method is used for spatial discretisation in PRISSMA. The governing RTE Eq. 6.5 is discretised as,

$$\int_A I_{\tilde{\nu}} \mathbf{s} \cdot \mathbf{n} dA = \int_V \mathbf{K}_{\tilde{\nu}} (I_{b\tilde{\nu}} - I_{\tilde{\nu}}(\mathbf{s})) dV \tag{6.10}$$

Here the subscript $\tilde{\nu}$ denotes the spectral property at a frequency equal to $\tilde{\nu}$. dA and dV denote the area and volume of the face and cell under consideration. Approximating the above integral using the cell averaged values, one can write the above equation numerically as,

$$\sum_{j=1}^{N_f} I_{\tilde{\nu},j}(\mathbf{s}) (\mathbf{s} \cdot \mathbf{n}_j) A_j = \kappa_{\tilde{\nu}} (I_{b\tilde{\nu},P} - I_{\tilde{\nu},P}(\mathbf{s})) V \tag{6.11}$$

where N_f is the number of faces in the cell element considered and $I_{\tilde{\nu},j}$ denotes the spectral intensity $I_{\tilde{\nu}}$ at the face j of the cell element. $I_{b\tilde{\nu},P}$ and $I_{\tilde{\nu},P}$ are the quantities evaluated at the cell centroid P . Eq. 6.11 is the fundamental discrete equation to be solved in DOM. This equation can be used solved using either the exponential scheme [208] or the mean flux scheme [209]. Since the latter method

6. MODELING RADIATIVE HEAT TRANSFER EFFECTS

is more suited to unstructured meshes, it is used in the present study. Using this method, the cell centroid value of the intensity can be calculated using (and only) the incoming radiative flux as,

$$I_{\bar{v},P} = \frac{\alpha V \kappa_{\bar{v}} I_{b\bar{v}} - \sum_{j|D_j < 0} D_j A_j I_{\bar{v},j}}{\alpha \kappa_{\bar{v}} V + A_{\Delta}} \quad (6.12)$$

The details of the derivation of the above expression is provided in [55]. In the above expression, α is a tunable constant used in the generalized mean flux discretisation scheme. For $\alpha = 1$ the scheme is called the step scheme and for $\alpha = 0.5$ the diamond mean flux scheme is obtained. The term D_j is defined as $D_j = s_i \dot{n}_j$ and A_{Δ} is the sum of projections of the area vectors in the direction of the radiation intensity. Using mean flux discretisation, only the incoming radiative flux needs to be known and outgoing fluxes can be calculated once the cell centroid values are available. In order to speed up the solution of the above equation using the mean flux scheme and taking advantage of the previously mentioned property, a cell sweep procedure is incorporated wherein the near boundary cell values are calculated first followed by the adjacent cells sharing the face in the direction of the intensity. This procedure is explained in detail in [210].

6.3.3 Spectral discretisation

The spectral models incorporated in PRISSMA are listed in the decreasing order of their complexity as follows.

- Spectral Narrow Band Correlated-K model (NBCK)
- Full Spectrum Spectral Narrow Band Correlated-K model (FSNBCK)
- Tabulated Full Spectrum Spectral Narrow Band Correlated-K model (TF-SNBCK)
- Weighted sum of gray gas model (WSGG)

The details of the implementation of these models in PRISSMA are not provided here and can be found in [55]. The gray gas model with the optical thin assumption is already available as a radiation model in the stand-alone version of AVBP.

6.4 LESAULTS-PRISSMA Coupling Strategy

The fluid flow solution and radiative heat transfer effects impose different temporal and spatial scales in the case under study. The numerical solution methodologies for both these physical problems are also considerably different as explained in the previous section and in Chapter 3. Hence, the approach taken in addressing such multiphysics problems is that of developing codes independently that solve these problems on different spatial structures (grids) using different numerical approaches. The codes are then coupled during run time using appropriate coupling frameworks such CWIPI ([211]) and necessary information required in the solution procedure for the codes are exchanged.

Using this philosophy, the LES solver AVBP and the RTE solver PRISSMA are developed and executed independently and coupled using CWIPI. While PRISSMA provides the radiative source term required by AVBP to be used in the energy equation, AVBP in turn provides the species mole fractions, temperature and pressure required for solving RTE in PRISSMA. Before discussing the specifics of the coupling approach it is necessary to introduce the fluid and radiative time scales.

The fluid time scale associated with most of the engineering computations is given by $t_{Flow} = \frac{L}{c}$, where L is the flow length scale and c is the acoustic speed. Under discrete computing, the flow time scale is modified as, $t_{Flow} = N_c \frac{h}{c}$ where h is the grid size and N_c is the CFL number introduced in Chapter 3. Similarly, the time scale associated with radiative effects due to a reactive flow is given by,

$$t_{Rad} = \frac{h}{u} \tag{6.13}$$

$$\tag{6.14}$$

This is essentially the time taken by a fluid vortex to travel through a cell element of size h . The ratio of the two time scales is then given by,

$$\frac{t_{Rad}}{t_{Flow}} = \frac{h}{u} \frac{c}{N_c h} \tag{6.15}$$

$$= \frac{1}{N_c M} \tag{6.16}$$

$$t_{Rad} = \frac{1}{N_c M} t_{Flow} \tag{6.17}$$

where M is the Mach number of the flow. The expression above indicates that the coupling frequency between PRISSMA and AVBP is $\frac{1}{N_c M}$. The maximum value of N_c used in LES computation is 0.7 at the smallest cell, while the

6. MODELING RADIATIVE HEAT TRANSFER EFFECTS

typical Mach number is less than 0.1 in the rest of the domain. Poiteau et al. [203] suggested that a coupling frequency $N_{it} = 100$ should be a good enough approximation to be used.

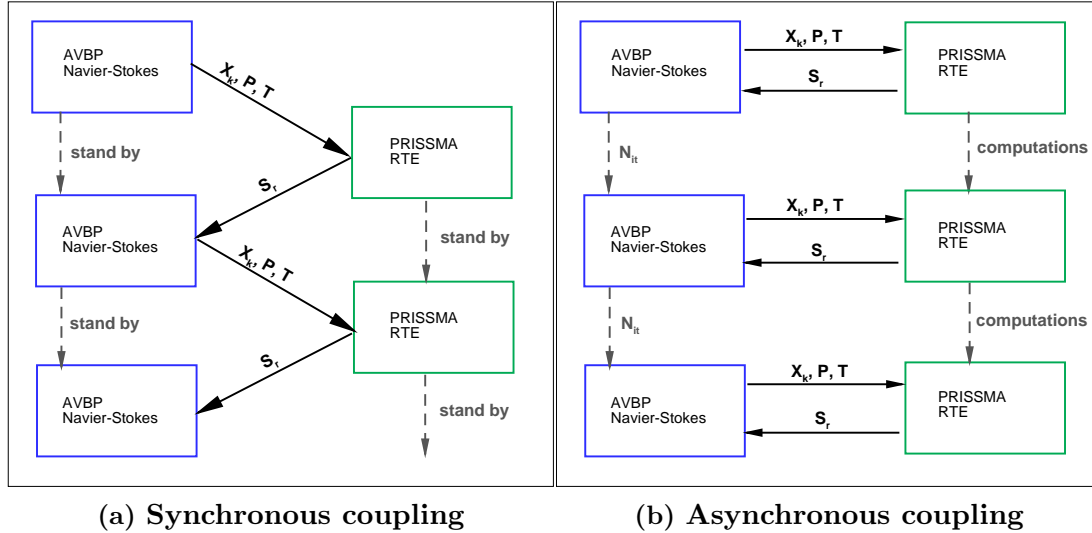


Figure 6.1: Coupling approaches used for the AVBP-PRISSMA configuration. (a) Synchronous coupling (b) Asynchronous coupling

Having derived the coupling frequency between AVBP and PRISSMA, the coupling approaches used in the conventional AVBP-PRISSMA as described in [203] is discussed next. There are two approaches of coupling in use, namely, the synchronous and the asynchronous approach. A schematic of the approaches is shown in Figure 6.1. Consider the simulation of an AVBP-PRISSMA configuration using C_{tot} number of computing cores. In the synchronous approach, both the codes and the associated data is shared among all the computing cores C_{tot} . Each of the codes is executed sequentially and the data exchange occurs after the code execution is completed. This is shown in Figure 6.1 (a). While one code is being executed, the other code remains on standby. Although, in this approach, the full set of computing cores are used by both the codes, the standby phase of each code makes the approach inefficient and time-consuming.

The second coupling approach is the asynchronous coupling approach and is shown in Figure 6.1(b). In this approach, both the codes execute independently and exchange flow and radiation information asynchronously. This approach is computationally efficient as it avoids the wasteful standby phase of either of the codes.

To calculate the number of cores to be dedicated to each of the codes, consider the following coupling configuration. Let the number of mesh nodes in the grid used for AVBP be N_{AVBP} and let the number of computing cores dedicated

6.4 LESAULTS-PRISSMA Coupling Strategy

to AVBP be C_{AVBP} . Let the same parameters for PRISSMA be $N_{PRISSMA}$ and $C_{PRISSMA}$ respectively. Let the physical time taken by AVBP to complete 1 iteration using C_{AVBP} number of computing cores be denoted as ${}^p_1t_{AVBP}$. In the notation used here, the right subscript (C_{AVBP}) denotes the number of computing cores, the right subscript (1) denotes the number of iterations and the left superscript (p) indicates the physical time. Then the time taken for AVBP to compute N_{it} iterations is given by,

$${}^p_{N_{it}}t_{C_{AVBP}} = \frac{k_{AVBP}N_{AVBP}N_{it}}{C_{AVBP}} \quad (6.18)$$

The constant k_{AVBP} is a characteristic of the solver AVBP and is a function of the numerics used as well as the HPC environment where AVBP is executed. Using similar notations, the physical time taken by PRISSMA to compute steady solution is given by,

$${}^p_1t_{PRISSMA} = \frac{k_{PRISSMA}N_{PRISSMA}}{C_{PRISSMA}} \quad (6.19)$$

For perfect load balancing, it is desirable to have both the physical times equal. Hence,

$$\frac{k_{AVBP}N_{AVBP}N_{it}}{C_{AVBP}} = \frac{k_{PRISSMA}N_{PRISSMA}}{C_{PRISSMA}} \quad (6.20)$$

$$(6.21)$$

This provides expressions for the computing core division between AVBP and PRISSMA as,

$$C_{PRISSMA} = \frac{\tau_P C_{tot}}{(\tau_A N_{it} + \tau_P)} \quad (6.22)$$

$$C_{AVBP} = \frac{\tau_A C_{tot}}{(\tau_A N_{it} + \tau_P)} \quad (6.23)$$

where τ_P and τ_A are the physical times taken by AVBP and PRISSMA to compute 1 iteration using 1 computational core.

Next, the coupling procedure for LESAULTS-PRISSMA configuration is detailed. Due to its efficiency and speed up, the asynchronous coupling approach is considered here. Consider the same configuration as described above. Let the AVBP grid now be divided into N_{sub} number of sub-domains with the time step ratio of sub-domain i indicated as $R_{\delta t, i}$. The synchronization of the LESAULTS and PRISSMA solvers is shown in the schematic in Figure 6.2. When using

6. MODELING RADIATIVE HEAT TRANSFER EFFECTS

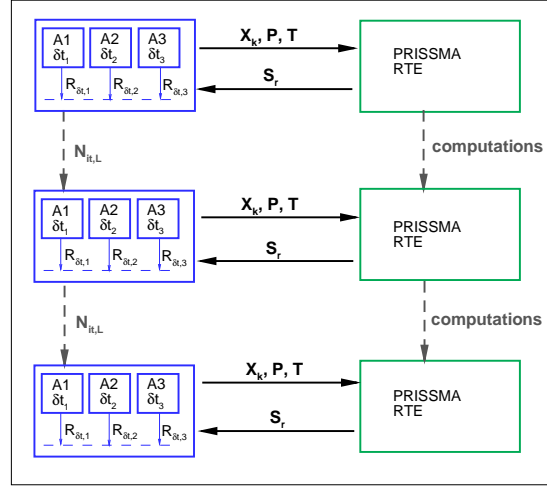


Figure 6.2: Coupling approach used for the LESAULTS-PRISSMA configuration. LESAULTS configuration comprises of three sub-domains ($N_{sub} = 3$).

the LESAULTS approach, each of the sub-domain i now integrates by $N_{it,i} = \frac{N_{it}}{\max(R_{\delta t,i})} R_{\delta t,i}$ time steps before coupling itself with PRISSMA. Let the number of computing cores dedicated to each sub-domain in LESAULTS be denoted by $C_{L,i}$. Hence,

$$C_{tot} = C_{PRISSMA} + \sum_{i=1}^{N_{sub}} C_{L,i} \quad (6.24)$$

Let the number of mesh nodes in sub-domain i be denoted as $N_{L,i}$ such that

$$N_{AVBP} \simeq \sum_{i=1}^{N_{sub}} N_{L,i} \quad (6.25)$$

As derived for the conventional AVBP solver in the previous paragraph, the physical time taken by each sub-domain in LESAULTS approach is given by,

$${}_{N_{it,i}}^p t_{L,i} = \frac{k_{AVBP} N_{L,i} N_{it,i}}{C_{L,i}} \quad (6.26)$$

while the time taken by PRISSMA remains unchanged as given by Eq. 6.19. For perfect load balancing between the processors,

$$\frac{k_{AVBP} N_{L,i} N_{it,i}}{C_{L,i}} = \frac{k_{PRISSMA} N_{PRISSMA}}{C_{PRISSMA}} \quad (6.27)$$

Thereby, the core distribution between each of the sub-domains in LESAULTS

and PRISSMA is given by,

$$C_{L,i} = \frac{1}{\left[\frac{\sum_{i=1}^{N_{sub}} N_{L,i} R_{\delta t,i}}{N_{L,i} R_{\delta t,i}} + \frac{\tau_P}{\tau_{L,i} N_{it,i} R_{\delta t,i}} \right]} \quad (6.28)$$

$$C_{PRISSMA} = C_{tot} - \sum_{i=1}^{N_{sub}} C_{L,i} \quad (6.29)$$

where $\tau_{L,i}$ is the physical time taken by sub-domain i and using 1 computing core.

Then, the speed up obtained while using LESAULTS-PRISSMA for the given core distribution is defined as,

$$speedup_{L-P} = \frac{N_{it}^p t_{AVBP}}{N_{it,L}^p t_{L,i}} \quad (6.30)$$

Substituting Eqs. 6.18 and 6.26 in Eq. 6.30, one obtains the relation for speed up as,

$$speedup_{L-P} = \frac{1}{\left[\frac{\sum_{i=1}^{N_s} N_{L,i} R_{\delta t,i}}{N_{L,i} R_{\delta t,max}} + \frac{\tau_P}{\tau_{L,i} R_{\delta t,i} N_{it,i}} \right]} \quad (6.31)$$

The first term in the denominator of the above equation is the inverse of the speed up obtained using LESAULTS method and without any coupling with the PRISSMA solver and has been derived in Eq. 4.16. Hence, simplifying the above equation one obtains,

$$speedup_{L-P} = \frac{1}{\left[\frac{1}{S_{th}} + \frac{\tau_P}{\tau_{L,i} R_{\delta t,i} N_{it,i}} \right]} \quad (6.32)$$

6.5 Validation of LESAULTS-PRISSMA Coupled solver

To validate the coupling approach described above and to ascertain the speed up obtained in computations the coupling approach is applied to simulate a reactive flow configuration. The axisymmetric, laminar jet flame configuration detailed in [212] is chosen. This particular flame configuration is chosen since the radiative heat transfer measurement data is available for comparison with CFD results.

The experimental configuration used in the study is that of the modified Sontaro burner [213]. The flame configuration consists of a cylindrical fuel injector

6. MODELING RADIATIVE HEAT TRANSFER EFFECTS

of inner diameter 11.1 mm and outer diameter 12.7 mm. The injector is located inside an annular tube of diameter 101.6 mm through which the coflowing air emanates. The fuel injector exit is located 64 mm downstream of the coflow exit. The authors in [213] have used methane with different ratios of CO₂ and N₂ as diluents and have studied the effect of varying dilution ratios on the radiative heat transfer properties for flames with constant power as well as for constant fuel flow rates. In the present chapter, the flame configuration with no CO₂ or N₂ dilution is chosen for simulation. This flame is particularly chosen because of its similarity with the flame to be simulated in the furnace. This flame also provides an opportunity to use the reduced mechanism, albeit indirectly, using the radiative heat transfer measurement.

As mentioned previously, the flame CP0100C00 (mentioned in [213]) is chosen for the present analysis. The fuel (CH₄) flow rate for this flame is 1 L/min and the coflow air flow rate is 100 L/min. The temperature of fuel and air are fixed as 298 K and the experiment is conducted at ambient pressure. In these conditions, the bulk flow velocity in the fuel and air stream are 0.172 m/s and 0.209 m/s respectively. The flow and the flame are observed to be laminar in nature. The radiative heat flux measurements are made along an axis parallel to that of the flame and at a radial distance of 54.3 mm from the flame centerline. A heat flux transducer is used for the heat flux measurement. Further details of the experimental setup are provided in [213].

For the numerical solution of the above flame, a cylindrical computational domain is chosen. The computational domain and its dimensions are shown in Figure 6.3(a). The fuel injector and the annular coflow tube are modeled as in the experiments. The outer boundary of the computational domain is modeled as a cylinder (of diameter 102 mm) with slip velocity on the boundary to simulate the real open domain. The fluid boundary conditions imposed on the computational domain are shown in Figure 6.3 (b). The fuel and air inlets are modeled as characteristic based boundary conditions with target mass flow rates and temperatures imposed. Target pressure of 1 Atmosphere is fixed at the outlet boundary as well. The fuel injector walls are modeled as isothermal walls at room temperature.

For the radiative boundary conditions, all boundaries except that of the fuel injectors are treated as black walls with a temperature of 298 K. At the outlet boundary, the mean temperature of the flue gas is imposed. On the fuel injector wall, an emissivity of 0.8 is used.

In order to use the LESAULTS approach, the computational domain is split into sub-domains in a manner similar to that used in Sandia-D flame discussed

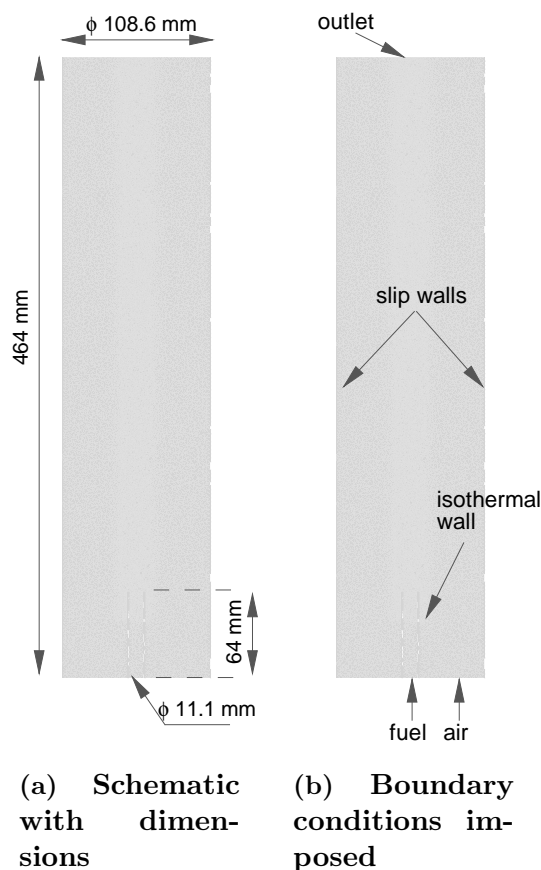


Figure 6.3: Computational domain used for simulating the diffusion flame. (a) The geometrical dimensions (b) Boundary conditions used in the analysis

in Chapter 4. The method of discretisation and the computational domains (AVBP01 and AVBP02) used are shown in Figure 6.4. The smaller domain AVBP01 encloses the region immediately downstream of the fuel injector lip. When using a conventional AVBP simulation, this is the region where typically small elements and hence smallest time steps are observed. Hence, it is desirable to demarcate this zone from the rest of the computational domain where relatively larger time steps are allowed numerically. For the present study, this region is chosen such that it has a diameter of 20 mm and extends downstream to approximately 10 times the diameter of the fuel jet. The overlapped zone between AVBP01 and AVBP02 can also be observed in the Figure. Tetrahedral elements are used to generate the meshes in AVBP01 and AVBP02. The smallest element size used (in AVBP01) is 0.25 mm while in regions far away from the flame, the maximum element size of 4 mm is used. The mesh elements generated near the fuel injector lips and at the midplane are shown in Figure 6.4. For implementing the LESAULTS approach, a time step of $1.0 \times 10^{-8} \text{ sec}$ is used in AVBP01 while

6. MODELING RADIATIVE HEAT TRANSFER EFFECTS

the time step used in AVBP02 is $5.0 \times 10^{-8} \text{sec}$ ($R_{\delta t,1} = 5$). The grid and time step details are provided in Table 6.1.

Similar to the flow configuration, the same computational domain is chosen for the PRISSMA solver. Tetrahedral elements are used to generate the mesh in the computational domain. Fine mesh elements (size 0.5 mm) is used in the near flame region while a coarser mesh size (2 mm) is chosen near the outer boundaries. The mesh generated at the midplane is shown in Figure 6.5.

The coupled LESAULTS-PRISSMA simulation is carried out using 540 computational cores. The τ_P and τ_A values obtained while carrying out simulation using 1 core is found to be 73.5 and 52.8 seconds respectively. Based on these values and using Eqs. 6.29, 417 and 96 cores are dedicated to AVBP01 and AVBP02 respectively. The remaining 27 cores are used for PRISSMA computations. To obtain the numerically observed speed up and to demonstrate the speed up using LESAULTS, simulation was also carried out using the conventional (asynchronous) AVBP-PRISSMA coupling approach for 100 AVBP iterations and one iteration of PRISSMA. By comparing the conventional and LESAULTS coupling approach, the numerically observed speed up value is found to be 1.55. The theoretical speed up limit for this configuration obtained from Eq. 6.32 is found to be 1.69 and is very close to that found in the numerical experiment as well thereby proving the speed-up capability using LESAULTS-PRISSMA approach.

Sub-domain	Number of nodes	Δt (sec.)	$R_{\delta t}$	speedup $_{L-P}$
AVBP01	969128	1.0×10^{-8}	5	1.69
AVBP02	1063194	5.0×10^{-8}	1	

Table 6.1: Details of the mesh and time step size used in the LESAULTS approach, along with the speed up obtained

For the LESAULTS approach, the Lax-Wendroff scheme is used. The analytically reduced mechanism derived in Chapter 5 using 23 transported and 19 QSS species is used for simulating the reacting flow. The PRISSMA solution is carried out using the S4 quadrature (24 directions). The FSK model is used for spectral integration. The convergence criterion is set to an error level of 0.01.

The fluid flow results obtained using the LESAULTS approach is shown in Figure 6.6. The contours of steady-state temperature and mass fractions of CO, CO₂ and H₂O at the mid-plane are shown in the Figure. The midplane temperature contour is shown in Figure 6.6(a). The peak temperature observed in the domain is 1900 K while the adiabatic flame temperature for CH₄-Air configuration and for the POLIMI mechanism is 2100 K. Hence a reduction of 200 K in temperature

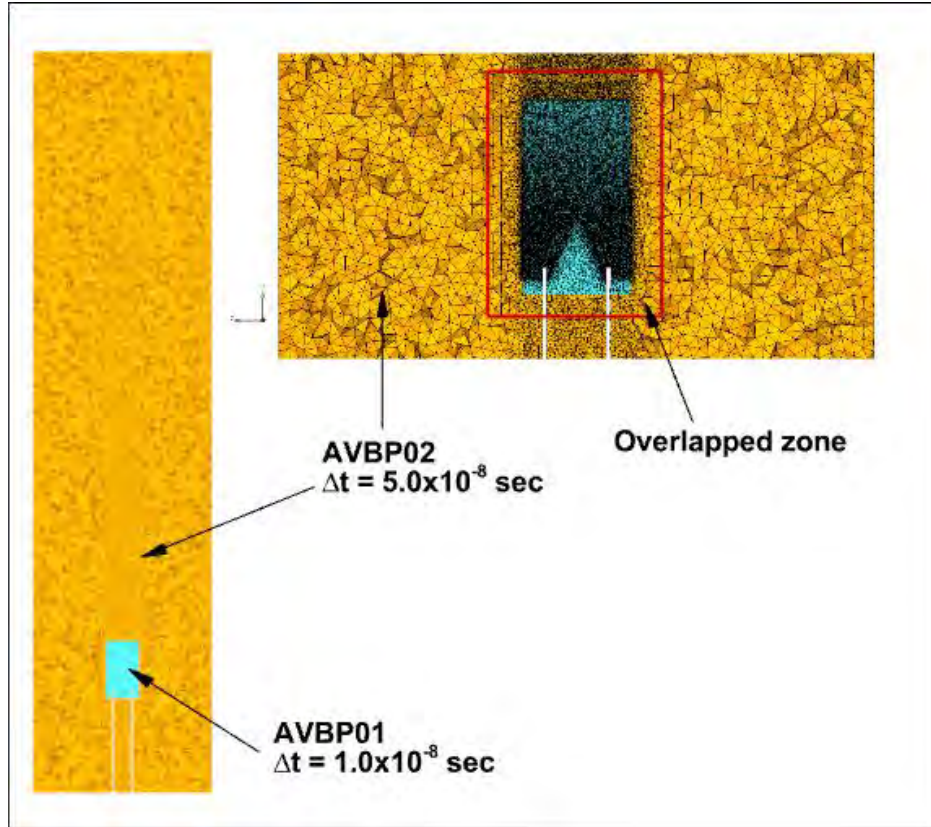


Figure 6.4: Domain decomposition employed for LESAULTS method along with a view of the mesh at the mid-plane.

is observed due to the radiative losses. The flame length (L_f) is calculated based on the OH profile at the flame centerline. The peak gradient in OH is observed at 0.2 m downstream of the fuel jet and hence the flame length is calculated to be 0.2 m. The CO production region and its subsequent conversion to CO_2 from the CO- CO_2 equilibrium can also be observed in Figure 6.6(b,c). The peak concentration regions of H_2O can also be observed in Figure 6.6(d).

The results from the PRISSMA solver is shown in Figures 6.7 (a-c). The divergence of the heat flux vector (S_r) is shown in Figure 6.7(a) and coincides with the region where the CO_2 and H_2O mass fractions are high. This underlines the contribution of CO_2 and H_2O in the radiative heat losses. The x-component of the heat flux in the flame midplane is shown in Figure 6.7(c). The heat flux component is high in regions near the flame, up to the flame height of 0.2 m. Above the flame height, the heat flux component tends to decrease drastically (both in the direction of the fuel injection point as well as in the direction of flow downstream). This is consistent with heat flux measurements made at a radial distance of 0.0543 m and is shown in Figure 6.8. A good match with experimental measurement is observed till the non-dimensional height (y/L_f) of

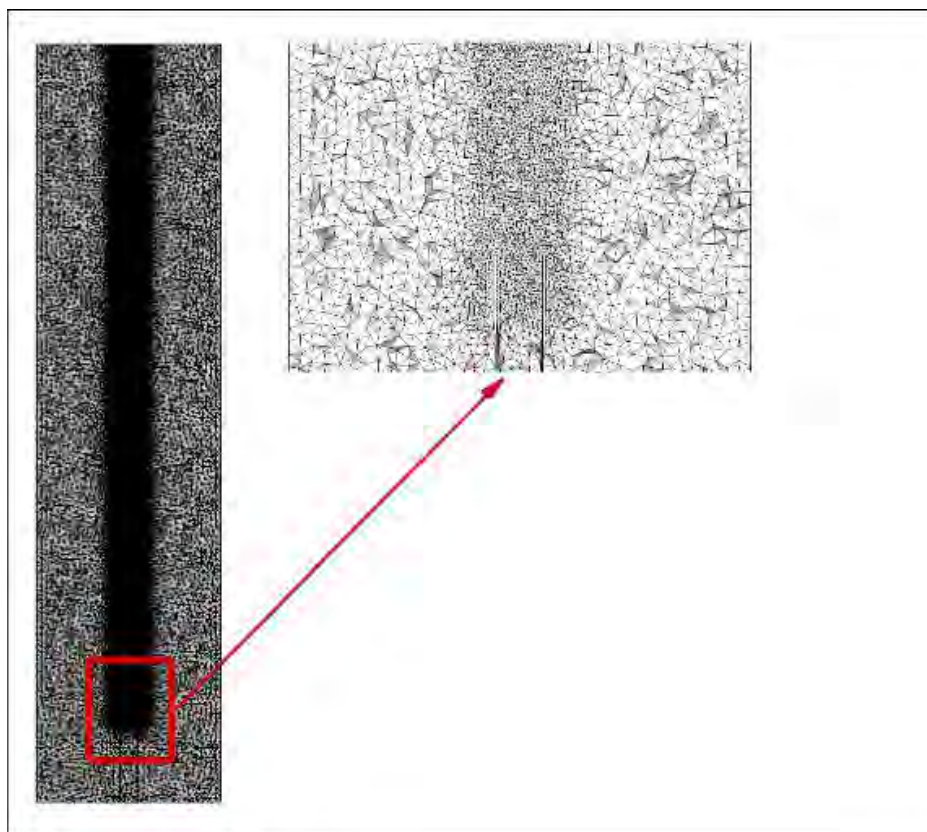


Figure 6.5: Computational domain used for simulating the diffusion flame. (a) The geometrical dimensions (b) Boundary conditions used in the analysis

1. Downstream of this location small discrepancies are observed between the measurements and computations.

6.6 Conclusions

In this chapter, the PRISSMA RTE solver is introduced. A brief description of the solver, namely, the angular and spatial discretisation methods used and the spectral models available are described. The two main approaches used for coupling AVBP and PRISSMA solvers are explained. Following this, the coupling approach used for LESAULTS method and PRISSMA solver is detailed. The expressions for optimum computing core distribution in such a configuration is analysed and the theoretical speed up limit obtained using this approach is derived. This approach of coupling is validated using a laminar jet diffusion flame. The calculated and obtained speed up obtained using the approach is in close agreement thereby underlining the efficiency of this approach. The computed and measured heat flux profiles are also observed to be in good agreement with

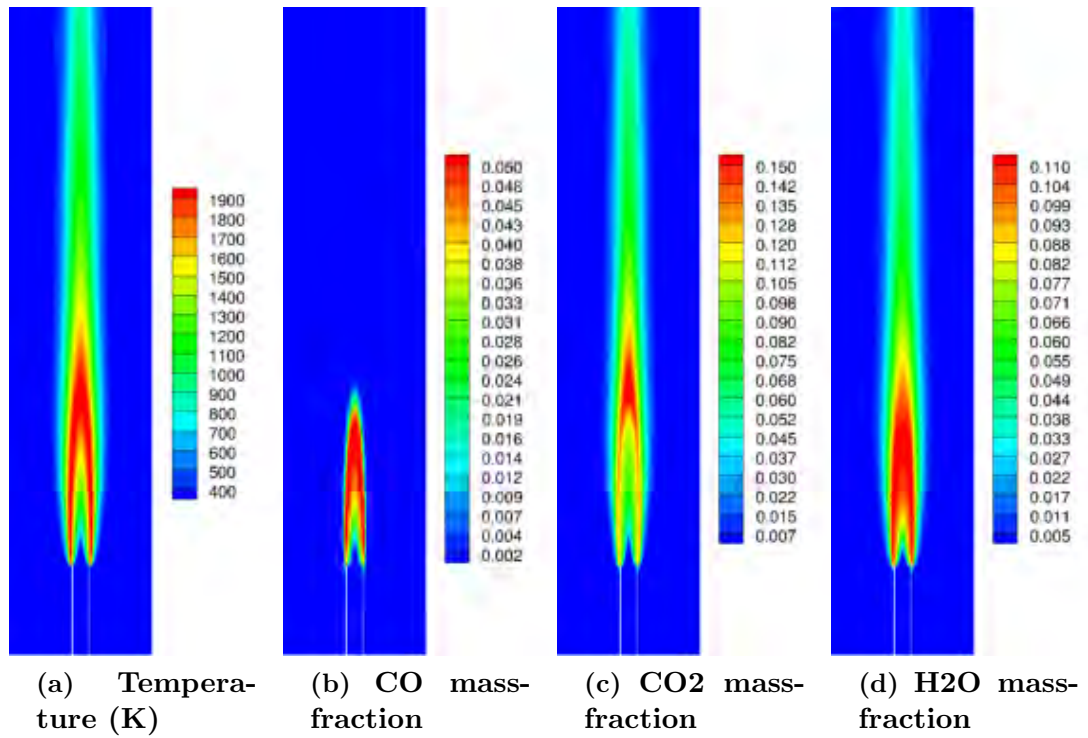


Figure 6.6: Computed solution at the midplane

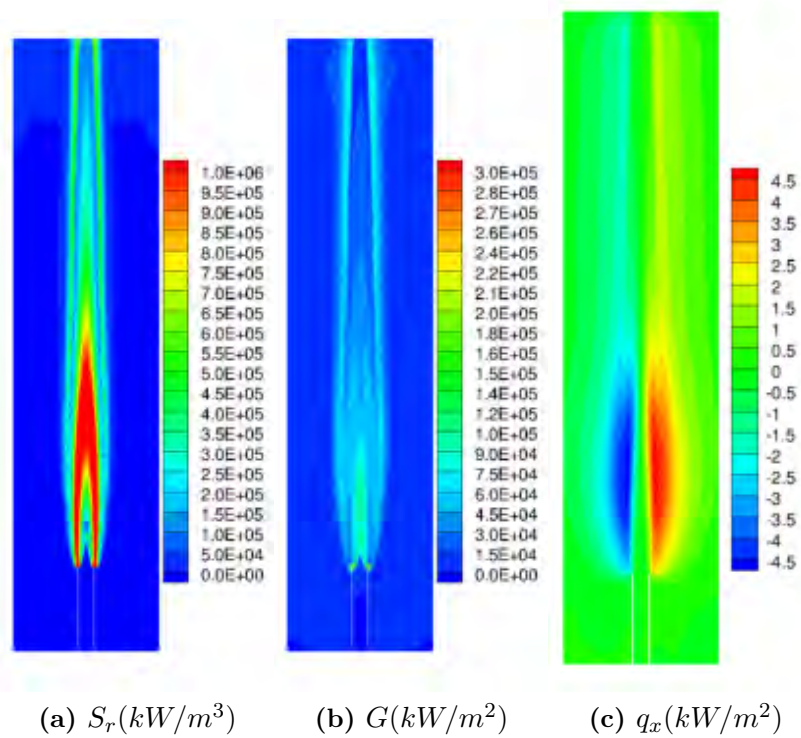


Figure 6.7: The computed radiative source term and heat flux at the midplane

6. MODELING RADIATIVE HEAT TRANSFER EFFECTS

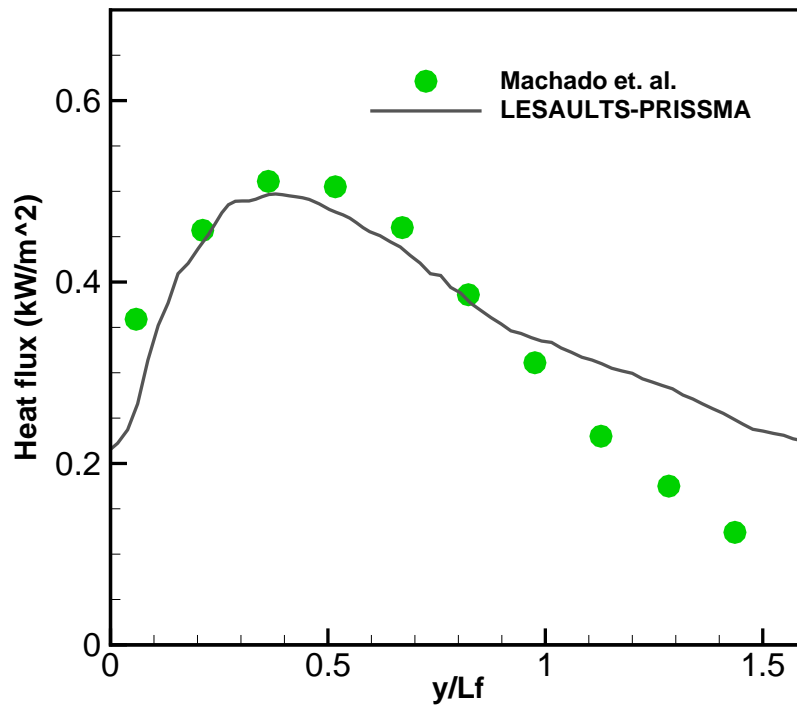


Figure 6.8: A comparison of the measured and computed radiative heat flux

each other further emphasizing the accuracy of LESAULTS-PRISSMA coupling strategy.

Chapter 7

Application to LES of steam cracking furnace

As cited in the introduction, the final objective of this thesis is to perform the LES of a steam cracking furnace. The various sub-models developed towards this objective have been detailed in the prior chapters. These sub-models are now applied simultaneously to simulate the LES of a steam cracking furnace, the details of which are explained in this chapter. This chapter is organized as follows. The description of the test furnace which is numerically simulated is provided in Section 7.1. This is followed by a brief description of the geometry of the furnace simulated and mesh generated for the application of the LESAULTS method in Sections 7.2 and 7.3 respectively. Finally, the results of the LES performed are elucidated in Section 7.5 and the conclusions from this chapter are listed in Section 7.6.

7.1 Test Furnace Configurations

The test furnace used in this study is physically located at the JZHC facility at Oklahoma, USA. This facility is primarily used to test the performance of burners developed at JZHC. A schematic of the furnace is shown in Figure 7.1 (a). The furnace floor is $2.89\text{m} \times 1.98\text{m}$ in cross-section and 13.72m in height. The furnace is of natural draft type and houses two CoolStar[®] burners separated by a centerline-to-centerline (burner pitch) distance of 1.195m from each other and are located equidistant from both the side walls of the furnace. 8 vertical reactor coils are located close to the furnace wall opposite to that of the burners to simulate the flow of the process gases. The diameter of each of these coils is 32.65 mm and is covered with an insulation (Durablank sheet) of thickness 1 inch. The firebox walls are also insulated using brick walls and ceramic insulation material.

7. APPLICATION TO LES OF STEAM CRACKING FURNACE

Each of the CoolStar burners used in the study is of 2.23 MW power rating. A schematic of the CoolStar burner used in the test is shown in Figure 7.1(b). The air enters the burner through the windbox and passes the muffler to suppress noise. The incoming air is then deflected upwards using a baffle located inside the plenum. Fuel for combustion is provided to the burner through the fuel manifold (colored in green). The main fuel manifold is divided into 9 fuel injection pipes located circumferentially around the burner tile. Each of these fuel injection pipes is separated from each other by an angle of 36° with respect to the burner centerline. Out of the 9 fuel injection pipes, 4 are used to provide fuel to staged fuel injection ports and 4 are connected to primary fuel injection ports. The remaining fuel pipe is connected to the front primary fuel injection port. The staged ports consist of 3 fuel injection orifices directed upwards such that the fuel issuing out of these injection orifices skim vertically and parallel to the burner tile walls. The primary fuel ports on the other hand comprise of 5 fuel injection orifices, out of which two are directed radially inward towards the burner centerline and the remaining three injection holes are directed upwards similar to the staged injection holes. The front primary port consists of 4 injection orifices out of which two are directed radially while the remaining are directed vertically upwards. The top view of the burner in Figure 7.1(b) shows the location of the fuel injection ports.

Experiments are performed with natural gas as the fuel and air as the oxidizer. The fuel and air inlet properties are listed in Table 7.1. Respecting the confidentiality requirements of JZHC, these properties and results are expressed in terms of non-dimensional quantities. The temperature of the fuel is denoted as T_f and is measured to be 1.0112 times the temperature of the air (T_a) entering the plenum. The mass flow rate of fuel (\dot{m}_f) and air (\dot{m}_a) are also measured and are related to each other by $\dot{m}_f = 0.0528\dot{m}_a$. The gauge pressure at the draft outlet of the furnace is measured as 0.98 Atm. Water at a temperature of T_w K is sent through the reactor coils to simulate the flow of process gas. The exit temperature as well as the flow rate of water are available from measurements. Experimental measurements of the temperature at three locations inside the firebox are available. Also, heat flux measurements at the firebox mid-plane is also available for comparison with data.

Boundary	Temperature (K)	Mass flow rate (kg/s)
Air inlet	T_a	\dot{m}_a
Fuel manifold inlet	$T_f = 1.0112T_a$	$\dot{m}_f = 0.0528\dot{m}_a$

Table 7.1: Air and fuel flow rate and temperature measured in the test

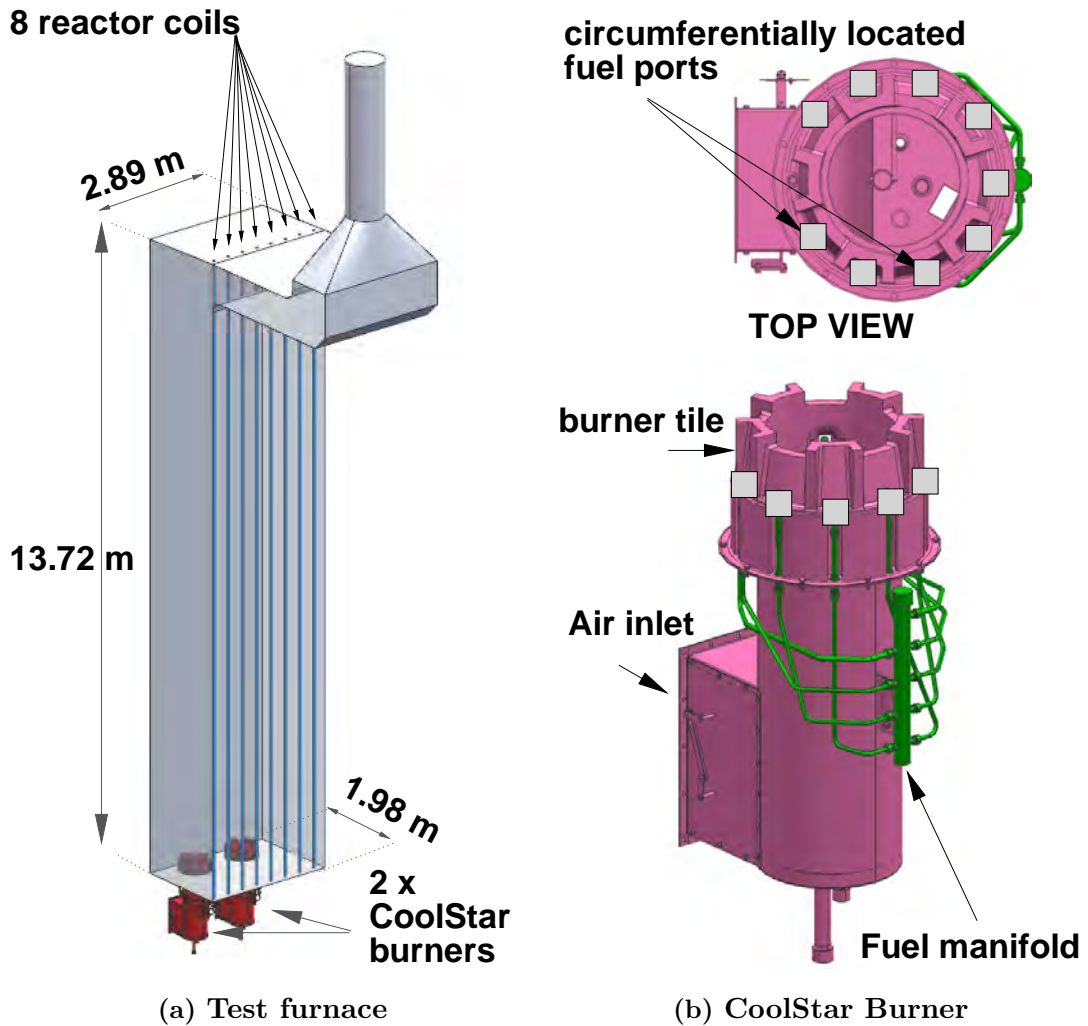


Figure 7.1: Schematic of the test furnace and the burner used in this study

7.2 Geometric modeling

7.2.1 Computational Domain

Having described in brief the experimental test facility, the geometric modeling aspects are discussed next. Taking advantage of the symmetric configuration of the test furnace, only one-half of the test furnace comprising of a single burner and 4 reactor coils is simulated. The simplified computational domain is shown in

7. APPLICATION TO LES OF STEAM CRACKING FURNACE

Figure 7.2(a). The plane passing through the middle of the two burners is treated as a symmetric boundary condition. The burner geometry is cleaned using CAD software to remove all irrelevant geometrical features that can potentially create small elements at locations irrelevant to the objectives of this study. The fuel manifold is simplified by modeling only the individual fuel injection pipes rather than the entire fuel manifold. The fuel flow rates through these pipes are provided in Table 7.2. The fuel port locations and their nomenclature are mentioned in Figure 7.2(b).

Boundary	Temperature (K)	Mass flow rate (kg/s)
Front primary fuel	T_f	$0.045 \dot{m}_f$
Side primary fuel	T_f	$0.521 \dot{m}_f$
Side staged fuel	T_f	$0.434 \dot{m}_f$

Table 7.2: Fuel flow rates and temperature through various fuel circuits modeled as boundary conditions

The same computational domain with one burner used for AVBP is also used for the PRISSMA RTE solver.

7.2.2 Boundary conditions

At the air inlet, characteristic based inlet boundary condition is provided with the measured mass flow rate and temperature at the boundary specified as targets. The same boundary condition is also specified at the fuel injection pipes with specified mass flow rate, temperature and species mass fraction. As mentioned in the previous section, the fuel used in the test is natural gas and is simulated as pure methane in this study. The temperature and the fraction of the total fuel flow rate flowing through the different fuel pipes are provided in Table 7.2. At the outlet boundary, the characteristic based outflow boundary condition is specified with target pressure specified as the experimentally observed value (0.98 gauge pressure). Since no measurement or computational data is available on the temperature or heat flux on the furnace and burner walls, adiabatic boundary conditions are enforced on these walls. Also, an approximate boundary condition is used to model the heat loss through the reactor coils. In this method, the reactor coils are not geometrically modeled. Rather, the projected areas of the reactor coils on the furnace walls are modeled as non-adiabatic walls with specified enthalpy loss. By using this approach, the presence of small elements to resolve the reactor coil curvature is avoided while still preserving the overall enthalpy balance of the furnace. The enthalpy loss through the walls are calculated from

the mass flow rates of water and the difference in inlet and outlet temperatures which are available from measurements. This way, the overall enthalpy balance of the system is fully modeled while still using simple and robust boundary conditions. The enthalpy loss (non-dimensionalised by the total enthalpy loss through all the 4 reactor coils) through the modeled reactor coil boundaries are provided in Table 7.3.

Reactor coil	T_{in} (K)	T_{out} (K)	\dot{m}_w^*	ΔH^*
T1	T_w	$1.104 T_w$	0.342	0.496
T2	T_w	$1.045 T_w$	0.189	0.117
T3	T_w	$1.045 T_w$	0.247	0.153
T4	T_w	$1.076 T_w$	0.221	0.234

Table 7.3: Inlet and outlet water temperature and flow rate of water flowing through the reactor coils. The reactor coil T4 is the closest to the symmetry plane and T1 is the farthest

The boundary conditions used in the PRISSMA solver is detailed next. The air and fuel flow inlets are treated as perfect emitters with emissivity of 1.0 and the known gas temperature enforced. All the wall boundaries are modeled as diffuse. Based on the inputs provided by JZHC, the reactor coil boundary condition is modelled as a diffusive wall with an emissivity value of 0.9. The furnace and burner wall emissivities are fixed at a constant, uniform value of 0.8. At the symmetry boundary, a symmetric boundary condition discussed in section 2.3.3 is used.

7.3 Grid generation

LESAULTS method along with the reduced mechanism derived in Chapter 5 is applied to the LES of JZHC pilot furnace configuration. The computational domain is divided into three overlapping sub-domains (AVBP01, AVBP02 and AVBP03) as shown in Figure 7.3 (a). Fine cells with a characteristic mesh element size of $0.1mm$ used to resolve the fuel jets are located in AVBP01 and hence a small value of time step ($1.0 \times 10^{-8}sec$) is used.

Most of the flame region in the furnace was anticipated to be in the sub-domain AVBP02 and hence fine elements of size ranging from 5 to 20 mm although with a relatively higher value of time step ($1.0 \times 10^{-7}sec$) is used here. It is also interesting to observe that a higher time step can be used in this sub-domain due to the alleviation of stiffness by the use of QSSA during the chemical mechanism reduction process. The sub-domain AVBP03 is the region comprising mostly of

7. APPLICATION TO LES OF STEAM CRACKING FURNACE

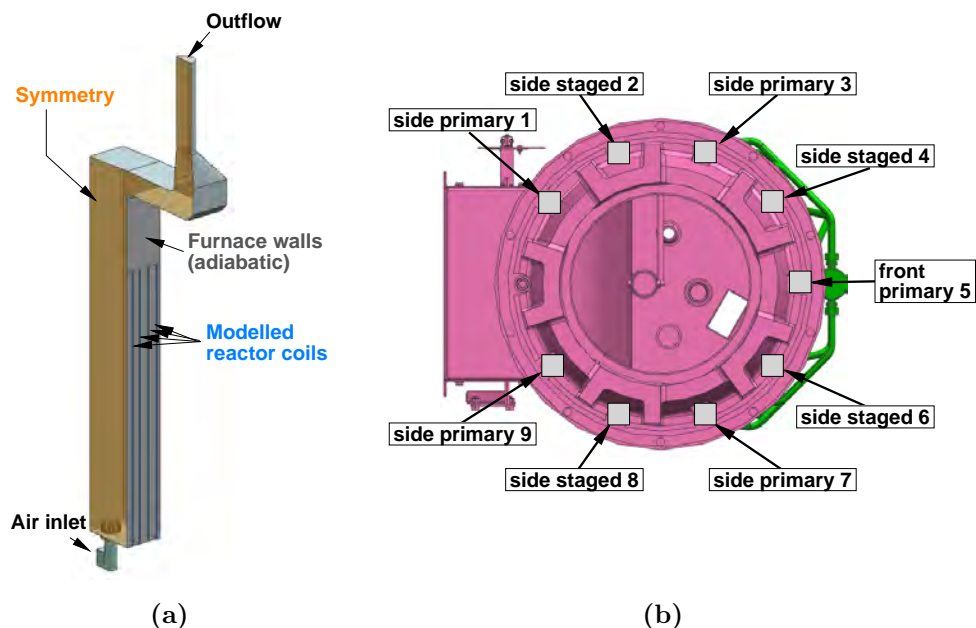


Figure 7.2: (a) The computational domain and boundary conditions used for LES of furnace. (b) Nomenclature of staged and primary fuel pipes

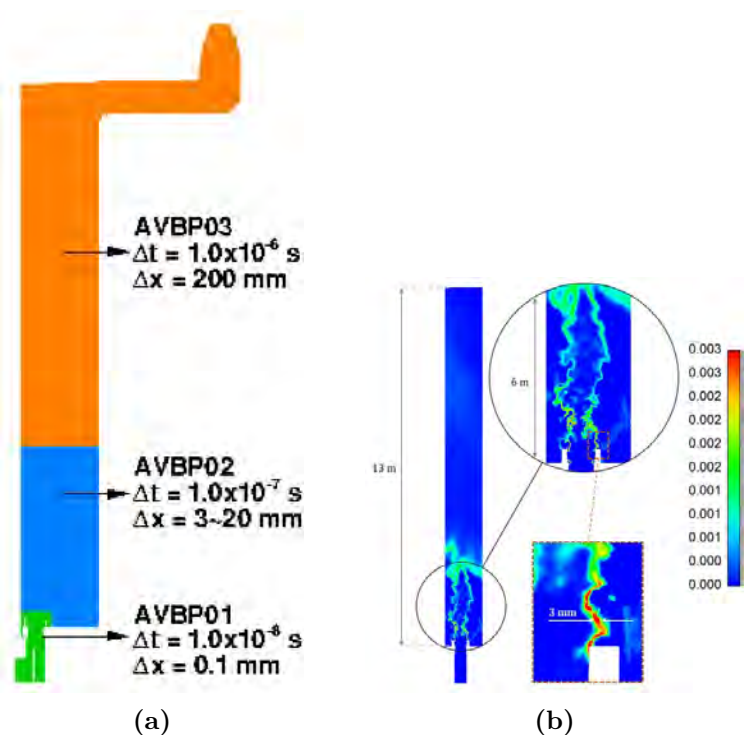


Figure 7.3: (a) The domain decomposition strategy used in LES. Furnace divided into 3 overlapping sub-domains with different time steps (b) OH mass fraction contours on a vertical plane passing through the center of the burner

the plume and not much of primary combustion reactions are anticipated to occur in this sub-domain. Hence a coarse mesh of size 200 mm and a larger time step ($1.0 \times 10^{-6} \text{sec}$) is used. The meshes in all the sub-domains are generated using tetrahedral elements. LES of the furnace is carried out using LESAULTS method based on the above-mentioned domain-decomposition strategy.

For the RTE analysis, a separate single mesh is generated in the same computational domain. The mesh consists of tetrahedral elements. Unlike the mesh used for LES, relatively coarser elements are used for PRISSMA solver. While coarser elements (of approximate size 100 mm) are used in the plenum where the flow is essentially non-reactive, finer elements (of size 50 mm) are used in the near-flame and plume regions.

7.4 Computational settings

The gas mixture based on the analytically reduced mechanism is used in the LES solver AVBP. The thermodynamic and transport properties of this mixture has already been discussed in chapter 5. The finer details of the mechanism is provided in Appendix A. Even though TTGC is proved to be more accurate, the LW scheme is used for this study due to its low computational cost when compared to TTGC. The Sigma model is used for sub-grid scale closure and both the turbulent Schmidt and Prandtl numbers are fixed at a value of 0.6. The artificial dissipation model due to Colin is also activated to reduce the high-frequency errors that can inadvertently arise to poor quality elements. For the present study, no turbulent combustion model is included. As will be shown later, the flame inside the furnace is predominantly non-premixed in nature. The behavior of turbulent non-premixed flames is quite different from that of a turbulent premixed flame when computed on coarse meshes. Hence, the thickened flame models currently available in AVBP is not specifically suited for non-premixed flame computations. Specifically, non-premixed flames do not exhibit any specific consumption speed or flame thickness and hence adapts itself to the coarse mesh used for computation. This particular aspect and preliminary work on developing a combustion model for non-premixed flame is provided in [214]. The inclusion of this model for the LES of a furnace is left as possible work for the future.

For the radiation solver PRISSMA, the FSK model is used for spectral integration. The diamond mean flux scheme is used for spatial integration along with S4 quadrature for angular discretisation.

To begin with, the LES simulation is initialised with stagnant air in the entire computational domain. Once the simulation progresses and adequate fuel-air

7. APPLICATION TO LES OF STEAM CRACKING FURNACE

mixing is achieved the fuel-air mixture is numerically ignited by artificially enforcing adiabatic temperature in the gas mixture lying close to the stoichiometric mixture fraction surface. This step initiates the combustion reactions and a sustained flame is observed to develop in the domain. The LESAULTS-PRISSMA coupling is not activated, to begin with. Once the dominant flow structures develop, the coupling is activated. As discussed in chapter 6, the asynchronous coupling approach is used with the coupling between the codes occurring after every 100 iterations of the LESAULTS solver. The simulation is performed for a total flow through time of 20 secs. LES using the LESAULTS-PRISSMA method provided an actual speedup of 3.4 when compared to the conventional LES simulation. This is close to the theoretical speedup value of 3.6. This value of speed-up could be even further augmented by optimizing the domain decomposition strategy based on the now available knowledge of the flow and reaction zones that demand restrictive time steps.

In order to demonstrate the effectiveness of LESAULTS method in resolving the various scales in the furnace, an instantaneous field of the OH mass fraction is visualized in Figure 7.3 (b). The multiple length scales present in the reaction zone ranging from the large ones (characteristic size of 6 m) in the plume to the smallest ones near the flame stabilization region (characteristic size of 3mm) close to the burner tile top is well captured.

7.5 Results

Mean Flow Field

Time-averaged vertical velocity component on a vertical plane passing through the burner center is visualized in Figure 7.4 (a) . After combustion occurs near the burner, the hot combustion products rise upward and gradually lose heat near the front furnace wall where the reactor coil heat loss is applied. This results in the formation of a strong recirculation zone, (RZ1). A portion of the recirculating flow from RZ1, skims along the furnace walls and the symmetry plane and eventually gets entrained by the burner jet near the rear furnace wall. This results in the high values of the vertical velocity component observed near the rear furnace and burner walls. The entrainment of RZ1 slightly bends the burner jet flow direction causing an additional, weak recirculation zone (RZ2) close to the rear furnace wall. RZ1 has a height of 4m while RZ2 is relatively weak in strength and measures only 1.5m in height. Farther downstream of RZ1 and RZ2, the velocity is reduced although its profile on a horizontal plane peaks closer to the front furnace wall.

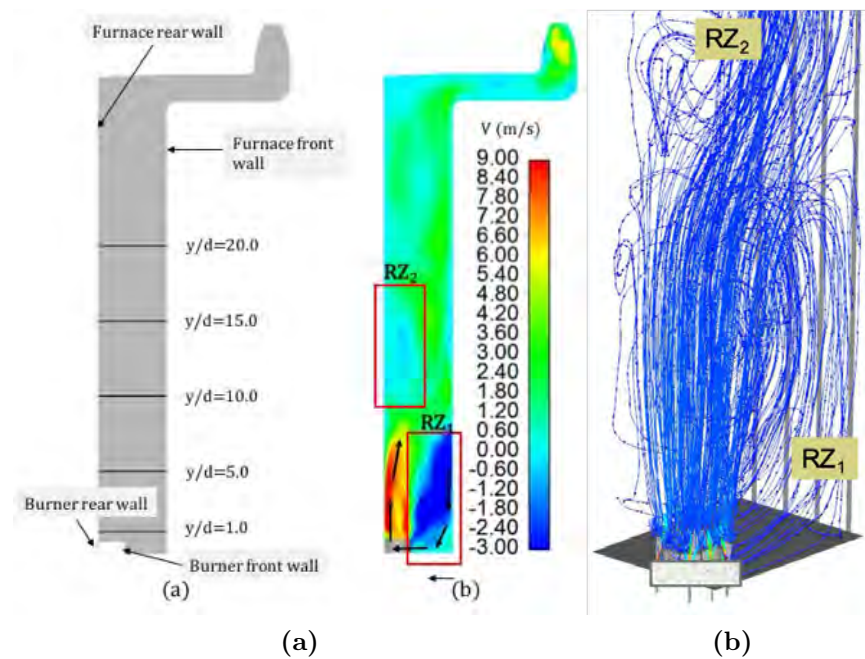


Figure 7.4: (a) The mean vertical velocity contours on the furnace mid-plane. (b) Streamlines from the mean velocity field inside the furnace

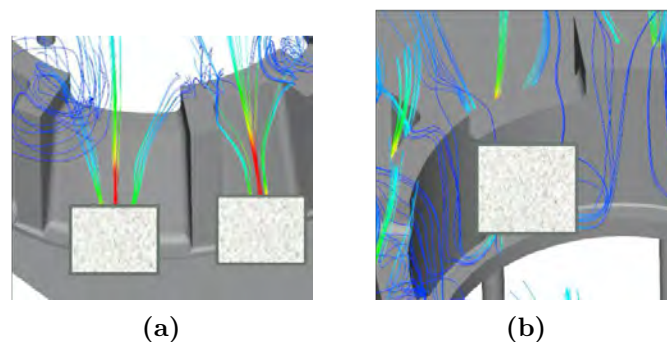


Figure 7.5: (a) Mean streamlines emanating from the staged and primary fuel ports outside the burner (b) Mean streamlines entering radially into the burner

7. APPLICATION TO LES OF STEAM CRACKING FURNACE

This is evident from the streamlines from the mean velocity field in the furnace shown in Figure 7.4(b). The flow field in the recirculation zones RZ1 is clearly visible with the streamlines converging towards the burner after losing heat to the reactor coils and entraining the fuel jet. The mean streamlines inside the burner is also shown in Figure 7.5 (a) and (b). The fuel jets emanating the staged fuel ports is observed to be guided by the burner tile and are ejected vertically upwards to be ultimately mixed with the air coming from the burner center. On the other hand, radial fuel jets emanating from the primary fuel ports travel radially towards the center of the burner. These jets traverse along the coanda surfaces on the burner tiles where they lose momentum. The jets are then diverted vertically upwards by the vertical stream of air coming from the plenum. These aspects of the flow field determine the manner in which fuel-air mixing occurs and in determining the flame shape and flame anchoring as will be shown in the later sections.

Turbulence field

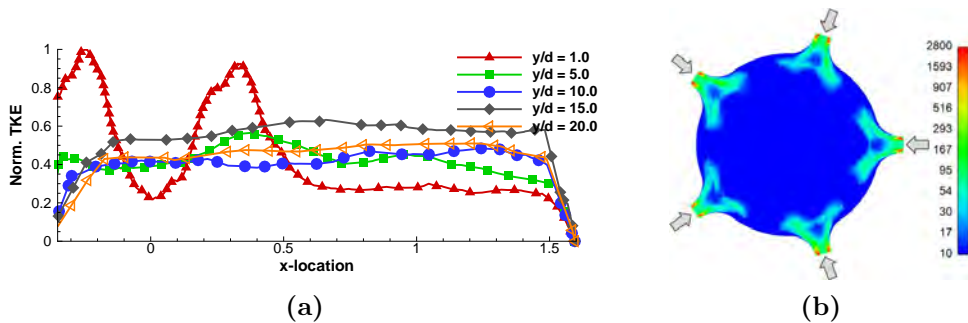


Figure 7.6: Non-dimensional TKE (a) profiles at various heights along the furnace mid-plane (b) contours at the horizontal plane passing through fuel orifice.

The turbulent kinetic energy (TKE) is a measure of the turbulent fluctuations in velocity and is an indicator of the level of turbulent mixing present in the flow. The TKE values are extracted from the flow statistics its values in the furnace and burners are plotted in Figure 7.6. Figure 7.6(a) shows the profiles of TKE at horizontal planes located at various heights above the burner. These horizontal planes are chosen at $y/D = 1, 5, 10, 15$ and 20 . The $y/D = 1$ plane is located just downstream of the burner tile while the $y/D = 20$ plane is located downstream of the flame. These planes are plotted and shown in the schematic in Figure 7.4(a). The profiles are non-dimensionalised using the maximum value of TKE at the $y/D = 1$ plane. At $y/D = 1$, two peaks on the TKE profiles can be observed.

This arises from the mixing of the fuel and air stream near the burner tile exits. A relatively high value of TKE, when compared to the other planes is also observed. This indicates a high level of mixing of the jets. At planes downstream, the TKE profiles assume uniform profiles indicating more or less uniform turbulent mixing. The peak values of TKE on these planes is also found to be low indicating lower levels of turbulence.

The TKE contours on the horizontal plane containing the fuel jet orifices is shown in Figure 7.6 (b). Very high values of TKE (when compared to the values observed in the firebox) can be observed near the fuel orifice ports. This is due to the strong shear created by the high speed fuel jet-air mixing and is indicative of good fuel-air mixing.

Mixing and Thermal field

The velocity field inside the burner determines the shape and extent of the fuel-air mixing field. To analyse this aspect, the mean mixture fraction field is analysed. The definition of Bilger is adopted to compute the mean mixture fraction field and is shown in Figures 7.7. In mean mixture fraction field at a horizontal plane passing through the radial fuel injection ports is shown in Figure 7.7(a). Being a passive scalar, the field of mixture fraction traces how fuel is convected and diffused in the flow. At the horizontal plane, the presence of Coanda surfaces results in a flower-shaped stoichiometric mixture fraction field shown in black color in the Figure. One can observe that inside the burner, the field is anchored on the curved surface of the burner tile. However, this is not the only location where the stoichiometric mixture fraction surface is observed. The fuel ejecting out of the vertical fuel injection holes interacts with air from the burner and results in the stoichiometric surface being anchored on the top of the burner tile as shown in Figure 7.7(b). Hence one observed two distinct regions where the mixture fraction field is found to anchor.

The iso-surface of mixture fraction is also found to be coincident with that of the flame surface indicating a predominantly non-premixed flame. This can be observed from the temperature field inside the burner shown in Figures 7.8. The mean temperature field on two horizontal planes, one passing through the radial fuel injection holes and the other located immediately downstream of the burner tile are shown. The flower-shaped flame typical of ultra low-NO_x burners is evident in the contour. This shape of the flame helps in increasing the flame surface area thereby aiding in NO_x reduction. Apart from this flame which is located completely inside the burner tile, the secondary flame is found to anchor

7. APPLICATION TO LES OF STEAM CRACKING FURNACE

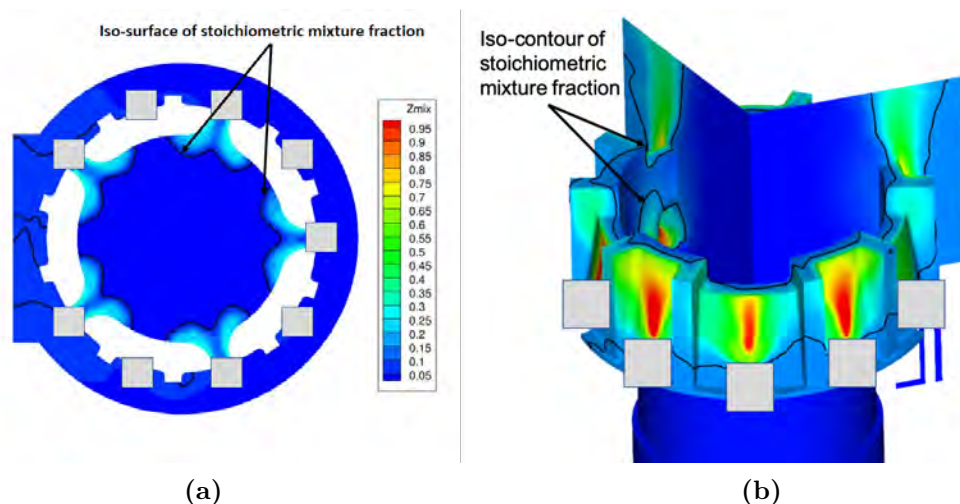


Figure 7.7: (a) Mean mixture fraction field at a horizontal plane passing through the fuel injection holes. (b) Mean mixture fraction field inside the burner tile

on the burner tile top as shown in Figure 7.8(b). Hence, two separate combustion zones, typical of staged fuel burners, are observed in this simulation.

A stable flame with two distinct combustion zones namely, the primary and the secondary flame zones are found to occur inside the furnace. The primary flame zone is located inside the burner where the radially injected primary fuel burns with air coming from the plenum. This zone is compact in shape, occupying less than 1% of the total furnace volume and contributing only 8% to the total heat output to the process gas. On the other hand, the secondary flame zone is formed from the staged fuels and is stabilized on the burner tile top. This can be observed from the time-averaged temperature field at a horizontal plane immediately downstream of the burner tile shown in Figure 7.9

The high temperature zones on the tile walls indicate secondary flame anchoring. High temperature region can also be observed near the burner rear wall due to the entrainment effect of RZ1 as explained previously. This zone aids in the heating of the process gas by contributing the remaining 92% of the heat of combustion. This zone also occupies nearly 25% of the furnace volume and determines the shape of the heat flux profile incident on the reactor coils. The mean flame surface in the secondary zone identified as an isotherm with a temperature of 1600K is shown in Figure 7.9 (b).

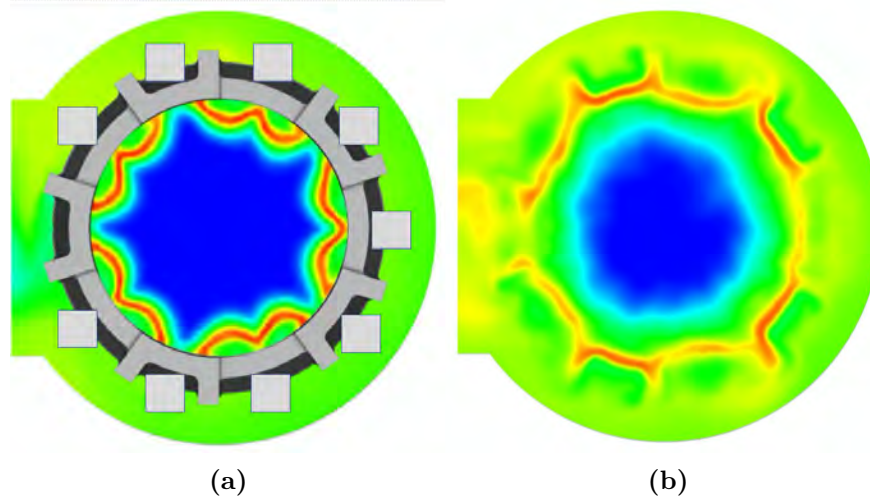


Figure 7.8: (a) Mean temperature contours on a horizontal plane passing through the radial fuel injection holes. (b) The mean temperature contour at a horizontal plane immediately downstream of the burner tile

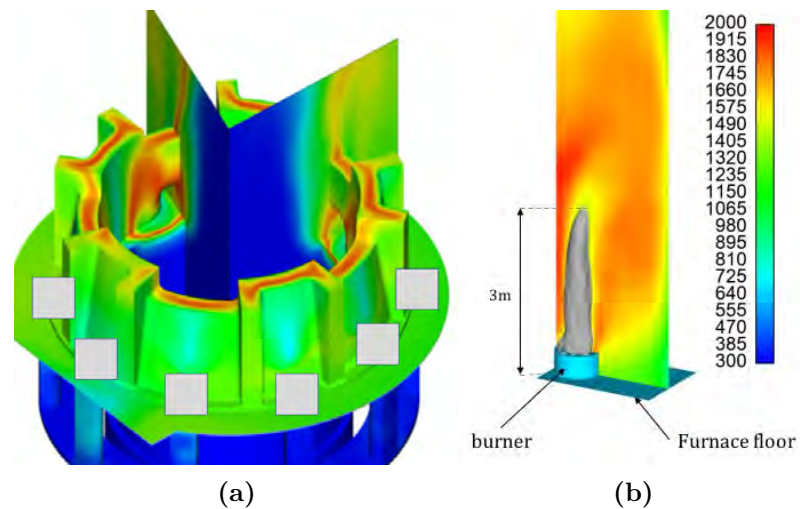


Figure 7.9: (a) Mean flame temperature observed at a plane in the vicinity of burner tile (b) Mean temperature field on the vertical plane passing through burner center

7. APPLICATION TO LES OF STEAM CRACKING FURNACE

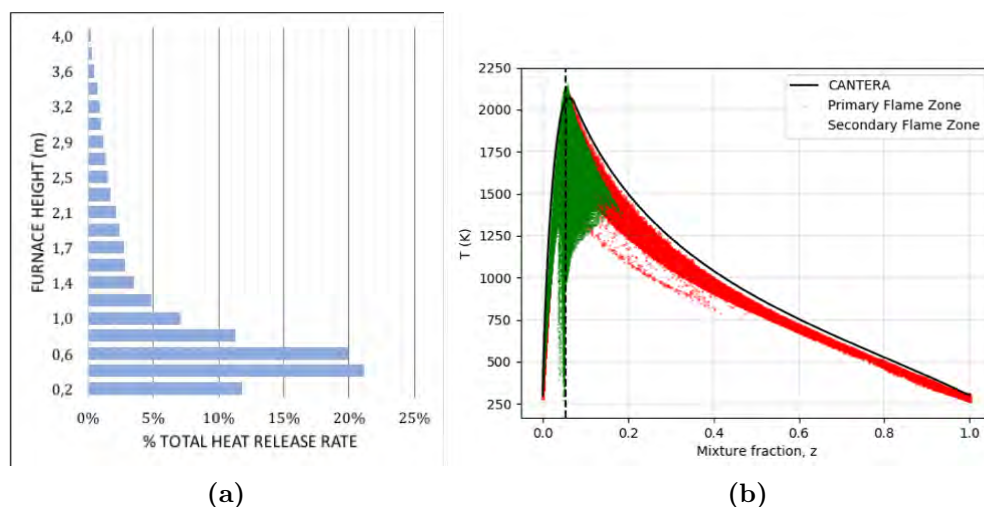


Figure 7.10: (a) Integrated heat release rate as a function of furnace height. (b) Scatter plot of instantaneous temperature in the mixture fraction space

Figure 7.10(a) shows the total heat released from combustion as a function of furnace height. It is observed that 98% of the heat of combustion occurs within 4m height of the furnace and 80% of which is restricted in the bottom 2m. This implies that the flame inside the furnace is compact as most of the combustion reactions are completed by a short height of the furnace. The remaining height of the furnace essentially comprises of burnt combustion products.

To study the structure of the flame, a scatter plot of temperature is made in the mixture fraction space and is shown in Figure 7.10(b). The plot is prepared by considering the points in the zones AVBP01 and AVBP02 as a function of the mixture fraction. The red dots indicate points on the flame belonging to the primary flame zone. One can observe points in the zone present along all values of the mixture fraction. This indicates combustion of fuel and fresh air occurring in the primary zone. The green dots in the plot correspond to points outside of the burner and fall in the secondary combustion zone. Most of the points in the zone fall in towards the oxidizer region of the plot. This is indicative of mixing and combustion of air with flue gases. Low temperature green points lying on the stoichiometric mixture fraction line are also observed and are the points which lose heat to the reactor coils and are cooled down after combustion.

A comparison of the measured and computed mean temperature inside the furnace is shown in Figure 7.11(a). An overall good match in the temperature predictions is observed although temperature is slightly over predicted at the mid-furnace. The mean heat flux profiles are also compared with experimental values in Figure 7.11(b) and exhibit good agreement with each other.

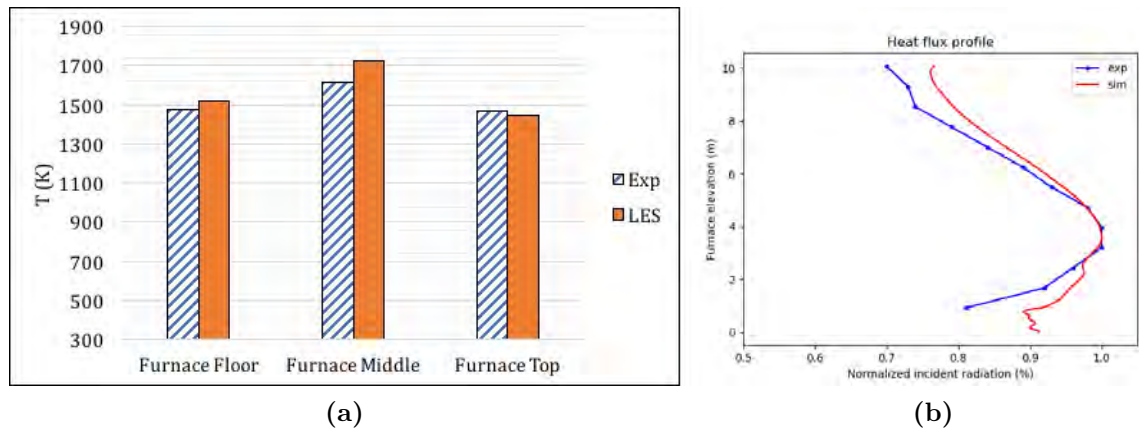


Figure 7.11: (a) Measured and calculated temperature values at three vertical locations inside the furnace. (b) Measured and computed heat flux profiles

Figure 7.12 shows the linear variation of time-averaged mass fractions of CO_2 , CO and NO on horizontal planes located at 1, 2, 5 and 10 diameters downstream of the furnace floor. The burner centerline is located at $x = 0$. The CO_2 mass fraction exhibits a nearly flat profile for planes with $y/D = 5$ and 10 with their values close to that of equilibrium values. This is indicative of complete combustion and high residence time of the recirculation zones. For $y/D = 1$ and 2, low non-zero values of CO_2 mass fraction is observed on the burner centerline due to the combustion occurring in the primary flame zone. The high temperature region near the rear furnace wall is conducive for the oxidation of methane to form CO. This can be observed from the regions of high CO mass fraction near the rear furnace wall observed till $y/D = 5$. Downstream of this plane, the CO mass fraction tends to decrease due to its oxidation to CO_2 . The location of peak CO mass fraction is also observed to shift to the right as one moves downstream, due to the bending of the flame due to recirculation zone. The high temperature zone near the rear furnace wall causes NO to be produced through the thermal mechanism as can be observed from the NO mass fraction values on all horizontal planes. The high temperature zone near the front furnace wall at $y/D = 5$ also explains the region of high NO at $x = 0.8\text{m}$. Downstream of this plane, the NO profiles tend to acquire a uniform profile.

7. APPLICATION TO LES OF STEAM CRACKING FURNACE

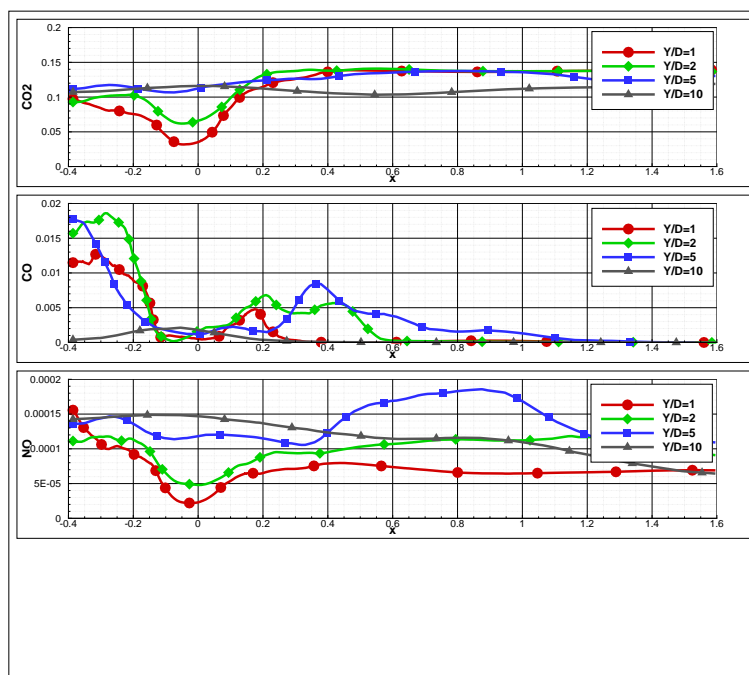


Figure 7.12: Mean species mass fraction profiles at various horizontal planes downstream of the burner

7.6 Conclusions

The objective of the chapter is to demonstrate the application of the LESAULTS approach coupled with an RTE solver in the LES of a steam cracking furnace. The various sub-components in addressing this objective have been derived and discussed in the previous chapters. The LESAULTS method is used in this study by decomposing the full domain of the furnace into three sub-domains with different grid resolution and time steps. Finer grid cells are generated in regions where fine flow and reactive features are anticipated such as inside the burner and in regions close to the fuel injection holes. In the other regions, much larger cells are used to keep the computational cost low. The sub-domains are geometrically overlapping and the mesh in the overlapped zones are generated based on the results from the study recommended in chapter 4. Appropriate and most accurate boundary conditions based on the currently available information are enforced on the boundaries. To keep the computational cost low, the LW scheme is used for the LES in this study. The analytically reduced mechanism derived in chapter 5 with 23 transported species is used in the present LES. These configurations are coupled with the RTE solver PRISMA to account for radiative heat losses inside the furnace. The results show indicate two predominant flow recirculation zones that aid in flue gas recirculation. The peculiar design of the burner tiles

including the presence of coanda surface generates a mixing field that gives rise to a flower-like flame shape inside the burner. The presence of two combustion zones, in the furnace is also observed with both the reaction zones predominantly non-premixed in nature. The combustion reactions are also found to occur very near to the burners thereby indicating a compact flame zone.

Chapter 8

Conclusions and Perspectives

The objective of this thesis is to design, validate and apply a numerical framework for carrying out LES of large combustion devices such as furnaces. This overall objective is achieved by independantly addressing smaller sub-objectives and finally implementing them to study the reactive flow inside a steam cracking furnace.

Firstly, the numerical analysis of two of the most popular schemes in AVBP is carried out using GSA. GSA of these schemes (LW and TTGC schemes) when applied to the linear convection, convection-diffusion and convection-diffusion-reaction equations provide deeper insights into the properties of the schemes when applied to LES. Of particular interest to combustion applications, is the way in which the diffusion and chemical reactions source terms are modeled. The numerical diffusion coefficient can be quiet different from the real diffusion coefficient of the flow thereby changing the properties of the flow and flame. For example, changing the diffusion coefficient can alter the numerically obtained flame speed values in premixed flames and can change the flame thickness and heat release rate in a diffusion flame. Similarly, if not chosen in a DRP compliant manner, the numerical reaction source terms can be considerably different from the real reactive flow scenario. This would imply that numerically, a lower Damkohler number reactive flow is solved for. Hence, it is absolutely imperative for the user to chose the numerical properties (N_c, Pe and Da) such that they are DRP. This thesis also leaves open the following questions: Can these learnings about the properties of schemes be used to derive new combustion/flow models? For example, once the numerical diffusion coefficient is estimated from the local N_c, Pe and Da properties at a grid point, can the diffusion coefficient values be 'corrected' to reproduce the real flame? The author feels it should be possible to develop such models.

Secondly, a new LES acceleration technique (LESAULTS method) is designed and implemented in AVBP that works on overset grids and local time stepping. The method is analysed again using GSA for the LW and TTGC schemes. The regions in the $(kh, N_c$ and $Pe)$ space are identified where the method is found to perform the best. These are also the regions in which conventional LES solvers operate, hence making this method suitable for accelerating LES solvers that use explicit time integration schemes. The theoretical speed up limits of this method are studied and are found to be in very good agreement with the numerically obtained speed up values obtained from numerical tests on the Sandia-D flame and in the case of incompressible flow past a cylinder. The method is also found to perform equally well for different cell element types and found to preserve the order of accuracy of the original numerical schemes (LW and TTGC). In this study, the method is implemented and validated for single phase, gaseous flows. The extension of this method to multiphase flows should be straightforward and can be explored in the future. Also, the extension of this method to moving grid such as in stator-rotor interaction problems can also be looked at in the future.

A new reduced mechanism is derived from the state of the art detailed mechanism (POLIMI mechanism) using the in-house code ARCANE. Even though the predictions using the POLIMI mechanism is quite close to that of other available mechanisms such as GRI and UCSD as far as properties such as laminar flame speed, peak flame temperature and ignition delay times are concerned, POLIMI mechanism is found to predict NO emissions in counter flow diffusion flames accurately. Hence, the POLIMI mechanism is used for deriving the reduced mechanism. The reduced mechanisms consisting of 23 transported species and 19 QSS species is then validated with respect to the detailed mechanism using canonical 0D and 1D flames. The reduced mechanism is found to reproduce all the key flame properties of interest accurately (within 5% tolerance for laminar flame speed, 10 K for peak flame temperature and 10% for species production rates). The reduced mechanism is further validated with respect to a 3-D, laminar jet diffusion flame for which radial species profile and temperature measurements are available. The computed solution using the reduced mechanism is found to be in very good agreement with the experimental values thereby ascertaining the accuracy of the mechanism.

The LESAULTS method is then coupled with the RTE solver PRISSMA in an asynchronous manner. The theoretical speed up limit attainable using this approach is derived. The method is then applied to study the 3-D, axisymmetric laminar jet diffusion flame for which radiative heat flux measurements are available. The numerically observed speed-up is found to be very close to the

8. CONCLUSIONS AND PERSPECTIVES

theoretical speed-up limit derived earlier. Computed heat flux values are also observed to be in good agreement with experimentally observed values.

Finally, all the sub-models described above are applied to simulate the reactive flow inside the steam cracker. The LESAULTS-PRISSMA coupling provided a speed-up of approximately three times to that of the conventional solver. The mean flow and combustion fields obtained from LES reveal interesting features which are hitherto observable using RANS. By developing a framework for accelerating LES simulations of big combustion devices, the author is confident that the steam-cracking community will embrace LES in their design and analysis workflows in the near future.

Appendix A

Analytically reduced mechanism

The transported species in the reduced mechanism derived in Chapter 5 and their transport properties are provided in Table A.1 below.

Species Name	Schmidt Number	Lewis Number	Prandtl Number
N ₂	0.7067	1.0315	
H ₂	0.2062	0.3010	
H	0.1234	0.1801	
O ₂	0.7485	1.0925	
O	0.4816	0.7030	
H ₂ O	0.5555	0.8108	
OH	0.4910	0.7166	
CO	0.7513	1.0965	
CO ₂	0.9411	1.3736	
CH ₄	0.5783	0.8441	
CH ₃	0.6751	0.9853	
CH ₂	0.6598	0.9631	0.6851
CH	0.4500	0.6568	
CH ₃ OH	0.8831	1.2890	
CH ₂ O	0.8635	1.2604	
C ₂ H ₄	0.7741	1.1299	
C ₂ H ₂	0.8166	1.1919	
NO	0.7575	1.1057	
N ₂ O	0.9367	1.3672	
NO ₂	0.8513	1.2426	
HCN	0.8616	1.2576	
NNH	0.7697	1.1234	
NH ₂	0.4669	0.6815	

Table A.1: Transported species and their transport properties in the reduced mechanism

The QSS species in the reduced mechanism are listed as follows:
HO₂, CH₂(S), C, CH₃O, CH₂OH, HCO, C₂H₆, C₂H₅, C₂H₃, CH₂CHO,

A. ANALYTICALLY REDUCED MECHANISM

HCCO,HNC,HNCO,HOCN,N,NH,NCN,NCO,H₂CN

The viscosity of the mixture of gases in the reduced mechanism is given by the power law,

$$\mu = 5.73 \times 10^{-5} \left(\frac{T}{1666.78} \right)^{0.7803} \quad (\text{A.1})$$

Bibliography

- [1] EIA energy outlook 2020 with projections to 2050. 58(12):7250–7257, 2019. viii, 2, 3
- [2] Global Energy Review 2020. *Global Energy Review 2020*, 2020. 4
- [3] Ismaël Amghizar, Laurien A. Vandewalle, Kevin M. Van Geem, and Guy B. Marin. New Trends in Olefin Production. *Engineering*, 3(2):171–178, 2017. 4, 7
- [4] Heinz Zimmerman and Roland Walzl. Ethylene. *Ullmann's Encyclopedia of Industrial Chemistry*, pages 797–809, 2012. 4
- [5] C. Chang, W. H. Lang, and R. Smith. The conversion of methanol and other o-compounds to hydrocarbons over zeolite catalysts: Ii. pressure effects. *Journal of Catalysis*, 56:169–173, 1979. 5
- [6] Michael Stöcker. Methanol-to-hydrocarbons: Catalytic materials and their behavior. *Microporous and Mesoporous Materials*, 29(1-2):3–48, 1999. 5
- [7] Samia Ilias and Aditya Bhan. Mechanism of the catalytic conversion of methanol to hydrocarbons. *ACS Catalysis*, 3(1):18–31, 2013. 5
- [8] Unni Olsbye, Stian Svelle, Karl Petter Lillerud, Z. H. Wei, Y. Y. Chen, Junfen F. Li, Jianguo G. Wang, and Weibin B. Fan. The formation and degradation of active species during methanol conversion over protonated zeotype catalysts. *Chemical Society Reviews*, 44(20):7155–7176, 2015. 5
- [9] Veronique Van Speybroeck, Kristof De Wispelaere, Jeroen Van Der Mynsbrugge, Matthias Vandichel, Karen Hemelsoet, and Michel Waroquier. First principle chemical kinetics in zeolites: The methanol-to-olefin process as a case study. *Chemical Society Reviews*, 43(21):7326–7357, 2014. 5
- [10] Unni Olsbye, Stian Svelle, Morten Bjrgen, Pablo Beato, Ton V.W. Janssens, Finn Joensen, Silvia Bordiga, and Karl Petter Lillerud. Conversion of

BIBLIOGRAPHY

- methanol to hydrocarbons: How zeolite cavity and pore size controls product selectivity. *Angewandte Chemie - International Edition*, 51(24):5810–5831, 2012. 5
- [11] Irina Yarulina, Abhishek Dutta Chowdhury, Florian Meirer, Bert M. Weckhuysen, and Jorge Gascon. Recent trends and fundamental insights in the methanol-to-hydrocarbons process. *Nature Catalysis*, 1(6):398–411, 2018. 5
- [12] Peng Tian, Yingxu Wei, Mao Ye, and Zhongmin Liu. Methanol to olefins (MTO): From fundamentals to commercialization. *ACS Catalysis*, 5(3):1922–1938, 2015. 5
- [13] China methanol demand to improve on MTO start-up; downstream weak. <https://www.icis.com/explore/resources/news/2019/06/28/10384502/china-methanol-demand-to-improve-on-mto-start-up-downstream-weak>. Accessed: 2020-11-18. 5
- [14] Hirsu M. Torres Galvis and Krijn P. De Jong. Catalysts for production of lower olefins from synthesis gas: A review. *ACS Catalysis*, 3(9):2130–2149, 2013. 6
- [15] Kang Cheng, Bang Gu, Xiaoliang Liu, Jincan Kang, Qinghong Zhang, and Ye Wang. Direct and Highly Selective Conversion of Synthesis Gas into Lower Olefins: Design of a Bifunctional Catalyst Combining Methanol Synthesis and Carbon-Carbon Coupling. *Angewandte Chemie*, 128(15):4803–4806, 2016. 6
- [16] Feng Jiao, Jinjing Li, Xiulian Pan, Jianping Xiao, Haobo Li, Hao Ma, Mingming Wei, Yang Pan, Zhongyue Zhou, Mingrun Li, Shu Miao, Jian Li, Yifeng Zhu, Dong Xiao, Ting He, Junhao Yang, Fei Qi, Qiang Fu, and Xinhe Bao. Selective conversion of syngas to light olefins. *Science*, 351(6277):1065–1068, 2016. 6
- [17] Tiejun Lin, Kun Gong, Caiqi Wang, Yunlei An, Xinxing Wang, Xingzhen Qi, Shenggang Li, Yongwu Lu, Liangshu Zhong, and Yuhua Sun. Fischer-Tropsch Synthesis to Olefins: Catalytic Performance and Structure Evolution of Co₂C-Based Catalysts under a CO₂ Environment. *ACS Catalysis*, 9(10):9554–9567, 2019. 6

- [18] C. Boyer, J. Gazarian, V. Lecocq, S. Maury, A. Forret, J. M. Schweitzer, and V. Souchon. Development of the Fischer-Tropsch Process: From the Reaction Concept to the Process Book. *Oil and Gas Science and Technology*, 71(3), 2016. 6
- [19] Liangshu Zhong, Fei Yu, Yunlei An, Yonghui Zhao, Yuhan Sun, Zhengjia Li, Tiejun Lin, Yanjun Lin, Xingzhen Qi, Yuanyuan Dai, Lin Gu, Jinsong Hu, Shifeng Jin, Qun Shen, and Hui Wang. Cobalt carbide nanoprisms for direct production of lower olefins from syngas. *Nature*, 538(7623):84–87, 2016. 6
- [20] D. Salerno, H. R. Godini, A. Penteado, E. Esche, and G. Wozny. *Techno-Economic Evaluation of an Oxidative Coupling of Methane Process at Industrial Scale Production*, volume 38. Elsevier Masson SAS, 2016. 6
- [21] H. Godini. Analysis of individual integrated packed-bed membrane reactors for oxidative coupling of methane. *PhD Thesis*, 2014. 6
- [22] Madhav Ghanta, Darryl Fahey, and Bala Subramaniam. Environmental impacts of ethylene production from diverse feedstocks and energy sources. *Applied Petrochemical Research*, 4(2):167–179, 2014. 6
- [23] Yu Zhang. *Computational Fluid Dynamics-Based Fire-Side Modeling of Steam Cracking Furnaces*. 2016. viii, 7
- [24] Charles E. Baukal. *The John Zink Hamworthy combustion handbook, second edition: Volume 3: Applications*. 2013. 9, 12
- [25] . https://www.kubota.com/products/materials/products/cracking_coil/mert.html. Accessed: 2021-03-24. 11
- [26] Manqi Zhu. Simulation Aux Grandes Echelles Du Craquage Thermique Dans L’Industrie Petrochimique. *PhD Thesis*, 2015. 11
- [27] Charles E. Baukal. *The John Zink Hamworthy Combustion Handbook, second edition: Volume 2 - Design and Operations*, volume 2. 2013. viii, 16
- [28] Ismaël Amghizar, Jens N. Dedeyne, David J. Brown, Guy B. Marin, and Kevin M. Van Geem. Sustainable innovations in steam cracking: Co₂ neutral olefin production. *Reaction Chemistry and Engineering*, 5(2):239–257, 2020. 17, 19

BIBLIOGRAPHY

- [29] Carl M. Schietekat, Marco W.M. van Goethem, Kevin M. Van Geem, and Guy B. Marin. Swirl flow tube reactor technology: An experimental and computational fluid dynamics study. *Chemical Engineering Journal*, 238:56 – 65, 2014. Proceedings of the XX International conference on Chemical Reactors CHEMREACTOR-20. 17
- [30] Seyed Abotorab, Mousazadeh Moosavi, and Reza Tahery. Integrating Gas Turbines with Cracking Heaters in Ethylene Plants. (July), 2014. 19
- [31] Walter E. Lobo and James E. Evans. Heat transfer in the radiant section of petroleum heaters. *Transactions of the AIChE*, 16(3):316–324, 1939. 21, 23
- [32] Richard W. J. Robertson and Deran Hanesian. An Optimization Study of the pyrolysis of ethane in a tubular reactor. *Industrial & Engineering Chemistry*, 16(3):316–324, 1975. 21, 23
- [33] Patrick M. Plehiers and Gilbert F. Froment. Firebox Simulation of Olefin Units. *Chemical Engineering Communications*, 80(1):81–99, 1989. 21, 23
- [34] J. J. De Saegher, T. Detemmerman, and G. F. Froment. Three Dimensional Simulation of High Severity Internally Finned Cracking Coils for Olefins Production. *Revue de l'Institut Français du Pétrole*, 51(2):245–260, 1996. 21
- [35] T. Detemmerman and G. F. Froment. Three Dimensional Coupled Simulation of Furnaces and Reactor Tubes for the Thermal Cracking of Hydrocarbons. *Oil & Gas Science and Technology*, 53(2):181–194, 1998. 21, 23
- [36] Arno J M Oprins, Geraldine J Heynderickx, and Guy B Marin. Three-Dimensional Asymmetric Flow and Temperature Fields in Cracking Furnaces. *Industrial & Engineering Chemistry Research*, 40:5087–5094, 2001. 22, 23
- [37] A. J.M. Oprins and G. J. Heynderickx. Calculation of three-dimensional flow and pressure fields in cracking furnaces. *Chemical Engineering Science*, 58(21):4883–4893, 2003. 22, 23
- [38] Q Tang, M Bockelie, M Cremer, M Denison, C Montgomery, and A Sarofim. Advanced CFD Tools for Modeling Lean Premixed Combustion in Ultra-Low NO_x Burners in Process Heaters. *AFRC-JFRC Joint International Symposium*, (x):1–22, 2004. 22, 23, 180

- [39] Yun Long Han, Rui Xiao, and Mingyao Zhang. Combustion and pyrolysis reactions in a naphtha cracking furnace. *Chemical Engineering and Technology*, 30(1):112–120, 2007. 22, 23
- [40] X. Lan, J. Gao, C. Xu, and H. Zhang. Numerical simulation of transfer and reaction processes in ethylene furnaces. *Chemical Engineering Research and Design*, 85(12 A):1565–1579, 2007. 22, 23
- [41] Gasser Hassan, Mohamed Pourkashanian, Derek Ingham, Lin Ma, Paul Newman, and Anand Odedra. Predictions of CO and NO_x emissions from steam cracking furnaces using GRI2.11 detailed reaction mechanism - A CFD investigation. *Computers and Chemical Engineering*, 58(x):68–83, 2013. 22, 23
- [42] Hossein Mohammad Ghasemi, Neda Gilani, and Jafar Towfighi Daryan. CFD Simulation of Propane Thermal Cracking Furnace and Reactor: A Case Study. *International Journal of Chemical Reactor Engineering*, 15(3), 2017. 22, 23
- [43] H A J Vercaemmen and G F Froment. Simulation of Thermal Cracking Furnaces. *Chemical Reaction Engineering*, 1978. 23
- [44] Geraldine J. Heynderickx, Arno J.M. Oprins, Guy B. Marin, and Erik Dick. Three-dimensional flow patterns in cracking furnaces with long-flame burners. *AIChE Journal*, 47(2):388–400, 2001. 23
- [45] Hu Guihua, Wang Honggang, and Qian Feng. Numerical simulation on flow, combustion and heat transfer of ethylene cracking furnaces. *Chemical Engineering Science*, 66(8):1600–1611, 2011. 23
- [46] Guihua Hu, Honggang Wang, Feng Qian, Kevin M. Van Geem, Carl M. Schietekat, and Guy B. Marin. Coupled simulation of an industrial naphtha cracking furnace equipped with long-flame and radiation burners. *Computers and Chemical Engineering*, 38:24–34, 2012. 23
- [47] Denis Veynante Thierry Poinso. Theoretical and Numerical Combustion, Second Edition. *Decision Support Systems*, 38(4):557–573, 2005. 32, 36
- [48] Kenneth K. Kuo and Ragini Acharya. *Fundamentals of turbulent and multiphase combustion*. 2012. 32, 34
- [49] Kenneth K. Kuo. *Principle of Combustion*. John Wiley Sons, Inc., second edition, 2005. 33

BIBLIOGRAPHY

- [50] Alexandre Ern and Vincent Giovangigli. Impact of detailed multicomponent transport on planar and counterflow hydrogen/air and methane/air flames. *Combustion science and technology*, 149(1):157–181, 1999. 35
- [51] E Garnier, Nikolaus Adams, and Pierre Sagaut. *LES for compressible flows*. 2009. 37
- [52] Stephen B. Pope. *Turbulent Flows*. Cambridge University Press. 37
- [53] Franck Nicoud, Hubert Baya Toda, Olivier Cabrit, Sanjeeb Bose, and Jungil Lee. Using singular values to build a subgrid-scale model for large eddy simulations. *Physics of Fluids*, 23(8), 2011. 38
- [54] Michael F. Modest. *Radiative Heat Transfer*. Number 2. 2003. 41, 180
- [55] Jorge Amaya. *Unsteady coupled convection, conduction and radiation simulations on parallel architectures for combustion applications*. PhD thesis, Institut Nationale Polytechnique de Toulouse, 2011. 43, 184
- [56] Damien Poitou, Mouna El Hafi, and Bénédicte Cuenot. Analysis of radiation modeling for turbulent combustion: Development of a methodology to couple turbulent combustion and radiative heat transfer in les. *Journal of Heat Transfer*, 133(6), 2011. 43
- [57] Charney J. G., R Fjortoft, and J. Von Neumann. Te l I u s. *A Quarterly Journal of Geophysics*, 2(4), 1950. 47
- [58] Charles Hirsch. *Numerical Computation of Internal and External Flows*, volume 9780521871. 2007. 48
- [59] Tapan Sengupta. *High Accuracy Computing Methods: Fluid Flows and Wave Phenomena*. Cambridge University Press, 2013. 48
- [60] T. K. Sengupta, A. Dipankar, and P. Sagaut. Error dynamics: Beyond von Neumann analysis. *Journal of Computational Physics*, 226(2):1211–1218, 2007. 48
- [61] V. K. Suman, Tapan K. Sengupta, C. Jyothi Durga Prasad, K. Surya Mohan, and Deepanshu Sanwalia. Spectral analysis of finite difference schemes for convection diffusion equation. *Computers and Fluids*, 150:95–114, 2017. 48

- [62] Soumyo Sengupta, Tapan K. Sengupta, Jyothi Kumar Puttam, and Keshava Suman Vajjala. Global spectral analysis for convection-diffusion-reaction equation in one and two-dimensions: Effects of numerical anti-diffusion and dispersion. *Journal of Computational Physics*, 408, 2020. 48
- [63] Manoj K. Rajpoot, Tapan K. Sengupta, and Pravir K. Dutt. Optimal time advancing dispersion relation preserving schemes. *Journal of Computational Physics*, 229(10):3623–3651, 2010. 49
- [64] Olivier Colin and Michael Rudgyard. Development of High-Order Taylor-Galerkin Schemes for LES. *Journal of Computational Physics*, 162(2):338–371, 2000. 49, 58, 103
- [65] N Lamarque. Schémas numériques et conditions limites pour la simulation aux grandes échelles de la combustion diphasique dans les foyers d’hélicoptère. *Thesis*, page 213, 2007. 49
- [66] C. W. Hirt. Heuristic stability theory for finite-difference equations. *Journal of Computational Physics*, 2(4):339–355, 1968. 49
- [67] D. F. Griffiths, I. Christie, and A. R. Mitchell. Analysis of error growth for explicit difference schemes in conductionconvection problems. *International Journal for Numerical Methods in Engineering*, 15(7):1075–1081, 1980. 49
- [68] J. L. Siemieniuch and I. Gladwell. Analysis of explicit difference methods for a diffusion-convection equation. *International Journal for Numerical Methods in Engineering*, 12(6):899–916, 1978. 49
- [69] P Wesseling. Von Neumann stability conditions for the convection-diffusion equation. *IMA Journal of Numerical Analysis*, pages 583–598, 1996. 49
- [70] K. W. Morton. Stability of finite difference approximations to a diffusionconvection equation. *International Journal for Numerical Methods in Engineering*, 15(5):677–683, 1980. 49
- [71] Yue-Kuen Kwok. Stability analysis of six-point finite difference schemes for the constant coefficient convective-diffusion equation. *Computers & mathematics with applications*, 23(12):3–11, 1992. 49
- [72] Ercilia Sousa. Finite differences for the convection-diffusion equation: On stability and boundary conditions. *Phd. Thesis*, 2001. 50

BIBLIOGRAPHY

- [73] A. C. Hindmarsh, P. M. Gresho, and D. F. Griffiths. The stability of explicit Euler time-integration for certain finite difference approximations of the multi-dimensional advection-diffusion equation. *International Journal for Numerical Methods in Fluids*, 4(9):853–897, 1984. 50
- [74] J. G. Verwer and B. P. Sommeijer. Stability Analysis of an Odd-Even-Line Hopscotch Method for Three- Dimensional Advection- Diffusion Problems. *SIAM Journal on Numerical Analysis*, 34(1):376–388, 1997. 50
- [75] VK Suman, Tapan K Sengupta, C Jyothi Durga Prasad, K Surya Mohan, and Deepanshu Sanwalia. Spectral analysis of finite difference schemes for convection diffusion equation. *Computers & Fluids*, 150:95–114, 2017. 50, 62
- [76] Tony W.H. Sheu, S. K. Wang, and R. K. Lin. An Implicit Scheme for Solving the Convection-Diffusion-Reaction Equation in Two Dimensions. *Journal of Computational Physics*, 164(1):123–142, 2000. 50
- [77] C. Michoski, A. Alexanderian, C. Paillet, E. J. Kubatko, and C. Dawson. *Stability of Nonlinear Convection–Diffusion–Reaction Systems in Discontinuous Galerkin Methods*, volume 70. 2017. 50
- [78] Tom Gustafsson, Rolf Stenberg, and Juha Videman. A stabilised finite element method for the plate obstacle problem. *arXiv*, 2017. 50
- [79] Naveed Shahid, Nauman Ahmed, Dumitru Baleanu, Ali Saleh Alshomrani, Muhammad Sajid Iqbal, Muhammad Aziz Ur Rehman, Tahira Sumbal Shaikh, and Muhammad Rafiq. Novel numerical analysis for nonlinear advection-reaction-diffusion systems. *Open Physics*, 18(1):112–125, 2020. 50
- [80] Eleonore Cuenot, Bénédicte and Riber. Simulation des Grandes Echelles de flammes de spray et modélisation de la combustion non-prémélangée. 2017. 74
- [81] Vincent Brunet, Emma Croner, Alexandre Minot, Jérôme De Laborderie, Eric Lippinois, Stéphane Richard, Jean François Boussuge, Jérôme Dombard, Florent Duchaine, Laurent Gicquel, Thierry Poinot, Guillaume Puigt, Gabriel Staffelbach, Luis Segui, Olivier Vermorel, Nadège Villedieu, Jean Sébastien Cagnone, Koen Hillewaert, Michel Rasquin, Ghislain Lartigue, Vincent Moureau, Vincent Couailler, Emeric Martin, Marta De La

- Llave Plata, Jean Marie Le Gouez, and Florent Renac. Comparison of various CFD codes for les simulations of turbomachinery: From inviscid vortex convection to multi-stage compressor. *Proceedings of the ASME Turbo Expo*, 2C-2018, 2018. 84
- [82] Haecheon Choi and Parvez Moin. Effects of the Computational Time Step on Numerical Solutions of Turbulent Flow, 1998. 86
- [83] Tapan K. Sengupta, V. K. Sathyanarayanan, M. Sriramkrishnan, and Akhil Mulloth. Role of Time Integration in Computing Transitional Flows Caused by Wall Excitation. *Journal of Scientific Computing*, 65(1):224–248, 2015. 86
- [84] Y. A. Omelchenko and H. Karimabadi. Self-adaptive time integration of flux-conservative equations with sources. *Journal of Computational Physics*, 216(1):179–194, 2006. 87
- [85] Thomas Unfer. An asynchronous framework for the simulation of the plasma/flow interaction. *Journal of Computational Physics*, 236(1):229–246, 2013. 87
- [86] Asma Toumi, Guillaume Dufour, Ronan Perrussel, and Thomas Unfer. Asynchronous numerical scheme for modeling hyperbolic systems. *Comptes Rendus Mathematique*, 353(9):843–847, 2015. 87
- [87] Thomas Unfer, Jean Pierre Boeuf, François Rogier, and Frédéric Thivet. An asynchronous scheme with local time stepping for multi-scale transport problems: Application to gas discharges. *Journal of Computational Physics*, 227(2):898–918, 2007. 87
- [88] Thomas Unfer, Jean Pierre Boeuf, François Rogier, and Frédéric Thivet. Multi-scale gas discharge simulations using asynchronous adaptive mesh refinement. *Computer Physics Communications*, 181(2):247–258, 2010. 87
- [89] V. A. Semiletov and S. A. Karabasov. CABARET scheme for computational aero acoustics: Extension to asynchronous time stepping and 3D flow modelling. *International Journal of Aeroacoustics*, 13(3-4):321–336, 2014. 87
- [90] J Berger and Joseph Olinger. Adaptive Mesh Refinement for Hyperbolic Partial Differential Equations *. 512:484–512, 1984. 87

BIBLIOGRAPHY

- [91] M. J. Berger and P. Colella. Local adaptive mesh refinement for shock hydrodynamics. *Journal of Computational Physics*, 6484:249, 1989. 87
- [92] A. S. Almgren, J. B. Bell, and W. Y. Crutchfield. Approximate projection methods: Part I. Inviscid analysis. *SIAM Journal on Scientific Computing*, 22(4):1139–1159, 2001. 87
- [93] John B Bell, Phillip Colella, and Harland M Glaz. In this paper we develop a second-order projection method for the incompressible Navier-Stokes equations. *Journal of Computational Physics*, 283:257–283, 1989. 87
- [94] John B. Bell, Phillip Colella, and Louis H. Howell. An efficient second-order projection method for viscous incompressible flow. *10th Computational Fluid Dynamics Conference, 1991*, 1991. 87
- [95] Daniel F. Martin, Phillip Colella, and Daniel Graves. A cell-centered adaptive projection method for the incompressible Navier-Stokes equations in three dimensions. *Journal of Computational Physics*, 227(3):1863–1886, 2008. 87
- [96] Mark Sussman, Ann S. Almgren, John B. Bell, Phillip Colella, Louis H. Howell, and Michael Welcome. An adaptive level set approach for incompressible two-phase flows. *American Society of Mechanical Engineers, Fluids Engineering Division (Publication) FED*, 238:355–360, 1996. 87
- [97] Stanley Osher and Richard Sanders. Numerical Approximations to Nonlinear Conservation Laws with Locally Varying Time and Space Grids. *Mathematics of Computation*, 41(164):321, 1983. 88
- [98] Clint Dawson and Robert Kirby. High Resolution Schemes for Conservation laws with locally varying time steps. *Society for Industrial and Applied Mathematics*, 22(6):2256–2281, 2001. 88
- [99] Li Liu, Xiaodong Li, and Fang Q. Hu. Nonuniform time-step Runge-Kutta discontinuous Galerkin method for Computational Aeroacoustics. *Journal of Computational Physics*, 229(19):6874–6897, 2010. 88
- [100] Li Liu, Xiaodong Li, and Fang Q. Hu. Nonuniform-time-step explicit Runge-Kutta scheme for high-order finite difference method. *Computers and Fluids*, 105:166–178, 2014. 88

- [101] Oswald Knoth and Ralf Wolke. Implicit-explicit Runge-Kutta methods for computing atmospheric reactive flows. *Applied Numerical Mathematics*, 28(2-4):327–341, 1998. 88
- [102] Adrian Sandu. A class of multirate infinitesimal Gark methods. *SIAM Journal on Numerical Analysis*, 57(5):2300–2327, 2019. 88
- [103] G. Jeanmasson, I. Mary, and L. Mieussens. On some explicit local time stepping finite volume schemes for CFD. *Journal of Computational Physics*, 397, 2019. 88
- [104] Weilun Quan, Steven J. Evans, and Harold M. Hastings. Efficient integration of a realistic two-dimensional cardiac tissue model by domain decomposition. *IEEE Transactions on Biomedical Engineering*, 45(3):372–385, 1998. 88
- [105] Olivier Esnault, Matthieu Boileau, Ronan Vicquelin, Benoît Fiorina, and Olivier Gicquel. A method to accelerate LES explicit solvers using local time-stepping. *48th AIAA Aerospace Sciences Meeting Including the New Horizons Forum and Aerospace Exposition*, (January), 2010. 88
- [106] Adèle Poubeau, Roberto Paoli, Antoine Dauplain, and Florent Duchaine. Large-Eddy Simulations of a Single-Species Solid Rocket Booster Jet. *AIAA Journal*, 53(6):1477–1491, 2014. 88
- [107] G. Wang, S. Moreau, F. Duchaine, N. Gourdain, and L. Gicquel. Large Eddy Simulations of the MT1 high-pressure turbine using TurboAVBP. *Proceeding of 21st Annual Conference of the CFD Society of Canada*, (May), 2013. 88
- [108] T.K. Sengupta. *Fundamentals of Computational Fluid Dynamics*. Universities Press, 2004. 102
- [109] X. Ma, G. S. Karamanos, and G. E. Karniadakis. Dynamics and low-dimensionality of a turbulent near wake. *Journal of Fluid Mechanics*, 410:29–65, 2000. 130, 133
- [110] S. Dong, G. E. Karniadakis, A. Ekmekci, and D. Rockwell. A combined direct numerical simulation-particle image velocimetry study of the turbulent near wake. *Journal of Fluid Mechanics*, 569:185–207, 2006. 130

BIBLIOGRAPHY

- [111] Rajat Mittal and Parviz Moin. Suitability of upwind-biased finite difference schemes for large-Eddy simulation of turbulent flows. *AIAA Journal*, 35(8):1415–1417, 1997. 130
- [112] G.B. Deng, J. Piquet, P. Queutey, and M. Visonneau. Vortex-shedding flow predictions with eddy-viscosity models. In W. RODI and F. MARTELLI, editors, *Engineering Turbulence Modelling and Experiments*, pages 143–152. Elsevier, Oxford, 1993. 130
- [113] Jared Cox, Christopher Rumsey, Kenneth Brentner, and B. Younis. Computation of sound generated by viscous flow over a circular cylinder. 05 1997. 130
- [114] L. Ong and J. Wallace. The velocity field of the turbulent very near wake of a circular cylinder. *Experiments in Fluids*, 20(6):441–453, 1996. 130
- [115] Arthur G. Kravchenko and Parviz Moin. Numerical studies of flow over a circular cylinder at $Re_D=3900$. *Physics of Fluids*, 12(2):403–417, 2000. 130, 133
- [116] B. N. Rajani, A. Kandasamy, and Sekhar Majumdar. LES of flow past circular cylinder at $Re = 3900$. *Journal of Applied Fluid Mechanics*, 9(3):1421–1435, 2016. 131
- [117] Thomas Jaravel, Riber Eleonore, Cuenot Benedicte, and Perrine Pepiot. Prediction of flame structure and pollutant formation of sandia flame d using large eddy simulation with direct integration of chemical kinetics. *Combustion and Flame*, 188:180–198, 02 2018. 139, 140
- [118] Benedetta Franzelli, Eleonore Riber, and Bénédicte Cuenot. Impact of the chemical description on a Large Eddy Simulation of a lean partially premixed swirled flame. *Comptes Rendus - Mécanique*, 341(1-2):247–256, 2013. 140
- [119] Thomas Jaravel, Eleonore Riber, Bénédicte Cuenot, and Perrine Pepiot. Prediction of flame structure and pollutant formation of Sandia flame D using Large Eddy Simulation with direct integration of chemical kinetics. *Combustion and Flame*, 188:180–198, 2018. 141, 142, 161
- [120] . <https://www.ansys.com/products/fluids/ansys-chemkin-pro>. Accessed: 2021-03-24. 150
- [121] . <https://cantera.org/>. Accessed: 2021-03-24. 150, 158

- [122] H. Pitsch. A C ++ Computer Program for 0D Combustion and 1D Laminar Flame Calculation. <https://www.itv.rwth-aachen.de/downloads/flamemaster/>. Accessed: 2021-03-24. 150
- [123] Alberto Cuoci, Alessio Frassoldati, Tiziano Faravelli, and Eliseo Ranzi. A computational tool for the detailed kinetic modeling of laminar flames: Application to C₂H₄/CH₄ coflow flames. *Combustion and Flame*, 160(5):870–886, 2013. 150
- [124] C. Correa et. al. O. Deutschmann, S. Tischer. DETCHEM User Manual. <https://www.detchem.com/home>. Accessed: 2021-03-24. 150
- [125] James A. Miller, Robert J. Kee, and Charles K. Westbrook. Chemical kinetics and combustion modeling. *Annual Review of Physical Chemistry*, 41(3):345–387, 1990. 150
- [126] Eliseo Ranzi, Tiziano Faravelli, Paolo Gaffuri, and Angelo Sogaro. Low-temperature combustion: Automatic generation of primary oxidation reactions and lumping procedures. *Combustion and Flame*, 102(1-2):179–192, 1995. 150
- [127] G. M. Côme, V. Warth, P. A. Glaude, R. Fournet, F. Battin-Leclerc, and G. Scacchi. Computer-aided design of gas-phase oxidation mechanisms-Application to the modeling of n-heptane and iso-octane oxidation. *Symposium (International) on Combustion*, 26(1):755–762, 1996. 150
- [128] W. H. Green, P. I. Barton, B. Bhattacharjee, D. M. Matheu, D. A. Schwer, J. Song, R. Sumathi, H. H. Carstensen, A. M. Dean, and J. M. Grenda. Computer construction of detailed chemical kinetic models for gas-phase reactors. *Industrial and Engineering Chemistry Research*, 40(23):5362–5370, 2001. 150
- [129] Michael Frenklach, Hai Wang, and Martin J. Rabinowitz. Optimization and analysis of large chemical kinetic mechanisms using the solution mapping method-combustion of methane. *Progress in Energy and Combustion Science*, 18(1):47–73, 1992. 150
- [130] John M. Simmie. Detailed chemical kinetic models for the combustion of hydrocarbon fuels. *Progress in Energy and Combustion Science*, 29(6):599–634, 2003. 150

BIBLIOGRAPHY

- [131] Stephen J. Klippenstein. From theoretical reaction dynamics to chemical modeling of combustion. *Proceedings of the Combustion Institute*, 36(1):77–111, 2017. 150
- [132] J. O. Hirschfelder, C. F. Curtiss, and Dorothy E. Campbell. The theory of flame propagation. IV. *Journal of Physical Chemistry*, 57(4):403–414, 1953. 151
- [133] D B Spalding, Phil Trans, and R Soc Lond. The theory of flame phenomena with a chain reaction. *Philosophical Transactions of the Royal Society of London. Series A, Mathematical and Physical Sciences*, 249(957):1–25, 1956. 151
- [134] Craig T. Bowman. An Experimental and Analytical Investigation of the High-Temperature Oxidation Mechanisms of Hydrocarbon Fuels. *Combustion Science and Technology*, 2(2-3):161–172, 1970. 151
- [135] Charles K. Westbrook and Frederick L. Dryer. Chemical kinetic modeling of hydrocarbon combustion. *Progress in Energy and Combustion Science*, 10(1):1–57, 1984. 151
- [136] Jürgen Warnatz. The structure of laminar alkane-, alkene-, and acetylene flames. *Symposium (International) on Combustion*, 18(1):369–384, 1981. 151
- [137] Philippe Dagaut, Jean Claude Boettner, and Michel Cathonnet. Methane oxidation: Experimental and kinetic modeling study. *Combustion Science and Technology*, 77(1-3):127–148, 1991. 151
- [138] Philippe Dagaut, Michel Cathonnet, and Jean claude Boettner. Kinetics of ethane oxidation. *International Journal of Chemical Kinetics*, 23(5):437–455, 1991. 151
- [139] Barbe, P, Battin-Leclerc, F, and Côme, GM. Experimental and modelling study of methane and ethane oxidation between 773 and 1573 k. *J. Chim. Phys.*, 92:1666–1692, 1995. 151
- [140] James A Miller and Craig T. Bowman. Mechanism and Modeling of Nitrogen Chemistry in Combustion. *Progress in Energy and Combustion Science*, 15(1-2):287–338, 1989. 151
- [141] . <http://combustion.berkeley.edu/grimech/releases.html>. Accessed: 2021-03-24. 151

- [142] . <http://web.eng.ucsd.edu/mae/groups/combustion/mechanism.html>. Accessed: 2021-03-24. 151
- [143] . http://ignis.usc.edu/Mechanisms/USC-Mech20II/USC_Mech20II.htm. Accessed: 2021-03-24. 151
- [144] . <http://web.stanford.edu/group/haiwanglab/JetSurF/JetSurF2.0/index.html>. Accessed: 2021-03-24. 151
- [145] E. Ranzi, A. Frassoldati, R. Grana, A. Cuoci, T. Faravelli, A. P. Kelley, and C. K. Law. Hierarchical and comparative kinetic modeling of laminar flame speeds of hydrocarbon and oxygenated fuels. *Progress in Energy and Combustion Science*, 38(4):468–501, 2012. 151
- [146] Wayne K. Metcalfe, Sinéad M. Burke, Syed S. Ahmed, and Henry J. Curran. A hierarchical and comparative kinetic modeling study of C1 - C2 hydrocarbon and oxygenated fuels. *International Journal of Chemical Kinetics*, 45(10):638–675, 2013. 151
- [147] N. Cohen and K. R. Westberg. Chemical Kinetic Data Sheets for High Temperature Chemical Reactions. *Journal of Physical and Chemical Reference Data*, 12(3):531–590, 1983. 151
- [148] N. Cohen and K. R. Westberg. Chemical Kinetic Data Sheets for High-Temperature Reactions. Part II. *Journal of Physical and Chemical Reference Data*, 20(6):1211–1311, 1991. 151
- [149] W. Tsang and R. F. Hampson. Chemical Kinetic Data Base for Combustion Chemistry. Part I. Methane and Related Compounds. *Journal of Physical and Chemical Reference Data*, 15(3):1087–1279, 1986. 151
- [150] Wing Tsang. Chemical Kinetic Data Base for Combustion Chemistry. Part 2. Methanol. *Journal of Physical and Chemical Reference Data*, 16(3):471–508, 1987. 151
- [151] D. L. Baulch, M. J. Pilling, C. J. Cobos, R. A. Cox, C. Esser, P. Frank, Th Just, J. A. Kerr, J. Troe, R. W. Walker, and J. Warnatz. Evaluated Kinetic Data for Combustion Modelling. *Journal of Physical and Chemical Reference Data*, 21(3):411–734, 1992. 151

BIBLIOGRAPHY

- [152] D. L. Baulch, C. T. Bowman, C. J. Cobos, R. A. Cox, Th Just, J. A. Kerr, M. J. Pilling, D. Stocker, J. Troe, W. Tsang, R. W. Walker, and J. Warnatz. Evaluated kinetic data for combustion modeling: Supplement II. *Journal of Physical and Chemical Reference Data*, 34(3):757–1397, 2005. 151
- [153] . <https://webbook.nist.gov/chemistry/>. Accessed: 2021-03-24. 151
- [154] . https://www.dlr.de/vt/en/desktopdefault.aspx/tabid-7603/12862_read-32379/. Accessed: 2021-03-24. 151
- [155] . <https://atct.anl.gov/>. Accessed: 2021-03-24. 151
- [156] Charles K. Westbrook, Yasuhiro Mizobuchi, Thierry J. Poinso, Phillip J. Smith, and Jürgen Warnatz. Computational combustion. *Proceedings of the Combustion Institute*, 30(1):125–157, 2005. 151, 152
- [157] Tianfeng Lu and Chung K. Law. Toward accommodating realistic fuel chemistry in large-scale computations. *Progress in Energy and Combustion Science*, 35(2):192–215, 2009. 151, 152
- [158] N. Zettervall, K. Nordin-Bates, E. J.K. Nilsson, and C. Fureby. Large Eddy Simulation of a premixed bluff body stabilized flame using global and skeletal reaction mechanisms. *Combustion and Flame*, 179:1–22, 2017. 153
- [159] U. Maas and S. B. Pope. Simplifying chemical kinetics: Intrinsic low-dimensional manifolds in composition space. *Combustion and Flame*, 88(3-4):239–264, 1992. 153
- [160] U Maas and S B Pope. Implementaion of simplified chemical kinetics based on intrinsic low-dimensional manifolds. pages 103–112, 1992. 153
- [161] J A Van Oijen and L P H De Goey. Modelling of Premixed Laminar Flames using Flamelet- Generated Manifolds. *Combustion Science and Technology*, 161(1):113–137, 2000. 153
- [162] Olivier Gicquel, Nasser Darabiha, and Dominique Thévenin. Laminar premixed hydrogen/air counterflow flame simulations using flame prolongation of ILDM with differential diffusion. *Proceedings of the Combustion Institute*, 28(2):1901–1908, 2000. 153
- [163] B. Yang and S. B. Pope. Treating chemistry in combustion with detailed mechanisms-in situ adaptive tabulation in principal directions-premixed combustion. *Combustion and Flame*, 112(1-2):85–112, 1998. 154

- [164] S B Pope. Computationally efficient implementation of combustion chemistry using in situ adaptive tabulation. *Combustion Theory and Modelling*, 1(May 2012):41–63, 2010. 154
- [165] Thomas Jaravel. *PREDICTION OF POLLUTANTS IN GAS TURBINES USING LARGE EDDY SIMULATION*. PhD thesis, 2016. 154
- [166] Anne Felden. Development of Analytically Reduced Chemistries (ARC) and applications in Large Eddy Simulations (LES) of turbulent combustion. 2017. 154
- [167] Lucien Gallen. *Prediction of soot particles in Gas Turbine Combustors using Large Eddy Simulation*. PhD thesis, 2020. 154
- [168] J. F. Griffiths. Reduced kinetic models and their application to practical combustion systems. *Progress in Energy and Combustion Science*, 21(1):25–107, 1995. 154
- [169] H Rabitz, M Kramer, and D Dacol. Sensitivity Analysis in Chemical Kinetics. *Annual Review of Physical Chemistry*, 34(1):419–461, 1983. 154
- [170] D M Hamby. A Review of Techniques for Parameter Sensitivity. *Environmental Monitoring and Assessment*, 32(c):135–154, 1994. 154
- [171] Tamás Turányi. Sensitivity analysis of complex kinetic systems. Tools and applications. *Journal of Mathematical Chemistry*, 5(3):203–248, 1990. 154
- [172] Nancy J. Brown, L. I. Guoping, and Michael L. Koszykowski. Mechanism reduction via principal component analysis, 1997. 154
- [173] T. Turányi. Reduction of large reaction mechanisms. *New Journal of Chemistry*, 14:795–803, 1990. 154
- [174] A. Tomlin, M. Pilling, T. Turányi, J. Merkin, and J. Brindley. Mechanism reduction for the oscillatory oxidation of hydrogen; sensitivity and quasi-steady-state analyses. *Combustion and Flame*, 91:107–130, 1992. 154
- [175] Tianfeng Lu and C. Law. Strategies for mechanism reduction for large hydrocarbons: n-heptane. *Combustion and Flame*, 154:153–163, 2007. 155
- [176] P. Pepiot-Desjardins and H. Pitsch. An efficient error-propagation-based reduction method for large chemical kinetic mechanisms. *Combustion and Flame*, 154:67–81, 2008. 155

BIBLIOGRAPHY

- [177] R W Bilger, M B Esler, and S H Starner. Methane-Air Combustion. *Reactions*, (i), 2006. 156
- [178] Christine M. Vagelopoulos and Fokion N. Egolfopoulos. Direct experimental determination of laminar flame speeds. *Symposium (International) on Combustion*, 27(1):513–519, 1998. 157, 159
- [179] K. J. Bosschaart and L. P.H. De Goey. The laminar burning velocity of flames propagating in mixtures of hydrocarbons and air measured with the heat flux method. *Combustion and Flame*, 136(3):261–269, 2004. 157, 159
- [180] A. N. Mazas, B. Fiorina, D. A. Lacoste, and T. Schuller. Effects of water vapor addition on the laminar burning velocity of oxygen-enriched methane flames. *Combustion and Flame*, 158(12):2428–2440, 2011. 157, 159
- [181] K. Ya Troshin, A. A. Borisov, A. N. Rakhmetov, V. S. Arutyunov, and G. G. Politenkova. Burning velocity of methane-hydrogen mixtures at elevated pressures and temperatures. *Russian Journal of Physical Chemistry B*, 7(3):290–301, 2013. 157, 159
- [182] Guihua Hu, Carl M. Schietekat, Yu Zhang, Feng Qian, Geraldine Heynderickx, Kevin M. Van Geem, and Guy B. Marin. Impact of radiation models in coupled simulations of steam cracking furnaces and reactors. *Industrial and Engineering Chemistry Research*, 54(9):2453–2465, 2015. 158, 159
- [183] R V Ravikrishna and Normand M Laurendeau. Laser-induced fluorescence measurements and modeling of nitric oxide in methane-air and ethane-air counterflow diffusion flames. *Combustion and Flame*, 120(3):372–382, 2000. 160
- [184] A. A. Konnov. Implementation of the NCN pathway of prompt-NO formation in the detailed reaction mechanism. *Combustion and Flame*, 156(11):2093–2105, 2009. 161
- [185] . <https://chemistry.cerfacs.fr/en/arcane/>. Accessed: 2021-03-24. 162
- [186] P. Magre, F. Aguerre, G. Collin, P. Versaevel, F. Lacas, and J. Rolón. Temperature and concentration measurements by cars in counterflow laminar diffusion flames. *Experiments in Fluids*, 18:376–382, 1995. 169

- [187] S Ebrahim Abtahizadeh. *Numerical study of mild combustion: From laminar flames to Large Eddy Simulation of turbulent flames with Flamelet Generated Manifolds*. Number 2014. 2014. 170
- [188] Ebrahim Abtahizadeh, Alexey Sepman, Francisco Hernández-Pérez, Jeroen van Oijen, Anatoli Mokhov, Philip de Goey, and Howard Levinsky. Numerical and experimental investigations on the influence of preheating and dilution on transition of laminar coflow diffusion flames to Mild combustion regime. *Combustion and Flame*, 160(11):2359–2374, 2013. 170, 176
- [189] R. Viskanta and M. P. Mengü. Radiation heat transfer in combustion systems. *Progress in Energy and Combustion Science*, 13:97–160, 1987. 179
- [190] S. Manickavasagam and M. P. Menguc. Effective optical properties of pulverized coal particles determined from ft-ir spectrometer experiments. *Energy Fuels*, 7:860–869, 1993. 179
- [191] Vitali Kez, J. Consalvi, F. Liu, Tim Gronarz, J. Ströhle, R. Kneer, and B. Epple. Investigation of gas and particle radiation modelling in wet oxy-coal combustion atmospheres. *International Journal of Heat and Mass Transfer*, 133:1026–1040, 2019. 179
- [192] Y. Sivathanu, J. Gore, and J. Dolinar. Transient scalar properties of strongly radiating jet flames. *Combustion Science and Technology*, 76:45–66, 1991. 179
- [193] Y. Sivathanu and J. Gore. Transient structure and radiation properties of strongly radiating buoyant flames. *Journal of Heat Transfer-transactions of The Asme*, 114:659–665, 1992. 179
- [194] K. Maruta, M. Yoshida, Y. Ju, and T. Niioka. Experimental study on methane-air premixed flame extinction at small stretch rates in microgravity. 1996. 179
- [195] Liang Guo-fu. Study on the radiation properties and flame structure of hydrocarbon pool fires. *Fire Science and Technology*, 2009. 179
- [196] T. Guiberti, D. Durox, P. Scouffaire, and T. Schuller. Impact of heat loss and hydrogen enrichment on the shape of confined swirling flames. 2015. 179

BIBLIOGRAPHY

- [197] J. Consalvi and F. Liu. Radiative heat transfer in the core of axisymmetric pool fires i: Evaluation of approximate radiative property models. *International Journal of Thermal Sciences*, 84:104–117, 2014. 179
- [198] P. J. Coelho. Numerical simulation of the interaction between turbulence and radiation in reactive flows. *Progress in Energy and Combustion Science*, 33(4):311–383, 2007. 180
- [199] P. DesJardin and S. Frankel. Two-dimensional large eddy simulation of soot formation in the near-field of a strongly radiating nonpremixed acetylene-air turbulent jet flame. *Combustion and Flame*, 119:121–132, 1999. 180
- [200] W. Jones and M. Paul. Combination of dom with les in a gas turbine combustor. *International Journal of Engineering Science*, 43:379–397, 2005. 180
- [201] D. Joseph, M. Hafi, R. Fournier, and B. Cuenot. Comparison of three spatial differencing schemes in discrete ordinates method using three-dimensional unstructured meshes. *International Journal of Thermal Sciences*, 44:851–864, 2005. 181
- [202] R. G. Santos, M. Lecanu, S. Ducruix, O. Gicquel, E. Iacona, and D. Veynante. Coupled large eddy simulations of turbulent combustion and radiative heat transfer. *Combustion and Flame*, 152:387–400, 2008. 181
- [203] Damien Poitou, Mouna El Hafi, and Bénédicte Cuenot. Analysis of radiation modeling for turbulent combustion: Development of a methodology to couple turbulent combustion and radiative heat transfer in les. *Journal of Heat Transfer*, 133(6), 2011. 181, 186
- [204] . <https://www.cerfacs.fr/prisma/>. Accessed: 2021-03-24. 181
- [205] K. A. Jensen, J. Ripoll, A. Wray, D. Joseph, and M. Hafi. On various modeling approaches to radiative heat transfer in pool fires. *Combustion and Flame*, 148:263–279, 2007. 183
- [206] D. Joseph, P. Perez, M. Hafi, and B. Cuenot. Discrete ordinates and monte carlo methods for radiative transfer simulation applied to computational fluid dynamics combustion modeling. *Journal of Heat Transfer-transactions of The Asme*, 131:052701, 2009. 183

- [207] N. Kayakol, N. Sel, I. Campbell, and Ö. Gülder. Performance of discrete ordinates method in a gas turbine combustor simulator. *Experimental Thermal and Fluid Science*, 21:134–141, 2000. 183
- [208] M. Sakami, A. Charette, and V. L. Dez. Radiative heat transfer in three-dimensional enclosures of complex geometry by using the discrete-ordinates method. *Journal of Quantitative Spectroscopy Radiative Transfer*, 59:117–136, 1998. 183
- [209] J. Ströhle, U. Schnell, and K. Hein. A mean flux discrete ordinates interpolation scheme for general co-ordinates. 2001. 183
- [210] D. Joseph. Modélisation des transferts radiatifs en combustion par méthode aux ordonnées discrètes sur des maillages non structurés tridimensionnels. 2004. 184
- [211] . <https://w3.onera.fr/cwipi/bibliotheque-couplage-cwipi>. Accessed: 2021-03-24. 185
- [212] R. Santoro, H. Semerjian, and R. Dobbins. Soot particle measurements in diffusion flames. *Combustion and Flame*, 51:203–218, 1983. 189
- [213] I. M. Machado, P. Pagot, and F. M. Pereira. Experimental study of radiative heat transfer from laminar non-premixed methane flames diluted with CO₂ and N₂. *International Journal of Heat and Mass Transfer*, 158, 2020. 189, 190
- [214] B. Cuenot, F. Shum-Kivan, and S. Blanchard. The thickened flame approach for non-premixed combustion: Principles and implications for turbulent combustion modeling. *Combustion and Flame*, (xxxx):111702, 2021. 203